UNIVERSITÀ
DI PARMA

UNIVERSITA' DEGLI STUDI DI PARMA

DOTTORATO DI RICERCA IN
"SCIENZA E TECNOLOGIA DEI MATERIALI"

Ciclo XXXI

Fabrication and characterization of fibre reinforced UHTC composites

Coordinatore:
Prof. Enrico Dalcanale

Relatori:
Dott.ssa Diletta Sciti
Dott. Luca Zoli

Dottorando: Antonio Vinci

Anni 2015/2018

Anni 2015/2018

A me stesso

TABLE OF CONTENTS

Abstract **1**

List of publications **3**

1. Introduction **4**

1.1 Aim of the work 4

2. State of the art **6**

2.1 Ultra-high temperature ceramics 6

2.1.1 Introduction 6

2.1.2 Synthesis 7

2.1.3 Crystal structure 9

2.1.4 Sintering 13

2.1.5 Mechanical properties 15

2.1.6 Thermal properties 18

2.1.7 Electrical properties 20

2.1.8 Applications 21

2.2 Ceramic matrix composites 22

2.2.1 Introduction 22

2.2.2 Process 22

2.3 Ultra-high temperature ceramic matrix composites 23

2.3.1 Introduction 23

2.3.2 Process 23

2.3.3 Mechanical properties 25

2.3.4 Oxidation resistance 26

2.4 References 28

3. Experimental **37**

3.1 Process 37

3.1.1 Powder ball milling 37

3.1.2 Slurry infiltration 38

3.1.3 Hot pressing 39

3.2 Microstructural characterization 39
3.2.1 X-Ray diffraction analysis 39
3.2.2 Scanning electron microscopy 42
3.2.3 Energy-dispersive X-ray spectroscopy 45
3.3 Mechanical testing 47
3.3.1 Elastic modulus 48
3.3.2 Flexural strength 49
3.3.3 Fracture toughness 51
3.4 Oxidation resistance 53
3.4.1 Thermo-gravimetric analysis 53
3.4.2 Air furnace oxidation testing 55
3.5 Thermal diffusivity 56
3.5.1 Laser flash analysis 56
3.6 References 59

SECTION I

4. ZrB_2/SiC based UHTCMCs 61
4.1 Introduction 61
4.2 ZS10 61
4.2.1 Sintering behaviour 61
4.2.2 Microstructure 61
4.3 Mechanical properties 63
4.4 Influence of SiC content on the mechanical properties 65
4.4.1 Mixture compositions 65
4.4.2 Microstructure 66
4.4.3 Flexural strength 67
4.4.4 Fracture toughness 74
4.5 Oxidation resistance 82
4.5.1 Thermo-gravimetrix analysis 82
4.6 Influence of SiC content on the oxidation resistance 93
4.6.1 Microstructure 95
4.6.2 Oxidation model 99
4.7 Conclusions 102
4.8 References 104

5. ZrB_2/SiC/WC based UHTCMCs **108**
5.1 Introduction 108
5.2 ZSW 108
5.2.1 Sintering behaviour 108
5.2.2 Microstructure 109
5.2.3 Mechanical properties 111
5.2.4 Oxidation resistance 113
5.3 Conclusions 114
5.4 References 116

SECTION II
6. ZrC/SiC based UHTCMCs **118**
6.1 Introduction 118
6.2 ZC20 0/0 118
6.2.1 Sintering behaviour 119
6.2.2 Microstructure 120
6.2.3 High temperature strength 122
6.2.4 Microstructure after testing 124
6.2.5 Thermal diffusivity 128
6.3 References 129

7. TaC/SiC based UHTCMCs **131**
7.1 Introduction 131
7.2 TC20 0/0 131
7.2.1 Sintering behaviour 131
7.2.2 Microstructure 132
7.2.3 High temperature strength 134
7.2.4 Microstructure after testing 135
7.2.5 Thermal diffusivity 137
7.3 References 139

8. HfC/SiC based UHTCMCs **140**
8.1 Introduction 140
8.2 HC20 0/0 140
8.2.1 Sintering behaviour 140
8.2.2 Microstructure 141
8.2.3 High temperature strength 142
8.2.4 Microstructure after testing 144
8.2.5 Fracture surfaces 147
8.2.6 Thermal diffusivity 149
8.3 Influence of carbon fibre content 150
8.3.1 Microstructure 150
8.3.2 Mechanical behaviour 151
8.4 Conclusions 153
8.5 References 154

SECTION III

9. ZrB_2/ZrC based UHTCMCs **155**
9.1 Introduction 155
9.2 RMI of C-B/ZrB_2 with Zr_2Cu 158
9.2.1 Mixture compositions 158
9.2.2 Microstructure 158
9.2.3 Mechanical properties 159
9.4 Conclusions 160
9.5 References 161
10. Conclusions **164**
11. Acknowledgements **165**

Abstract

The thermal, chemical and mechanical environments typical of aero-propulsion applications, such as those characteristic of combustion chambers of high performance propulsion engines, introduce many problems from the point of view of materials. Next generation solid propellants have become more energetic, resulting in higher temperatures and pressures, and very hostile, erosive environments. The resistance of the materials currently used limits the maximum operational pressure; moreover materials such as graphite for boost throat applications have repeatedly shown unacceptable ablation/erosion rates, leading to a loss in performance due to throat widening. At the same time, external thermal protection systems (TPS) of civil space vehicles flying at Mach 7 must be able to withstand high temperature (beyond 2000°C), high heat flux (up to 15 MWm^{-2}) and the mechanical stresses associated with vibrations at launch and re-entry into Earth's atmosphere. Therefore, new thermal protection materials endowed with good oxidation, thermal shock and ablation resistance above 2000°C are required. Ultra-high temperature ceramics (UHTCs) have been gaining increasing interest among the scientific community as potential candidates for the application in extreme environments owing to their high melting points (> 3000°C) and high temperature strength but they have low fracture toughness and thermal shock resistance. In order to increase the damage tolerance of UHTCs, carbon fibres were considered as reinforcements. This thesis deals with the development and characterization of long fibre reinforced ultra-high temperature ceramics, with the objective of providing an understanding of the high temperature behaviour. The PhD activity was divided into three parts:

- The first part was focused on the development and characterization of fibre reinforced ZrB_2/SiC composites for the fabrication of thermal protection systems. A baseline material containing ZrB_2 + 10 vol% SiC was produced by slurry infiltration of carbon fibre preforms with an aqueous suspension containing the UHTC powders and hot pressed. The microstructure was analysed on the polished and fracture surface of the sample with SEM, EDX and XRD techniques. Then the flexural strength and fracture toughness were studied and correlated to the microstructure features. Following the mechanical characterization, the kinetics of oxidation were investigated via TGA in order to find the critical temperatures for the oxidation process. On the results obtained during this part of the work, the influence of SiC content on the mechanical properties and oxidation resistance was

studied. SiC was varied in amounts ranging between 5 – 20 % and the oxidation behaviour was studied up to 1650°C in air, showing how high amount of SiC lead to the full coverage of the specimens with a protective borosilicate layer. From this activity four papers have been published.

- The second part of the PhD activity was focused on the thermo-mechanical characterization from room temperature up to 2100°C of fibre reinforced composites with higher refractoriness, based on ZrC, TaC and HfC, for the application in nozzle inserts. In collaboration with Missouri University of Science and Technology (MS&T) and thanks to the JECS trust funding, under the supervision of professor Bill Fahrenholtz and Greg Hilmas, high temperature mechanical tests up to 2100°C were carried out on carbide composites produced at ISTEC. The determination of the yield strength at high temperature is of great importance for the design of engineering components that must withstand severe stresses in hostile environments. The studied composites retained high strength even above 2000°C, displaying plastic behaviour only at 2100°C and rupturing only at high strains. From this work, two publications were prepared and submitted (one has been recently accepted).

- The third part of the PhD activity dealt with a novel joint processing route based on slurry infiltration followed by reactive melt infiltration to produce carbon fibre reinforced ZrB_2/ZrC composites. In collaboration with the German Aerospace Centre (DLR) in Stuttgart, under the supervision of professor Dietmar Koch, carbon fibre preforms were infiltrated with B/ZrB_2 powders via slurry infiltration and then with liquid Zr_2Cu via reactive melt infiltration. The boron present in the starting powders led to the formation of fine ZrB_2 particles in the metal matrix, while the fibres reacted partially with the zirconium alloy to produce core rims of ZrC around the fibres. From mechanical tests, these specimens possess higher strength than the ZrB_2/SiC studied during the first section of this thesis but are also stiffer and more brittle, and therefore better suited for applications where high ultimate strains are not mandatory. From this activity 1 paper is in preparation and 2 orals are going to be presented at the next International Conference and Exposition on Advanced Ceramics and Composites 2019 (ICACC'19).

This three years activity has been carried out in the framework of the European Union's Horizon 2020 "Research and innovation programme" under grant agreement N°685594 (C^3HARME) and this thesis summarizes the highlights of the research activity.

List of publications

1. L. Zoli, A. Vinci, L. Silvestroni, D. Sciti, M. Reece, S. Grasso, Rapid spark plasma sintering to produce dense UHTCs reinforced with undamaged carbon fibres, Mater. Des. 130 (2017) 1–7. doi:10.1016/j.matdes.2017.05.029.

2. A. Vinci, L. Zoli, E. Landi, D. Sciti, Oxidation behaviour of a continuous carbon fibre reinforced ZrB_2–SiC composite, Corros. Sci. 123 (2017) 129–138. doi:10.1016/j.corsci.2017.04.012.

3. A. Vinci, L. Zoli, D. Sciti, C. Melandri, S. Guicciardi, Understanding the mechanical properties of novel UHTCMCs through random forest and regression tree analysis, Mater. Des. 145 (2018) 97–107. doi:10.1016/j.matdes.2018.02.061.

4. A. Vinci, L. Zoli, D. Sciti, Influence of SiC content on the oxidation of carbon fibre reinforced ZrB_2/SiC composites at 1500 and 1650 °C in air, J. Eur. Ceram. Soc. 38 (2018) 3767–3776. doi:10.1016/j.jeurceramsoc.2018.04.064.

5. L. Zoli, A. Vinci, P. Galizia, C. Melandri, Di. Sciti, On the thermal shock resistance and mechanical properties of novel unidirectional UHTCMCs for extreme environments, Sci. Rep. 8 (2018) 1–9. doi:10.1038/s41598-018-27328-x.

6. A. Vinci, L. Zoli, D. Sciti, J. Watts, G.E. Hilmas, W.G. Fahrenholtz, Mechanical behaviour of carbon fibre reinforced TaC/SiC and ZrC/SiC composites up to 2100°C, J. Eur. Ceram. Soc. 39 (2019) 780-787, doi:j.jeurceramsoc.2018.11.017

7. S. Failla, P. Galizia, L. Zoli, A. Vinci, D. Sciti, Toughening effect of non-periodic fiber distribution on crack propagation energy of UHTC composites, J. Alloys & Comp. 777 (2019) 612-618, doi:j.jallcom.2018.11.043

8. A. Vinci, L. Zoli, D. Sciti, Processing and characterization of carbon fibre reinforced ZrB_2/SiC/WC composites – Proceedings of the First Workshop for Young Ceramists, November 26-27, 2018, Bologna, Italy

9. S. Mungiguerra, G.D. Di Martino, A. Cecere, R. Savino, L. Silvestroni, A. Vinci, L. Zoli, D. Sciti, Arc-jet wind tunnel characterization of ultra-high-temperature ceramic matrix composites, Corros. Sci. (2019), in press, corrected proof, doi:10.1016/j.corsci.2018.12.039

10. L. Silvestroni, D. Sciti, L. Zoli, S. Failla, A. Vinci, V. Rubio, J. Binner, Effect of $MoSi_2$, $HfSi_2$ or WSi_2 on the ablation behaviour of ultra-high temperature ceramics, – under review

11. A. Vinci, L. Zoli, D. Sciti, J. Watts, G.E. Hilmas, W.G. Fahrenholtz, Influence of carbon fibre content on the strength of C/HfC-SiC at 2100°C, J. Eur. Ceram. Soc. - submitted

1. Introduction

1.1 Aim of the work

The demand for advanced thermal protection systems (TPS) related to hypersonic flight and rocket propulsion for use in extreme conditions, where temperatures as high as 2000°C are reached, has fostered the development of a new class of ultra-high temperature materials.

In the past few years, ultra-high temperature ceramics (UHTC) have gained increasing interest for the fabrication of reusable TPS for the leading edges of hypersonic aerospace vehicles. In particular, transition metal borides, such as zirconium and hafnium diborides, have been extensively investigated due to their high melting temperature, high thermal and electrical conductivity, good ablation resistance and ability to withstand extreme conditions. The major drawbacks of these materials are their low fracture toughness and propensity for catastrophic failure, and the high temperature required to achieve full densification.

Carbon/Carbon and Carbon/SiC composites currently used in aerospace applications, display excellent thermo-mechanical properties, low density, low thermal expansion and good thermal shock resistance. However, in C/C composites, the carbon fibres start oxidising at temperatures as low as 500 °C, and in C/SiC composites the protective layer of liquid SiO_2, originated from the oxidation of SiC, becomes chemically active above 1650 °C, leading to high erosion rates and the sublimation of its constituents, therefore compromising the life of the material.

By coupling the good fracture toughness and thermal shock resistance of CMCs and the oxidation and ablation resistance of UHTC materials, the above mentioned limits could be potentially overcome.

This thesis focuses on the fabrication and characterization of continuous fibre reinforced ultra-high temperature ceramics, with the objective of providing an understanding of the mechanical properties and high temperature behaviour of this novel class of materials. This work is composed of three sections:

1) In the first section the mechanical properties and oxidation behaviour of carbon fibre reinforced ZrB_2/SiC composites were studied. Then the effect of WC on the mechanical properties and oxidation resistance was investigated.

2) In the second section the high temperature mechanical behaviour of carbon fibre reinforced composites based on a carbide matrix, were studied up to 2100°C and the effect of fibre content on the plastic behaviour was assessed.
3) In the third section a novel processing route based on slurry infiltration followed by reactive melt infiltration to produce carbon fibre reinforced ZrB_2/ZrC composites was investigated.

The majority of this work was carried out at the Institute of Science and Technology for Ceramics – National Research Council (ISTEC – CNR) in Faenza. The measurements of thermal diffusivity and flexural strength at 2000°C were carried out at Missouri University of Science and Technology, in Rolla (MO), while reactive melt infiltration was conducted at the German Aerospace Center (DLR) in Stuttgart.

2. State of the art

2.1 Ultra-high temperature ceramics

2.1.1 Introduction

Ultra-high temperature ceramics (UHTCs) are a class of materials comprising the borides, carbides and nitrides of early transition metals characterized by high melting points, high hardness, chemical stability and oxidation resistance [1–5]. Majority of the research was motivated by unmet material needs for hypersonic aviation [2]. More specifically, improved materials are required in order to survive the conditions encountered by wing leading edges and propulsion system components in hypersonic aerospace vehicles as well as the harsh conditions associated with re-entry in earth's atmosphere and rocket propulsion. The combination of extreme temperatures, corrosive environments, high heat fluxes and temperature gradients is beyond the capabilities of current materials and this has led to the research of ultra-refractory materials. A common definition is that UHTCs are materials with a melting point above 3000°C. Another criterion used to classify these materials is their resistance in air; since there already exist materials that can withstand temperatures up to 1600°C, the ultra-high temperature regime is defined as any corrosive environment at temperatures above 1600°C. Since most UHTCs are borides, carbides and nitrides of early transition metals, any transition metal coupled with boron, carbon and nitrogen is considered a potential UHTC.

Among UHTCs, the diborides were extensively investigated due to their superior oxidation resistance compared to other refractory compounds such as carbides, nitrides and silicides . In particular, zirconium diboride (ZrB_2) and hafnium diboride (HfB_2) were identified as potential candidates for the application in harsh environment for the fabrication of nose cones, sharp leading edges, scramjet engines and components for the use in supersonic flight [1–4,6].

The high melting points, hardness and moduli of UHTCs are the result of strong covalent bonding between the constituent elements [6,7]. Moreover UHTCs are characterized by very negative energies of formation, resulting in excellent thermal and chemical stability under extreme conditions [6,7]. The higher thermal conductivities of the diborides, compared to carbides and nitrides, allows for a faster heat dissipation and imparts them better thermal shock resistance, making these materials more suitable as

thermal protection systems for the fabrication of leading edges and spatial nose cones [7,8]. On the other hand, the higher melting points and ablation resistance of the carbides make them more suitable for the fabrication of nozzle inserts. The mechanical properties and oxidation resistance of both diborides and carbides will be discussed.

2.1.2 Synthesis

The diborides, such as ZrB_2, HfB_2, TiB_2, NbB_2 and TaB_2, were the first to be investigated as potential candidates for hypersonic flight and re-entry in earth atmosphere [1]. Metal carbides were already known since 1800, and by 1900 the first refractory carbide, SiC, was discovered. Research then moved to the carbides of early transition metals such as ZrC, HfC and TaC that were characterized by the highest melting points and by high hardness at high temperatures. They were also investigated for the fabrication of protective coatings on graphite for solar, aerospace and nuclear applications. Several routes have been identified for the production of UHTCs:

- Elemental reactions: this is the simplest process and consists in the reaction between the elemental constituents of the desired diboride or carbide compound of general formula MeB_2 for diborides and MeC for carbides (Me = Zr, Hf, Ti, Ta, Nb, Cr, etc.) (reaction 1 and 2)

$$Me + 2\ B \rightarrow MeB_2 \quad (1)$$

$$Me + C \rightarrow MeC \quad (2)$$

These are highly exothermic reactions that can sustain themselves once initiated. The high heat generated can even melt the metal phase and accelerate the reaction further.

- Carbothermal reduction: another method is based on the reduction of a transition metal oxide and carbon for the production of carbides (reaction 3).

$$MeO_2 + 3C \rightarrow MeC + 2\ CO \quad (3)$$

For the synthesis of diborides, boron oxide is added to the mixture (reaction 4):

$$MeO_2 + B_2O_3 + 5\ C \rightarrow MeB_2 + 5\ CO \quad (4)$$

In the case of the diborides, due to B_2O_3 volatility, an excess B_2O_3 is usually required to bring the reaction to completion. Moreover it is important to minimize the presence of unreacted carbon. It was found that a threefold increase of the amount of B_2O_3 allowed to obtain stoichiometric ZrB_2 with carbon contamination below 1%. However using such large excess of B_2O_3 leads to an expensive process. Current synthesis of ZrB_2 uses

an excess of B_2O_3 of 10-30%, which results in pure ZrB_2 powders with very little carbon contamination.

- Carbo/borothermal reduction: for the production of diborides, a third method employs B_4C as the reducing agent and boron source and MeO_2 as the transition metal source. Several researchers have proposed that this reaction goes through more than one step based on thermodynamic calculations. For instance, for the synthesis of ZrB_2, possible intermediate reactions that can take place are reported as follows:

$$2\ MeO_2 + B_4C + 3\ C \rightarrow 2\ MeB_2 + 4\ CO \quad (5)$$

$$ZrO_2 + {}^5/_6\ B_4C \rightarrow ZrB_2 + {}^2/_3\ B_2O_3 + {}^5/_6\ C \quad (6)$$

$$ZrO_2 + {}^5/_7\ B_4C \rightarrow ZrB_2 + {}^3/_7\ B_2O_3 + {}^5/_7\ CO \quad (7)$$

Thermo-dynamical and empirical data show that the overall synthesis process goes to completion above 1500°C. Moreover the loss of B_2O_3 can lead to the formation of ZrC according to reaction 8

$$ZrO_2 + 3C \rightarrow ZrC + 2\ CO_{(g)} \quad (8)$$

An excess of B_2O_3 deriving from B_4C can be used to minimize the formation of ZrC (reaction 9)

$$ZrC + B_2O_3 + 2\ C \rightarrow ZrB_2 + 3\ CO_{(g)} \quad (9)$$

- Borothermal reduction: the main disadvantage of the carbothermal and carbo/borothermal reduction for the synthesis of diborides is that some of the starting carbon may remain in the final ceramic as impurity. The use of elemental boron to synthetize borides can help minimize the formation of carbon or carbides. The reaction involves the use of a oxide as the source of the transition metal and elemental boron, reaction (10):

$$MeO_2 + B \quad MeB_2 + B_2O_3 \quad (10)$$

The excess B can be converted into BO by reaction with the B_2O_3 formed according to reaction (11):

$$B + B_2O_3 \rightarrow BO(g) \quad (11)$$

Even though this process does not introduce carbon impurities, the residual B_2O_3 is still an issue. The latter can be removed by evaporation at 1500°C which results in pure

diboride powders. The aforementioned processes can also be used for the removal of oxide species.

2.1.3 Crystal structure

The strong covalent bonding of carbides, borides and nitrides confers them very high melting points and excellent thermal stability [4,7,9].

Carbides offer very high strength even at elevated temperature but are difficult to machine because of their hardness and they suffer from oxidation at low temperature due to the non-passivating nature of the material that tends to give off volatile oxides according to reaction 12, where Me is Ta, Zr or Hf [9–11]:

$$2\ MeC + 3\ O_2 \rightarrow 2\ MeO_2 + 2\ CO \qquad (12)$$

However they can find application as rocket nozzle inserts where the corrosive atmosphere is mostly constituted by combustion gases, such as CO or H_2O and where high ablation resistance is required against fluxes of hot solid propellant particles. Interstitial carbides such as ZrC, TaC and HfC, are characterized by strong carbon networks where the carbon-metal bond is very strong, and they possess the highest melting points known. The carbides of Ta and Hf are particularly interesting because they possess the highest melting temperature of any known compounds (3980 and 3930°C respectively). The extremely high melting points are attributed to the combination of the covalent and ionic nature of their bonding. Even though the strong interatomic forces are associated to covalent bonding, the true bonding nature is still being investigated. They adopt the face-centered cubic structure of NaCl with carbon atoms in the octahedral sites (figure 2.1)

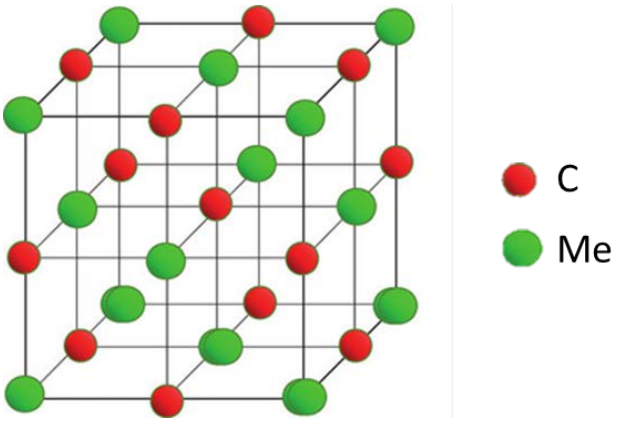

Figure 2.1 Face-centered cubic structure of metal carbides. Carbon atoms are found in the octahedral sites of the lattice.

Even though the general formula for the carbides is MeC, (Me = Ti, Zr, Hf, V, Nb, Ta) monocarbides are often found in substoichiometric structures and the formula MeC_x is more appropriate (x = ratio between Me and C). An example of phase homogeneity is shown in the phase diagram of HfC (Fig. 2.2)

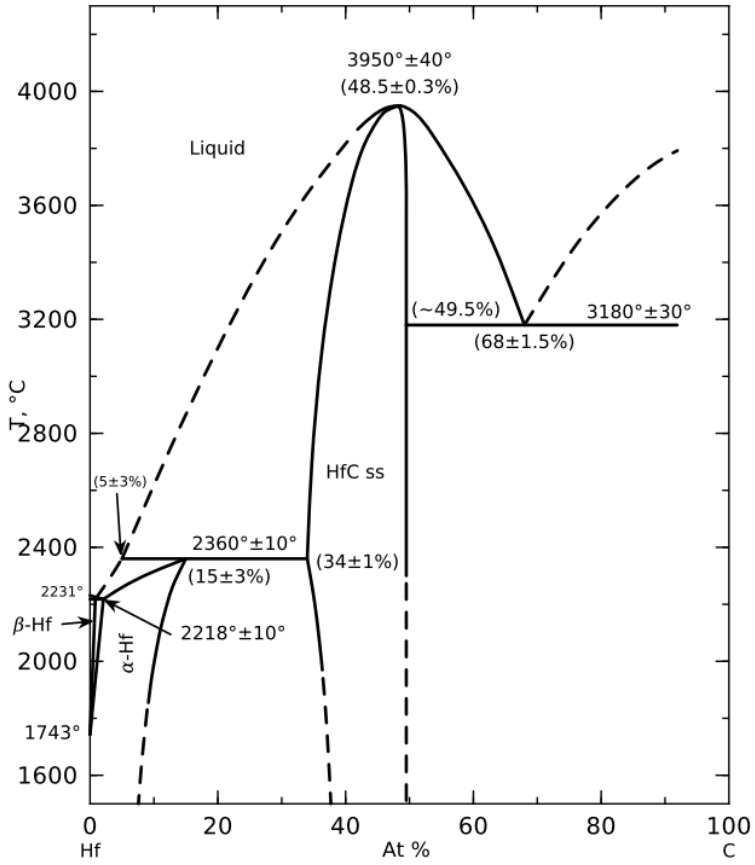

Figure 2.2 Phase diagram of hafnium carbide.

The borides are characterized by very strong covalent bonds between boron and the transition metal and adopt a layered structure with alternating graphite-like boron layers and hexagonal close packed metal layers (Fig. 2.3) [5,12,13].

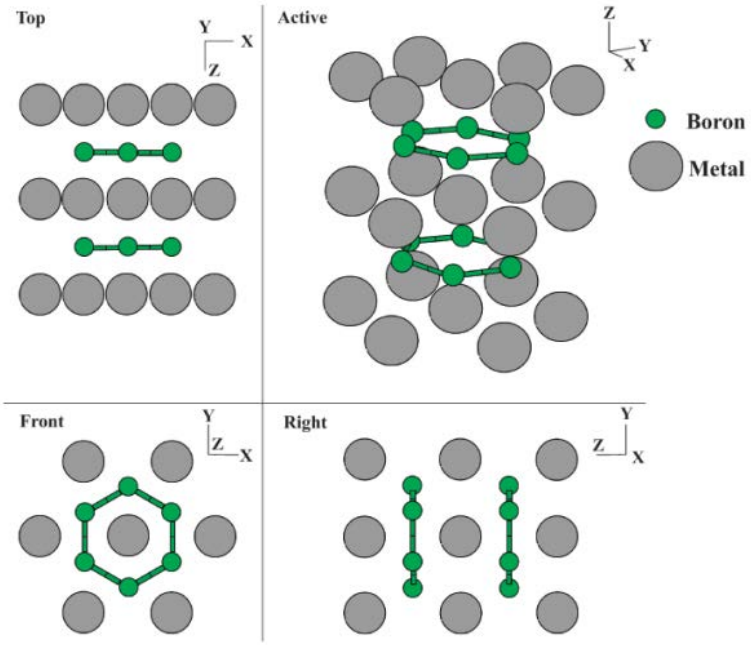

Figure 2.3 Crystal structure of metal diborides

The nitrides share similar properties to the carbides, such as high hardness and chemical inertness, even though the bonding is weaker than the carbides [7,10]. The most common are silicon and boron nitrides. They typically adopt cubic structure. The crystal structure, density and melting points of some UHTCs are reported in table 2.1 [14–18]:

Table 2.1 Crystal structure, density and melting points of UHTCs. SiC and nitrides have been reported even though they have melting points below 3000°C.

Material	**Crystal structure**	**Density (g/cm^2)**	**Melting Point (°C)**
TiB_2	Hexagonal	4.52	3225
ZrB_2	Hexagonal	6.10	3245
HfB_2	Hexagonal	11.19	3380
TaB_2	Hexagonal	12.54	3040
TiC	FCC	4.94	3100
ZrC	FCC	6.56	3400
HfC	FCC	12.76	3900
TaC	FCC	14.50	3800
TiN	Cubic	5.39	2950
ZrN	Cubic	7.29	2950
HfN	Cubic	13.9	3385
TaN	Cubic	14.30	2700
SiC	Polymorphic	3.21	2820

- Secondary phase

SiC is typically added as secondary phase during the fabrication of carbides and borides to aid densification and limit grain growth of the UHTC phase. It comes in many different crystal structures, all characterized by atoms bonded in a tetrahedral configuration with four heteroatoms [19–21]. More than 250 crystalline forms were identified and they can all be considered as polytypes consisting of identical structures in two dimensions that differ only for the stacking sequence of the atom layers in the third dimension [22]. The notation of these polytypes consists of one number describing the number of closest-packed layers and a letter indicating the unit cell (C for cubic, H for hexagonal and R for rhombohedral) as shown in figure 2.4.

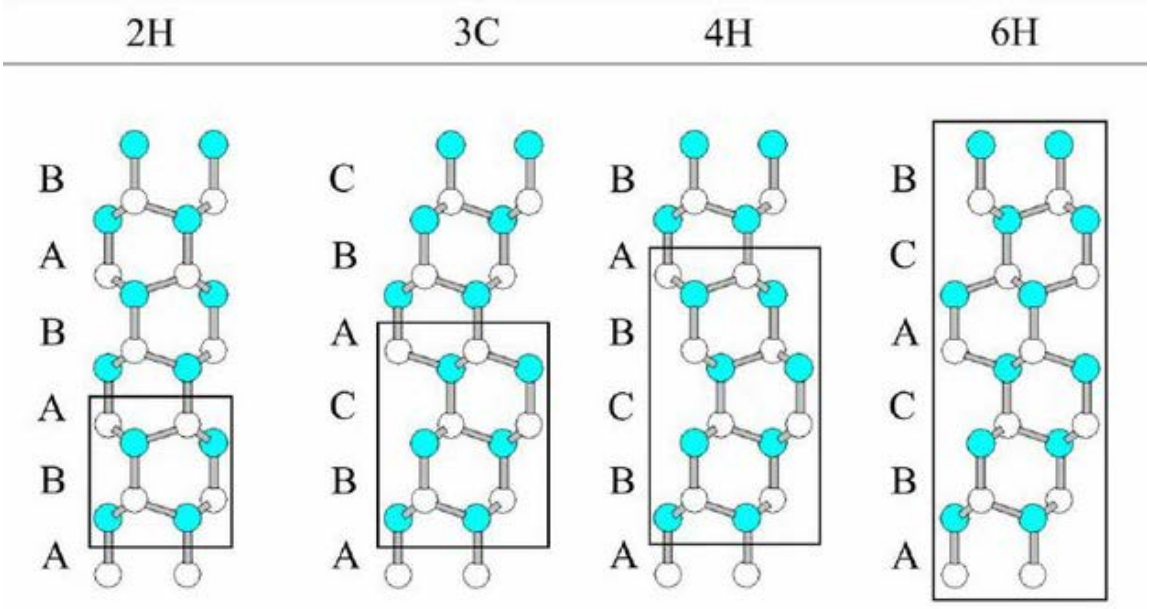

Figure 2.4 Crystal structures of polytypes 3C (cubic), 2H, 4H and 6H for silicon carbide.

The cubic polytype is designated as beta silicon carbide, β-SiC, while the hexagonal variants are referred to as alpha silicon carbide, α-SiC. The 2H polytype is not stable above 1400°C and undergoes transformation to the 4H and 6H polytypes [23]. The electrical properties of SiC are strongly dependent on the polytype. The 3C polytype, β-SiC, is usually observed at relatively low temperatures and turns into α-SiC at high temperatures, even though other polytypes should be more thermodynamically stable at low temperatures according to quantum-mechanical studies. β-SiC is the first structure that forms during crystal growth of SiC, highlighting how the cubic polytype is the kinetically-favoured structure thanks to the high symmetry of the cubic lattice and the ease of rearrangement of the tedrahedrons in low energy conditions. The β → α

transformation during heat treatments is usually associated to the formation of elongated grains which can be exploited as reinforcement [24–28].

2.1.4 Sintering

Because of the high melting points of UHTCs, the processing of these materials require heat treatments during which powders are consolidated to form a dense material with the desired shape and properties. This process is called sintering and is affected by several parameters, such as temperature, holding time, particle size, pressure and atmosphere. Sintering allows to control the microstructure of the material and therefore to tailor its mechanical, thermal and electrical properties to the desired application. Sintering is based on the consolidation of small solid particles via a diffusion process. It is activated by matter transport mechanisms that are promoted at high temperatures. Grains move along each other, filling the voids and reducing the porosity in the process [29]. The driving force is given by a decrease of Gibbs free energy due to the decrease of the volume. The two main sintering mechanisms are described:

- Solid state sintering: it involves heating a green body to a temperature which is 70 – 90% of its melting point. The high temperature promotes the diffusion of atoms at the interface between grains, ultimately bonding the particles together. As the grain boundaries grow, porosity decreases progressively leaving little to no interconnected porosity. In solid state sintering no glassy phase is needed, resulting in improved properties such as high thermal and electrical conductivity or higher strength.
- Liquid phase sintering: it involves the coexistence of solid particles with a liquid phase. The latter can derive from melting one of the components or from the formation of an eutectic. In order to have a good matter transport, the temperature must be high enough to maintain a liquid phase during the sintering process. Moreover a good wettability of the particles is required to increase sintering efficiency. This process is divided in three steps [29]: during the first phase, particles rearrange under the influence of capillary forces and start to fill all the porosity with the liquid phase. Solution-re-precipitation processes lead to the development of microstructure, shape and grain growth. Smaller grains dissolve in the liquid phase and are transported to larger grains by diffusion where they re-precipitate. This mechanisms is called Ostwald ripening [30]. During the last stage further rearrangement is hindered by the previously formed solid skeleton. The densification during this stage is slow and is usually accompanied by grain coarsening.

Liquid phase sintering allows to obtain near full density ceramics at lower temperatures. The main drawback is related to creep resistance, because the low melting phase between grains tends to soften at high temperature, jeopardizing the high temperature performance of the material.

UHTCs can be consolidated with different technologies:

- Hot pressing (HP): the green powder compact is heated to the target temperature under an uniaxial applied pressure to accelerate the sintering process. This process is carried out in vacuum or in inert atmosphere. It records the shrinkage of the material as function of the temperature and time by monitoring the displacement of the graphite pistons. This allows to control sintering parameters during hot pressing. The data collected from these experiments can be used for kinetic studies.
- Reactive sintering: the synthesis and sintering of the material occur simultaneously during the heat treatment. It is typically employed for the sintering of nitrides where the metal element is reacted with nitrogen gas to produce the metal nitride in-situ.
- Self-propagating high-temperature synthesis: even in this case synthesis and sintering occur at the same time. Heat is generated by an arc furnace and is passed through a powder mixture in a controlled environment which starts an exothermic reaction. Typically the reaction generates very high temperatures and sustains itself. This process is relatively economical compared to other processes since it takes advantage of the heat generated during the reaction.
- Hot isostatic pressing: the green powder compact is wrapped in a metallic or glassy casing and a uniform pressure is applied in all directions. The inner pressure is generated by inert gases such as argon or nitrogen that compress the green body without permeating the glassy casing.
- Spark plasma sintering (SPS): a direct current is passed through the green powder compact in a graphite die at very high current intensities and under applied pressures in the range of 10 – 100 MPa. With this technique it is possible to reach very high heating rates and to obtain very large specimens. The sintering mechanism is ascribed to the formation of a plasma around the powder particles that promotes diffusion processes and densification. Few minutes are required to fully sinter a ceramic body [31–33].
- Microwave sintering: the green powder compact is placed inside the furnace and is exposed to a radiation of a specific wavelength which heats the sample from the inside. This process allows high heating rates but the main drawback is related to the non-uniform heating rates through the sample which become more marked with the increase

of the specimen size. It was found that high frequencies preferably heat only the external regions of the sample; a solution could be a multi-frequency generator that would allow a more homogenous heating during heating.

- Pressure-less sintering: the green powder compact is heated and kept to the target temperature for a determined amount of time. It can be carried out either in inert or reactive atmosphere. Higher temperature and holding times aid densification and allow to reach very high values of relative densities but also promote grain growth which is detrimental to mechanical properties. Sintering aids such as SiC or B_4C are usually required to lower the sintering temperature and minimize grain growth.

2.1.5 Mechanical properties

The mechanical properties of common UHTCs, such as elastic modulus, flexural strength and hardness are reported in table 2.2 [3,18,34–39]. The elastic modulus ranges from 350 to 540 GPa while flexural strength at room temperature ranges from 300 to 570 MPa. The high values of elastic modulus are due to the strong covalent bonding in UHTCs. The mechanical properties of un-doped UHTCs are often affected by a lot of scattering due to the difficulty in obtaining full density materials. Other factors influencing mechanical properties are stoichiometry, the presence of impurities such as oxygen or free carbon, grain size, grain orientation, structural defects and the presence of different phases. Moreover the addition of additives can drastically change the mechanical behaviour of UHTCs.

Ceramics based on ZrB_2 doped with SiC exhibit room temperature strengths above 1000 MPa, fracture toughness up to 5.5 $MPa \cdot m^{0.5}$ and hardness exceeding 22 GPa [5]. The effect of SiC on the mechanical properties has been extensively investigated. Even though ZrB_2 grain size changes with the increase of SiC content, the determining factor for the room temperature strength is the size of SiC particles. The critical flaw sizes have been correlated to SiC cluster sizes which were consistent with the CTE mismatch between ZrB_2 and SiC. Watts *et al.* found that the critical flaw size range for micro-cracking was between 6.5 and 13.8 μm, which matches the particle size of SiC observed by the same author empirically [40]. Since SiC particle size controls the strength, a uniform dispersion of SiC is required to minimize SiC particle size and maximize strength.

Table 2.2 Mechanical properties of UHTCs: the elastic modulus, flexural strength and hardness are reported.

Material	Temperature (°C)	Elastic Modulus (GPa)	Flexural Strength (MPa)	Hardness (GPa)	Ref.
SiC	23	415	359 - 532	25 - 32	35, 39
	1000	392	397	8.9	35
ZrB_2	23	500	380	25.3 – 28.0	3
	800	480	430	-	3
	1400	360	150	-	3
	1800	-	200	-	3
ZrB_2/20% SiC	23	540	400	-	3
	800	500	450	-	3
	1400	430	340	-	3
	1800	-	270	-	3
ZrC	23	348	-	27.0	34
TiB_2	23	551	300 - 370	25 – 33	18
TiC	23	451	-	30	34
HfB_2	23	530	480	21.2 – 28.4	3
	800	485	570	-	3
	1400	300	170	-	3
	1800	-	280	-	3
HfB_2/20% SiC	23	540	520	-	3
	800	530	380	-	3
	1400	410	180	-	3
	1800	-	280	-	3
HfC	23	352	-	26.0	34
TaB_2	23	257 – 570	-	19 – 25	18
TaC	23	285	-	18.2	34

The influence of SiC content on the strength of ZrB_2/SiC ceramics was also investigated. Chamberlain *et al.* found that the strength of ZrB_2 increased with the increase of SiC content from 560 to 1090 MPa [41]. The enhancement of mechanical properties was still attributed to SiC particle size. Liu and Neuman found that for SiC contents above 30 vol%, SiC particles start aggregating, forming clusters that act as critical flaws and reduce the strength [42,43]. Similar results were obtained from Zhang *et al.* [44].

As far as fracture toughness is concerned, it was found that an increase in SiC content led to an increase in fracture toughness. The fracture toughness of ZrB_2 increases from 3.5 MPa·$m^{0.5}$ (un-doped) to 5.3 MPa·$m^{0.5}$ (30 vol% SiC). Similar trends were obtained by other researchers [3,45,46]. The reason behind the increased toughness was ascribed to the higher complexity of the crack path, promoting inter-granular fracture.

Mechanical properties of UHTCs are strongly affected by temperature. Typically elastic modulus decreases with the increase of temperature due to the weakening of covalent bonding. Works carried out on ZrB_2 bulk ceramics reported a decrease of elastic modulus from 525 GPa at room temperature to 490 GPa at 1100°C [4]. Other works from Neuman showed how elastic modulus decreases more rapidly after 1200°C, which was attributed to grain boundary sliding and diffusional creep mechanisms [43]. ZrB_2/SiC ceramics show similar behaviour: elastic modulus decreases steadily from room temperature to 1400°C, then it drastically decreases at 1600°C [47]. Even in this case, the decrease of elastic modulus was attributed to grain boundary sliding and diffusional creep.

High temperature strength follows a different trend. Pure ZrB_2 strength increases from 325 MPa at room temperature to 420 MPa at 800°C due to thermal stress relief. Then it decreased to 145 MPa at 1400°C and increased again to 200 MPa at 1900°C. This second increase in strength was attributed to stress relief coupled with creep mechanisms. At 2200°C creep phenomena are more marked and strength falls down to 50 MPa [43].

SiC-doped ZrB_2 ceramics follow a similar trend: the strength increases from 390 MPa at room temperature to 420 MPa at 800°C, but then steadily decreases to 245 MPa at 1800°C. Above 1800°C the decrease in strength is faster [43,48].

The mechanical properties of carbides are harder to measure due to the intrinsic difficulty in obtaining fully dense materials. Many works on carbides are often incomplete or do not clearly report the starting materials. Studies from Sanders on HfC reported values of flexural strength at room temperature of 235 MPa which decreased to 109 MPa at 1315°C [3]. The same tests were performed on a different batch of powders with smaller particle size but higher oxygen content; the resulting ceramics had relative densities between 91-96% but overall lower strength, implying that impurities content played a major role. Works from Fahrenholtz on cermets based on tungsten doped with ZrC showed strength of ~400 MPa [49].

Plastic deformation of carbides was observed only at very high temperatures and were found to be strongly dependent on stoichiometry. Stoichiometric HfC has a ductile-to-brittle transition temperature of 2100°C which decreases down to 1000°C in the case of sub-stoichiometric $HfC_{0.67}$ [4].

2.1.6 Thermal properties

The values of coefficients of thermal expansion (CTE) and thermal conductivity of common UHTC materials are reported in table 2.3 [4,17,34,50–52]. These properties are dependent on temperature and the temperature variation should be taken into account during designing. Due to their crystal structure, borides exhibit higher thermal conductivities compared to carbides or nitrides [7]. Even though the conductivities of borides steadily decrease with the increase of temperature, they tend to remain higher than those of nitrides and carbides. Higher thermal conductivity reduced thermal stresses within the material by reducing the magnitude of thermal gradients. Moreover it allows heat to be dissipated more quickly and radiated away from the surface of the component, reducing the surface temperature for a specific incident heat flux, in contrast with the effect of an insulator.

Table 2.3 Coefficients of Thermal Expansion (CTE) and Thermal conductivities of UHTCs

Material	Temperature range (°C)	CTE (10^{-6}/K)	Temperature (°C)	Thermal Conductivity (W/mK)
SiC	20	1.1	20	114
	1000	5.0	1000	35.7
	1500	5.5	1500	26.3
ZrB_2	20 - 1027	5.9	10	-
	1027 – 2027	6.5	-	-
	20 - 2205	8.3	-	-
ZrB_2/20% SiC	400 - 1600	5 – 7.8	100	98.7
	-	-	500	84.5
	-	-	1000	78
ZrC	20 – 1500	6.7	20	20.5
TiB_2	20 – 1027	4.6	-	-
	20 – 2205	5.2	-	-
	1027 – 2027	8.6	-	-
TiC	20 - 1500	7.7	-	-
HfB_2	20 – 1027	6.3	20	105
	1027 – 2027	6.8	400	75
	20 - 2205	7.6	800	70
HfB_2/20% SiC	-	-	100	79
	-	-	500	74
	-	-	1000	62
HfC	20 - 1500	6.6	20	20
	-	-	400	23
	-	-	800	30
TaB_2	20 – 1027	8.2	20	16
	1027 – 2027	8.4	1027	16.1
	20 - 1650	8.4	2027	36.2
TaC	20 - 1500	6.3	20	22

The benefits of higher thermal conductivities are more evident in the case of sharp leading edges. Conventional carbon/carbon composites used for the production of leading edges have low thermal conductivity, therefore the maximum surface

temperature is determined by the design of the leading edge; sharper leading edges result in higher thermal fluxes which translates in higher surface temperatures. Due to the low conductivity of these materials, there is little conduction of heat away from the tip of the leading edge. Due to the operational temperature limits of 1600°C for SiC based composites, current leading edges have relatively blunt tips. However, blunt leading edges significantly affect the space vehicles speed and performance. In order to maximize performance, sharp leading edges are required and hence the need for highly conductive materials (Fig. 2.4)

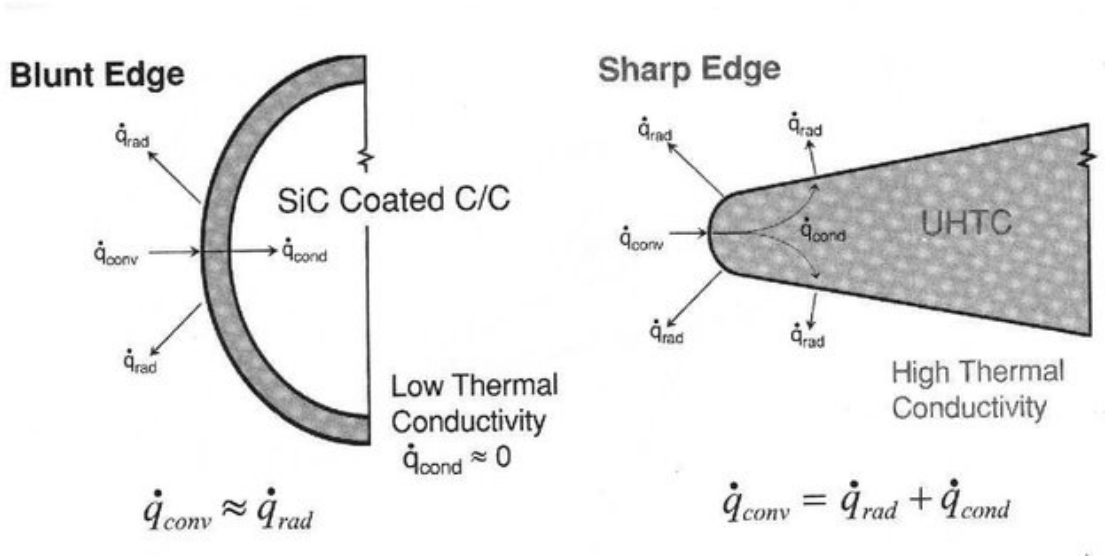

Figure 2.4 Difference in heat conduction for blunt and sharp leading edges

2.1.7 Electrical properties

Electrical resistivity values for common UHTC materials are reported in table 2.4 [10,17,18,34,51,53]. Borides typically display lower electrical resistivity than carbides and this affects machining. Borides can be easily machined by Electrical Discharge Machining (EDM) and produced in several complex shapes, whereas carbides are more difficult to machine due to their higher electrical resistivity and intrinsic hardness that makes diamond machining even more expensive.

Table 2.4 Electrical resistivity of common UHTCs.

Material	Temperature (°C)	Electrical resistivity (10^{-6} Ω cm)
ZrB_2	20	12.1
	1000	44.0
ZrB_2/SiC	20	10.2
	1000	54.5
ZrC	25	63
TiB_2	25	9
TiC	25	68
HfB_2	25	11
HfB_2/SiC	20	9.6
	1000	57.8
HfC	25	109
TaB_2	25	33
TaC	25	30

2.1.8 Applications

Potential applications of UHTC materials span from the industry to the aerospace and military field. UHTCs can find application in foundry and steelmaking industry as refractory processing materials. Because of their chemical inertness and stability at high temperature, they can be used as crucibles for molten metals or as components for electrical devices such as heating elements or igniters [3].

In the aerospace field they can find application as rocket nozzles inserts or thermal protection systems for the leading edges of hypersonic re-entry vehicles [54]. Thanks to their high thermal conductivity, they can be shaped in sharper leading edges, leading to an improvement of current aerospace vehicles. However, as mentioned before, sharp leading edges also result in very high thermal fluxes and high temperatures on the surface of the material which are beyond the capabilities of current materials. Therefore UHTCs are potential candidates for this application.

UHTCs can also find application in the nuclear field. Specifically, diborides can find application as neutron-shielding materials due to boron high neutron capture cross section [55].

2.2 Ceramic Matrix Composites

2.2.1 Introduction

Ceramic Matrix Composites (CMCs) are a class of materials consisting of carbon or SiC fibres embedded in a ceramic matrix of pyrolysed carbon or SiC. The fibre reinforcement is used to increase the strength and the resistance to crack propagation, and to overcome the low fracture toughness of conventional ceramics that are typically subject to catastrophic failure when scratches or defects are present.

Generally CMCs labels indicate the type of fibre and the type of matrix (e.g. C/SiC stands for carbon fibre reinforced silicon carbide). These composites are characterized by good thermo-mechanical properties, low thermal expansion, low density and good thermal shock resistance. Typical values of strength for C/SiC or SiC/SiC composites are in the range of 160 – 410 MPa while fracture toughness is in the range of 5 – 25 $MPam^{0.5}$ [56–61]. However in C/C composites the carbon fibres undergo oxidation already at 500°C, while in C/SiC or SiC/SiC composites the protective layer of liquid SiO_2, originating from the oxidation of SiC matrix at 1100 °C, becomes chemically active above 1650 °C, leading to high removal rates, therefore limiting their application to temperatures below 1600°C [14–16] [62–64].

2.2.2 Process

The most common routes for the production of C/C or C/SiC composites are PIP or CVI:

- Polymer Infiltration and Pyrolysis (PIP) is based on the infiltration of a carbon fibre preform with phenolic resin which is then pyrolysed to leave behind a graphitic matrix reinforced with carbon fibres. This step can be repeated many times until near full density composites are obtained [59,65].
- Chemical Vapour Infiltration (CVI) is based on the deposition of the ceramic matrix from the gas phase [66–68]. The Carbon fibre preform is exposed to a mixture of argon and light hydrocarbons at 1000°C and under a pressure of 100 kPa. The gas decomposes on the surface of the fibres, depositing the carbon matrix around the fibres. This process can also be applied for the production of a SiC matrix using SiCN precursors. Several CVI cycles are repeated until full density is reached. It can require several days to obtain dense composites [69].
- Reactive melt infiltration is based on the preliminary infiltration of a carbon preform with phenolic resin, followed by the reaction with liquid silicon which forms SiC in-situ

[70,71]. The composites are typically fully dense since the liquid silicon fills any voids left by the PIP process. Silicon can be substituted with other elements to form in-situ carbides such as ZrC from a liquid zirconium melt [71–73].

2.3 Ultra-high temperature ceramic matrix composites

2.3.1 Introduction

The demand for advanced thermal protection systems (TPS) related to hypersonic flight and rocket propulsion for use in extreme conditions, where temperatures as high as 2000°C are reached, has fostered the development of a new class of ultra-high temperature materials. UHTCs possess high melting points and ablation resistance but they are brittle. On the other hand CMCs have excellent mechanical properties but are limited to service temperatures below 1600°C [74]. By coupling the good fracture toughness and thermal shock resistance of CMCs and the oxidation and ablation resistance of UHTC materials, the above mentioned limits could be potentially overcome.

2.3.2 Process

Many approaches have been investigated in order to incorporate the good properties of CMCs with the refractoriness of UHTCs. Techniques employed in the fabrication of these composites include Slurry Infiltration (SI), Chemical Vapour Infiltration (CVI), Polymer Infiltration and Pyrolysis (PIP), Chemical Vapour Deposition (CVD), Hot Pressing (HP), Liquid Silicon Infiltration (LSI), Vapour Silicon Infiltration (VSI):

- CMCs with a UHTC coating: one approach is based on the protection of C/C composites with UHTC coatings [75–80]. The main issue lies in achieving a good adhesion between the C/C composite and the UHTC phase due to the different chemistry of the materials and the thermal expansion mismatch that can cause the detachment of the coating under severe thermal stresses. Corral *et al.* [77] have successfully achieved a good interface between the CMC and the coating by dip coating the C/C composite, previously heat treated at 1600 °C for 4h to induce graphitization on the surface, in a suspension of ZrB_2/SiC particles dispersed in a phenolic resin. Zhou *et al.* [75] have obtained a homogeneous and dense coating of ZrB_2/SiC devoid of cracks via VSI on C/C composites which showed good oxidation resistance up to 1500 °C.

- CMCs with UHTC particles: another way of implementing these properties is by embedding UHTC particles in the ceramic matrix of C/C or C/SiC composites. Corral and Tang fabricated C/SiC composites with 4 - 18 vol.% of ZrB_2 inclusions via CVI and compared it to a C/SiC composite, showing how the former had increased oxidation resistance above 1000°C due to the synergy between B_2O_3 and SiO_2 forming a protective borosilicate scale with higher viscosity [56,81]. Li and Zhang obtained C/ZrB_2-SiC composites a with high SiC content and observed increased oxidation resistance [82].

- UHTCs with carbon particles or short fibres: a way to increase the toughness of UHTCs is to reinforce the matrix with the addition of carbon particles or short fibres [83–90]. The process is simple and usually involves conventional sintering techniques such as HP and SPS. The final composites usually display lower strength due to the generation of internal stresses but the presence of short fibres improves the fracture toughness by promoting graceful failure.

- UHTCs with continuous carbon fibres: there is still a limited amount of literature regarding continuous fibre reinforced ceramic composites with a UHTC-rich matrix owing to the difficult infiltration of long carbon fibres. The main technique involves slurry infiltration of carbon fibre bundles or fabrics with aqueous or organic suspensions of the UHTC powders. Important parameters are the slurry rheology and chemical activity of the powders. In order to achieve a good degree of infiltration, the solid loading in the suspension has to be the highest possible. However, increasing the solid loading leads to an increase of viscosity which hinders infiltration. Therefore preliminary studies need to be carried out in order to assess the rheology of the system and the susceptibility of the powders to oxidation when working in aqueous medium.

Previous work was done by Sciti *et al.* in the field of this novel class of materials labelled as UHTCMCs (Ultra High Temperature Ceramic Matrix Composites), using SiC and carbon fibres embedded in a ZrB_2/SiC matrix, which showed non-brittle fracture behaviour [91–94]. Binner et al fabricated 2.5 D fibre reinforced HfB_2 composites by slurry infiltration with a phenolic resin – UHTC suspension, followed by pyrolysis and CVI to obtain fully dense materials [95,96]. Works on long fibre reinforced UHTCs has also been carried by Kütemeyer et al via RMI of a carbon fibre preform with zirconium alloys to produce in-situ UHTCs (ZrB_2 or ZrC) [73]. In the present work, carbon fibre reinforced UHTC composites were produced via slurry infiltration and hot pressing. In the last section of this thesis, a joint process involving SI and RMI was investigated.

2.3.3 Mechanical properties

It is difficult to make direct comparisons of the mechanical properties of fibre reinforced UHTCs due to the many different and scattered testing methods reported in literature. For some materials only the flexural strength or hardness are reported, while other works focus mainly on the ablation resistance or fracture toughness. Tang reported strengths of 148 MPa and K_{Ic} of 5.6 $MPam^{0.5}$ for ZrB_2/SiC composites with 30% long fibres. Yang reported improved fracture toughness for ZrB_2-20%SiC composites reinforced with 20% short carbon fibres [97]. Padmavathi obtained tensile strengths of ~190 MPa for C/SiC composites reinforced with ZrB_2 and ZrC, observing a decrease of strength with the addition of the UHTC phase due to internal stresses. Guo obtained strengths of 160 – 290 MPa for ZrB_2-20% SiC reinforced with 30 – 50% short carbon fibres [85]. Works on fibre reinforced ZrC/SiC composites reported tensile strength of 190 – 260 MPa, while studies on the more refractory composites based on HfC showed tensile strength of only 26 MPa. Generally the addition of fibres has been found to lower the strength of the baseline UHTCs because of higher porosities or internal stresses originating from the different CTE of the fibre and the matrix. On the other hand, the presence of a fibre reinforcement has been shown to promote graceful failure and allow a higher ultimate failure strain which is crucial for applications where a high damage tolerance is required. In this thesis, the mechanical behaviour of fibre reinforced borides and carbides was investigated.

2.3.4 Oxidation resistance

Transition metal borides, such as zirconium and hafnium diborides, have been extensively investigated due to their high melting temperature, high thermal and electrical conductivity, good ablation resistance and ability to withstand extreme conditions [4,98,99]. Among the UHTCs, ZrB_2 is the most attractive because of its low theoretical density and high thermal conductivity [100]. However the oxidation resistance of ZrB_2 is low at temperatures above 1400 °C because of the evaporation of B_2O_3 and the formation of a non-protective, porous layer of ZrO_2. In this regard, it was found that the addition of SiC and metal silicides such as $TaSi_2$ or $MoSi_2$, leads to the formation of a viscous borosilicate layer with higher melting temperature and low vapour pressure which results in improved oxidation resistance [5,101–104]. Table 2.5 provides a summary of previous studies on the oxidation resistance of carbon fibre reinforced UHTCs.

Table 2.5 Summary of the previous works done on C/ZrB_2-SiC composites, their composition and the testing methods used to evaluate oxidation resistance.

Techniques	Materials	Fibre vol.%	UHTC vol.%	SiC vol.%	Testing	Authors
PIP, VSI	C/C + ZrB_2-SiC coating	n/a	n/a	n/a	Muffle furnace, 1500°C, 40min	H. Zhou etal. [75]
CVI, PC	C/C + ZrB_2-SiO_2 coating	n/a	n/a	n/a	Muffle furnace, 1500°C, 300h	O. Haibo et al. [76]
CVI	C/C + ZrB_2-SiC coating	n/a	n/a	n/a	Solar furnace, 1700-2600°C	E.L. Corral et al. [77]
CVI	C/SiC-ZrB_2	25	4	71	Electric furnace, 1000-1400°C, 5 min	S. Tang et al. [56]
PIP, SI, CVD	C/ZrB_2-SiC	54	n/a	n/a	Blow torch, 3000°C, 20 s	H. Li et al. [82]
HP	C/ZrB_2-SiC	20	60	20	Blow torch, 1890°C, 3 min	F. Yang et al. [90]
SI, HP	C/ZrB_2-SiC	42	52	6	TGA, 800-1550°C, 6h	Present work

Previous studies on the effect of different oxygen partial pressures on the oxidation resistance of ZrB_2 ceramics doped with 20% and 30% SiC have shown that higher SiC contents are beneficial in oxygen-rich environments but the effect is reversed in oxygen-poor atmospheres due to the active oxidation of SiC to SiO(g) [105]. The latter issue has raised many concerns regarding the use of SiC in ceramic composites. However, the majority of these works has been carried out on bulk ceramics with high SiC contents (> 20 vol.%) [106–109]. There is still a limited amount of literature on the oxidation resistance of low sic-bearing UHTC composites reinforced with fibres and how the fibre orientation influences oxidation depending on the final application. Moreover for fibre reinforced ceramics the amount of readily available SiC is actually halved, since ~50% of the composite is constituted by the fibre reinforcement. Previous works on the short-term oxidation of continuous fibre reinforced ZrB_2/SiC composites showed the ability of the UHTC matrix to protect fibres

from oxidation [110], but no comprehensive study was conducted on the kinetics of oxidation and long term exposition to an oxidant atmosphere.

In the first section of this thesis, the oxidation kinetics of a carbon fibre reinforced ZrB_2/SiC composite were studied via Thermo-gravimetric analysis. Following this preliminary study, the influence of SiC content on the oxidation resistance in air was investigated via short term oxidation tests in a bottom-up loading furnace in air up to 1650°C.

2.4 References

1. Kaufman, L. & Clougherty, E. V. Investigation of Boride Compounds for Very High Temperature Applications, Part II. (1965).

2. Clougherty, E. V., Kalish, D. & Peters, E. T. Research and development of refractory oxidation resistant diborides. *AFML-TR-68-190* (1968).
3. *Ultra-High Temperature Ceramics: Materials for Extreme Environment Applications*. (John Wiley & Sons Inc., 2014). doi:10.1002/9781118700853
4. Opeka, M. M., Talmy, I. G., Wuchina, E. J., Zaykoski, J. a. & Causey, S. J. Mechanical, Thermal, and Oxidation Properties of Refractory Hafnium and zirconium Compounds. *J. Eur. Ceram. Soc.* **19,** 2405–2414 (1999).
5. Fahrenholtz, W. G., Hilmas, G. E., Talmy, I. G. & Zaykoski, J. A. Refractory diborides of zirconium and hafnium. *J. Am. Ceram. Soc.* **90,** 1347–1364 (2007).
6. Courtright, E. L., Graham, H. C., Katz, A. P. & Kerans, R. J. Ultrahigh temperature assessment study - ceramic matrix composites. *WL-TR-91-4061* (1992).
7. Cutler, R. A. Engineering properties of borides. *Eng. Mater. Handb.* **4,** 787–803 (1991).
8. Grimvall, G. & Fernández Guillermet, A. Phase stability properties of transition metal diborides. in *AIP Conference Proceedings* (1991). doi:10.1063/1.40811
9. Hampshire, S. Engineering properties of nitrides. *ASTM Eng. Mater. Handb.* **4,** 811–820 (1991).
10. Shaffer, P. T. B. Engineering properties of carbides. *Eng. Mater. Handb.* **4,** 804–811 (1991).
11. Laboratories, B. C. Engineering property data on selected ceramics: carbides. *Rep. MCIC-HB-07* **2,** (1979).
12. Spear, K. E. Chemical bonding in AlB_2-types borides. *J. less common Met.* **47,** 195–201 (1976).
13. Burdett, J. K., Canadell, E. & Miller, G. J. Electronic structure of transition metal borides with the AlB_2 structure. *J. Am. Ceram. Soc.* **108,** 6561–6568 (1986).
14. Jenkins, R. Joint Committee on Powder Diffraction Standards. *from Int. Cent. Diffr. Data, Swart. PA* (1988).
15. Schwetz, K.-A.-, Reinmoth, K. & Lipp, A. in *Handbook of Ceramic Composites* 568–585 (1981).
16. McColm, I. J. *Ceramic science for materials technologists*. (Leonard Hill, 1983).
17. Exner, H. E. Physical and chemical nature of cemented carbides. *Int. Met. Rev.* **24,** 149–173 (1979).
18. Pankratz, L. B., Stuve, J. M. & Gokcen, N. A. *Thermodynamic data for mineral*

technology. (1984).

19. Yamada, K. & Mohri, M. *Silicon Carbide Ceramics—1*. (Springer, Dordrecht, 1991).
20. Popper. Special ceramics. in (ed. Popper, P.) (The British Ceramic Research Association, 1960).
21. Tagai, T., Sueno, S. & Sadanaga, R. Thermal transformation in SiC crystals. *Mineral. J.* **6,** 240–248 (1971).
22. Cheung, R. *Silicon Carbide Microelectromechanical Systems for Harsh Environments*. (Imperial College Press, 2006).
23. Shaw, J. J. A. & Heine, V. The nature of interplanar interactions in SiC polytypes. *J. Phys. Condens. Matter* **2,** 4351 (1990).
24. Padture, N. P. & Lawn, B. R. Toughness Properties of a Silicon Carbide with an in Situ Induced Heterogeneous Grain Structure. *J. Am. Ceram. Soc.* **77,** 2518–2522
25. Kim, Y.-W., Mitomo, M. & Hirotsuru, H. Grain Growth and Fracture Toughness of Fine-Grained Silicon Carbide Ceramics. *J. Am. Ceram. Soc.* **78,** 3145–3148
26. Moberlychan, W. J. & De Jonghe, L. C. Controlling interface chemistry and structure to process and toughen silicon carbide. *Acta Mater.* **46,** 2471–2477 (1998).
27. Sciti, D., Guicciardi, S. & Bellosi, A. Effect of annealing treatments on microstructure and mechanical properties of liquid-phase-sintered silicon carbide. *J. Eur. Ceram. Soc.* **21,** 621–632 (2001).
28. Zhan, G.-D., Xie, R.-J., Mitomo, M. & Kim, Y.-W. Effect of β-to-α Phase Transformation on the Microstructural Development and Mechanical Properties of Fine-Grained Silicon Carbide Ceramics. *J. Am. Ceram. Soc.* **84,** 945–950
29. Kingery, W. D., Bowen, H. K. & Uhlmann, D. R. *Introduction to Ceramics*. (John Wiley, 1960).
30. Ratke, L. & Voorhees, P. W. *Growth and Coarsening Ostwald Ripening in Material Processing*. (Springer-Verlag Berlin Heidelberg, 2002). doi:10.1007/978-3-662-04884-9
31. Groza, J. R. & Zavaliangos, A. Sintering activation by external electrical field. *Mater. Sci. Eng. A* **287,** 171–177 (2000).
32. Gao, L. *et al.* Mechanical Properties and Microstructure of Nano-SiC–Al_2O_3 Composites Densified by Spark Plasma Sintering. *J. Eur. Ceram. Soc.* **19,** 609–

613 (1999).

33. Gao, L., Wang, H., Kawaoka, H., Sekino, T. & Niihara, K. Fabrication of YAG–SiC nanocomposites by spark plasma sintering. *J. Eur. Ceram. Soc.* **22,** 785–789 (2002).
34. Munro, R. G. Material Properties of a Sintered α-SiC. *J. Phys. Chem. Ref. Data* **26,** 1195–1203 (1997).
35. Upadhya, K., Yang, J.-M. & Hoffmann, W. P. Materials for ultrahigh temperature structural applications. *Am. Ceram. Soc. Bull.* **76,** 51–56 (1997).
36. Okada, S., Kudou, K., Higashi, I. & Lundström, T. Single crystals of TaB, Ta_5B_6, Ta_3B_4 and TAB_2, as obtained from high-temperature metal solutions, and their properties. *J. Cryst. Growth* **128,** 1120–1124 (1993).
37. Pichon, T. *et al.* CMC thermal protection system for future reusable launch vehicles: Generic shingle technological maturation and tests. *Acta Astronaut.* **65,** 165–176 (2009).
38. Laszkiewicz-Łukasik, J., Jaworska, L., Putyra, P., Klimczyk, P. & Garzeł, G. The influence of SPS heating rates on the synthesis reaction of tantalum diboride. *Boletín la Soc. Española Cerámica y Vidr.* **55,** 159–168 (2016).
39. Magnani, G., Minoccari, G. L. & Pilotti, L. Flexural strength and toughness of liquid phase sintered silicon carbide. *Ceram. Int.* **26,** 495–500 (2000).
40. Watts, J., Hilmas, G. & Fahrenholtz, W. G. Mechanical characterization of ZrB_2-SiC composites with varying SiC particle sizes. *J. Am. Ceram. Soc.* **94,** 4410–4418 (2011).
41. Chamberlain, A. L., Fahrenholtz, W. G., Hilmas, G. E. & Ellerby, D. T. High-strength zirconium diboride-based ceramics. *J. Am. Ceram. Soc.* **87,** 1170–1172 (2004).
42. Liu, H., Liu, L., Ye, F., Zhang, Z. & Zhou, Y. Microstructure and mechanical properties of the spark plasma sintered TaC/SiC composites: Effects of sintering temperatures. *J. Eur. Ceram. Soc.* **32,** 3617–3625 (2012).
43. Neuman, E. W., Hilmas, G. E. & Fahrenholtz, W. G. Mechanical behavior of zirconium diboride–silicon carbide–boron carbide ceramics up to 2200 °C. *J. Eur. Ceram. Soc.* **35,** 463–476 (2015).
44. Zhang, R., Cheng, X., Fang, D., Ke, L. & Wang, Y. Ultra-high-temperature tensile properties and fracture behavior of ZrB_2-based ceramics in air above 1500??C. *Mater. Des.* **52,** 17–22 (2013).

45. Yue, C., Liu, W., Zhang, L., Zhang, T. & Chen, Y. Fracture toughness and toughening mechanisms in a (ZrB_2-SiC) composite reinforced with boron nitride nanotubes and boron nitride nanoplatelets. *Scr. Mater.* **68,** 579–582 (2013).
46. Khoeini, M., Nemati, A., Zakeri, M., Tamizifar, M. & Samadi, H. Comprehensive study on the effect of SiC and carbon additives on the pressureless sintering and microstructural and mechanical characteristics of new ultra-high temperature ZrB_2 ceramics. *Ceram. Int.* **41,** 11456–11463 (2015).
47. Zapata-Solvas, E., Jayaseelan, D. D., Lin, H. T., Brown, P. & Lee, W. E. Mechanical properties of ZrB_2- and HfB_2-based ultra-high temperature ceramics fabricated by spark plasma sintering. *J. Eur. Ceram. Soc.* **33,** 1373–1386 (2013).
48. Neuman, E. W., Hilmas, G. E. & Fahrenholtz, W. G. Mechanical behavior of zirconium diboride-silicon carbide ceramics at elevated temperature in air. *J. Eur. Ceram. Soc.* **33,** 2889–2899 (2013).
49. Zhang, S. C., Hilmas, G. E. & Fahrenholtz, W. G. Zirconium Carbide–Tungsten Cermets Prepared by In Situ Reaction Sintering. *J. Am. Ceram. Soc.* **90,** 1930–1933
50. Samsonov, G. V. & Serebryakova, T. I. Classification of borides. *Sov. Powder Metall. Met. Ceram.* **17,** 116–120 (1978).
51. Clougherty, E. V. & Wilkes, K. E. Research and development or refractory oxidation resistant diborides, Part II. *AFML-TR-68-190* **V,** (1969).
52. RADOSEVICH, L. G. & WILLIAMS, W. S. Thermal Conductivity of Transition Metal Carbides. *J. Am. Ceram. Soc.* **53,** 30–33
53. Samsonov, G. V. & Vinitskii, I. M. *Handbook of refractory compounds*. (Plenum press, 1980).
54. Rahman, M., Wang, C. C., Chen, W., Akbar, S. A. & Mroz, C. Electrical Resistivity of Titanium Diboride and Zirconium Diboride. *J. Am. Ceram. Soc.* **78,** 1380–1382
55. Sears, V. F. Neutron scattering lengths and cross sections. *Neutron News* **3,** 29–37 (1992).
56. Tang, S., Deng, J., Wang, S. & Liu, W. Fabrication and characterization of an ultra-high-temperature carbon fiber-reinforced ZrB_2-SiC matrix composite. *J. Am. Ceram. Soc.* **90,** 3320–3322 (2007).
57. Padmavathi, N., Kumari, S., Bhanu Prasad, V. V., Subrahmanyam, J. & Ray, K. K. Processing of carbon-fiber reinforced (SiC + ZrC) mini-composites by soft-

solution approach and their characterization. *Ceram. Int.* **35,** 3447–3454 (2009).

58. Padmavathi, N., Ghosal, P., Eswara Prasad, N., Subramanyam, J. & Ray, K. K. Synthesis of carbon fibre-reinforced, silicon carbide composites by soft-solution approach. *Sadhana - Acad. Proc. Eng. Sci.* **37,** 493–502 (2012).
59. Yu, H. J. *et al.* Mechanical properties of 3D KD-I SiCf/SiC composites with engineered fibre-matrix interfaces. *Compos. Sci. Technol.* **71,** 699–704 (2011).
60. Lamon, J. Interfaces and interfacial mechanics: influence on the mechanical behavior of ceramic matrix composites (CMC). *J. Phys.* **3,** 1607–1616 (1993).
61. Droillard, C. & Lamon, J. Fracture toughness of 2-D woven SiC/SiC CVI-composites with multilayered interphases. *Journal of the American Ceramic Society* **79,** 849–858 (1996).
62. Lamouroux, F., Bertrand, S., Pailler, R., Naslain, R. & Cataldi, M. Oxidation-resistant carbon-fiber-reinforced ceramic-matrix composites. *Compos. Sci. Technol.* **59,** 1073–1085 (1999).
63. Hald, H. Operational limits for reusable space transportation systems due to physical boundaries of C/SiC materials. *Aerosp. Sci. Technol.* **7,** 551–559 (2003).
64. Jayaseelan, D. D., Xin, Y., Vandeperre, L., Brown, P. & Lee, W. E. Development of multi-layered thermal protection system (TPS) for aerospace applications. *Compos. Part B Eng.* **79,** 392–405 (2015).
65. Nannetti, C. A., Ortona, A., de Pinto, D. A. & Riccardi, B. Manufacturing SiC-fiber-reinforced SiC matrix composites by improved CVI/slurry infiltration/polymer impregnation and pyrolysis. *J. Am. Ceram. Soc.* **87,** 1205–1209 (2004).
66. Bang, K.-H., Chung, G.-Y. & Koo, H.-H. Preparation of C/C composites by the chemical vapor infiltration (CVI) of propane pyrolysis. *Korean J. Chem. Eng.* **28,** 272–278 (2011).
67. Delhaès, P. *et al.* Chemical vapor infiltration of C/C composites: Fast densification processes and matrix characterizations. *Carbon N. Y.* **43,** 681–691 (2005).
68. Naslain, R. R. & Pomeroy, M. Ceramic Matrix Composites: Matrices and Processing. *Ref. Modul. Mater. Sci. Mater. Eng.* (2016). doi:10.1016/B978-0-12-803581-8.02317-1
69. Vignoles, G. L. Chemical vapor deposition/infiltration processes for ceramic composites. *Adv. Compos. Manuf. Process Des.* 147–176 (2015).

doi:10.1016/B978-1-78242-307-2.00008-7

70. Tong, Y., Bai, S., Liang, X., Qin, Q. H. & Zhai, J. Reactive melt infiltration fabrication of C/C-SiC composite: Wetting and infiltration. *Ceram. Int.* **42,** 17174–17178 (2016).
71. Chen, S., Zhang, C., Zhang, Y. & Hu, H. Influence of pyrocarbon amount in C/C preform on the microstructure and properties of C/ZrC composites prepared via reactive melt infiltration. *Mater. Des.* **58,** 570–576 (2014).
72. Chen, S., Zhang, C., Zhang, Y. & Hu, H. Preparation and properties of carbon fiber reinforced ZrC–ZrB_2 based composites via reactive melt infiltration. *Compos. Part B Eng.* **60,** 222–226 (2014).
73. Kütemeyer, M., Schomer, L., Helmreich, T., Rosiwal, S. & Koch, D. Fabrication of ultra high temperature ceramic matrix composites using a reactive melt infiltration process. *J. Eur. Ceram. Soc.* **36,** 3647–3655 (2016).
74. Tian, C. *et al.* Oxidation behaviour of zirconium diboride-silicon carbide ceramic composites under low oxygen partial pressure. *Corros. Sci.* **53,** 3742–3746 (2011).
75. Zhou, H., Gao, L., Wang, Z. & Dong, S. ZrB_2-SiC oxidation protective coating on C/C composites prepared by vapor silicon infiltration process. *J. Am. Ceram. Soc.* **93,** 915–919 (2010).
76. Haibo, O. *et al.* Self-healing ZrB_2-SiO_2 oxidation resistance coating for SiC coated carbon/carbon composites. *Corros. Sci.* **110,** 265–272 (2016).
77. Corral, E. L. & Loehman, R. E. Ultra-high-temperature ceramic coatings for oxidation protection of carbon-carbon composites. *J. Am. Ceram. Soc.* **91,** 1495–1502 (2008).
78. Sun, C., Li, H., Fu, Q. & Zhang, J. Microstructure and ablation properties of carbon/carbon composites modified by $ZrSiO_4$. *Corros. Sci.* **79,** 100–107 (2014).
79. Liu, L. *et al.* Ablation in different heat fluxes of C/C composites modified by ZrB_2-ZrC and ZrB_2-ZrC-SiC particles. *Corros. Sci.* **74,** 159–167 (2013).
80. Fu, Q.-G. *et al.* Nanowire-toughened transition layer to improve the oxidation resistance of SiC–$MoSi_2$–ZrB_2 coating for C/C composites. *Corros. Sci.* **111,** 259–266 (2016).
81. Walker, L. S. & Corral, E. L. Self-Generating High-Temperature Oxidation-Resistant Glass-Ceramic Coatings for C–C Composites Using UHTC s. *J. Am. Ceram. Soc.* **97,** 3004–3011 (2014).

82. Li, H., Zhang, L., Cheng, L. & Wang, Y. Ablation resistance of different coating structures for C/ZrB_2 -SiC composites under oxyacetylene torch flame. *Int. J. Appl. Ceram. Technol.* **6,** 145–150 (2009).
83. Guo, S. Thermal and electrical properties of hot-pressed short pitch-based carbon fiber-reinforced ZrB_2–SiC matrix composites. *Ceram. Int.* **39,** 5733–5740 (2013).
84. Yang, F., Zhang, X., Han, J. & Du, S. Processing and mechanical properties of short carbon fibers toughened zirconium diboride-based ceramics. *Mater. Des.* **29,** 1817–1820 (2008).
85. Guo, S., Naito, K. & Kagawa, Y. Mechanical and physical behaviors of short pitch-based carbon fiber-reinforced HfB2-SiC matrix composites. *Ceram. Int.* **39,** 1567–1574 (2013).
86. Sha, J. J. *et al.* Improved microstructure and fracture properties of short carbon fiber-toughened ZrB_2-based UHTC composites via colloidal process. *Int. J. Refract. Met. Hard Mater.* **60,** 68–74 (2016).
87. Silvestroni, L., Sciti, D., Melandri, C. & Guicciardi, S. Tyranno SA3 fiber-ZrB_2 composites. Part II: Mechanical properties. *Mater. Des.* **65,** 1264–1273 (2015).
88. Zoli, L. *et al.* Rapid spark plasma sintering to produce dense UHTCs reinforced with undamaged carbon fibres. *Mater. Des.* **130,** 1–7 (2017).
89. Hong, W., Gui, K., Hu, P., Zhang, X. & Dong, S. Preparation and characterization of high-performance ZrB_2-SiC-Cf composites sintered at 1450 {\textdegree}C. *J. Adv. Ceram.* **6,** 110–119 (2017).
90. Yang, F., Zhang, X., Han, J. & Du, S. Characterization of hot-pressed short carbon fiber reinforced ZrB_2-SiC ultra-high temperature ceramic composites. *J. Alloys Compd.* **472,** 395–399 (2009).
91. Zoli, L., Medri, V., Melandri, C. & Sciti, D. Continuous SiC fibers-ZrB2 composites. *J. Eur. Ceram. Soc.* **35,** 4371–4376 (2015).
92. Sciti, D. *et al.* From random chopped to oriented continuous SiC fibers-ZrB_2 composites. *Mater. Des.* **63,** 464–470 (2014).
93. Sciti, D., Savino, R. & Silvestroni, L. Aerothermal behaviour of a SiC fibre-reinforced ZrB_2 sharp component in supersonic regime. *J. Eur. Ceram. Soc.* **32,** 1837–1845 (2012).
94. Sciti, D., Natali Murri, A., Medri, V. & Zoli, L. Continuous C fibre composites with a porous ZrB_2 Matrix. *Mater. Des.* **85,** 127–134 (2015).
95. Paul, A., Binner, J. & Vaidhyanathan, B. in *Ultra-High Temperature Ceramics:*

Materials for Extreme Environment Applications 144–166 (2014). doi:10.1002/9781118700853.ch7

96. Paul, A. *et al.* UHTC-carbon fibre composites: Preparation, oxyacetylene torch testing and characterisation. *J. Eur. Ceram. Soc.* **33,** 423–432 (2013).
97. Yang, F., Zhang, X., Han, J. & Du, S. Mechanical properties of short carbon fiber reinforced ZrB_2–SiC ceramic matrix composites. *Mater. Lett.* **62,** 2925–2927 (2008).
98. Cecere, A., Savino, R., Allouis, C. & Monteverde, F. Heat transfer in ultra-high temperature advanced ceramics under high enthalpy arc-jet conditions. *Int. J. Heat Mass Transf.* **91,** 747–755 (2015).
99. Levine, S. R. *et al.* Evaluation of ultra-high temperature ceramics for aeropropulsion use. *J. Eur. Ceram. Soc.* **22,** 2757–2767 (2002).
100. Rezaie, A., Fahrenholtz, W. G. & Hilmas, G. E. Evolution of structure during the oxidation of zirconium diboride-silicon carbide in air up to 1500 °C. *J. Eur. Ceram. Soc.* **27,** 2495–2501 (2007).
101. Tripp, W. C. & Graham, H. C. Thermogravimetric study of the oxidation of ZrB2 in the temperature range of 800C to 1500°C. *J. Electrochem. Soc. J. Electrochem. Soc.* **118 No.7,** 1195–1199 (1971).
102. Zhang, L. & Kurokawa, K. Effect of SiC Addition on Oxidation Behavior of ZrB2 at 1273 K and 1473 K. *Oxid. Met.* **85,** 311–320 (2016).
103. Kazemzadeh Dehdashti, M., Fahrenholtz, W. G. & Hilmas, G. E. Effects of transition metals on the oxidation behavior of ZrB_2 ceramics. *Corros. Sci.* **91,** 224–231 (2015).
104. Silvestroni, L. & Sciti, D. Densification of ZrB2-TaSi2 and HfB_2-$TaSi_2$ Ultra-High-Temperature Ceramic Composites. *J. Am. Ceram. Soc.* **94,** 1920–1930 (2011).
105. Han, J., Hu, P., Zhang, X. & Meng, S. Oxidation behavior of zirconium diboride-silicon carbide at 1800 °C. *Scr. Mater.* **57,** 825–828 (2007).
106. Karlsdottir, S. N. & Halloran, J. W. Oxidation of ZrB 2-SiC: Influence of SiC content on solid and liquid oxide phase formation. *J. Am. Ceram. Soc.* **92,** 481–486 (2009).
107. Williams, P. A., Sakidja, R., Perepezko, J. H. & Ritt, P. Oxidation of ZrB_2-SiC ultra-high temperature composites over a wide range of SiC content. *J. Eur. Ceram. Soc.* **32,** 3875–3883 (2012).

108. Wu, H. & Zhang, W. Fabrication and properties of ZrB_2-SiC-BN machinable ceramics. *J. Eur. Ceram. Soc.* **30,** 1035–1042 (2010).
109. Han, J., Hu, P., Zhang, X., Meng, S. & Han, W. Oxidation-resistant ZrB_2-SiC composites at 2200 °C. *Compos. Sci. Technol.* **68,** 799–806 (2008).
110. Zoli, L. & Sciti, D. Efficacy of a ZrB_2-SiC matrix in protecting C fibres from oxidation in novel UHTCMC materials. *Mater. Des.* **113,** 207–213 (2017).

3. Experimental

3.1 Process

Unlike conventional bulk ceramics for which a wide array of known processing techniques is available, the processing of UHTCMCs is complicated by the presence of the fibre reinforcement that poses a major obstacle to the consolidation of the ceramic powders. Previous studies on the fabrication of UHTCMCs showed that the presence of fibres hindered the sintering of the powders, ultimately leading to a higher degree of porosity in the final composite [12]. Conversely, obtaining fully dense UHTCMCs by increasing the temperature and pressure during sintering usually leads to excessive degradation of the fibre reinforcement, jeopardizing the properties of the composite [3]. Therefore it is of utmost importance to study the sintering parameters and find the best compromise in order to minimize both porosity and fibre degradation. The fabrication of carbon fibre reinforced UHTC composites requires several steps before obtaining the final material.

3.1.1 Powder ball milling:

The first step consists of the preparation of the powder mixtures and their homogenization. Ball milling technique is based on the capability of hard materials (such as SiC or Si_3N_4) to grind relatively softer powders and allow for the reduction of the starting particle size and their homogenization. The presence of a solvent, such as ethanol, aids the mixing of the powders and minimizes heat production and oxidation of the particles. Commercially available powders were used for the preparation of the ceramic composite materials:

- ZrB_2 (H.C. Starck, grade B, Germany, specific surface area 1.0 m2/g, particle size range 0.5-6 μm, impurities (wt.%): 0.25 C, 2 O, 0.25 N, 0.1 Fe, 0.2 Hf),
- ZrC (Treibacher Industrie AG, Austria, particle size range 1 to 2 μm, impurities (wt.%): 0.4 C, 0.6 O, 0.1 N)
- TaC (Treibacher Industrie AG, Austria, particle size range 1 to 2 μm, impurities (wt.%): 0.005 Al, 0.15 C, 0.005 Ca, 0.03 Fe, 0.05 N, 0.25 Nb, 0.3 O, 0.005 S, 0.005 Si, 0.05 Ti)

- HfC (Materion Advanced Material Group, UK, 325 mesh, impturities (wt.%): O < 0.6, Al < 0.001, Ca < 0.005, Fe < 0.001, Ti < 0.01, Zr < 0.1)
- α-SiC (H.C. Starck, Grade UF-25, Germany, specific surface area 23 to 26 m2/g, D50 0.45 µm Italian retailer: Metalchimica)

Unidirectional high modulus carbon fibres (Granoch Yarn XN80-6K fibres; tensile modulus of 780 GPa and tensile strength 3.4 GPa, 10 µm diameter. Supplier: Angeloni) were used as carbon preforms.

Depending on the desired composition, powder mixtures are prepared by wet ball milling of the starting powders with SiC grinding media in absolute ethanol (water content <0,05%) for 24h at 60 rpm. It is important to avoid the presence of water during this step in order to minimize the surface oxidation of the powders [4]. The ratio of the powder to solvent to grinding media is of 1 : 1 : 1 by weight. After ball milling, the powders are completely dried with a rotary evaporator at 90°C and then sieved. This procedure is depicted in figure 3.1.

Figure 3.1 Steps involved in the preparation of powders: 1st step is the wet ball milling of the raw powders with SiC grinding media. 2nd step is the evaporation of the solvent with a rotary evaporator. 3rd step consists in sieving the dried powders to break agglomerates.

3.1.2 Slurry infiltration:

The dry powders are dispersed in water using poly-acrylates at different molecular weight in order to adjust the final desired fibre content accordingly [5]. The suspensions are then mixed for 3h in a HDPE bottle in order to homogenize the powders with the dispersant and avoid precipitation. The as prepared slurries are used to infiltrate the

carbon fibre preforms which are later stacked either in a 0/0° or 0/90°. The infiltrated fibres are dried in a oven at 80°C for 1 h to remove the excess water.

3.1.3 Hot Pressing

The dried green pellet is cut in a graphite die and consolidated via hot pressing in vacuum (10^{-5} bar) at 1900°C and under a uni-axial pressure of 40 MPa for 10 min. For the samples containing ZrB_2 and SiC, an initial pressure of 20 MPa is applied starting at 900°C and then it is progressively increased to 30 MPa at 1700°C and 40 MPa at 1900°C, in order to allow for the gradual release and evaporation of B_2O_3 impurities and avoid the formation of gas bubbles in the final composite [6]. At 1900°C the pressure of 40 MPa is maintained for 10 min, then the load is removed and the sample is cooled down to 1000°C at a rate of 50 °C/min to avoid the formation of cracks due to thermal shock. For the sample containing the carbides of tantalum, zirconium and hafnium, a pressure of 40 MPa is applied already at 900°C and maintained at 1900°C for 10 min.

3.2 Microstructural characterization

The microstructure of a material comprises the compositional, morphological and crystallographic characteristics of its phases. The study of the microstructure can help us understand the chemical, thermal, electrical and mechanical properties of a material.

The analytical techniques employed in the analysis of the microstructure are X-Ray Diffraction (XRD), Scanning Electron Microscopy (SEM) and Energy Dispersive X-Ray Spectroscopy (EDS).

3.2.1 X-Ray diffraction analysis

X-Ray diffraction analysis is a non-destructive technique used to reveal information about the crystal structure of a material, its chemical composition, physical properties and crystallographic parameters. The information is obtained from analysing the intensity of the scattered beam of an X-Ray source hitting the sample as a function of the incident angle, polarization and energy.

X-rays are electromagnetic radiations with wavelengths in the range of 0.01 – 10 nm and occur in the region of the electromagnetic spectrum between ultraviolet and gamma-rays (fig. 3.2).

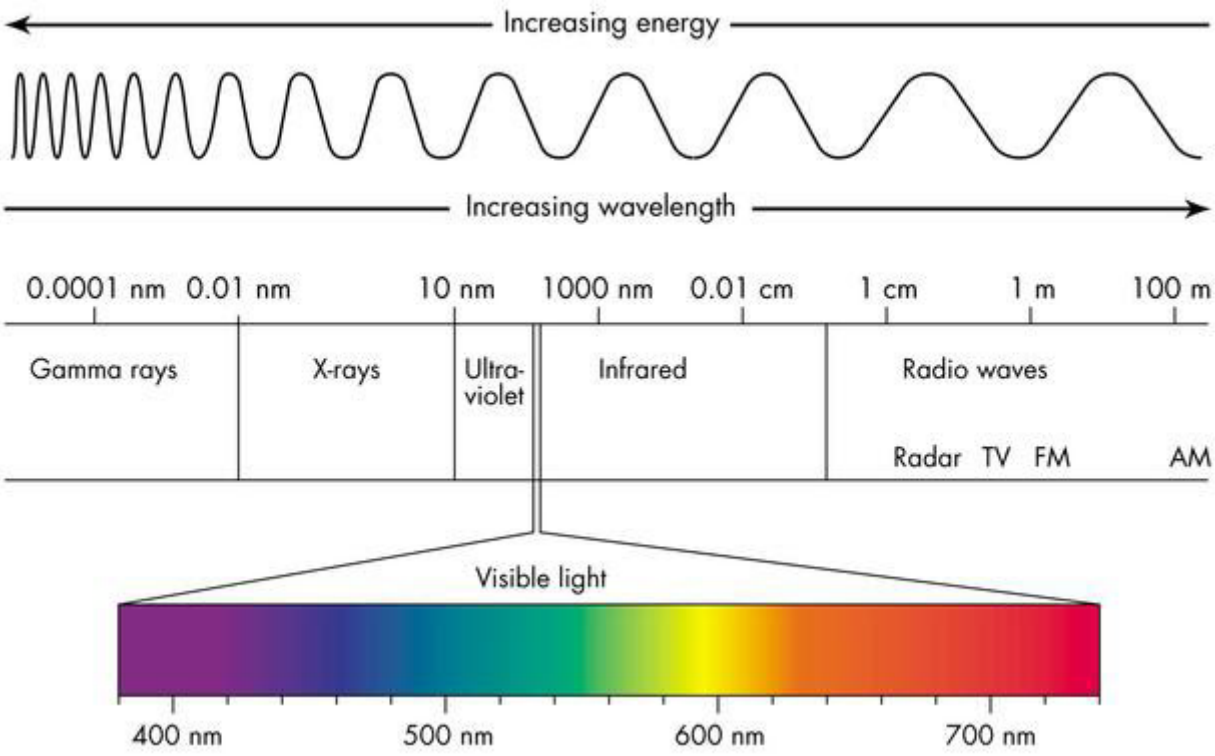

Figure 3.2 Range of frequencies of electromagnetic radiations. X-Rays fall in the range 0.01 – 10 nm and are second in energy only to Gamma rays.

X-ray diffraction analysis is used for the fingerprint characterization of crystalline materials and the determination of their structure. Each crystalline solid has its unique characteristic X-ray diffraction pattern which can be used as a univocal marker for their identification. After the chemical composition has been identified, X-ray crystallography can be used to determine the structure, such as the atoms packing, interatomic distance, distance between planes, etc. X-ray diffraction constitutes an important tool in solid state chemistry and material science, since it can help with the determination of the size and shape of the unit cell of any compound. The theoretical principles behind this technique are explained.

The distance between two crystallographic planes of polycrystalline materials, labelled d, has dimensions that fall in the wavelength range of X-rays and therefore the interaction between the electromagnetic radiation and atoms can give rise to radiation scattering and interference phenomena. This model can be assimilated to the reflection of an incident radiation on the crystallographic planes of a crystal for which, depending on the angle of incidence, θ, both destructive and constructive interference can be determined (fig. 3.3).

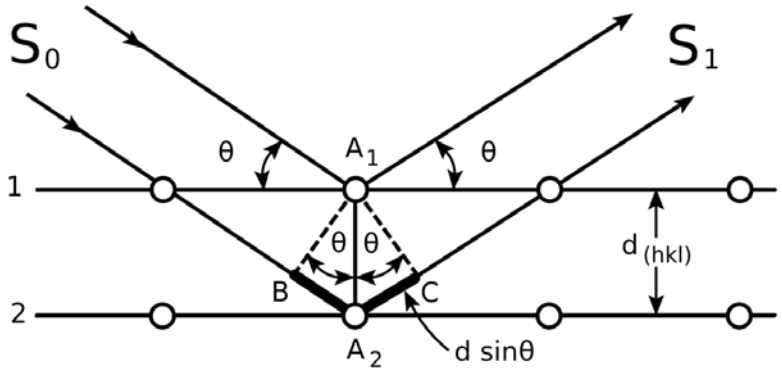

Figure 3.3 Bragg's diffraction: two beams approaching the atoms of a crystal are scattered in different directions. When the scattered beams are in coherence, diffraction occurs.

The path difference between two incident rays on the crystallographic planes of a material is (1):

$$\overline{BA_2} + \overline{A_2C} = 2\ d\ \sin\theta \qquad (1)$$

When the path difference is equal to an integer multiple of the wavelength, the reflected rays are in phase and constructive interference occurs. This relation is known as Bragg's law (2):

$$n\ \lambda = 2\ d\ \sin\theta \qquad (2)$$

From X-ray diffraction pattern, the most intense signals are obtained in correspondence of integer numbers of λ. From these signals it is possible to calculate the value of the interplanar spacing between atoms in the crystal, d.

The X-ray diffractometer is constituted by a X-ray source, a sample holder and a rotating detector. The scheme is ported in figure 3.3.

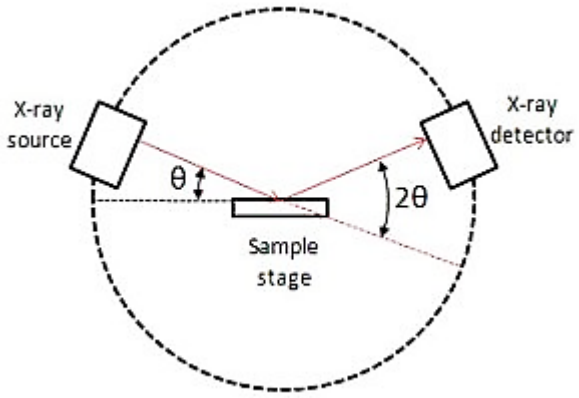

Figure 3.4 Schematic of a X-ray diffractometer with Bragg-Brentano geometry. The sample is fixed while the X-ray source and the detector rotate around an angle of θ

X-rays are produced by accelerating electrons on a metal plate, typically copper, from which characteristic radiation are emitted and collimated on the sample. When the incident beam collides with the sample, diffraction occurs. The diffracted beam can be detected by using a rotating detector that analysed the intensity of the diffracted beam as function of twice the incident angle, 2θ.

With X-ray diffraction analysis it is also possible to determine the grain size of crystallites constituting a powder sample, its lattice constants, potential induced stresses on samples that experienced mechanical deformation etc. Therefore X-ray diffraction is a very versatile and important tool in material science.

3.2.2 Scanning electron microscopy

The scanning electron microscope is a microscope that uses a focused beam of electrons to produce an image of the morphology of the sample. The main advantages of SEM are the large depth of field, which allows to retain focus on uneven samples, and the high magnification and resolution of the images [7]. Moreover the preparation of the samples is very simple and the only requirement is that the sample is conductive. In case of insulating materials, conductive tapes, glues or even sputter coater can be used in order to make it conductive. To observe the morphology, a gold coating is usually preferred, whereas a carbon coating can be used to investigate the compositions and phases. The combination of these characteristics make SEM one of the most important and used instruments in materials science. The theoretical concepts of SEM are explained.

The electron beam is produced by an electron gun which is constituted by a cathode, typically a tungsten filament, and an anode. An electric potential is applied to the filament, causing it to heat up and emit electrons which are attracted by the anode and accelerated down the column, to the sample (fig. 3.5)

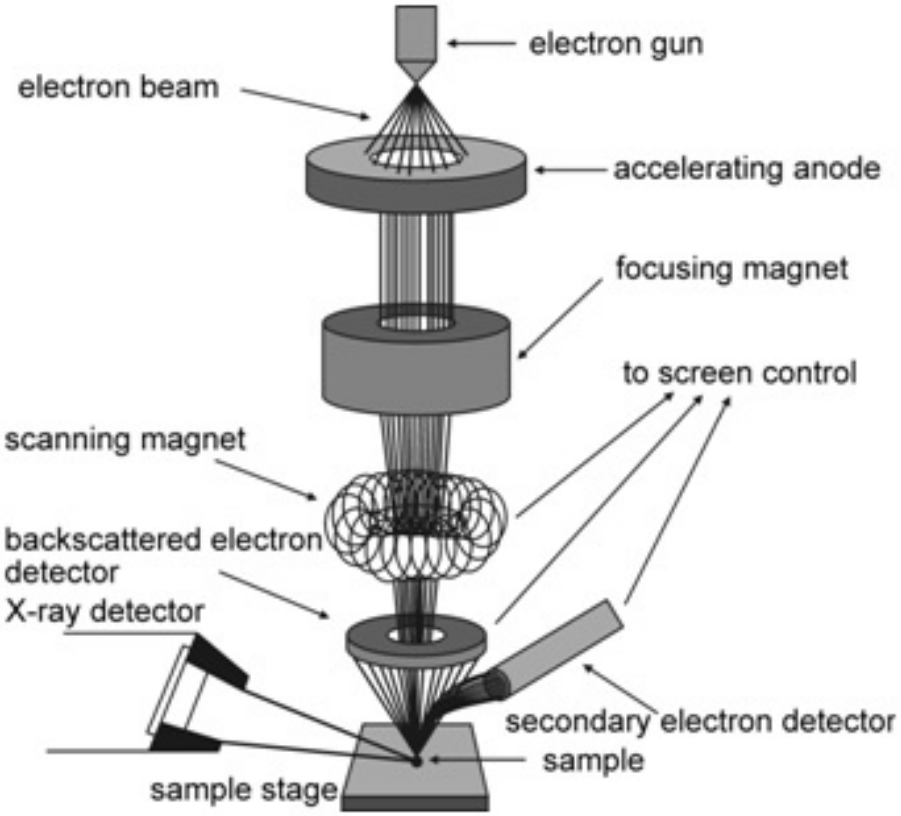

Figure 3.5 Schematics of a Scanning electron microscope. An electron beam generated by the acceleration of electrons by an electron gun is focused with a magnet on the sample. Each signal is revealed by different detectors (Secondary electrons, X-rays and backscattered detectors).

When the electron beam hits the sample, it provokes the emission of electrons from the surface of the sample which are collected by a secondary detector or a backscattered detector, and converted to a voltage which is amplified and computed. The amplified voltage is applied to the grid of CRT and causes the intensity of the spot of light to change. The image consists of thousands of spots of different intensity on the face of a CRT that correspond to the topography of the sample and are used to reconstruct the image.

Not all the signals generated are actually detected and analysed. The most commonly studied signals are the secondary electrons, the backscattered electrons and X-rays (Fig. 3.6). Secondary electrons are generated by the inelastic collisions of the source beam electrons with the specimen electrons. They typically possess energy below 50 eV.

Secondary electrons are mainly produced by the interactions between energetic beams electrons and weakly bonded conduction-band electrons in metals or valence electrons in insulators and semiconductors. There is a great difference between the amount of

energy contained by the beam electrons compared to the specimen electrons and due to this only a small amount of kinetic energy can be transferred to the secondary electrons.

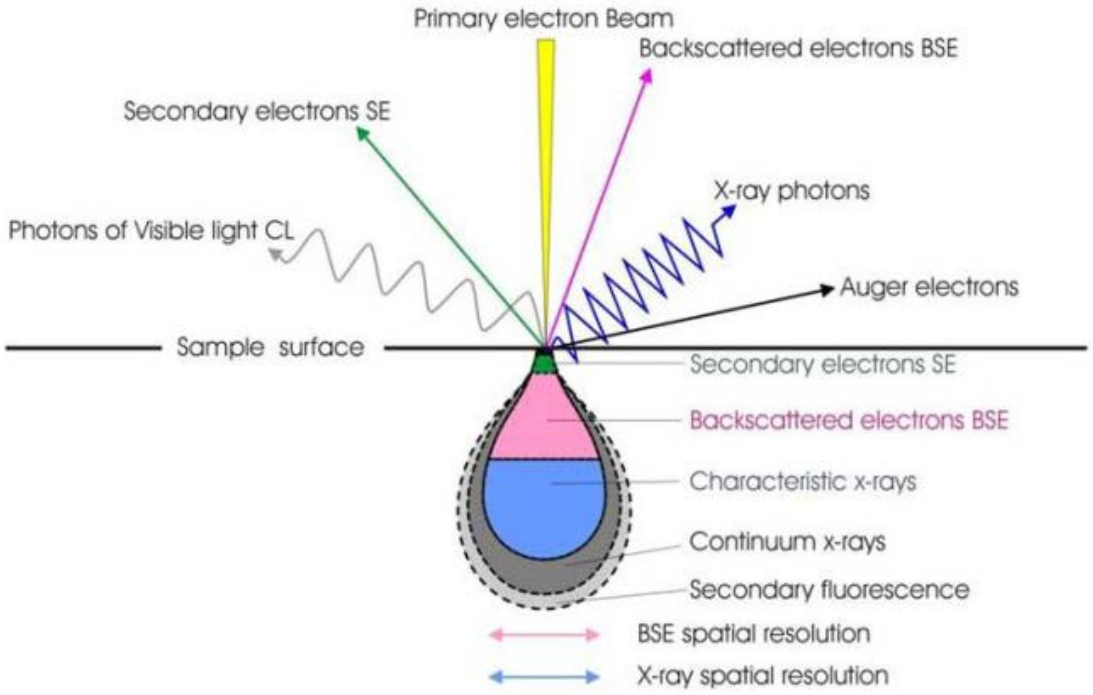

Figure 3.6 Signals generated by the action of the electron beams: secondary electrons, backscattered electrons, X-rays, photons of visible light, Auger electrons.

Elastic scattering occurs between the positive nucleus and the negative electrons and is called Rutherford scattering. When the angle is such that the electrons come back out of the sample, then they are called backscattered electrons.

During inelastic scattering, energy is transferred to the electrons surround the atoms and the kinetic energy of the energetic electron involved decreases. One inelastic event can transfer different amounts of energy from the electron beam ranging from few eV to many keV. The processes involved include phonon excitation, plasmon excitation, secondary electron excitation, continuum X-ray generation and ionization of the inner shell. In all these processes, energy is lost even if at different rates [7].

While operating the SEM, a good level of vacuum inside the column must be maintained at all times for multiple reasons. If the sample is in a gas filled environment, an electron beam cannot be generated or maintained because of the high instability in the beam. Gases could react with the electron source, causing its burnout , or could produce discharges and lead to instability in the beam. The transmission of the beam through the electron column could also be hindered by the presence of other molecules. The latter could be present on the sample or the microscope itself and form compounds

that could condense on the walls of the instrument or the sample, lowering the contrast and obscuring details in the image.

The spatial resolution of the SEM depends on the size of the electron spot. The latter is dependent on both the wavelength of the electron and the electrical-optical system that produces the electron beam. The resolution is also limited by the size of the interaction volume or the extent to which the material interacts with the electron beam. The spot size and the interaction volume are both large compared to the distance between atoms, so the resolution of the SEM is not high enough to map individual atoms. Depending on the instrument, the resolution can go from 20 nm to less than 1 nm.

3.2.3 Energy-dispersive X-ray spectroscopy

Energy dispersive X-ray spectroscopy (EDS or EDX) is a technique used for the analysis of elements and the chemical characterization of a specimen [7]. It is an instrument typically integrated with a SEM apparatus and it analyses the X-rays emitted by the sample due to the interaction with the electron beam of the SEM. When the electron beam hits the sample, an electron from the ground state is excited to a higher energy level and leaves behind an electron vacancy. This vacancy can be filled by an outer shell electron, releasing an amount of energy equal to the difference in orbital energies. The resulting energy can either be released in the form of X-rays, or can be absorbed to lose a second outer shell electron (fig. 3.7).

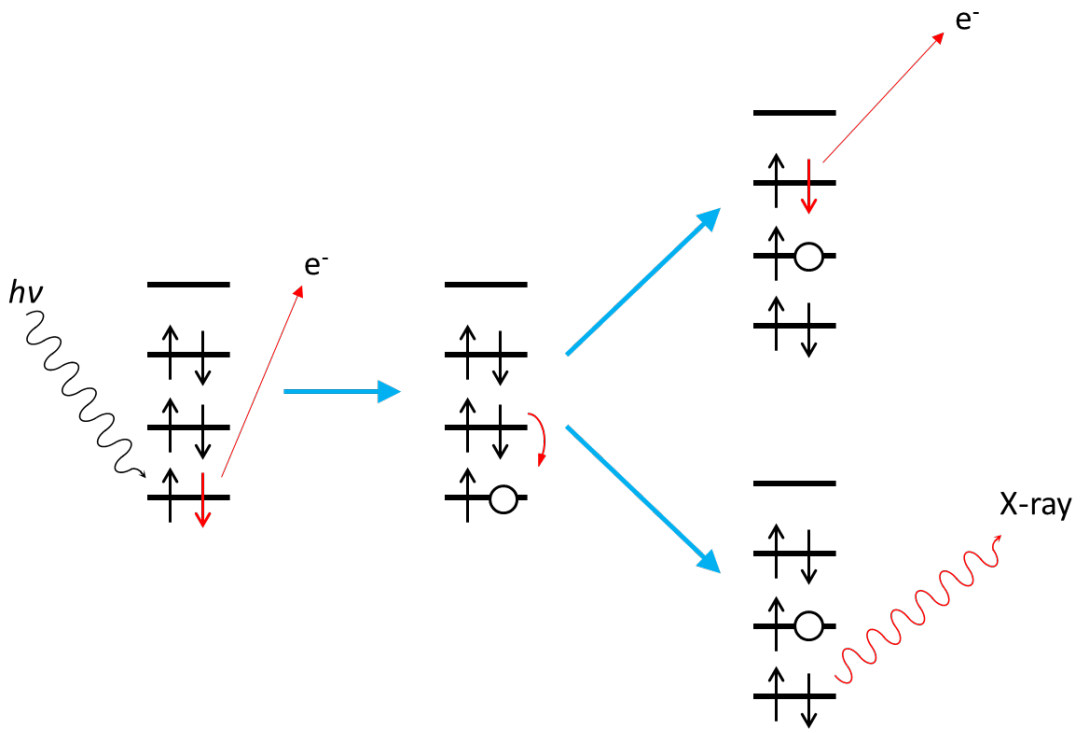

Figure 3.7 Illustration of the steps involved in the production of X-rays and Auger electrons. When the incident beam (hν) hits a bound electron in the inner shell, the target electron is ejected, generating a hole in the ground level. This is filled by an electron in the higher levels, with the release of energy. This energy can be either emitted in the form of X-rays, or used to eject a second outer shell electron (Auger electron) [8].

By analysing the emitted X-rays it is possible to map the elemental composition of the specimen. The apparatus is constituted by an excitation source, which in this case is the same as the SEM, and a detector that converts the X-ray radiation energy into a voltage that can be analysed. EDS is mainly a qualitative tool, even though it is possible to carry out quantitative analysis after appropriate calibration with a metal standard, typically a cobalt target. The accuracy of the analysis is affected by the nature of the sample and the energy of the electron beam. Heavy metal targets require higher energy to emit X-rays, but a high energy electron beam can negatively affect the accuracy on lighter elements due to the higher depth of penetration of the beam (fig. 3.8).

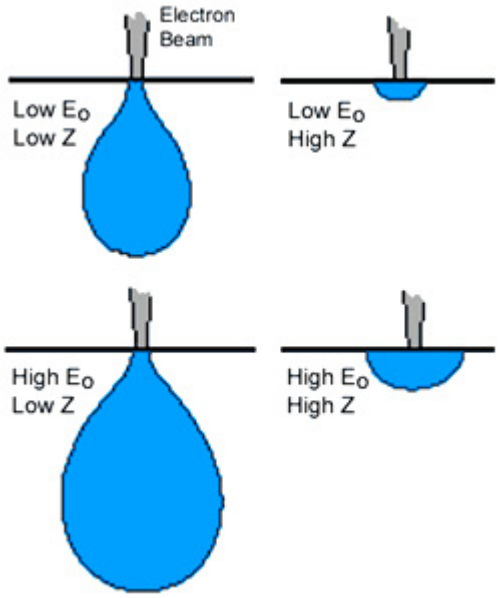

Figure 3.8 Depth of penetration of the electronic beam as function of the applied electric field and the atomic weight of the elements studied. Higher voltages are associated to a larger depth of penetration, leading to less accurate analysis.

In the present work, microstructures and compositions were analysed on polished and fracture surfaces of the specimens by field emission scanning electron microscopy (FE-SEM, Carl Zeiss Sigma NTS Gmbh Öberkochen, Germany), energy dispersive X-ray spectroscopy (EDS, INCA Energy 300, Oxford instruments, UK) and X-ray diffraction analysis (Bruker D8 Advance apparatus, Karlsruhe, Germany) before and after testing at high temperature. Samples were prepared for microscopy by cutting cross sections, mounting them in epoxy resin, and then polishing down to a 0.25 μm finish with diamond abrasives using a semi-automatic polishing machine (Tegramin-25, Struers, Italy). The polished samples were then washed with ethanol and acetone in an ultrasonic bath for 15 min, dried under IR light and treated in a plasma cleaner (Colibrì Plasma RF 50 KHz, Gambetti, Italy) at 40 W for 5 min. For oxidized samples, a thin carbon coating was applied with a turbo-pumped sputter coater (Q150T, Quorum Technologies Ltd, UK) on the surface of the specimens to avoid electron scattering on the insulating oxides.

3.3 Mechanical testing

In order for a material to be considered suitable for structural application, extensive mechanical characterization has to be carried out. The most important mechanical

properties of ceramic composites are Young's modulus, flexural strength at low and high temperature and fracture toughness.

3.3.1 Elastic modulus

Young's modulus or elastic modulus, E, is a measure of a material resistance to elastic deformation in the direction parallel to the applied load, and is defined as the ratio between stress, σ, and strain, ε (3) [9,10]:

$$E = \frac{\sigma}{\varepsilon} \qquad (3)$$

A specimen under tension or compression is subject to a strain in the direction of the applied load. When the stress is relatively low, only elastic deformation occurs, meaning that the specimen returns to its original shape when the load is removed. In these conditions, the strain is proportional to the applied stress and the Young's modulus represents the slope of the curve in the linear tract (fig. 3.9).

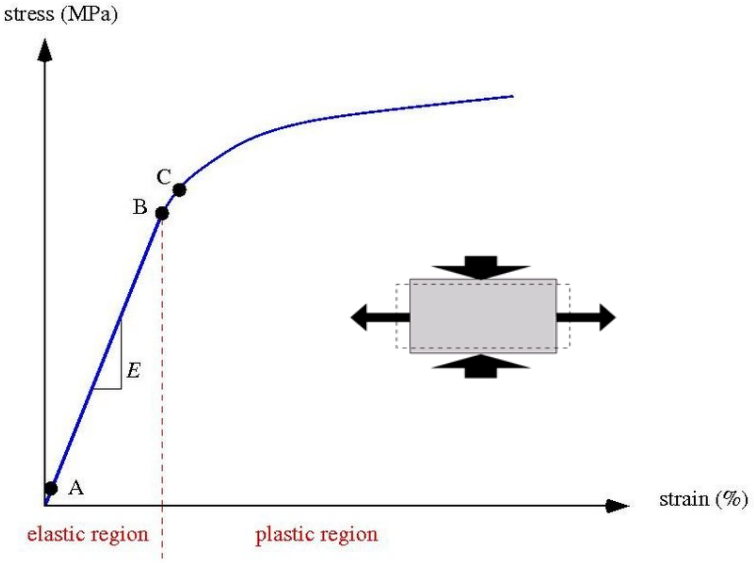

Figure 3.9 Typical stress/strain curve of a plastic material. The linear section of the curve (from A to B) is called elastic region and the slope is given by Young's modulus. The insert image represents transverse shrinkage as a consequence of assail strain.

As the material deforms in the direction of the applied load, transverse strain is induced on the specimen. Poisson's ratio, ν, is a measure of this deformation and is defined as the ratio of transverse strain to the corresponding axial strain.

Young's modulus must not be confused with stiffness, which is also dependent on the shape of the specimen. For example for the same material, a I shaped beam will have a

higher stiffness in bending than a rod of the same weight due to the different geometrical rigidity of the body.

The methods to measure the elastic properties of materials fall in two groups: static and dynamic. In static methods, a static load is applied on the specimen and the induced strain is measured with strain gauges. While this method gives reliable results for polymers or metals, it is not suited for ceramic materials which require high loads to induce a very small strain before rupturing the material. In this case it is preferable to use dynamic methods such as:

- ultrasonic wave method, a non-destructive method where the ultrasonic propagating velocity through a specimen of known geometry is measured. Then this measure can be correlated to the elastic properties of the material.
- resonant frequency method, a non-destructive technique that measures the resonant frequencies of a material. The specimen is attached to the ends of a single degree of freedom oscillator which is set into motion. By varying the frequency of the oscillations, it is possible to identify the natural frequency of the material which is given by following equation (4):

$$f_n = \frac{1}{2\pi}\sqrt{\frac{k}{m}} \qquad (4)$$

Where k is the stiffness constant, m is the mass and f_n the natural frequency. The elastic modulus can be calculated with equation (5):

$$E = 0.946\left(\frac{m{f_n}^2}{b}\right)\left(\frac{l}{h}\right)^3\left[1 + 6.585\left(\frac{h}{l}\right)^2\right]10^{-9} \qquad (5)$$

where m is the mass (g), f_n the natural frequency (Hz), and b, l and h are the width, length and thickness (mm) respectively [11,12]. In the present work, Young's modulus was measured both with the resonant frequency and ultrasonic wave methods.

3.3.2 Flexural strength

Tensile testing is the preferred method to test the mechanical strength of materials. However in the case of ceramics, tensile testing is often problematic due to the complex geometry of the specimens, the time and costs associated with the machining, and the tendency of ceramics to rupture prematurely at the clamps. Therefore flexural strength testing is often favoured. Rectangular bars are loaded either in a three or four point bending setup and the maximum strength at rupture is referred to as the flexural strength

[13]. The formula for the calculation of flexural strength of a rectangular bar is reported in equation (6) [10]:

$$\sigma = \frac{3F(L-L_0)}{2bd^2} \quad (6)$$

Where F is the force, L and L_0 are the outer and inner support span respectively (for three point bending, $L_0 = 0$), and b and d are the width and thickness respectively. The flexural strength of bulk ceramics is strictly dependent on size, shape, porosity, distribution of flaws and surface finishing. Pores are particularly detrimental to the strength of the ceramics because they reduce the area where the load is applied and act as defects where all the stresses are concentrated. Strength is also affected by grain size, typically decreasing with the increase of the grain dimensions, therefore sintering parameters such as temperature and pressure must be controlled in order to avoid excessive grain growth. In the case of grains in the range of 1 – 5 μm, strength is mostly affected by surface flaws or porosity. Residual stresses originating from thermal shock or the sintering process can also lower the mechanical properties.

Strengthening of ceramics can be achieved by minimizing the grain size of the main phase with the introduction of a secondary phase that hinders grain growth. In the case of ZrB_2 ceramics, this can be achieved by introducing small amounts of SiC or ZrC or WC [14,15]. Alternatively, the presence of a low melting phase can seal the cracks formed during sintering and lower the likelihood of the sample rupturing [16].

Due to the intrinsic anisotropy of fibre reinforced ceramic composites, the measure of strength is a more complex subject. For these materials, porosity is usually higher than the corresponding bulk material and achieving full density often results in damaged fibres [3]. Moreover the strength is dependent on the fibre strength, modulus and orientation. For samples tested in bending with the applied load perpendicular to the fibre orientation, the load is fully transferred to the fibres and the maximum strength value is obtained [17]. When the load is parallel to the fibres, the sample ruptures in a brittle mode because the fibres are not acting as reinforcement but as a defect. Specimens with alternating layers of fibres with a 0/90° orientation give rise to complex fracture modes.

In the present work, a baseline material with uni-directional fibres was extensively studied in order to investigate the mechanical behaviour while minimizing the number of variables. Then the study moved to composites with alternating layers of

fibres in the 0° and 90° orientation and the effect of secondary phase (SiC) and fibre content on the mechanical properties was addressed.

In the present work, four points bending strength tests were carried out on test bars 25 x 2.5 x 2 mm (length by width by thickness, respectively) using a semi-articulated test fixture with a lower span of 20 mm and an upper span of 10 mm using a screw-driven testing machine (Zwick/Roell, model Z050), following the guidelines of standard ISO 14704:2016(en).

For the tests at room temperature, the specimens were fractured using a fully-articulated steel four-point fixture using a screw-driven testing machine (Zwick/Roell, model Z050). For the tests at 1500°C, a screw-driven testing machine (model 1195, Zwick/Roell) was used; the specimens were mounted on a 4-point alumina test fixture and heated up to 1500°C with a rate of 10°C/min under a constant flow of argon (3,5 L/min) in a high temperature furnace (HTTF model 924, Severn Furnaces Limited). The samples were held for 15 min at 1500°C before testing. Finally a mechanical testing apparatus consisting of a screw-driven instrumented load frame (33R4204, Instron, Norwood, MA) coupled with an induction heated (SI-30KWLF, Superior Induction Technology, Pasadena, CA) graphite die enclosed in an environmental chamber, was used to perform tests at 1800 and 2100°C. Temperature was controlled using a two-color optical pyrometer (SR-35C15, Ircon Inc., Santa Cruz, CA) and a programmable PID controller (2404, Eurotherm, Ashburn, VA). Specimens were loaded onto a graphite fixture and secured using a cyanoacrylate adhesive. The chamber was flushed with argon for 45 minutes prior to heating. The specimens were heated to the target temperature with a heating rate of 50°C/min, followed by a 5 min isothermal hold, and then tested. At least three bars were tested for each material at each condition. Displacements were measured by crosshead displacement of the testing machine.

3.3.3 Fracture toughness

Fracture toughness, K_{IC}, is a measure of a material's resistance to crack propagation. For bulk ceramics, several methods are known for the determination of this parameter, such as Vickers hardness indentations [18–20]. In this method a diamond indenter penetrates the surface of the specimen, inducing the generation of cracks from the corners of the indentation. The length of the cracks produced can be measured and correlated to the resistance of the material to fracture toughness. However, the values of K_{IC} obtained with this method are not reliable or valid in the case of fibre reinforced

composites where the crack can be easily arrested by the presence of fibres, resulting in inflated values. Other techniques based on the introduction of a notch where all the stresses are concentrated is the preferred method for the evaluation of fracture toughness. According to this method, notches are introduced by very sharp cutting tools and the specimens are tested in bending [21]. Different notch geometries have been considered (fig. 3.10):

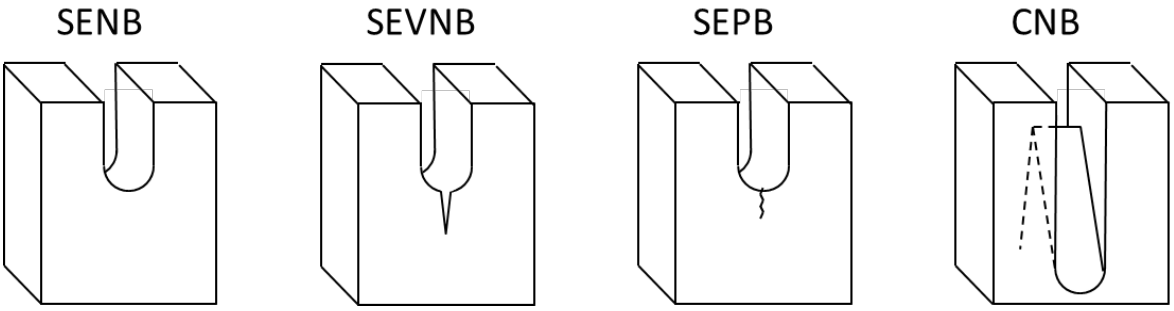

Figure 3.10 Schematic representation of the different notch geometries. The width of the notch is voluntarily exaggerated to better show the main differences.

- Single edge notched beam (SENB), where a flat notch is introduced. Due to the difficulty in introducing a notch with a radius below 25 μm, this method is affected by a lot of data scattering.
- Single edge V-notched beam (SEVNB), similar to SENB, where a smaller notch is introduced by sawing with a razor blade. This method allows to introduce a more critical defect, but the difficulty in making a straight notch is often the limiting factor
- Single edge pre-cracked beam (SEPB), similar to SENB, where the critical defect is introduced by pre-cracking the beam at low loads. A very small crack initiates at the notch tip and is used to test the sample in bending. This method allows for more accurate results, but in the case of fibre reinforced composites it is difficult to initiate the crack.
- Chevron notched beam (CNB), where a triangle-shaped notch is introduced with diamond blades . When the load is applied, the crack initiates at the tip of the triangle and propagates from there. This method has the advantage of not having issues related to the curvature radius at the tip. The CNB model and formulas are reported in figure 3.1.

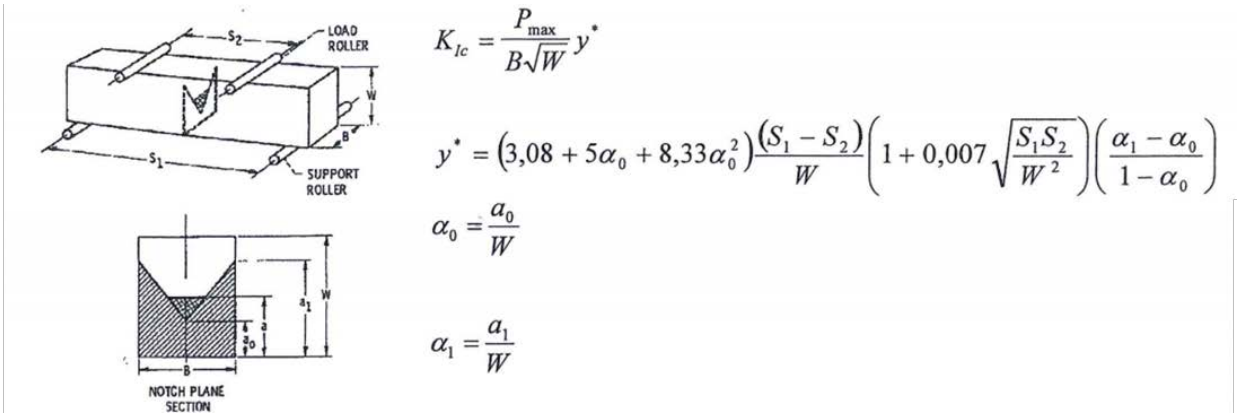

$$K_{Ic} = \frac{P_{max}}{B\sqrt{W}} y^*$$

$$y^* = \left(3{,}08 + 5\alpha_0 + 8{,}33\alpha_0^2\right)\frac{(S_1 - S_2)}{W}\left(1 + 0{,}007\sqrt{\frac{S_1 S_2}{W^2}}\right)\left(\frac{\alpha_1 - \alpha_0}{1 - \alpha_0}\right)$$

$$\alpha_0 = \frac{a_0}{W}$$

$$\alpha_1 = \frac{a_1}{W}$$

Figure 3.11 Chevron notched beam model and equations for the determination of K_{IC}

In the present work, fracture toughness was measured with the CNB method on bars with dimensions 2 x 2,5 x 25 (width x thickness x length). At least three bars per sample were tested.

3.4 Oxidation resistance

To evaluate the oxidation resistance of these composites, a preliminary thermo-gravimetric analysis study was carried out on a baseline ZrB_2/SiC/C sample in order to investigate the critical temperatures and the kinetics of oxidation. Following these preliminary tests, oxidation experiments were carried out in a bottom-up furnace at higher temperatures to assess the behaviour of these materials under rapid heating.

3.4.1 Thermo-gravimetric analysis

Thermo-gravimetric analysis (TGA) is a thermal analysis technique that allows to monitor the mass of a sample over time as function of the temperature. This analysis provides information about the physical and chemical phenomena taking place on the sample, such as oxidation reactions, evaporation of volatile compounds, phase transitions etc. The thermo-gravimetric analyser continuously measures the mass of a sample while the temperature is progressively increased at a fixed rate. With this technique it is also possible to study the kinetics of oxidation by conducting isothermal tests at different temperatures .

In the present thesis, TGA was used to study the oxidation behaviour of a baseline carbon fibre reinforced ZrB_2/SiC composite from 800 to 1550°C. Regular samples sized 14 x 2.5 x 2 mm3 were cut from the sintered pellet. The specimens were cleaned with acetone in an ultrasonic bath, dried at 100 °C and weighed (accuracy 0.01 mg). The oxidation tests were carried out in a thermogravimetric analyser (model

STA449, NETSCH, Geraetebau GmbH, Selb, Germany), in synthetic air (composition: 80 vol% N_2 + 20 vol% O_2, with 30 ml/min gas flow).

Four non isothermal stages (Tests 1-4, in Table 3.1) were carried out in air stopping at selected temperatures (i.e. 750, 1100, 1450 and 1550 °C), with a heating rate of 10 °C/min, in order to analyse the microstructure at critical oxidation stages for carbon fibres. One additional non-isothermal test in air up to 1550 °C was carried out at a rate of 45°C/min (Tests 5 in Table 3.1), in order to isolate the effect of heating rate on the oxidation of carbon fibres.

Then, isothermal runs were conducted at 800, 1000, 1200 and 1400 °C for 6 hours in air. For the isothermal tests, the samples were placed inside the furnace, on top of an alumina plate, and heated to their respective temperatures at a rate of 30 °C/min in a protective atmosphere of argon, in order to minimize oxidation effects before reaching the target temperature (tests 6-9 in Table 3.1).

Table 3.1 Summary of the TG experiments and operating conditions: Tests 1-5 are non-isothermal tests, with ramps from RT to the target temperature. Tests 6-9 are isothermal tests with an initial ramp in Ar, followed by exposure to flowing air for 6 h.

Sample	Heating Rate	Target temperature	Exposure time
1	10°C/min, air	750°C	/
2	10°C/min, air	1100°C	/
3	10°C/min, air	1450°C	/
4	10°C/min, air	1550°C	/
5	45°C/min, air	1550°C	/
6	30°C/min, argon	800°C	6 hours in air
7	30°C/min, argon	1000°C	6 hours in air
8	30°C/min, argon	1200°C	6 hours in air
9	30°C/min, argon	1400°C	6 hours in air

Afterwards, the samples were exposed to air for 6 hours and then cooled to room temperature.

The mass variation was recorded continuously with 10^{-3} mg sensitivity and normalized on the surface area: : $\frac{\Delta w}{S} = \frac{(w_{fin} - w_{ini})}{S}$. The TG measurements evaluation was

performed with the subtraction of Buoyancy effect correction curve for instrument errors.

Surfaces and polished cross-sections were analysed by scanning electron microscope (FE-SEM, Carl Zeiss Sigma NTS Gmbh Öberkochen, Germany) and energy dispersive microanalysis (EDS, Model INCA energy 300; Oxford Instruments, High Wycombe, UK).

3.4.2 Air furnace oxidation testing

Following these preliminary studies, harsher tests were conducted in a bottom-up loading furnace (fig. 3.12).

Figure 3.12 Bottom-up loading furnace scheme. The elevator plate with the sample holder (white cylinder) is used to load the samples in the oxidation chamber once a target temperature is reached.

This type of furnace is constituted by a vertically moving elevator plate used for the sample introduction. The furnace is heated to the target temperature and only then the samples are introduced in the chamber. This way it is possible to test the upward thermal shock resistance of materials which are directly exposed at the target

temperature (e.g. 1500°C), and test the quick exposition at high temperatures, by-passing potential oxidation phenomena that may occur at lower temperature.

In the present work, regular bars with dimensions 2.5 x 2 x 12 mm (Width x thickness x length) were machined from the sintered pellet. The samples were cleaned with acetone in an ultrasonic bath and dried at 100 °C under a infrared light. The oxidation tests were carried out in a bottom-up loading furnace (FC18-0311281, Nannetti Antonio Sauro S.R.L., Italy) at 1500 and 1650 °C in air for 1 min. The furnace was heated to the target temperature with a rate of 5 °C/min. Then the specimens were introduced in the furnace using a porous alumina sample holder. After thermal equilibrium was reached (30 s), the isothermal stage began (1 min). At the end of the oxidation test, the specimens were quickly taken out and let to cool down naturally in air. For the test at 1650 °C, an additional minute was needed to reach thermal equilibrium.

3.5 Thermal diffusivity

Thermal diffusivity is the thermal conductivity normalized on density and specific heat capacity of the material studied and is measured in m^2/s. It is usually denoted as α or D and is calculated from equation (7) [22]:

$$\alpha = \frac{k}{\rho c_p} \tag{7}$$

where k is the thermal conductivity, ρ the density and c_p the specific heat capacity. For a given volume of material, the heat required to raise the temperature a given amount depends on its heat capacity and the density. When the product of heat capacity and density is high, the thermal diffusivity may be low, even though the thermal conductivity is relatively high. Thermal diffusivity is often measured with the laser flash method.

3.5.1 Laser flash analysis

Laser flash analysis or laser flash method is the most common technique for the measurement of thermal diffusivity. The flash method is performed by irradiating the front face of a disk sample with a definite energy pulse (i.e. a laser) (fig. 3.13) [22].

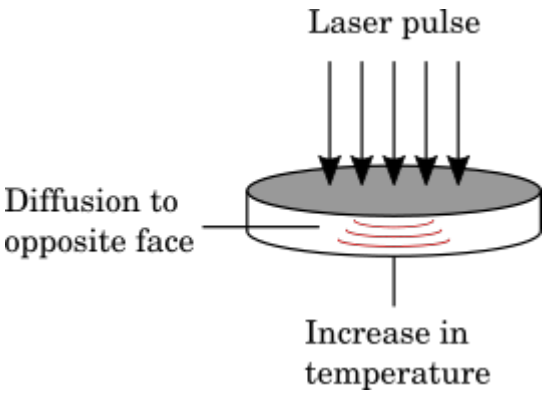

Figure 3.13 Representation of the laser flash analysis setup: a radiation source, typically a laser, heats the surface of the target at a fixed rate, and the temperature is monitored on the back side of the specimen as function of time.

The resulting temperature profile on the back face of the specimen is evaluated with either a thermocouple or a pyrometer. Parker et al. developed a model to describe the thermal diffusivity as function of sample thickness and time [23,24]. The relationship between the thermal diffusivity, D, the specimen thickness, x, and the half temperature rise time, $t_{1/2}$, is given by equation (8)

$$D = 1.38\frac{x^2}{\pi^2 t_{1/2}} \quad (8)$$

This theoretical model makes several assumptions:

- One dimensional heat flow is maintained
- No heat is lost from the side faces
- The pulse is uniformly absorbed
- The pulse duration is short relative to the temperature rise
- Energy is absorbed within a minimal thickness
- Materials properties are constant through the sample (no phase transition)

However these conditions are rarely satisfied all at once and experimental results may not perfectly match the theoretical model. Therefore several researches have investigated these contour conditions and made corrections to the mathematical model to better fit the empirical results [25–28].

This technique has several advantages, such as:

- small specimen size required
- simple specimen geometry (flat disks)
- no calibration required
- broad temperature range (from cryogenic temperature to 2000°C)

In the present work, the thermal diffusivity of fibre reinforced ZrC/SiC, TaC/SiC and HfC/SiC composites was evaluated with the laser flash method. Disks (dimensions: ∅ = 12.7 mm, h = 2 mm) were loaded on the sample holder together with a graphite standard and coated with a uniform layer of carbon to guarantee the same level of conduction on the surface. The specimens were introduced in the laser flash machine, cooled to room temperature with liquid nitrogen, and heated to 2000°C with a rate of x °C/min. Measurements were made in steps of 100°C. For each temperature analysed, the specimen's thermal diffusivity was averaged on a total of five measurements. The Clark and Taylor method was used to account for thermal diffusivity on the lateral faces.

3.6 References

1. Sciti, D., Natali Murri, A., Medri, V. & Zoli, L. Continuous C fibre composites with a porous ZrB_2 Matrix. *Mater. Des.* **85,** 127–134 (2015).
2. Zoli, L., Medri, V., Melandri, C. & Sciti, D. Continuous SiC fibers-ZrB_2 composites. *J. Eur. Ceram. Soc.* **35,** 4371–4376 (2015).
3. Zoli, L. *et al.* Rapid spark plasma sintering to produce dense UHTCs reinforced with undamaged carbon fibres. *Mater. Des.* **130,** 1–7 (2017).
4. Yin, J. *et al.* Hydrolysis behavior of zirconium diboride during attrition milling. *Mater. Chem. Phys.* **133,** 8–15 (2012).
5. Medri, V., Capiani, C. & Gardini, D. Slip casting of ZrB_2-SiC composite aqueous suspensions. *Adv. Eng. Mater.* **12,** 210–215 (2010).
6. Chamberlain, A. L., Fahrenholtz, W. G. & Hilmas, G. E. Low-temperature densification of zirconium diboride ceramics by reactive hot pressing. *J. Am. Ceram. Soc.* (2006). doi:10.1111/j.1551-2916.2006.01299.x
7. Goldstein, J. *et al. Scanning Electron Microscopy and X-ray Microanalysis*. *Scanning Electron Microscopy and Xray Microanalysis* (2003). doi:10.1007/978-1-4615-0215-9
8. Briggs, D., Grant, J. T. & Limited, S. *Surface Analysis by Auger and X-ray Photoelectron Spectroscopy*. (SurfaceSpectra, 2003).
9. Roylance, D. Stress-Strain Curves. *Test* (2001). doi:10.1361/aac
10. Vable, M. Mechanical Properties of Materials. *Springer* (2012). doi:10.1007/978-94-007-4342-7
11. Quinn, G. D. & Swab, J. J. Elastic Modulus by Resonance of Rectangular Prisms Corrections for Edge Treatments. *J. Am. Ceram. Soc.* (2000). doi:10.1111/j.1151-2916.2000.tb01192.x
12. ASTM. ASTM E1875-08 Standard Test Method for Dynamic Young' s Modulus, Shear Modulus, and Poisson's Ratio by Sonic Resonance. *ASTM B. Stand.* (2001). doi:10.1520/E1875-08.2
13. Davidge, R. W. & Evans, A. G. The strength of ceramics. *Materials Science and Engineering* (1970). doi:10.1016/0025-5416(70)90064-9
14. Watts, J., Hilmas, G. & Fahrenholtz, W. G. Mechanical characterization of ZrB_2-SiC composites with varying SiC particle sizes. *J. Am. Ceram. Soc.* **94,** 4410–4418 (2011).
15. Zhang, S. C., Hilmas, G. E. & Fahrenholtz, W. G. Mechanical properties of

sintered ZrB2-SiC ceramics. *J. Eur. Ceram. Soc.* **31,** 893–901 (2011).

16. Zhang, X., Xu, L., Du, S., Han, W. & Han, J. Preoxidation and crack-healing behavior of ZrB_2-SiC ceramic composite. *J. Am. Ceram. Soc.* (2008). doi:10.1111/j.1551-2916.2008.02760.x
17. Campbell, F. C. Structural Composite. *Struct. Compos. Mater.* (2010). doi:10.1016/B978-0-12-398460-9.00002-0
18. Quinn, G. D. & Bradt, R. C. On the vickers indentation fracture toughness Test. in *Journal of the American Ceramic Society* (2007). doi:10.1111/j.1551-2916.2006.01482.x
19. Evans, A. G. & Charles, E. A. Fracture Toughness Determinations by Indentation. *J. Am. Ceram. Soc.* (1976). doi:10.1111/j.1151-2916.1976.tb10991.x
20. Evans, A. G. Fracture toughness: the role of indentation techniques. *Fract. Mech. Appl. to brittle Mater.* (1979). doi:10.1520/STP36630S
21. Munz, D. G., Shannon, J. L. & Bubsey, R. T. Fracture toughness calculation from maximum load in four point bend tests of chevron notch specimens. *Int. J. Fract.* **16,** (1980).
22. Vozár, L. & Hohenauer, W. Flash method of measuring the thermal diffusivity. A review. *High Temp. Press.* **35/36,** 253–264 (2003).
23. Parker, W. J., Jenkins, R. J., Butler, C. P. & Abbott, G. L. Flash Method of Determining Thermal Diffusivity, Heat Capacity, and Thermal Conductivity. *J. Appl. Phys.* **32,** 1679–1684 (1961).
24. Baba, T. *et al.* Standard Test Method for Thermal Diffusivity by the Flash Method 1. *J. Appl. Phys.* (2001). doi:10.1520/E2585-09R15.required.
25. Cowan, R. D. Pulse method of measuring thermal diffusivity at high temperatures. *J. Appl. Phys.* (1963). doi:10.1063/1.1729564
26. Clark, L. M. & Taylor, R. E. Radiation loss in the flash method for thermal diffusivity. *J. Appl. Phys.* **46,** 714–719 (1975).
27. Heckman, R. C. Finite pulse-time and heat-loss effects in pulse thermal diffusivity measurements. *J. Appl. Phys.* **44,** 1455–1460 (1973).
28. Degiovanni, A. Thermal Diffusivity and Flash Method. *Rev Gen Therm* (1977).

4. ZrB_2/SiC based UHTCMCs

4.1 Introduction

The first system investigated in this study, chosen as the baseline material, is a carbon fibre reinforced ZrB_2 composite doped with 10 vol% SiC, labelled ZS10. In this chapter we first carry out preliminary studies in order to assess the mechanical properties of this baseline system, both in the 0/90 and in the 0/0 architectures. Then, we study the effect of different contents of SiC, from 5 to 20 vol% on the main properties, i.e. flexural strength and fracture toughness, using a statistical approach on the 0/90 architectures. Afterwards, we investigate the oxidation behaviour in air up to 1500°C with thermo-gravimetric analysis and then we present the study of the influence of SiC content on oxidation resistance evaluated from short-term oxidation tests at 1500°C and 1650°C in a bottom-up furnace.

4.2 ZS10

4.2.1 Sintering behaviour

The hot pressing curve of ZS10 is shown in figure 4.1. An initial pressure of 20 MPa was applied at 900°C. Then the pressure was gradually increased to 30 MPa at 1700°C and 40 MPa to 1900°C in order to allow degassing of oxide impurities before reaching full densification (fig. 4.1). The displacement of the hot pressing machine, which is related to the displacement of the sample, is monitored during the hot pressing cycle. At 1700°C a sudden increase of the shrinkage rate is observed due to the increase of pressure to 30 MPa. Only at 1900°C, when a pressure of 40 is applied, it is possible to observe displacement due to diffusional processes rather than only mechanical pressure.

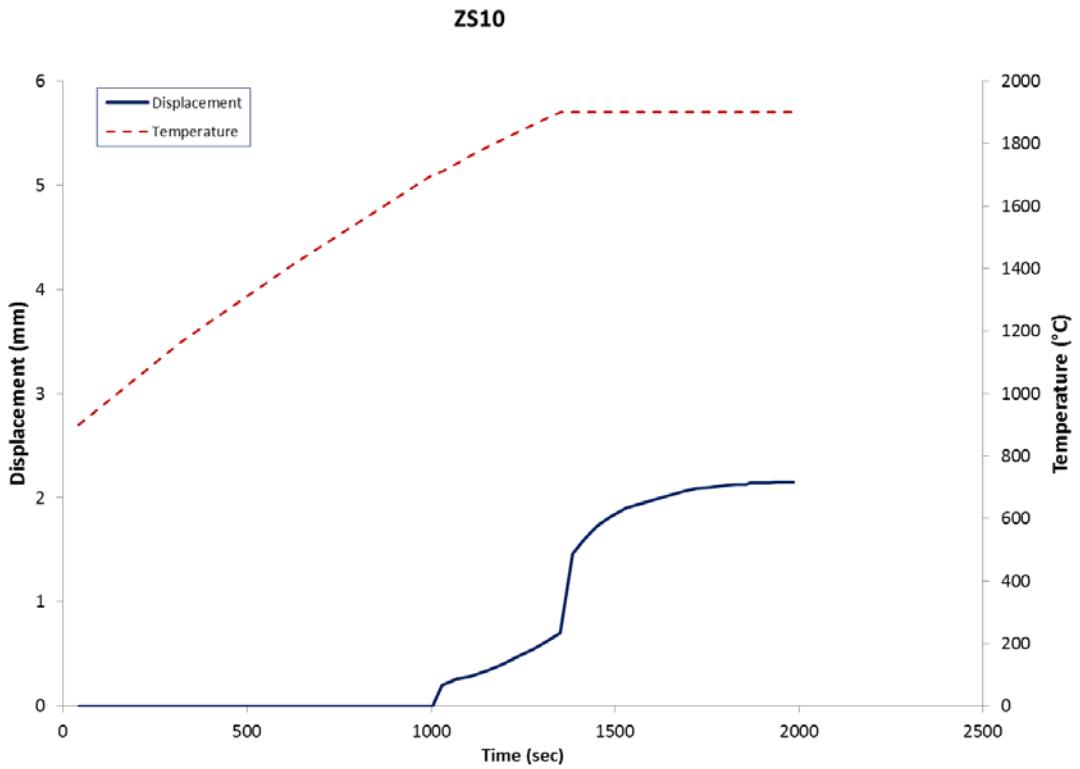

Figure 4.1 Load vs displacement of the hot pressing element showing the displacement of the ceramic composite. Pressures of 20, 30 and 40 MPa were applied at 900, 1700 and 1900°C respectively. Once a temperature of 1900°C is reached, pressure is maintained for 10 min.

4.2.2 Microstructure

The phase composition of the as sintered material is shown in figure 4.2, including an image of the texture and a high magnification image of the cross section. Apart from the fibre section in the centre of Fig 4.2b, SiC particles appear as grey inclusions, while the light regions represent ZrB_2. The small differences in the grey scale are due to the different orientations of ZrB_2 grains. The microstructure is very fine-grained, with an average grain size of ~2 μm, calculated from image analysis with Image Pro Analyser 7.0 software. The presence of fine SiC particles at grain boundaries inhibits the excessive grain growth of ZrB_2, in accordance with previous work from Talmy *et al.* [1]. The final density of the material is 3.88 g/cm^3, with a residual porosity of 10%, as ascertained by Archimedes density measurements. The volumetric fibre content, calculated as the ratio between the volume of fibres and the volume of the final material, amounted to ~ 45 vol.%.

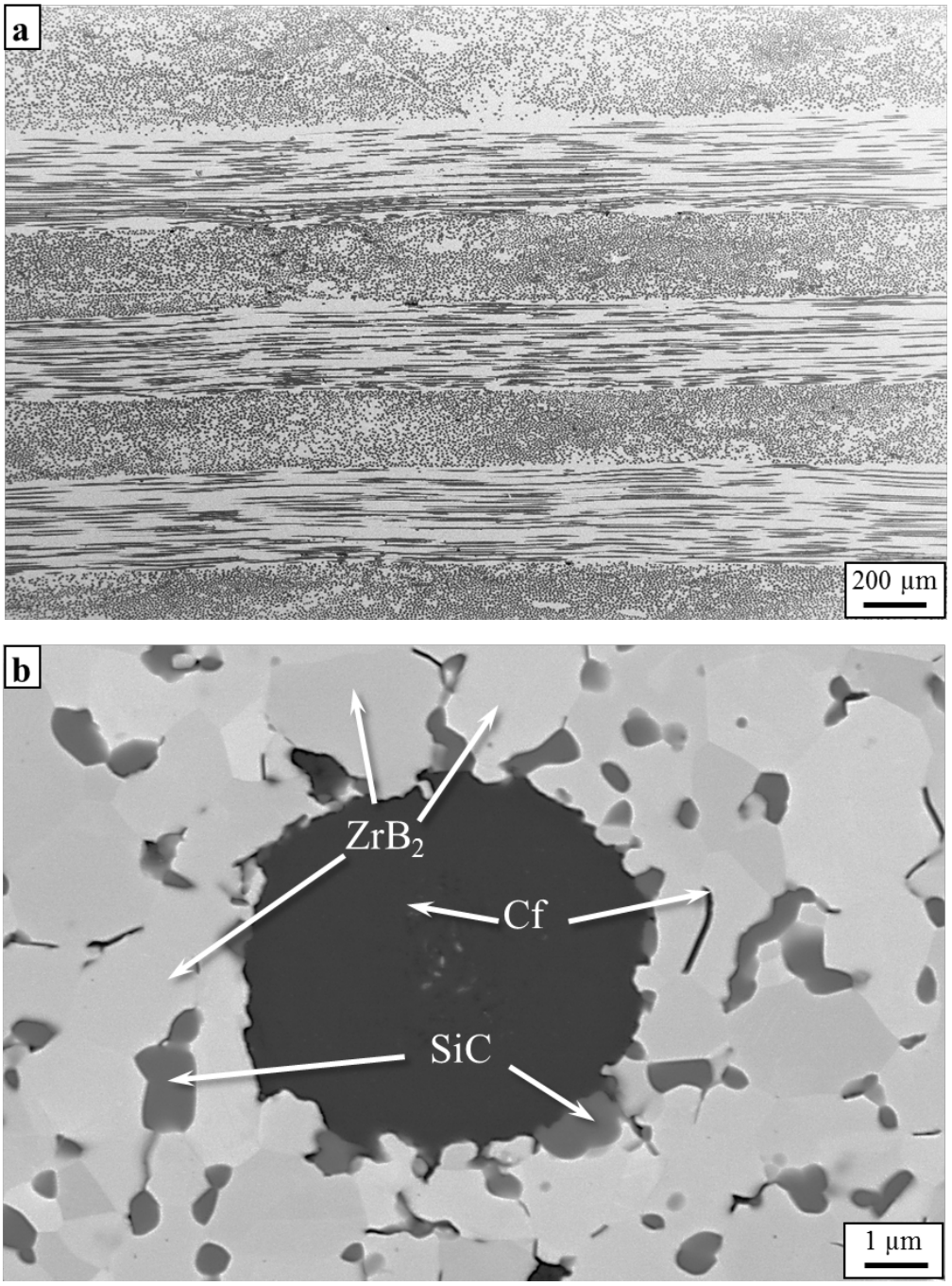

Figure 4.2. SEM micrograph (BSE signal) of the polished section of the as sintered material: a) 0-90° layer structure of the composite, b) high magnification of the microstructure, with focus on the carbon fibre section and ZrB_2 grain boundaries.

4.3 Mechanical properties

The flexural strength, Young's modulus and fracture toughness of ZS10 were measured according to the procedures described in 3.3.1. In order to study the mechanical properties in the 0° and 90° orientations, an additional composite was fabricated with the fibre plies stacked in the same orientation (0/0°) for a better

understanding of the microstructure/properties relationships. This allows to test the specimens with the fibres perpendicular (ZS10 0/0°) and parallel (ZS10 90/90°) to the applied load. A schematic of the 4-point bending setup and fibre orientation is shown in fig. 4.3.

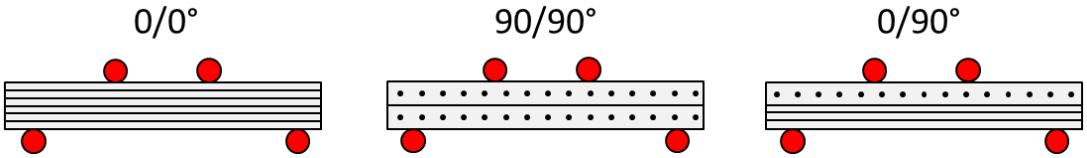

Figure 4.3 Representation of the fibre orientation for the bending tests. The black dots represent fibres in the 90° orientation, the black lines are the fibres in the 0° orientation.

The results of the mechanical tests are summarized in table 4.1. The properties are strongly influenced by the orientation of the fibres, with a maximum value of 355 MPa for ZS10 0/0° and a minimum of 63 MPa for ZS10 90/90°. Fracture toughness was not evaluated on ZS10 90/90° since it was too brittle.

Table 4.1 Values of 4-point flexural strength, fracture toughness and Young's modulus measured with the ultrasound method for ZS10 with different fibre orientations.

Sample	Young's modulus (GPa)	Flexural strength (MPa)	Fracture toughness ($MPa \cdot m^{0.5}$)
ZS10 0/0°	240	355 $\pm$ 40	9.6 $\pm$ 0.7
ZS10 90/90°	188	63 $\pm$ 7	-
ZS10 0/90°	158	218 $\pm$ 30	6.13 $\pm$ 0.3

The low strength observed for ZS10 90/90° was attributed to the fact that fibres do not offer any reinforcement when they are parallel to the applied stress, but they actually behave as large pores that lower the overall properties of the materials. On the other hand, when all the fibres are aligned perpendicularly to the applied stress, they all contribute to increase the strength of the material.

As expected, ZS10 (0/90°) displays intermediate values of strength since only half of the fibres provide structural reinforcement; the flexural strength is comparable with the average between the strength at 0/0° and 90/90°, even though other effects are to be taken into account, such as the number of layers under testing and the stress distribution across the sample which may not be constant. Looking at the load/displacement curves a different behaviour is observed depending on the fibre orientation. The measured modulus of ZS10 0/90° is lower than the respective moduli obtained in the 0/0° and 90/90° configurations, even though looking at the load/displacement curve of ZS10

tested in the different orientations (fig. 4.4) the initial slope of ZS10 0/90° is actually higher than ZS10 90/90° but then decreases rapidly. This was attributed to the faulty interface between the 0/90° plies that contribute to a rapid fibre/matrix de-bonding and delamination that lead to lower modulus. On the other hand the weak interface favours a higher failure strain.

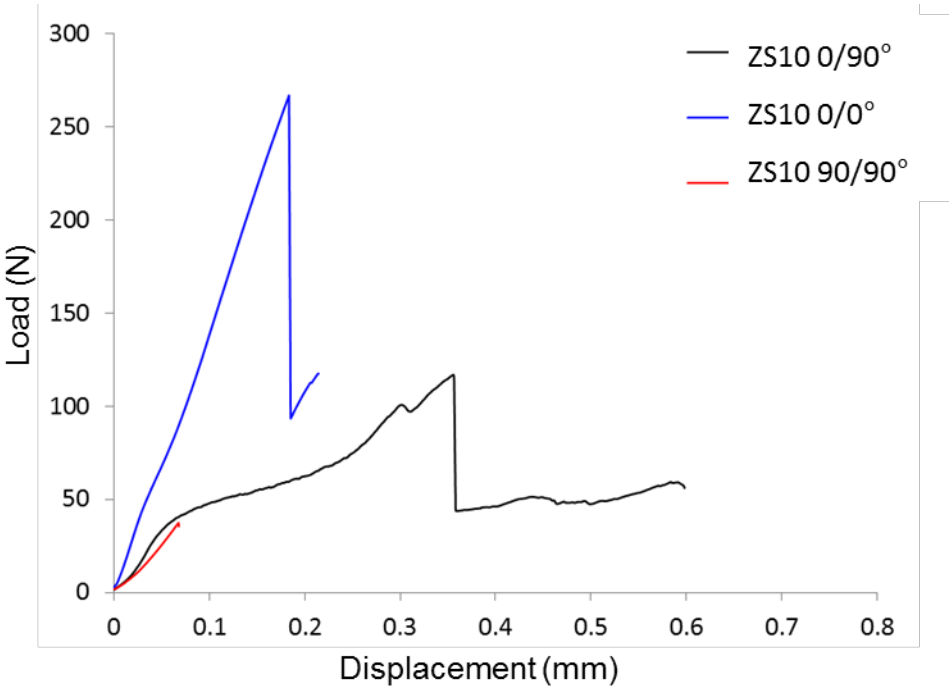

Figure 4.4 Load/displacement curves of ZS10 tested in the 0/0°, 90/90° and 0/90° orientations

As far as fracture toughness is concerned, the values obtained in this study are higher than those commonly reported for ZrB_2/SiC composites of 2 – 4 $MPam^{0.5}$ [2].

4.4 Influence of SiC content on the mechanical properties

4.4.1 Mixture compositions

Powder mixtures containing ZrB_2 and SiC ranging from 5 to 20 vol% were prepared by wet ball milling of the commercial powders and then dried with a rotary evaporator. The composites were prepared through slurry infiltration of unidirectional carbon fibre preforms and hand lay-up in a 0-90° configuration. Hot pressing cycles were carried out at 1900°C, using a pressure of 40 MPa and an holding time of 10 min, on the basis of previous studies [3]. For each composition, three variants, a, b and c, were fabricated by adjusting the powder suspension rheology according to three fixed values labelled as a,b,c in order to obtain different contents of carbon fibres. Due to process

limitations, it was not possible to obtain fibre contents higher than 40% for some compositions.

For the oxidation tests in the air furnace at 1500 and 1650°C, described in 3.1.3, only one sample per composition was selected.

4.4.2 Microstructure

For each composition, three composites (variants) were prepared by varying the slurry viscosity between three fixed values, in order to obtain different carbon fibre contents: a (highest fibre amount), b (intermediate fibre amount), c (lowest fibre amount). In some cases it was not possible to go beyond a specific fibre content due to the fact that the sole change of SiC content strongly modifies the slurry viscosity, therefore some variants (namely, b and c) may exhibit similar physical properties, see Table 4.3. Figure 4.10 shows the microstructure of the carbon fibre section of each sample.

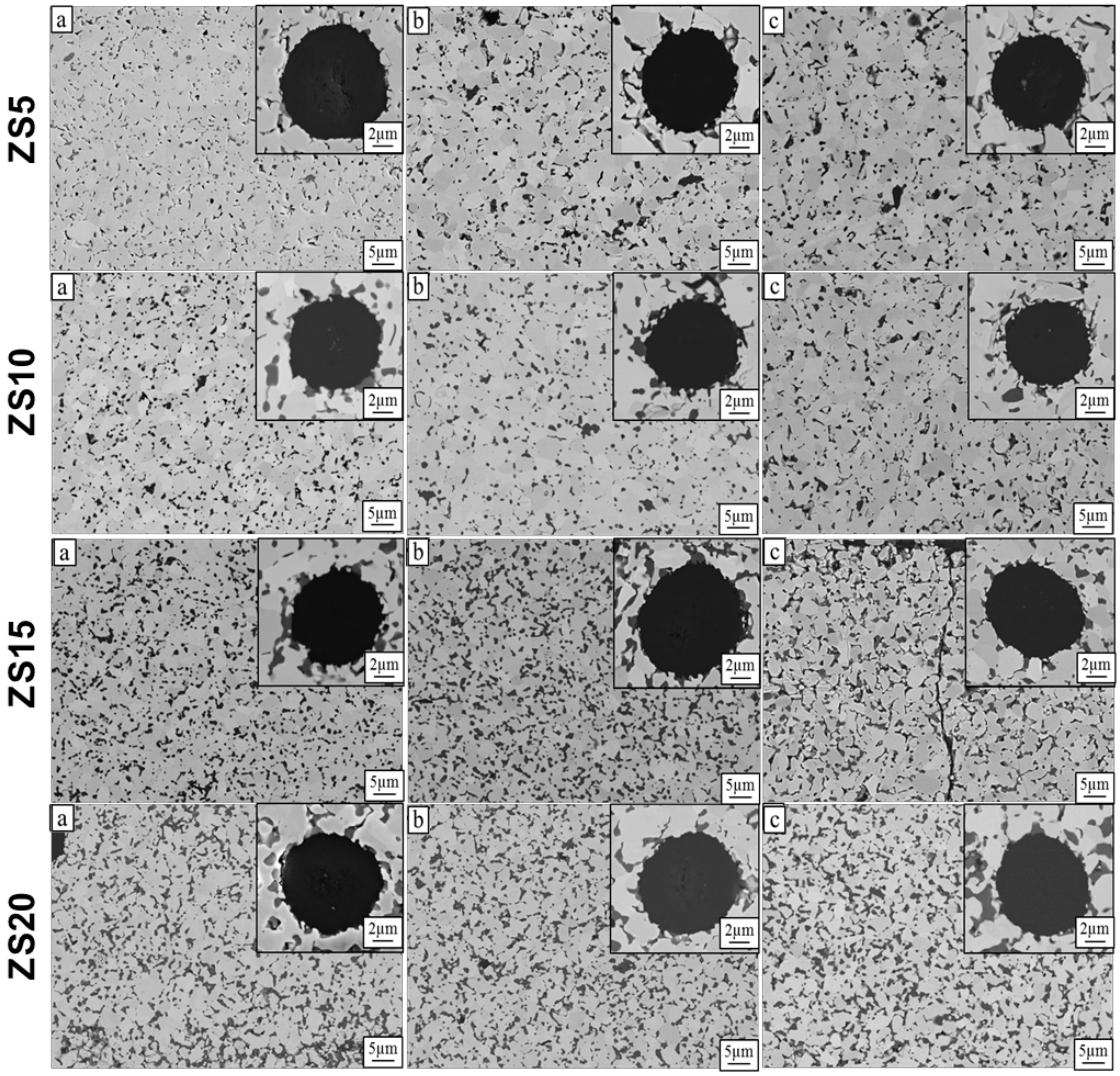

Figure 4.5 High magnification micrographs of the ceramic matrix of samples ZS5-20 a, b and c. In the insets, a magnification of a corresponding carbon fibre section with the surrounding matrix phase.

The samples were labelled as ZS# a,b,c, where # is the volumetric SiC content. The light grey regions represent ZrB_2, while SiC particles comprise the majority of dark grey phases. For low amounts of SiC, it is possible to observe the homogenous dispersion of fine particles in the ceramic matrix and around the carbon fibres, while increasing the SiC content above 15 vol.% results in the agglomeration of the finer SiC particles. Carbon fibres do not show significant signs of reaction with the ceramic matrix and maintain their original round shape, in agreement with previous studies on pitch carbon fibres [4]. Samples with high ceramic matrix content, e.g. ZS15 c (fig. 4.5), are characterized by the presence of cracks, while the other samples do not show relevant defects. The average ZrB_2 particle size is in the range 2.5 - 3 μm in all samples, as ascertained by image analysis, with a slight decrease in size for higher SiC contents. This could be due to the high amount of fibres in all specimens that is the main responsible for the hindered grain growth of ZrB_2. As for the matrix fibre interface, since no coating was adopted for the fibres, the interface was generally quite strong due to a good adhesion between the boride and the fibre layers. Of the four different compositions, the weaker interface was that of ZS5 due to slightly lower degree of densification of the matrix, in agreement with previous studies [3].

4.4.3 Flexural strength

For each bar, the geometric density, porosity, fibre vol%, ceramic matrix vol%, fibre/SiC ratio and layer thickness were measured (table 4.2). All samples display quasi-brittle fracture behaviour and the two halves of the specimen remain connected after the tests as shown in fig. 4.6. Because of the low span/thickness ratio, the failure modes were caused by flexural yield, inter-laminar shearing or a combination of the two. Inter-laminar shear failure is characterized by the opening of a void between the planes, while flexural yield failure is characterized by fibre rupture, which may result from plane bending. During the first part of the load-displacement curve, stresses are mainly concentrated on the ceramic matrix. As the load increases, cracks start to open in the ceramic matrix and the load is transferred to the fibres. Delamination may occur, as evidenced in some curves by the drop in applied load and the re-loading of the second layer.

Table 4.2 Flexural strength (mean ±1 standard deviation) and physical characteristics of samples ZS5, ZS10, ZS15, ZS20

	σ (MPa)	**Density (g/cm^3)**	**Porosity (vol.%)**	**Fibre (vol.%)**	**Matrix (vol.%)**	**SiC/fibre Ratio**	**SiC vol.% in matrix**
ZS5 a	198 ± 12	3.649	12.9	40.7	46.4	0.123	5
ZS5 b	207 ± 24	4.194	7.2	35.2	57.6	0.142	5
ZS5 c	247 ± 14	4.055	9.5	35.4	55.2	0.141	5
ZS10 a	218 ± 30	3.616	9.5	45.2	45.3	0.221	10
ZS10 b	171 ± 1	4.205	4.1	37.7	58.2	0.265	10
ZS10 c	196 ± 28	3.864	9.8	37.8	52.3	0.264	10
ZS15 a	190 ± 33	3.315	10.2	50.8	39.0	0.295	15
ZS15 b	167 ± 4	3.617	6.4	48.2	45.3	0.311	15
ZS15 c	186 ± 49	3.952	7.5	36.9	55.6	0.406	15
ZS20 a	221 ± 19	3.391	8.7	49.3	42.0	0.405	20
ZS20 b	247 ± 12	3.762	6.0	42.7	51.3	0.468	20
ZS20 c	164 ± 2	4.003	5.4	36.6	58.1	0.547	20

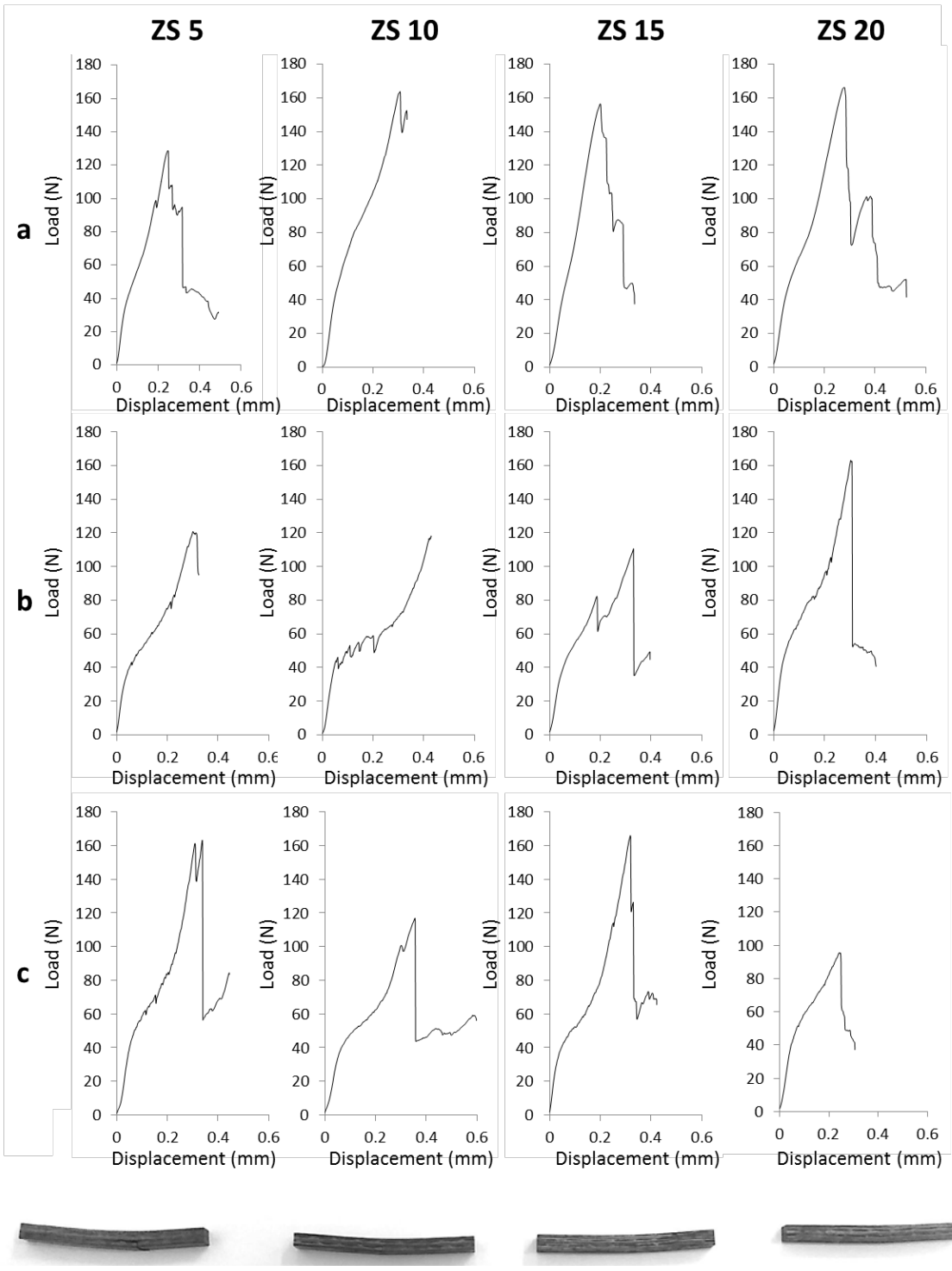

Figure 4.6 Load-displacement curves of 4-point bending tests for samples ZS5, ZS10, ZS15, ZS20 a,b,c. For each sample, only one curve is reported since all bars within the same sample display the same behaviour. At the bottom of the graphs, a lateral view of the specimens after test is shown.

The strength values obtained in this work ranging between 160 and 250 MPa are lower than those reported in literature for typical bulk ZrB_2/SiC composites, which are in the range of 400-700 MPa [2,5–9]. This could be due to the internal defects brought by

the introduction of carbon fibres in the ceramic matrix and the cracks generated due to CTE mismatch between the fibres and the matrix during hot pressing. Another reason could lie in the low interfacial strength between each layer which causes the sample to fail prematurely to inter-laminar shear stresses. A way to overcome this issue is the use of three-dimensional fibre reinforcements, which is however out of the scope of the present work.

According to previous works by Fahrenholtz *et al.* on the influence of SiC content on ZrB_2-SiC bulk ceramics [5], flexural strength is expected to increase with increasing SiC content from 10% to 30 vol% due to refinement of ZrB_2 mean grain size and the decrease of porosity. In the materials presented here with embedded carbon fibres there is not a clear correlation between the apparent flexural strength and SiC content. High values of strength were obtained for both compositions with 5 and 20 vol% SiC; moreover, the grain size for all the samples is in the range of 2.5 - 3 μm, with a very slight decrease with the increase of SiC content; in this case, the fibres themselves act as the main obstacle to grain growth and the problem related to the potential presence of SiO_2 is overcome thanks to the abundance of carbon from the carbon of fibres that can react to give SiC according to the reaction (1) [10]:

$$SiO_2 + C \rightarrow SiC + CO_{2(g)} \quad (1)$$

Since there is no parametric model which relates the mechanical response variable, strength or fracture toughness, to the microstructural features, two non-parametric learning machine techniques, Regression Tree and Random Forest, were considered in order to establish quantitative relationships between the response variables and the predictor variables. Regression tree analysis is a simple non-parametric machine learning technique that is based on the recursive partitioning of the each explanatory variables and then calculating the residual sum of squares (RSS) of the two corresponding groups of the response variable values [16]. The most important explanatory variable x_i is that whose cut point x_c minimizes the RSS (equation 2):

$$RSS = \sum_{j}^{n_1} \left(y_{j1} - \overline{y_1} \right)^2 + \sum_{j}^{n_2} \left(y_{j2} - \overline{y_2} \right)^2 \quad (2)$$

where y_{j1} and y_{j2} are the response variable values corresponding to the explanatory variable values $< x_c$ and $\geq x_c$, respectively, and $\overline{y_1}$ and $\overline{y_2}$ are the group means. The process is then repeated. The research of further split stops according to some criterion such as the minimum number of response values to split or the depth of the tree.

Moreover, to avoid overfitting, pruning is applied in order to obtain the optimal tree. The optimal tree is the smallest tree that has near minimum cross-validated relative error. The regression tree method has several advantages with respect to other more common statistical techniques like regression [11]: 1) trees do not require the user to specify the model in advance, 2) trees use automatic feature selection, which allows the approach to be used with a very large number of features, 3) trees are adept at capturing nonlinear or non-additive behaviour as interactions are automatically included, 4) trees are very easy to explain and can be displayed graphically.

The algorithm on which the regression tree is based is greedy in the sense that is optimal for the first split but does not look ahead to see if different ways of splitting are better at the end. Random Forest is an evolution of the tree-based model [12]. A Random Forest is generated by growing many full (no pruning) trees, usually $\geq$500, using a random subset of the explanatory variables for each tree and for each split. This method is trained on a subset, usually 2/3, of the response variable values with the remaining 1/3 used for testing. A single regression tree will obtain a single prediction result with a single input vector. However, a Random Forest will obtain multiple results from a single input as it grows many regression trees. Therefore, a Random Forest will use an average output for the prediction result of the regression with increased reliability [13]. A Random Forest model cannot be displayed graphically, however a plot of the importance of the explanatory variables on the mean square error (MSE) can be obtained.

For a more logical procedure, the Random Forest analysis will be presented first, to show which are the most important explanatory variables, and then the Regression Tree analysis will be shown to analytically display the impact of the explanatory variables on the response variable.

The following variables were chosen as explanatory variables: 1) the starting nominal amount of SiC particles with respect to the matrix and ranges from 5 to 20% (SiC amount), 2) the fibre volume (Fibre volume), 3) the ratio between the volume of SiC in the matrix and carbon fibre content (SiC/fibre ratio), 4) the overall volumetric amount of ceramic matrix (Matrix volume) and 5) the geometrical porosity across the sample calculated as the ratio between experimental and theoretical geometrical density (Porosity). Figure 4.7 shows the result of the explanatory variable importance according to Random Forest.

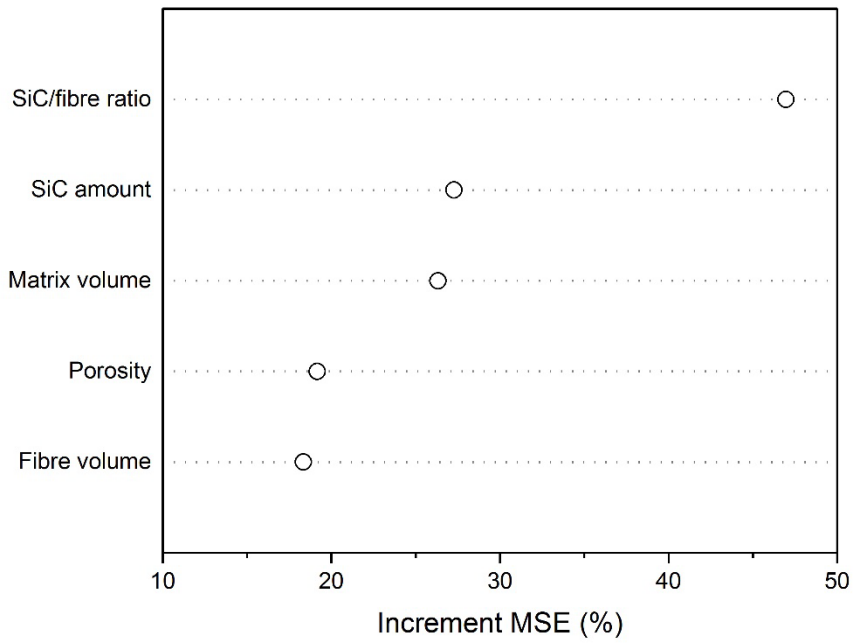

Figure 4.7 Plot of the importance of the explanatory variables on the flexural strength according to the Random Forest analysis. The importance is based on the increment of the mean square error (MSE) due to the removal of the corresponding explanatory variable.

As the plot indicates, the SiC/fibre ratio is the most important explanatory variable as its removal increments the mean square error (MSE) of about 46%. SiC amount and matrix volume follow with a lower influence. Finally, porosity and fibre volume seem to affect less the strength.

After this, a Regression Tree analysis was carried out in order to quantify the effect of each explanatory variable has on the apparent flexural strength and eventually identify potential correlations between the explanatory variables selected, see Fig. 4.8.

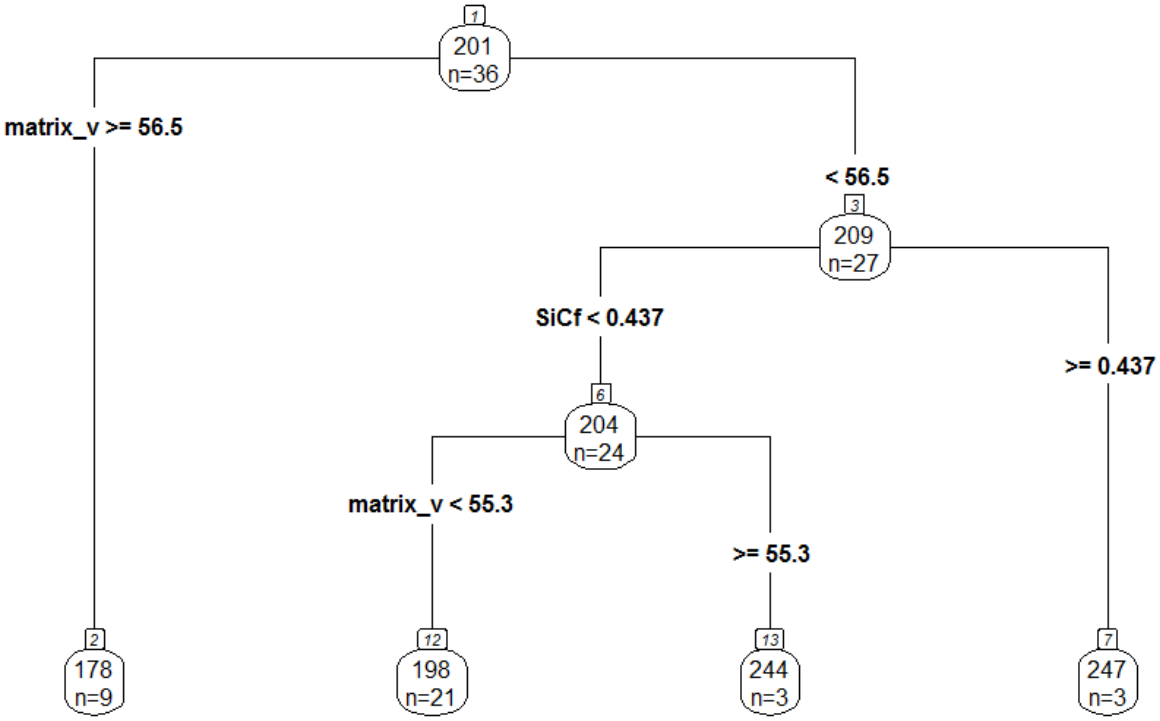

Figure 4.8 Regression tree analysis for the flexural strength. In each node, the mean strength and the number of values is reported. The value on top (201 MPa) is the average flexural strength of all the specimens (36). The condition for the split of the explanatory variable is indicated on the left branch below each node. The explanatory variables are ranked in order of importance from top to bottom with the following abbreviations: matrix_v = matrix volume, SiCf = SiC/fibre ratio. A final node (leaf) is where the split constrains prevent a further split. See text for a more detailed explanation.

In this plot, in each node, the mean value of the response variable and the number of values are indicated. For example, at node 1 the mean of all the strength value is 311 MPa and the initial number of all the data is 36.

The first split is made according to the most important explanatory variable as calculated by Regression Tree and is indicated on the left branch, which is the matrix volume in this case. If the matrix volume is equal or higher than 56.5 vol.%, then the mean strength is 178 MPa, as indicated by the leftmost final node (leaf), calculated on nine values. This is also the lowest mean strength value of all the split groups. When the matrix volume is lower than 56.5 vol.%, right branch from node 1, the mean values, calculated on 27 values, is 209 MPa, see node 3. In this case, the data can be split according to the explanatory variable SiC/fibre ratio. If the SiC/fibre ratio is equal or

higher than 0.437, right branch, the mean strength is 247 MPa, node 7 (leaf). This is the highest mean strength value of all the split groups. If the SiC/fibre ratio is lower than 0.437, left branch, then the mean strength is 204 MPa. This group can be further split according to the matrix volume: if less than 55.3 vol.%, the mean strength is 198 MPa, node 12 (leaf); if equal or higher than 55.3 vol.%, the mean strength is 244 MPa, node 13 (leaf).

We can see that in the Regression Tree analysis, the most important variable is the matrix volume followed by the SiC/fibre ratio. This is a rank inversion with respect to the Random Forest analysis, which should be however considered more reliable. Combining the main results of the Random Forest analysis and those of the Regression Tree, a low matrix volume and a high SiC/fibre ratio are necessary in order to obtain a high-strength composite. The first indication is clearly due to the lower strength of the matrix with respect to that of the fibres. The second indication comes from the observation that there must be a right amount of SiC around the fibres to promote a proper fibre/matrix interface through the reaction of the SiO_2 present on the SiC powders with the carbon fibre [10]. The fracture properties of the fibre composites are known to be strongly dependent on the fibre/matrix interface [14].

4.4.4 Fracture toughness

The average values of fracture toughness are reported in Table 4.4. The fracture toughness of the group ZS10 c was not evaluated. Typical fracture toughness values for bulk ZrB_2/SiC composites are in the range of 2-5 MPa·$m^{0.5}$, determined with single edge or chevron notch beam tests [1516], which increase up to 6.16 MPa·$m^{0.5}$ with the introduction of 30% of carbon fibres [17]. Values of indentation toughness up to 7.52 MPa·$m^{0.5}$ have been obtained by Guo with the introduction of carbon spheres [18]; however in the present work, due to significant amount of porosity and matrix discontinuity, the indentation-induced cracks are hardly observable and misleading. For the materials of the present work, the fracture toughness ranged from 4.75 to 8.35 MPa·$m^{0.5}$. The load-displacement curves display quasi-brittle fracture behaviour, Fig. 4.9.

Table 4.3 Fracture toughness and physical characteristics of samples ZS5, ZS10, ZS15 and ZS20. ZS10 c was not reported due to insufficient data.

	K_{Ic} (MPa·m$^{0.5}$)	**Density (g/cm^3)**	**Porosity (vol.%)**	**Fibre (vol.%)**	**Matrix (vol.%)**	**SiC/fibre ratio**	**SiC vol.% in matrix**
ZS5 a	4.75 ± 0.31	3.614	13.5	40.7	45.8	0.123	5
ZS5 b	7.02 ± 0.49	4.038	9.9	35.2	54.9	0.142	5
ZS5 c	5.20 ± 0.58	4.013	10.2	35.4	54.5	0.141	5
ZS10 a	6.13 ± 0.30	3.619	9.4	45.2	45.4	0.221	10
ZS10 b	6.39 ± 1.29	4.084	6.1	37.7	56.2	0.265	10
ZS15 a	8.35 ± 0.98	3.212	12.0	50.8	37.2	0.295	15
ZS15 b	5.52 ± 0.94	3.521	8.1	48.2	43.6	0.311	15
ZS15 c	6.33 ± 0.44	3.886	8.7	36.9	54.4	0.406	15
ZS20 a	6.93 ± 0.43	3.238	11.4	49.3	39.2	0.405	20
ZS20 b	6.68 ± 0.94	3.749	6.2	42.7	51.1	0.468	20
ZS20 c	5.01 ± 0.90	3.849	8.1	36.6	55.3	0.547	20

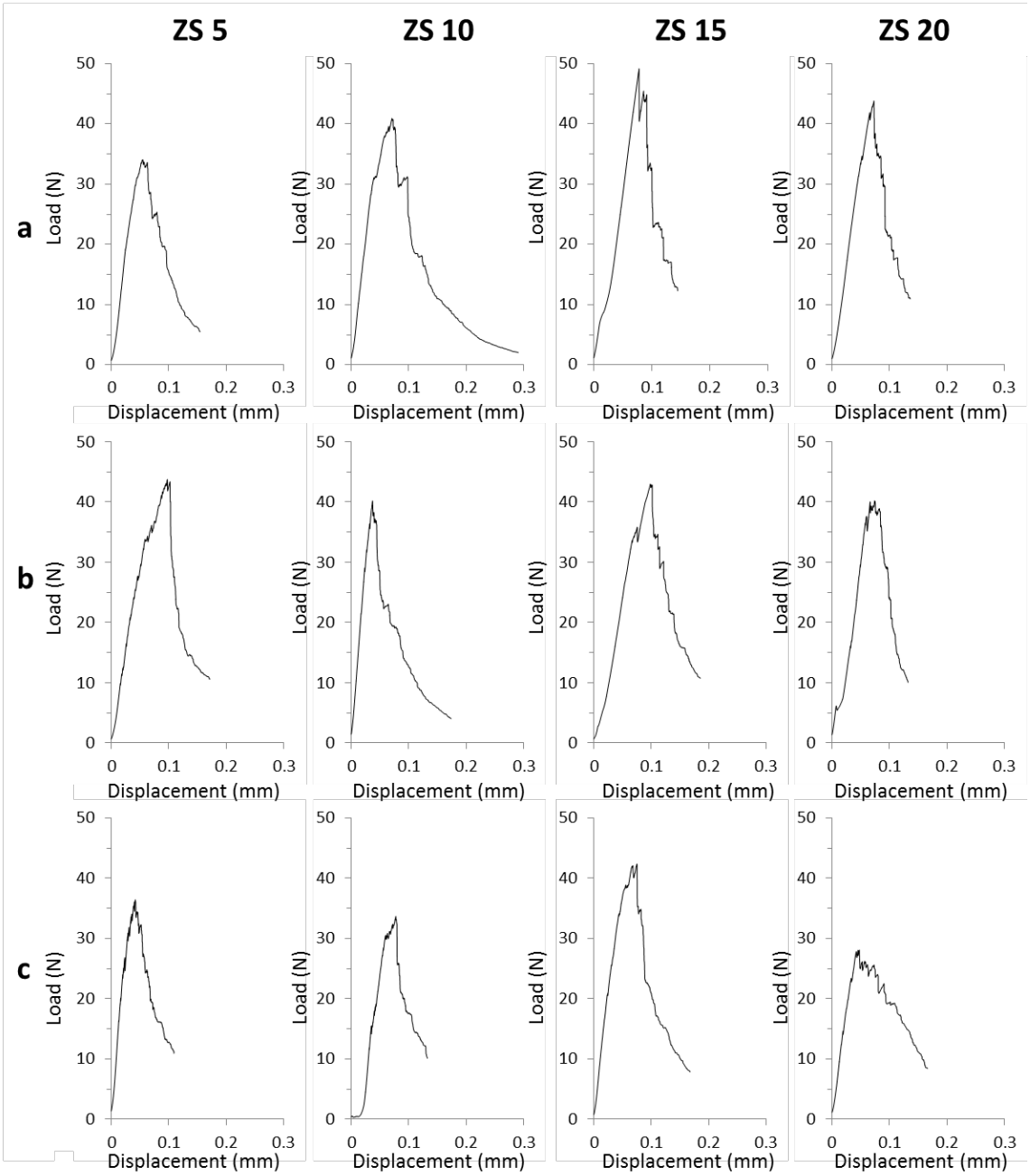

Figure 4.9 Load-displacement curves of 4-point Chevron notch bending tests of samples ZS5, ZS10, ZS15, ZS20. For each sample, only one curve is reported since all bars within the same sample display the same behaviour.

All samples exhibit very similar behaviours. An example of fracture surface is shown in Fig. 4.10, which reveals both fibre bundle pull-out and individual fibre pull-out. The extent of fibre pull-out should be strictly related to the cohesion between matrix and fibre that develops during the densification process. High temperatures and holding times during hot pressing will lead to significant reaction between carbon fibres and the ceramic matrix, which results in too strong interfaces and brittle behaviour [19].

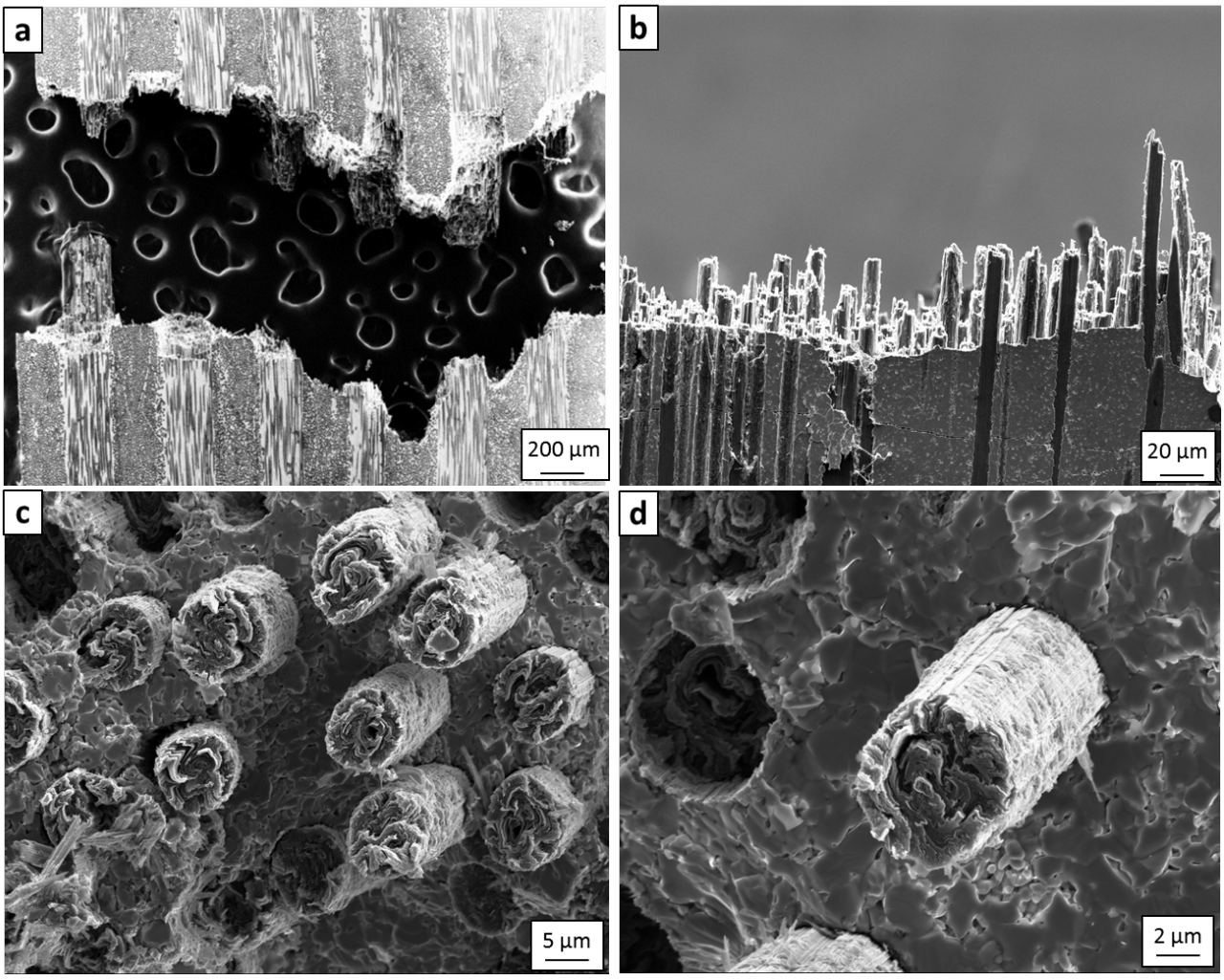

Figure 4.10 Fracture surfaces of sample ZS5c: a) Fracture profile and fibre bundle pull-out, b) Fibre pull-out profile view, c) Fibre pull-out section view, d) Individual fibre pull-out.

Previous studies from Hong *et al.* [20] showed a degradation of the mechanical properties with the increase of short carbon fibre content from 20 to 50%, but in our case there is not a clear correlation between fracture toughness and carbon fibre content, which is likely due to the different effect of continuous fibres.

The same explanatory variables used for the strength were considered for K_{Ic}. The Random Forest results regarding the importance of these explanatory variables are shown in Fig. 4.16.

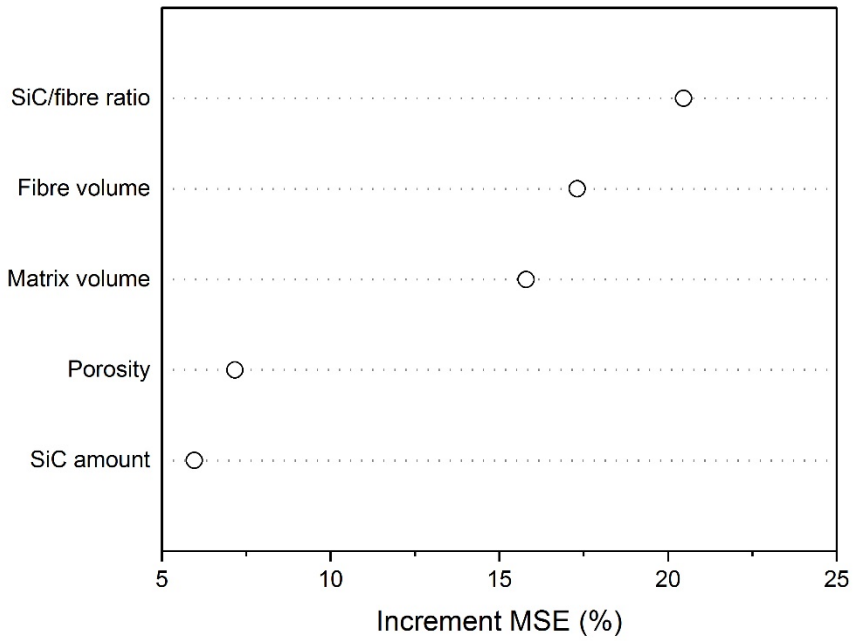

Figure 4.11 Plot of the importance of the explanatory variables on the fracture toughness according to the Random Forest analysis. The importance is based on the increment of the mean square error (MSE) due to the removal of the corresponding explanatory variable.

Even for fracture toughness, the ratio between SiC and carbon fibre emerges as the most important explanatory variable by the RF analysis. However, in this case the SiC/fibre ratio is followed by the fibre volume and matrix volume. Porosity and SiC amount are the least influencing explanatory variables.

The Regression Tree analysis is shown in Fig. 4.12. Differently from the RF analysis, the most important explanatory variable was the matrix volume. The highest mean value of K_{Ic} is obtained for a matrix volume less than 39.1 vol.%, 8.11 MPa·m$^{0.5}$. For matrix volume higher than 39.1 vol.%, the toughness drops to a mean value of 5.94 MPa·m$^{0.5}$. This last group can be however further split according to the SiC/fibre ratio values, which means an interaction between the two explanatory variables matrix volume and SiC/fibre ratio. For a SiC/fibre ratio lower than 0.142, the mean fracture toughness was the lowest of all the split groups, 4.98 MPa·m$^{0.5}$. When the SiC/fibre ratio was equal or higher than 0.142, the mean fracture toughness was 6.21 MPa·m$^{0.5}$. In turn, the latter group can be again split according to the same explanatory variable, i.e. the SiC/fibre ratio. In this case, there is an apparent optimal SiC/fibre ratio range: high values of fracture toughness are obtained when this ratio is between 0.142 and 0.508,

mean fracture toughness of 6.41 MPa·m$^{0.5}$. For SiC/fibre ratio higher than 0.508 the mean fracture toughness is 5.01. MPa·m$^{0.5}$.

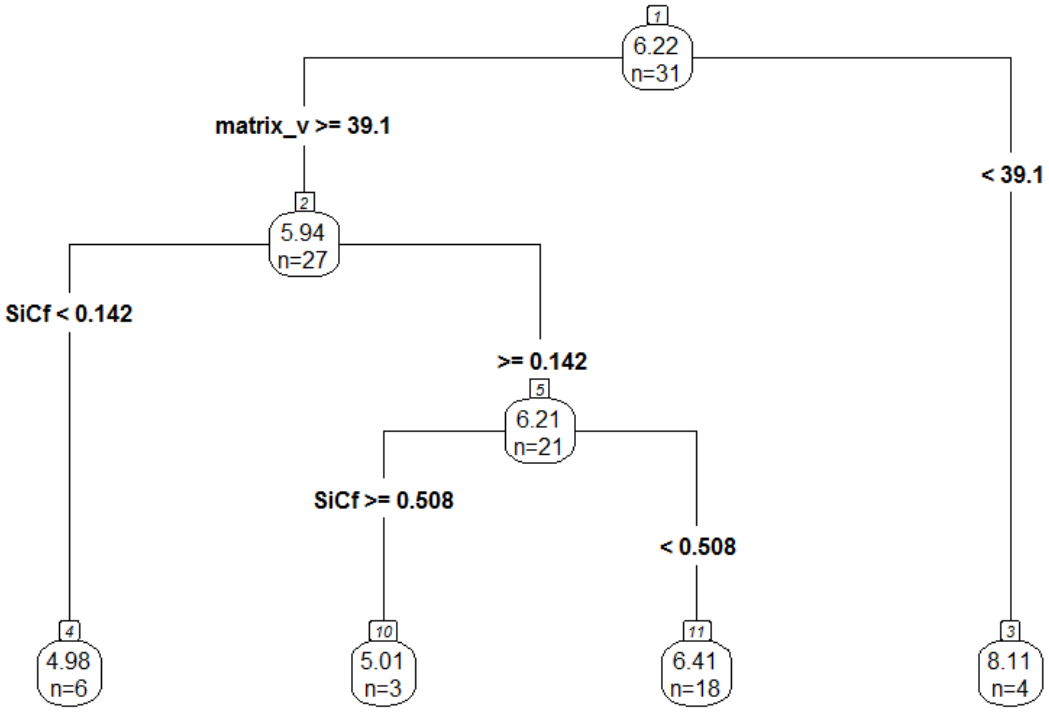

Figure 4.12 Regression tree analysis for the fracture toughness. In each node, the mean fracture toughness and the number of values is reported. The value on top is the average fracture toughness (6.22 MPa·m0$^{.5}$) of all the specimens (31). The condition for the split of the explanatory variable is indicated on the left branch below each node. The explanatory variables are ranked in order of importance from top to bottom with the following abbreviations: matrix_v = matrix volume, SiCf = SiC/fibre ratio. A final node (leaf) is where the constrains prevent a further split. See text for a more detailed explanation.

The high fracture toughness values associated to a low matrix volume are due to the fact that a low matrix volume corresponds in most cases to a high fibre volume. The SiC/fibre ratio, that was the most important explanatory variable for the apparent flexural strength, is apparently of less importance for fracture toughness even if a strong influence can be observed when the matrix volume was higher than 39.1%.

Since the results of Random Forest are more reliable than those of Regression Tree, we can affirm that to obtain high-toughness composites the SiC/fibre ratio should be primarily controlled followed by the volume of the fibre. As for the strength, the proper interface fibre/matrix is fundamental in determining the fracture behaviour. A too strong interface, as that obtained when the SiC/fibre ratio is higher than 0.508,

lowers both strength and fracture toughness as the mechanism of pull-out is ineffective. Following that, a high volume of fibre, i.e. a low matrix volume, positively affects the fracture toughness as well. Considering the flexural strength and the fracture toughness together, it is apparent that the SiC/fibre ratio is the most important explanatory variable for this type of composites.

There is however a minor trade-off between fibre and matrix volume regarding these two mechanical properties. Besides a proper fibre/matrix interface, high-strength composites seem to require a relatively high volume of matrix with respect to the fibre volume, the opposite holds for high-fracture toughness composites.

One of the fundamental issues encountered in conventional CMCs based on C/SiC or SiC/SiC is the interface between the fibre and the ceramic matrix. If the interface is too strong, the load is more efficiently transferred from the matrix to the fibres, but this can result in the fibres rupturing together with the matrix, leading to a brittle fracture. On the other hand, a weak interface will promote fibre pull-out and trigger other toughening mechanisms such as crack bridging or crack deviation. In this regard, carbon and BN coatings have been studied and applied on SiC or carbon fibres in order to obtain a weak interface and avoid matrix cracks to break through the fibre [21–23]. The main downside to this approach is associated to the weak oxidation resistance of the coating at high temperatures that can compromise the mechanical properties of the material, beside the added costs of manufacturing the coated fibres.

Since the SiC/Cf ratio seems to play an important role in the mechanical properties of these composites, the fracture surfaces were studied more in-depth to better understand the interaction of fibres with the interface and the extent of fibre pull-out. Two extreme cases, ZS5c and ZS20c, were taken into consideration to highlight the main difference.

As shown in figure 4.13, the extent of fibre pull-out is visibly more pronounced for the composition with 5 vol% SiC (pull-out extent higher than 10 μm) which is characterized by lower porosity and a lower degree of reaction at the interface of the fibre with the SiO_2 impurities. On the other hand, a SiC content of 20 vol% promotes a very dense and strong interface that limits fibre pull-out (pull-out extent less than 1 μm). Bundle pull-out is still present for both compositions. The composites with intermediate amounts of SiC, i.e. 10 vol% and 15 vol%, show very similar fibre/matrix interfaces and pull-out which are difficult to quantify due to the small range of values.

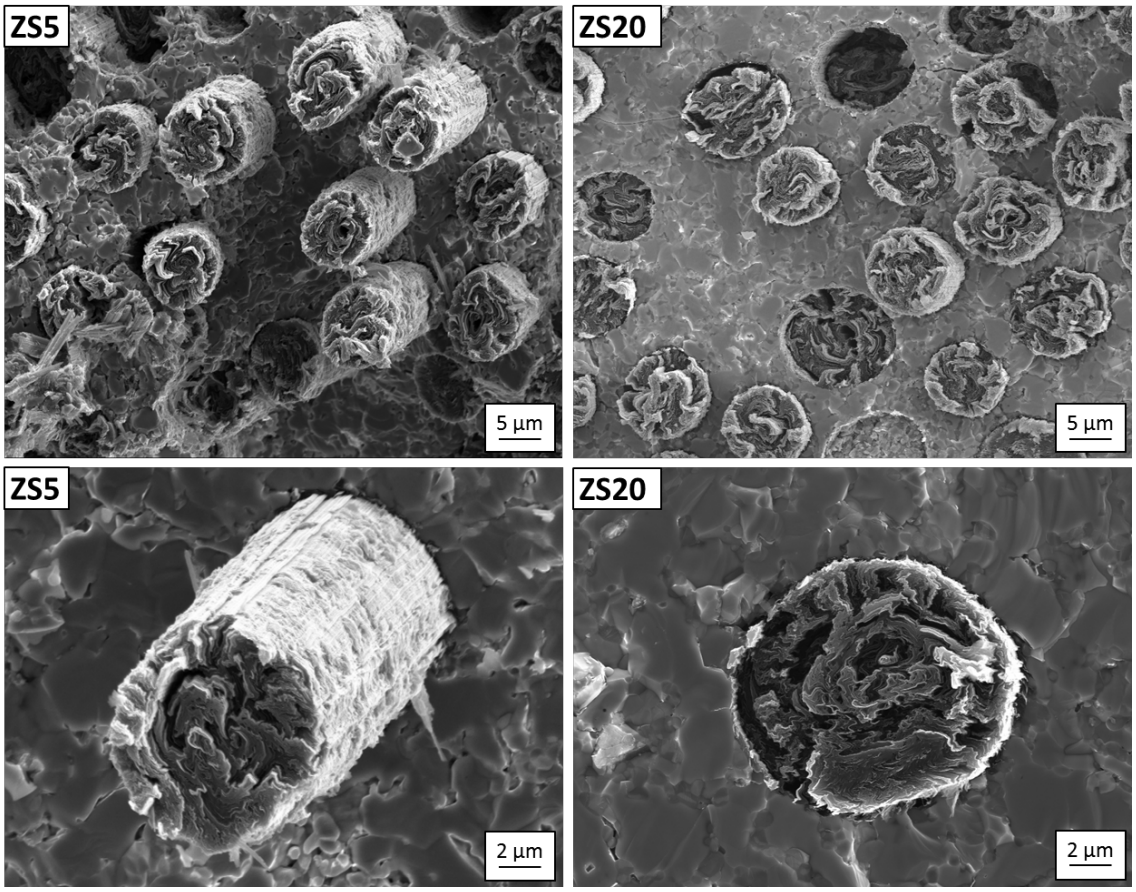

Figure 4.13. High magnification micrographs of the fracture surfaces of samples ZS5c on the left (weak fibre/matrix interface, higher pull-out) and ZS20c on the right (strong fibre/matrix interface, limited pull-out)

However, an excessively weak interface may lead to poor performance. In the present work it was possible to obtain a fibre pull-out extent up to 20-40 µm with low SiC content, but this in turn results in a weaker ceramic matrix. This may also lower the interfacial strength between each layer and promote delamination during testing [5]. On the other hand, a higher amount of SiC provides a stronger matrix but limits fibre pull-out. The best compromise can be reached by adjusting process parameters and matrix composition in order to both retain a strong matrix and a good fibre pull-out. In this regard, coated fibres may prove to be the solution and will be object of future works.

4.5 Oxidation resistance

4.5.1 Thermo-gravimetric analysis

TG analysis tests were carried out following the procedures described in 3.4.1 on the sample containing 10 vol% SiC (ZS10). Four non isothermal stages (Tests 1-4, in Table 4.4) were carried out in air stopping at selected temperatures (i.e. 750, 1100, 1450 and 1550 °C), with a heating rate of 10 °C/min, in order to analyse the microstructure at critical oxidation stages for carbon fibres. One additional non-isothermal test in air up to 1550 °C was carried out at a rate of 45°C/min (Tests 5 in Table 4.4), in order to isolate the effect of heating rate on the oxidation of carbon fibres.

Then, isothermal runs were conducted at 800, 1000, 1200 and 1400 °C for 6 hours in air. For the isothermal tests, the samples were placed inside the furnace, on top of an alumina plate, and heated to their respective temperatures at a rate of 30 °C/min in a protective atmosphere of argon, in order to minimize oxidation effects before reaching the target temperature (tests 6-9 in Table 4.4).

Table 4.4 Summary of the TG experiments and operating conditions: Tests 1-5 are non-isothermal tests, with ramps from RT to the target temperature. Tests 6-9 are isothermal tests with an initial ramp in Ar, followed by exposure to flowing air for 6 h.

Sample	Heating Rate	Target temperature	Exposure time
1	10°C/min, air	750°C	/
2	10°C/min, air	1100°C	/
3	10°C/min, air	1450°C	/
4	10°C/min, air	1550°C	/
5	45°C/min, air	1550°C	/
6	30°C/min, argon	800°C	6 hours in air
7	30°C/min, argon	1000°C	6 hours in air
8	30°C/min, argon	1200°C	6 hours in air
9	30°C/min, argon	1400°C	6 hours in air

Afterwards, the samples were exposed to air for 6 hours and then cooled to room temperature.

Fig. 4.14a shows the non-isothermal TG curve up to 1550 °C in air and labels indicate the critical temperature for the oxidation of carbon fibres, i.e. 750, 1100, 1450 and 1550 °C. Fig. 4.14b shows relevant features of samples surfaces oxidised at the same temperatures.

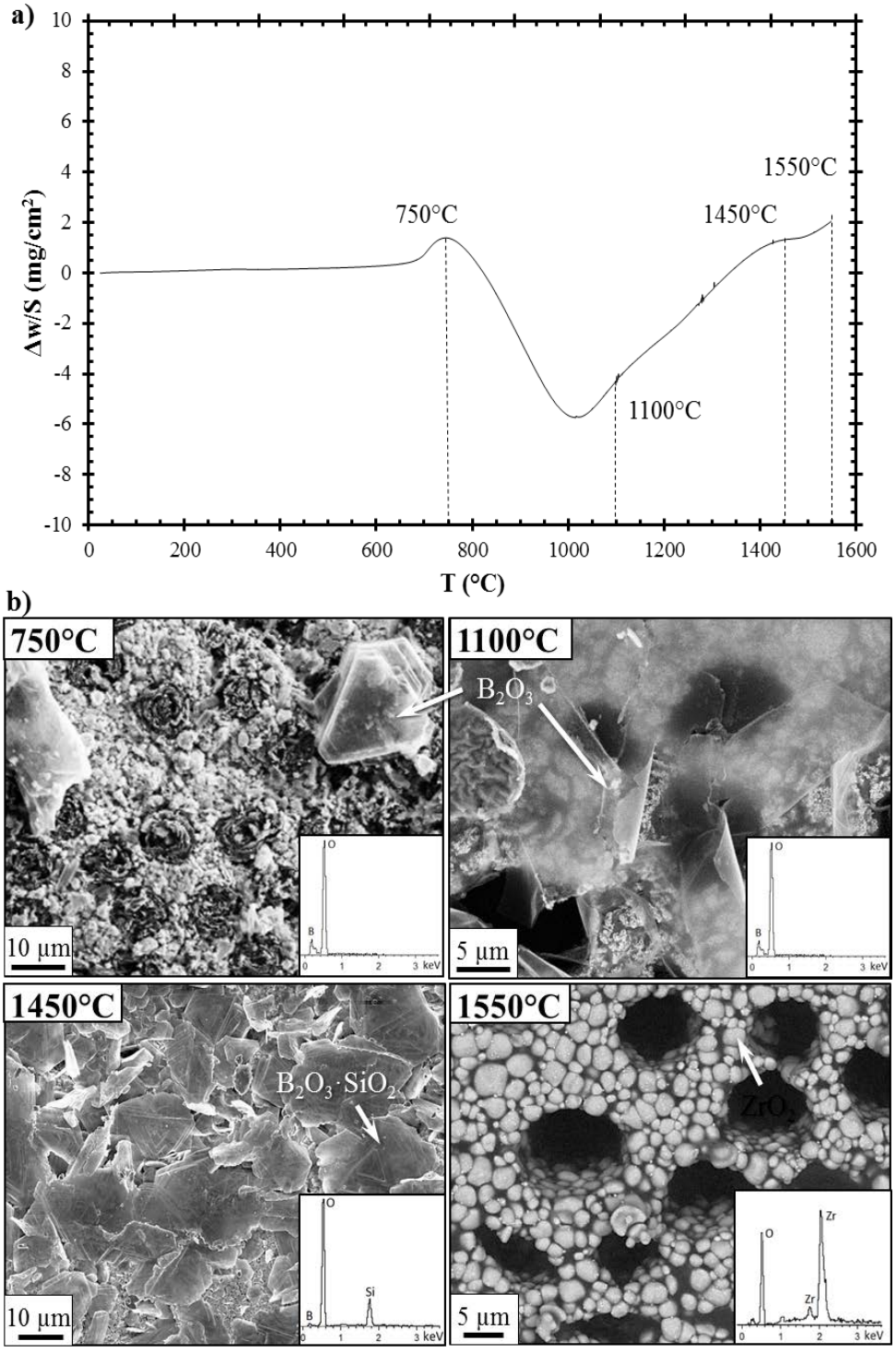

Figure 4.14 (a) Specific weight change (Δ*w*/*S*) vs temperature (*T*) of the test material and (b) the respective SEM micrographs of the oxidized surfaces at 750 °C (SE signal), 1100 °C (SE signal), 1450 °C (SE signal) and 1550 °C (BSE signal).

At 750 °C (Fig. 4.14a) a slight mass gain occurs due to the onset of ZrB_2 surface oxidation according to the Eq. 3:

$$ZrB_2 + \frac{5}{2} O_2 \rightarrow ZrO_2 + B_2O_3 \quad (3)$$

On the exposed surface, formation of B_2O_3 crystals and ZrO_2 grains is visible in Fig. 4.4b. Above 750 °C and up to 1100 °C a rapid weight loss occurs (Fig. 4.14a). This was attributed to the breakthrough oxidation of the exposed carbon fibres which led to the evolution of carbon oxides according to the following reactions:

$$C + \frac{1}{2} O_2 \rightarrow CO \quad (4)$$

$$C + O_2 \rightarrow CO_2 \quad (5)$$

$$CO + \frac{1}{2} O_2 \rightarrow CO_2 \quad (6)$$

Consistently, in the SEM micrographs of the exposed surface, holes left by the fibre consumption are observed (Fig. 4.14b). The surface is characterized by small zirconia grains in a glassy matrix of B_2O_3. Beyond 1100 °C and up to 1450 °C, mass gain becomes predominant again. This increase in weight is due to a major degree of ZrB_2 oxidation, as can be seen from the increase in grain size of ZrO_2 (Fig. 4.14b), coupled with the slower diffusion rates of oxygen. Moreover at this temperature the oxidation of SiC to SiO_2 becomes relevant and leads to the formation of a viscous borosilicate glass layer (Eq. 7) with higher melting temperature which covers the surface of the sample

$$SiC + O_2 \rightarrow SiO_2 + CO \quad (7)$$

The slope reduction from 1450 to 1500 °C was attributed to the volatilization of the borosilicate layer which exposed the ZrO_2 scale and the leftover borosilicate phase at grain boundaries. As can be seen in Fig. 4.14b, it was not possible to detect the presence of the borosilicate flakes on the surface, and only the holes left by the carbon fibre oxidation are visible. The weight loss due to carbon fibre oxidation in the temperature range of 700-1000 °C amounted to only 6%.

Xu *et al.* observed a similar trend in their work on porous C/C composites coated with ZrB_2 but in their case the weight loss due to fibre oxidation between 700 – 1000 °C was way more pronounced (30%) [24]. This is most likely due to the higher porosity of their specimen (>40%) which did not allow to effectively exploit the protection provided by the UHTC matrix. A dense ceramic matrix is needed in order to protect fibres and halt their oxidation.

One more test in air to 1550 °C with a heating rate of 45 °C/min was carried out. The TG of the samples and their respective SEM images are shown in Fig. 4.15.

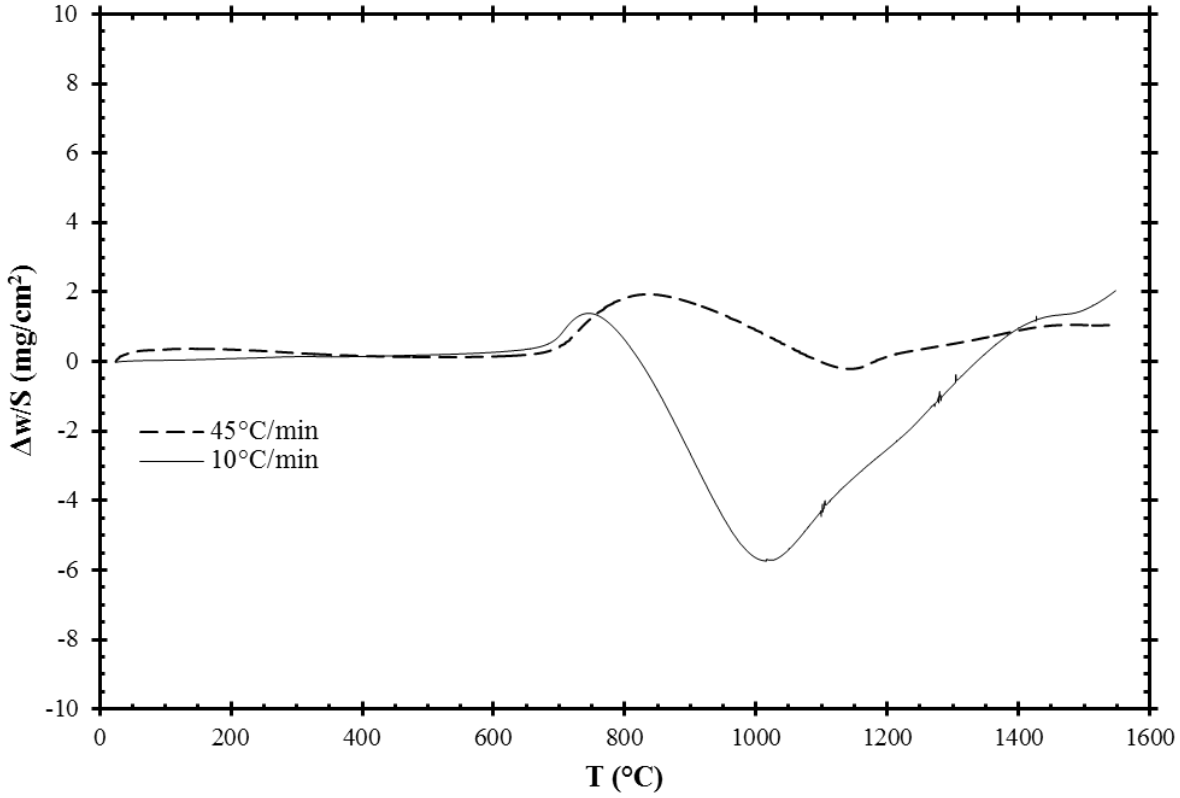

Figure 4.15 Specific weight change (Δ*w/S*) vs temperature (*T*) of the test material heated to 1550 °C in air at a rate of 45°C/min and 10°C/min.

It can be appreciated that with increasing the heating rate, the extent of weight loss due to fibre consumption is progressively reduced, due to reduced time of exposure: 34 min were enough to reach 1550 °C at 45 °C/min, compared with 153 min at 10 °C/min (Fig. 4.15). The sample heated at 45 °C/min displays a lower degree of volatilization of the borosilicate glass, as shown in Fig 4.16a; borosilicate flakes are still present on the surface and on top of the carbon fibres while the sample heated at 10 °C/min (Fig. 4.16b) is mainly characterized by larger ZrO_2 grains and residual B_2O_3 filaments on the surface and inside the porosities left by carbon fibre oxidation.

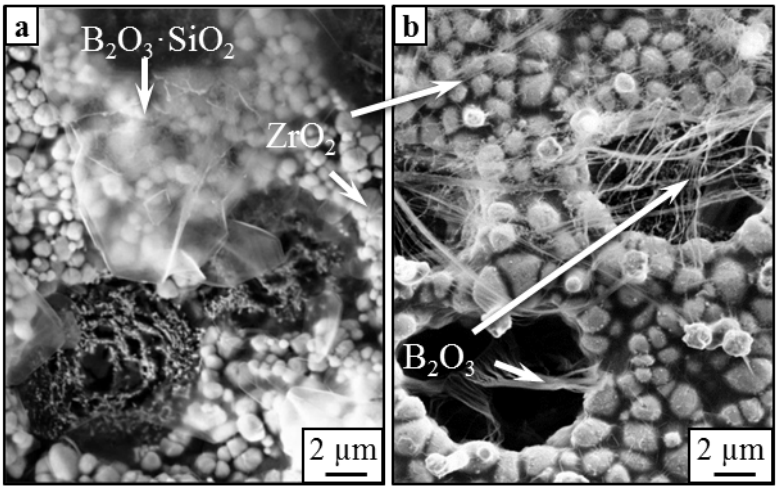

Figure 4.16 SEM micrographs (SE signal) of the surface of the sample heated to 1550 °C in air at heating rates of 45°C/min (a) and 10°C/min (b).

Following these preliminary tests, four isothermal runs were carried out at 800, 1000, 1200 and 1400 °C in order to study the kinetics behind each stage of reaction (Fig. 4.17)

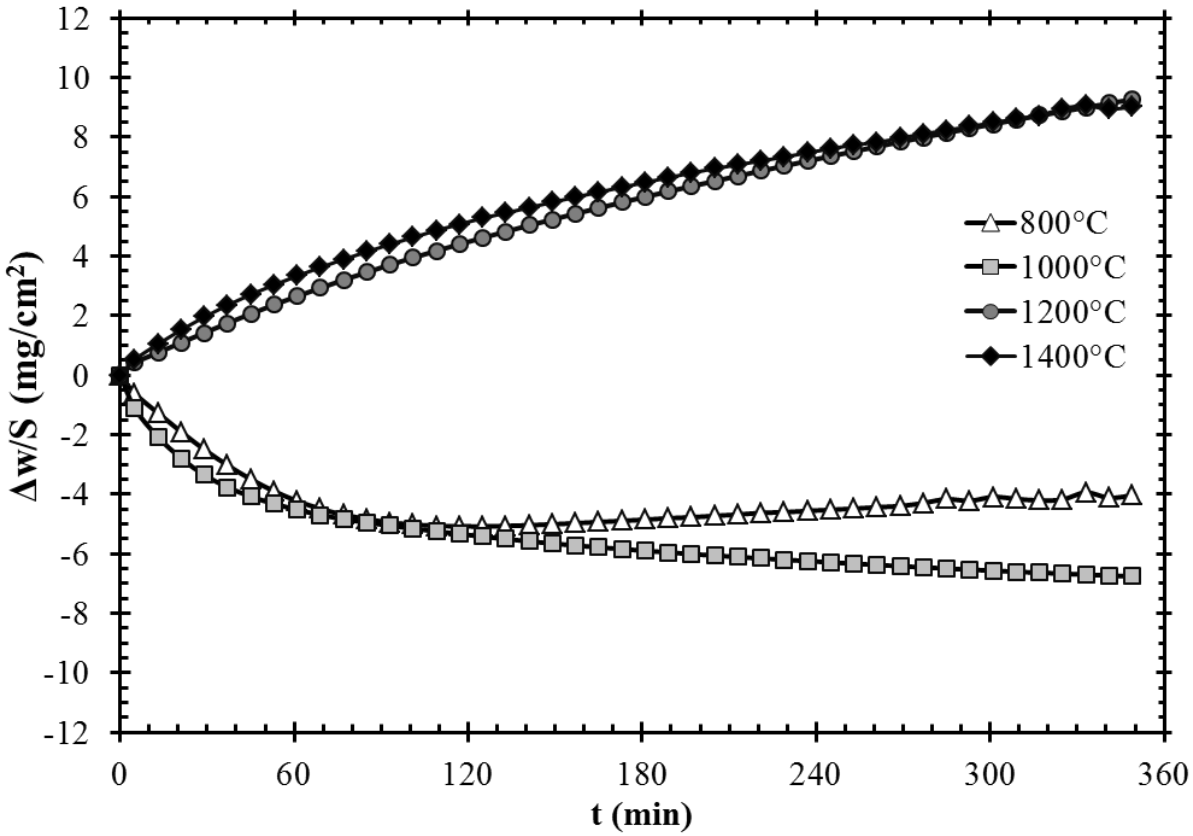

Figure 4.17 Specific weight change (Δ*w*/*S*) vs time (*t*) of the samples heated at 800, 1000, 1200 and 1400 °C for 6 h in flowing dry air.

According to this plot, isothermal stages at 800 °C and 1000 °C were characterized by an overall weight loss, whilst the stages at 1200 °C and 1400 °C ended up with a net weight increase. This result is in line with the work of Tang [25] carried out on C/SiC

composites with 4 vol.% ZrB_2 inclusions, even though in that case the predominant species was SiO_2 due to the higher SiC content in the starting material. SEM analysis was carried out at the end of each isothermal stage on the surface and cross sections of the samples (Fig. 4.18 and 4.19, respectively).

The sample heated at 800 °C (Fig. 4.17) is characterized by an exponential mass loss attributed to the oxidation of carbon fibres near the surface, which stops after about 120 min. At this time, a slow mass gain starts, which is due to the oxidation of ZrB_2 and the formation of a porous microcrystalline scale of ZrO_2.

On the sample surface (fig. 4.18a) it is possible to observe the partially oxidized carbon fibres and the fine grained layer of ZrO_2. The cross section (Fig. 4.19a) shows holes left by the evaporation of the outer fibres, but no other significant signs of oxidation could be appreciated.

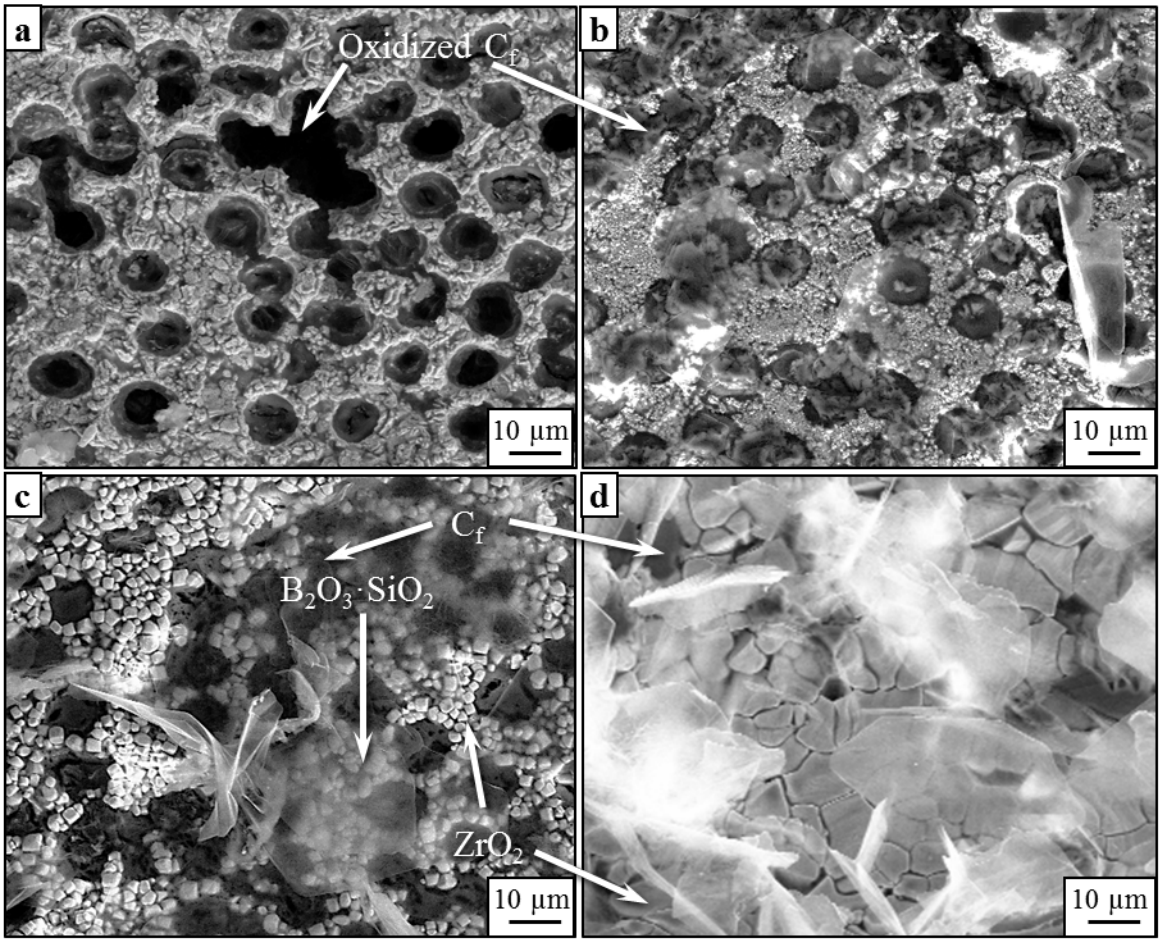

Figure 4.18 SEM micrographs of the surface of the samples after 6h flowing air at 800 °C (a), 1000 °C (b), 1200 °C (c) and 1400 °C (d) (SE).

At 1000 °C (Fig. 4.17), material loss due to carbon fibre oxidation far exceeds the weight increase due to ZrB_2 oxidation, resulting in the overall weight loss. The surface (Fig. 4.18b) is characterized by a higher degree of ZrB_2 oxidation, as can be seen from the formation of B_2O_3 platelets on the surface. The cross section (Fig. 4.19b) is characterized by a porous scale of ZrO_2 which exposes the carbon fibres below.

At 1200 °C (Fig. 4.17), the kinetics of the formation of SiO_2 is greatly enhanced and this results in the formation of a borosilicate glass that acts as a protective barrier against oxygen diffusion, leading to the rapid protection of carbon fibres [2,26–30]. From the SEM analysis of the surface (Fig 4.18c), the growth of the ZrO_2 grains and the formation of borosilicate glass platelets covering the carbon fibres can be observed, whilst in the cross section (Fig. 4.19c) it is possible to observe the formation of a inhomogeneous surface layer of SiO_2, a mixed layer of SiO_2 and ZrO_2 and a bulk scale of unreacted ZrB_2/SiC and carbon fibres, thus suggesting the ability of the liquid phase to fill and repair cracks and pores left by fibre degradation.

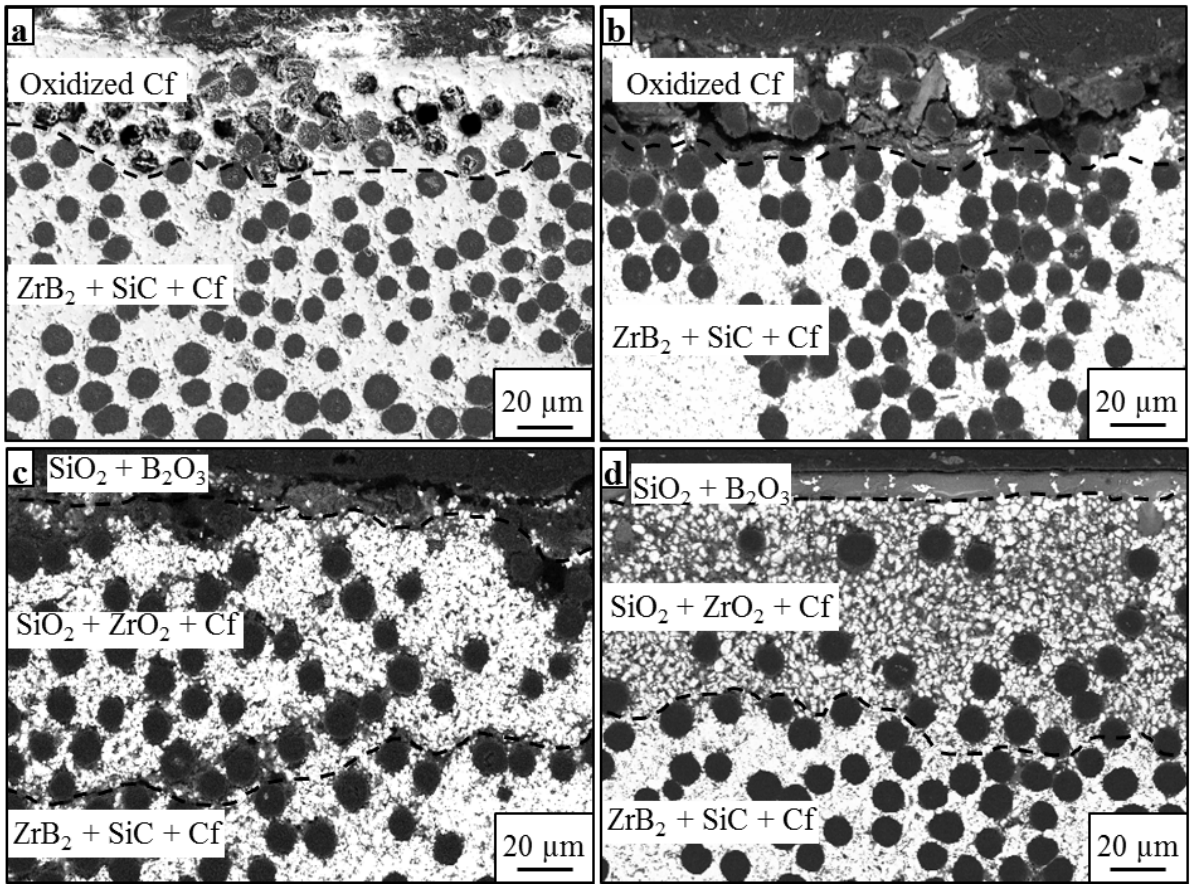

Figure 4.19 SEM micrographs of the cross section of the sample after 6h flowing air at 800 °C (a), 1000 °C (b), 1200 °C (c) and 1400 °C (d).

At 1400 °C (Fig. 4.17) a similar trend is observed. The SEM micrograph of the surface (Fig. 4.18d) shows the further grain growth of the ZrO_2 scale and the formation of an homogeneous borosilicate glass which covers the majority of the sample surface, while the cross section of the sample (Fig. 4.19d) emphasizes the formation of a uniform passive layer of SiO_2, a SiO_2/ZrO_2 layer and an inner scale of unreacted ZrB_2/SiC and carbon fibres, which is in accordance with previous work from Rezaie [31]. Even in this case, the formation of the protective layer of borosilicate is fast enough to prevent the further oxidation of carbon fibres, which appear to be fully covered. The small deviation observed in the isothermal curve (Fig. 4.17) can be attributed to the local cracking of the borosilicate scale, which leads to the breakthrough oxidation of the carbon fibres near the surface.

The data obtained from oxyacetylene torch tests and muffle furnace tests are not directly comparable with the results obtained from TGA experiments. For instance, torch tests are characterized by higher ablation rates, different gas composition and a temperature gradient throughout the specimen, whereas TGA allows for a stricter control of the chamber temperature, gas composition and flow rate, and heating rate. Moreover the fibres of the specimen tested in this work are purposely exposed to air in order to evaluate whether the UHTC matrix is able to inhibit fibre degradation quickly enough. Taking into account these considerations, it can be noted that the morphology of the sample tested by Yang under oxyacetylene torch for 3 min [32], which most closely resembles the composite studied in this work, is characterized by a higher degree of fibre oxidation and coarsening of ZrO_2 than the sample tested in air at 1400 °C for 6h. This is most likely due to the higher erosion rates and local temperatures on the surface of the sample that lead to the ablation of the liquid SiO_2 phase.

Ceramic composites are highly unlikely to show simple oxidation behaviour, thus a multiple regression analysis seems to be more suitable for the interpretation of experimental data. The empirical equation proposed by Nickel is useful to describe the phenomena that take place during corrosion processes (eq. 8) [33].

$$\frac{\Delta w}{S} = k_{par}\, t^{0.5} + k_{lin}\, t + k_{log} \log(t) \qquad (8)$$

According to this model, kinetic curves can be generally decomposed in a linear term, a parabolic term and a logarithmic term, if present. The physical meaning of this equation is that different phenomena can simultaneously take place during oxidation, such as

diffusion of inward and outward species, rupture of the scale, crystallization of new phases inside the scale, evaporation of scale material, etc. With the exception of the linear term (k_{lin}) which can be negative when significant development of gaseous products occurs, negative k parameters do not reflect a physical reality.

TGA curves were fitted with the curve-fitting tool of the software Matlab (MATLAB 9.0, The MathWorks Inc., Natick, MA, 2000) using the least squares method. A custom equation was set up in order to replicate the kinetic model proposed by Nickel in the form of (eq. 9)

$$y = a\,x + b\,x^{0.5} + c\,\log(x) \qquad (9)$$

where "y" is $\frac{\Delta w}{S}$ and "x" is t. a, b and c are respectively the linear, parabolic and logarithmic constants.

For the isothermal curves registered at 800 and 1000 °C, the trends of the curves were more similar to exponential decay laws; therefore a slightly different model was used that accounted for an exponential term describing the rapid oxidation of carbon fibres (eq. 10) [34] .

$$\frac{\Delta w}{S} = k_{exp}\exp(-a\,t^{b}) + k_{par}\,t^{0.5} + k_{lin}\,t \qquad (10)$$

where a and b are empirical positive constants. For $0 < b \leq 1$, the activation rate of fibres decreases as a function of time, while for $b > 1$ the kinetics of carbon fibre oxidation are enhanced and lead to faster degradation [34].

Conversely, for the curves at 1200 and 1400 °C, the equation suggested by Nickel was used to fit the data. Since the fitting of the curves did not give any logarithmic contribution, this was omitted (eq. 11).

$$\frac{\Delta w}{S} = k_{par}\,t^{0.5} + k_{lin}\,t \qquad (11)$$

Fig. 4.9 shows the original TG curves, the fitted lines and their decomposition into positive and negative terms. The equation parameters are summarized in table 4.5.

Table 4.5 Kinetic parameters of the fitted curves, relatively to linear (k_{lin}), parabolic (k_p) and exponential (k_{par}, a, b) contributions and R^2 (fit goodness) values. For the isotherms at 800 and 1000 °C no linear term was found.

TG isotherm	a (s^{-1})	b	k_{exp} (mg/cm^2)	k_p ($mg/cm^2 \cdot s^{-0.5}$)	k_{lin} ($mg/cm^2 \cdot s^{-1}$)	R^2
800°C	0.007428	1.265	6.923	0.1721	/	0.9983
1000°C	0.1466	0.3296	20.27	0.1611	/	0.9979
1200°C	/	/	/	0.6248	/	0.9998
1400°C	/	/	/	0.6998	- 0,005709	0.9999

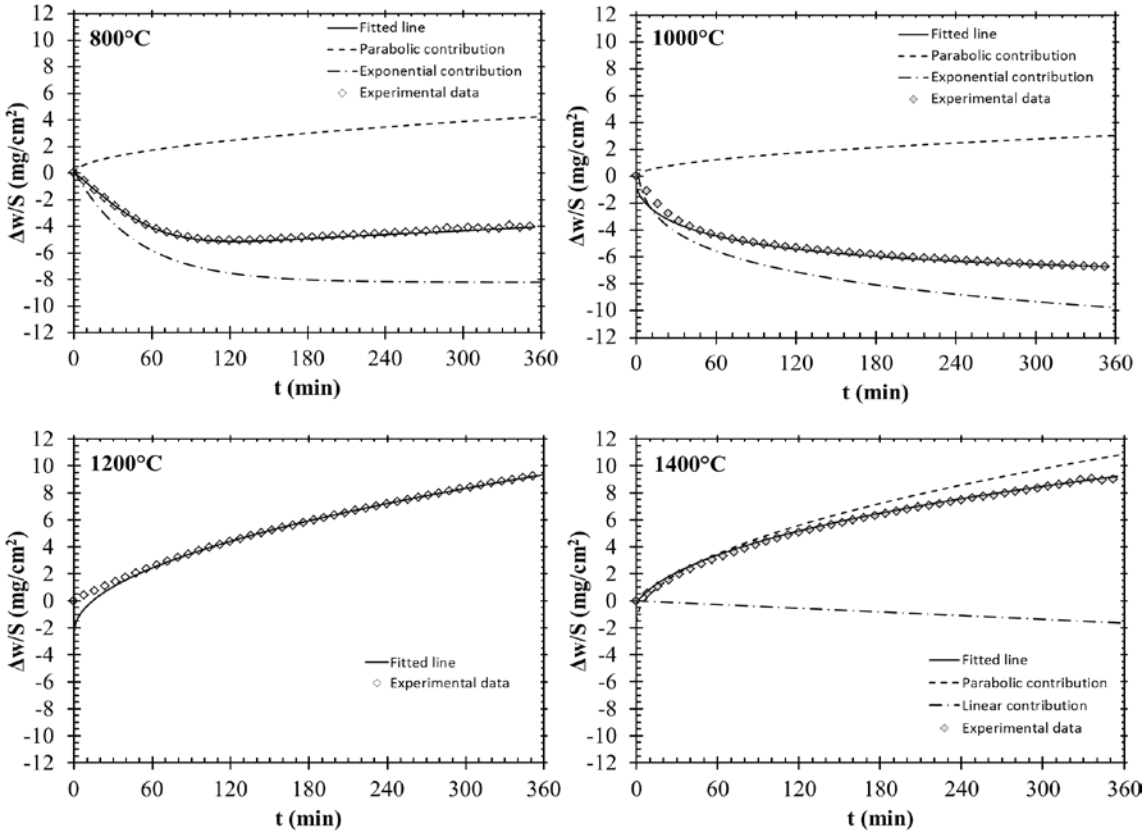

Figure 4.20 Specific weight change ($\Delta w/S$) vs time (t) of the samples heated at 800, 1000, 1200 and 1400°C for 6 h in flowing dry air and their respective fitted lines obtained by fitting the isotherms at 800 and 1000 °C with eq. 10 (positive parabolic term + exponential decay), and the curves at 1200 and 1400 °C with eq. 11 (para - linear kinetics) by fixing the offset at zero. The dashed lines represent the contribution of each single term to the fitted line. For the isotherm at 1200 °C, only the fitted line is shown since the parabolic term alone was enough to fit the curve.

The curves at 800 °C and 1000 °C are mainly characterized by the exponential decay term which overshadows the slight mass gain due to ZrB_2 oxidation. It is important to note that this model describes the two phenomena independently. The rapid oxidation of carbon fibres could lead to the bubbling and cracking of the B_2O_3 layer readily formed, promoting its evaporation, while the formation of liquid oxides on the surface could slow down fibre oxidation. It is assumed that at relatively low temperatures and with a steady air flow rate of only 30 ml/min, the interference between the two phenomena is negligible.

The curve at 1200 °C was purely parabolic and only the fitted line is represented in figure 4.20. The 1400 °C curve could be decomposed into a parabolic term and a slightly negative linear term. The parabolic term represents the rate of oxygen diffusion which is progressively decreased due to formation of a protective barrier, while the linear term accounts for gaseous species exit due to the local breakthrough oxidation of carbon fibres or evaporation of B_2O_3. Both curves exhibit very similar trends, indicating that the protective borosilicate glass formed at 1200 °C is able to inhibit further oxidation of the composite even at higher temperatures. The isothermal run at 1400 °C is characterized by a slightly higher value of k_{par} than the curve at 1200 °C, which is to be expected due to the higher temperature of oxidation.

The main implication of these results is that the protection of fibres only starts above 1200 °C, when SiC oxidises to form a protective layer of borosilicate glass. Below 1200 °C the oxidation of SiC is slow and the fibres in the composite are vulnerable to oxidation attack.

4.6 Influence of SiC content on the oxidation resistance

Following this preliminary study on the oxidation behaviour of ZS10, additional oxidation tests were carried out to assess the influence of SiC content. Short term oxidation tests were carried out in a bottom-up loading furnace at 1500°C and 1650°C in air, following the procedures described in 3.4. Samples were weighed before (w_{in}) and after (w_{fin}) oxidation cycles and the weight difference was normalized over the initial surface area, S $\left(\frac{\Delta m}{S} = \frac{w_{fin} - w_{in}}{S}\right)$. Although there were slight variations in the sample compositions and fibre content, and therefore the individual values were not perfectly comparable, all samples underwent weight loss after oxidation at 1500 and 1650 °C. Weight loss was notably higher at 1650 than at 1500 °C, except for sample ZS20 for which it was unchanged. (table 4.6).

Table 4.6 Mass variation normalized to the surface area after oxidation tests at 1500 and 1650 °C for samples ZS5-20.

	ZS5	ZS10	ZS15	ZS20
$\Delta m/S_{1500°C}$ (mg/cm^2)	- 1.9	- 1.9	- 3.6	- 2.4
$\Delta m/S_{1650°C}$ (mg/cm^2)	- 3.9	- 3.6	- 7.0	- 2.3

X-Ray diffraction was carried out on the surface layer of the samples after oxidation at 1500 and 1650 °C. At 1500 °C (Fig. 4.21) the predominant phase is monoclinic zirconia (PDF 83-0939) with trace amounts of tetragonal zirconia (PDF 88-1007); there is a small peak arising at 28 2-theta attributed to crystalline SiO_2 species (PDF 82-1559) that increases with the increase of SiC content. For the sample ZS15, a peak relative to ZrB_2 (PDF 75-1050) was also observed; this could be attributed to a locally damaged oxide scale which exposed the unreacted matrix.

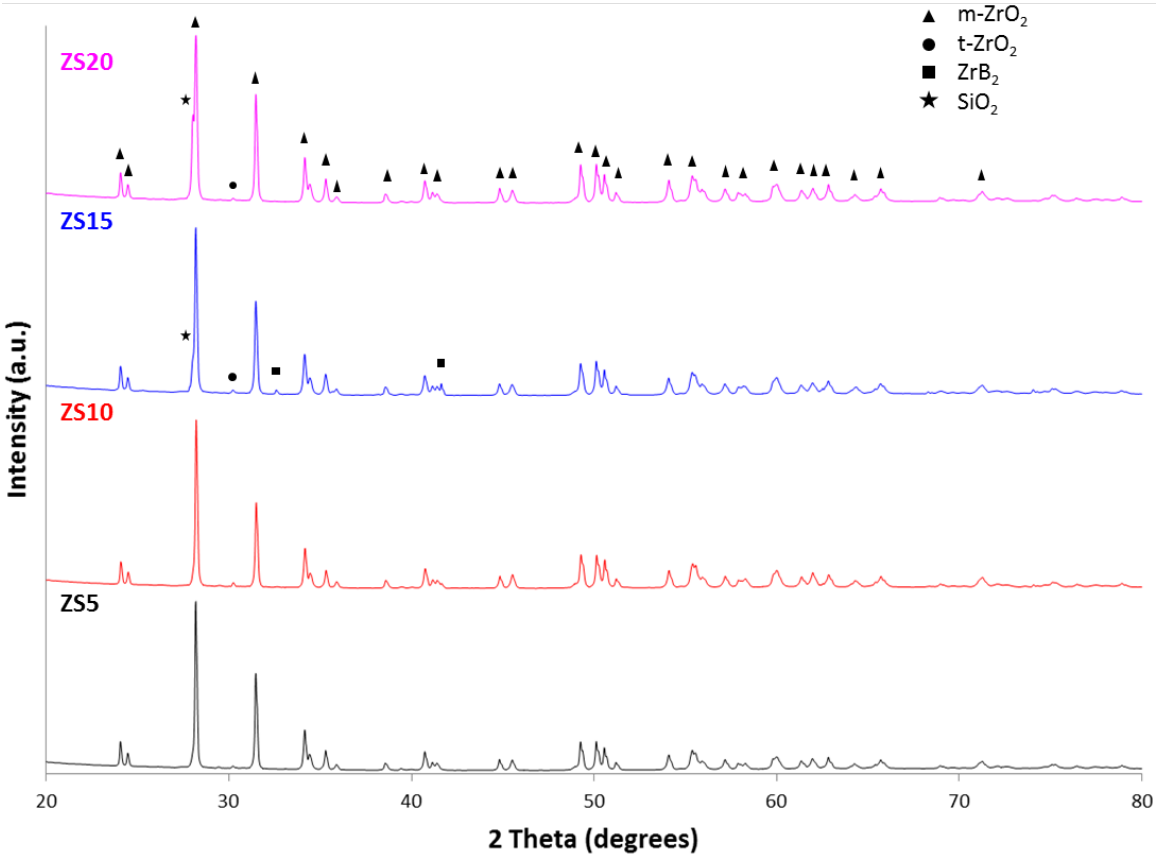

Figure 4.21 X-Ray diffraction patterns of the surface of samples ZS5, ZS10, ZS15, ZS20 oxidized at 1500 °C in air.

In previous studies on the oxidation of a ZrB_2 bulk ceramic doped with 20 vol. % of SiC, Gao et al. found evidence of the formation of zirconium silicate ($ZrSiO_4$) between 1200 and 1500 °C both at low and high oxygen partial pressure, highlighting that the zircon yield was higher in oxygen-poor atmosphere [35]. In our case no formation of zircon was observed at 1500 °C. This could be explained both by the short exposure times, the oxygen-rich atmosphere and the overall lower SiC content.

At 1650 °C (Fig. 4.22) only the peaks relative to monoclinic zirconia could be seen while no SiO_2 platelets were detected on the surface, in agreement with the aforementioned work [35]. This was attributed to the evaporation of the outer borosilicate layer which leaves behind only amorphous phases not detected by X-ray diffraction. The peaks relative to tetragonal zirconia were observed only in sample ZS20. No phases relative to carbon or the formation of carbides were observed.

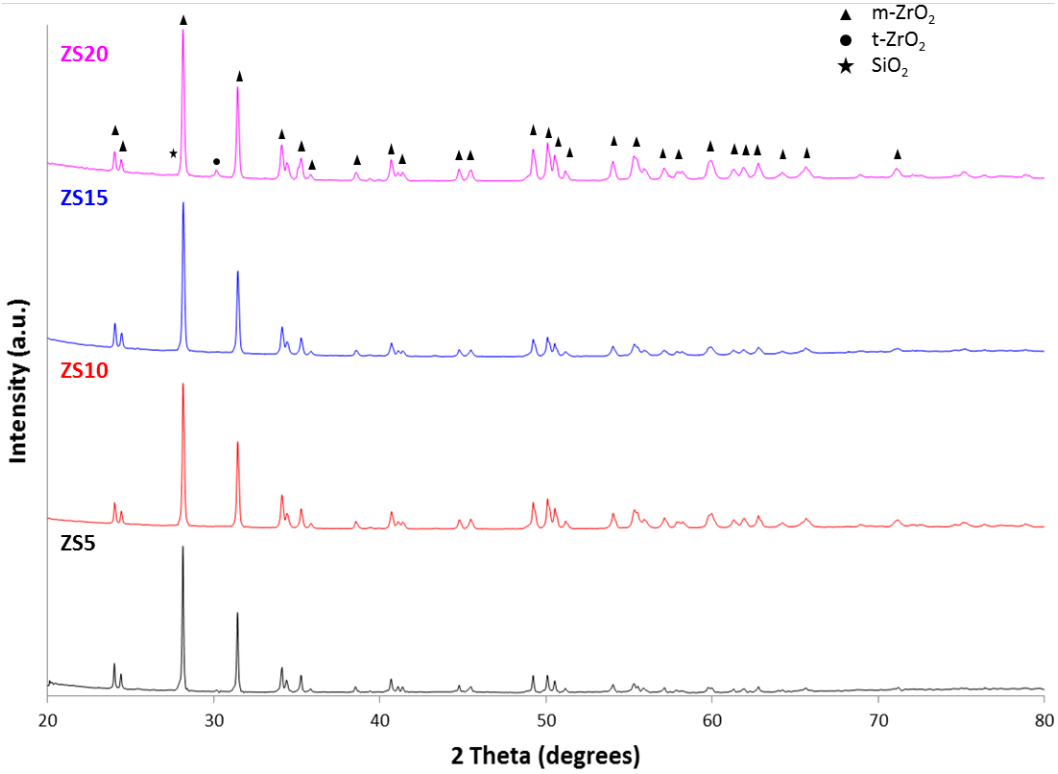

Figure 4.22 X-Ray diffraction patterns of the surface of samples ZS5, ZS10, ZS15, ZS20 oxidized at 1650 °C in air.

4.6.1 Microstructure

Following the XRD characterization, SEM analysis was carried out on the surface and cross section of the oxidized samples. It is possible to observe the formation of bubbles on the surface which are due to the evolution of volatile oxides (fig 4.23).

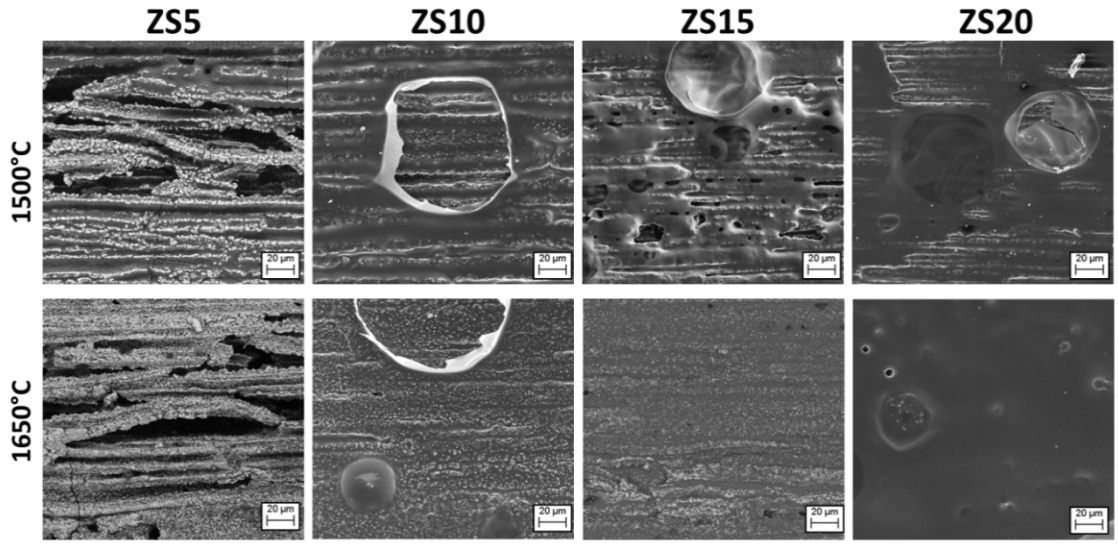

Figure 4.23 Top view of the oxidized samples at 1500 °C (top) and 1650 °C (bottom). The white area are constituted mainly by monoclinic sub-micrometric ZrO_2, while the dark grey zones consist mainly of amorphous borosilicate glass.

The samples containing a higher amount of SiC (ZS15 and ZS20) are the ones characterized by a higher amount of blisters on the surface; this is associated with the greater amount of liquid phase formed during the oxidation of SiC to $SiO_{2(l)}$. The specimen containing 5 vol. % SiC is visibly the most damaged. Moreover it is possible to notice that for the samples containing intermediate amount of SiC the oxidation is not homogeneous but takes place locally with the formation of silica channels, preferentially in the hollows left by the oxidation of the outer fibres.

In fig. 4.24, the high magnification micrographs of the surface and the cross section of samples ZS5-20 oxidized at 1500 °C is shown. The rapid exposition to high temperatures effectively limits the oxidation of fibres which is critical at 1000 °C [36]. Sample ZS5 is characterized by the lowest amount of SiC which is reflected in the lowest amount of silica glass formed during oxidation. Large ZrO_2 grains emerging from the glassy phase were observed. With the increase of SiC content it is possible to see the progressive coverage of the surface with a liquid borosilicate glass that fills the holes left by the outer fibre burnout and prevents further oxygen diffusion inside the material. The small white dots that can be seen in transparency are precipitated ZrO_2 grains in the borosilicate glass. At high temperature, the B_2O_3 partially dissolves the ZrO_2 but with the increase of SiC content, the size and amounts of precipitated zirconia decreases because the glassy phase becomes progressively impoverished of B_2O_3 [37].

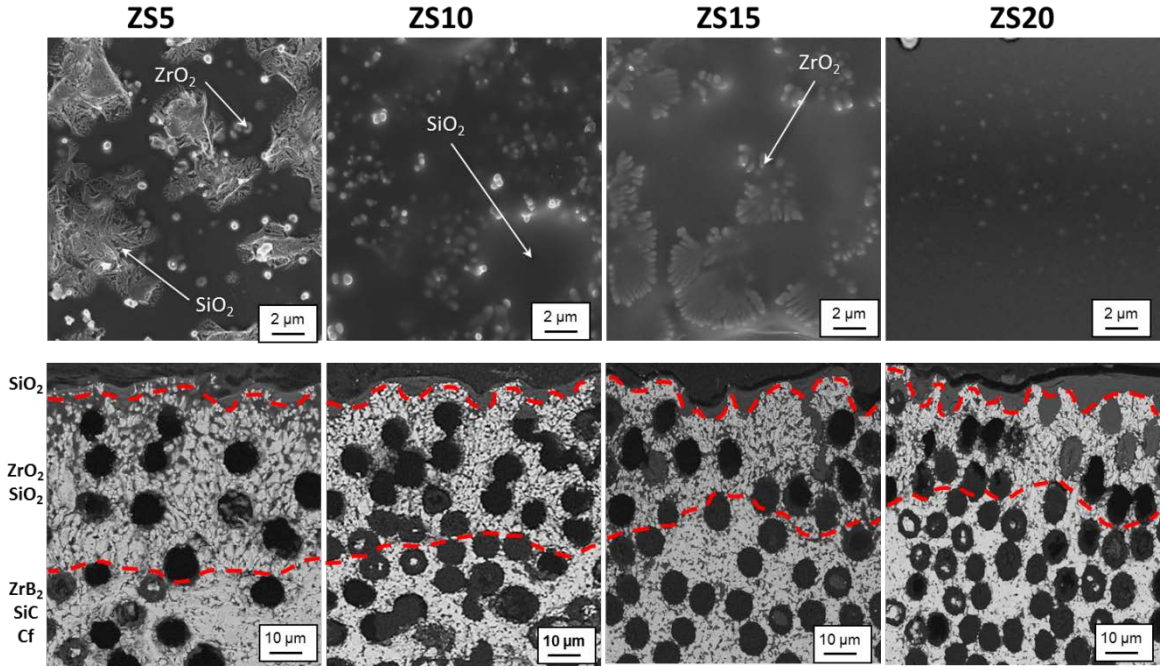

Figure 4.24 High magnification micrographs of the surface (top) and cross section (bottom) of the oxidized samples at 1500 °C. The dark and light grey phases represent SiO_2 and ZrO_2 respectively. The holes (black) are due to fibre burnout.

Closely inspecting the surface of sample ZS5 oxidized at 1500 °C, some platelets were observed and EDS analysis suggested their chemical composition (fig. 4.25), most likely originating from the cooling down of the boron-rich borosilicate melt.

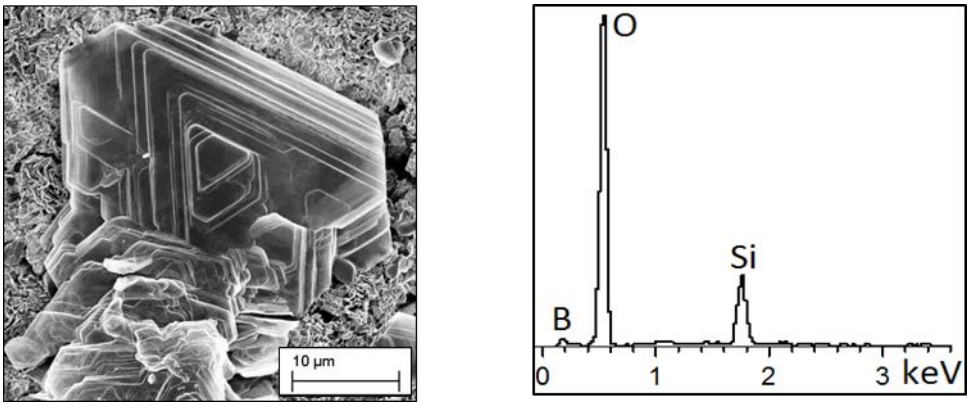

Figure 4.25 Platelets of B_2O_3-SiO_2 formed on the surface of sample ZS5 after oxidation at 1500 °C in air.

The cross section is characterized by three distinct layers: 1) an external borosilicate glass layer, 2) an intermediate zirconia-silica scale, where the holes left by the fibre oxidation are partially filled by silica, 3) unreacted matrix scale. The thickness of the oxidized layer slightly decreases with the increase of SiC content but remains in the range of 40-60 µm.

Previously Fahrenholtz studied and thoroughly discussed the formation of a SiC-depleted layer between the ZrO_2/SiO_2 scale and the unreacted matrix in a ZrB_2/SiC ceramic originating from the active oxidation of SiC to form volatile SiO [38]. The same author also investigated the influence of graphite addition in a ZrB_2/SiC composite and found out that the presence of carbon may lead to the preferential formation of CO which lowers the SiO partial pressure and allows to retain the SiC phase [31]. Assuming that the highly graphitic fibres used in this work have a similar reactivity to graphite, this could justify the lack of a SiC-depleted layer in our oxidized samples.

After oxidation at 1650°C the samples appear visibly more damaged (fig. 4.26). The zirconia grains, which were barely visible at 1500°C, are now exposed due to the partial evaporation of the outer silica layer. Sample ZS5 is characterized by large ZrO_2 particles on the surface, while the inner layer is thicker, more fragmented and porous. Samples ZS10 and ZS15 show very similar microstructure; dendritic zirconia can be observed growing in the glassy phase, but a good amount of silica glass is still present. Sample ZS20 is the least affected by the oxidation at 1650°C and the oxidized layer thickness is almost unchanged (35 µm), which is also reflected in the constant weight

loss (table 4.6). The sample is still fully covered by silica and the only observable changes are a higher amount of blisters on the surface and the appearance of ZrO_2 needles from below.

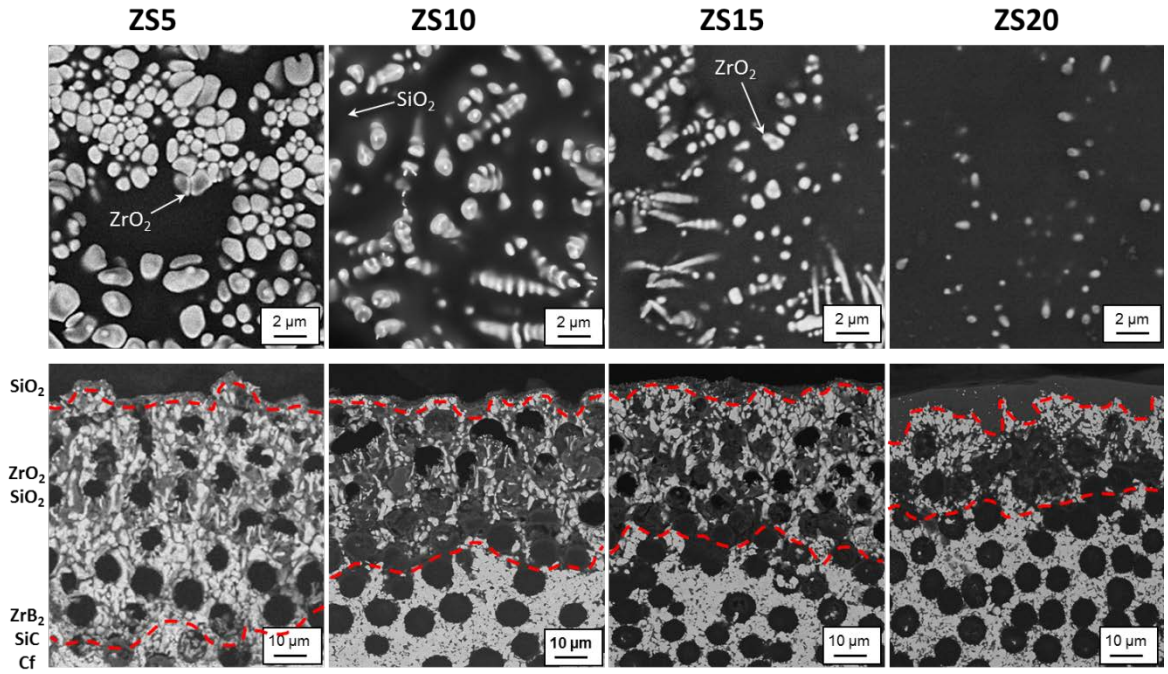

Figure 4.26. High magnification micrographs of the surface (top) and cross section (bottom) of the oxidized samples at 1650°C. The dark and light grey phases represent SiO_2 and ZrO_2 respectively. The holes (black) are due to fibre oxidation.

The thicknesses of the oxidized layer for samples ZS5-20 shown in table 4.7 tend to decrease with the increase of SiC content and for sample ZS15 and ZS20 are almost unchanged for the tests at 1500 and 1650°C.

Table 4.7 Average values of thickness of the oxidized layer (outer SiO_2/B_2O_3 layer + ZrO_2/SiO_2 scale) at 1500 and 1650 °C for samples ZS5-20:

	ZS5	ZS10	ZS15	ZS20
Oxide thickness 1500 °C (µm)	64	50	45	36
Oxide thickness 1650 °C (µm)	85	57	50	35

Further inspection on the small zirconia crystals found underneath the ruptured bubbles allowed to detect a coral-like structure (Fig. 4.24). These crystals are immersed in a glassy scale that was identified predominantly as SiO_2 by EDS. On the tip and the sides of these needles it is possible to observe the growth of small nuclei that remind the branches of a dendrite. This type of dendritic zirconia was previously described by

Halloran et al. as secondary zirconia crystals that precipitate from the molten borosilicate glass where they were dissolved [37,39].

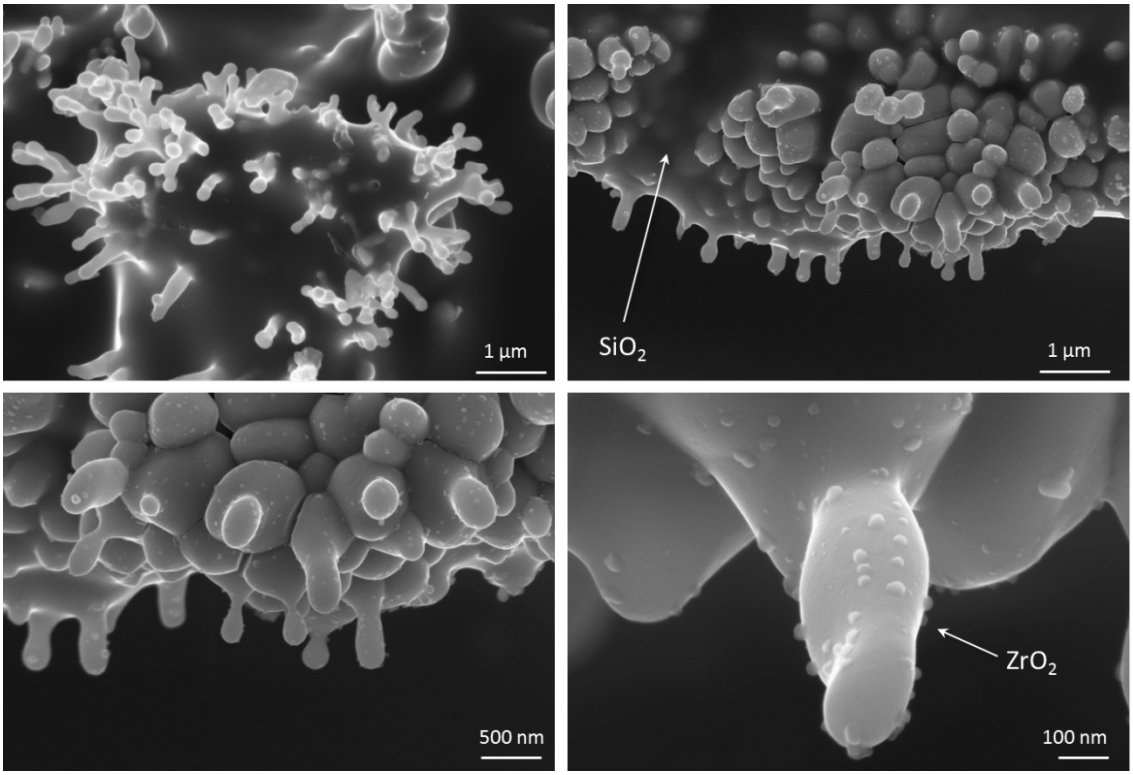

Figure 4.27 High magnification micrographs of secondary zirconia growing under the ruptured bubbles of sample ZS20 oxidized at 1500 °C. The dark and light grey phases represent SiO_2 and ZrO_2 respectively.

4.6.2 Oxidation model

Previous studies on the kinetics of oxidation of a carbon fibre reinforced ZrB_2/SiC composite concluded that the overall oxidation behaviour of these materials at temperatures from 800 to 1400 °C is the result of two competing phenomena; on one hand the weight loss due to fibre burnout (reactions 12, 13) and on the other the weight gain due to oxidation of ZrB_2 and SiC (reactions 14, 15)

$$C + ½\ O_2 \rightarrow CO_{(g)} \quad (12)$$

$$C + O_2 \rightarrow CO_{2(g)} \quad (13)$$

$$ZrB_2 + 5O_2 \rightarrow ZrO_{2(s)} + B_2O_{3(l,g)} \quad (14)$$

$$SiC + 3/2O_2 \rightarrow SiO_{2(l)} + CO_{(g)} \quad (15)$$

Reaction 12 begins at T >800 °C whilst formation of borosilicate glass starts at T >1200 °C. The faster is the formation of a protective borosilicate layer, the slower is the fibre oxidation [40]. The most critical temperature range is between 800 and 1200 °C, because there is no protective layer on the surface, apart from some poorly effective liquid B_2O_3. At temperatures higher than 1200 °C, formation of the borosilicate glass starts to protect the fibre from further oxidation and their oxidation is progressively halted.

The overall oxidation mechanisms for the present materials can be explained as follows. During introduction of the coupons inside the hot chamber, the samples experience an abrupt increase of temperature from RT to 1500 °C or 1650 °C. Although the permanence at the critical temperature range between 700 °C and 1200 °C is estimated to be ~10 s, this short time is enough for burning out of first layer of fibres, according to reactions 1,2. Then it is reasonable to speculate that formation of the borosilicate layer forming at T >1200 °C starts to slow down the oxygen diffusion by filling the cavities left by the burnt carbon fibres and covering the matrix surface. The effect of heating rate was already investigated and proven to minimize fibre oxidation by triggering the faster formation of a glassy phase [40]. The glass formation is more abundant for higher amounts of SiC which is consistent with the progressively thicker silica scale but overall thinner oxide scale (Fig. 4.26).

The overall mass loss after oxidation (table 4.6) can be attributed to the harsher conditions of these tests compared to those carried out in the thermo-gravimetric analyser. The exposure to air for 1 min at 1500°C in the bottom-up furnace led to almost the same degree of oxidation of the equivalent TGA test carried out up to 1550°C in the span of 2.5 hours. The increased oxidation rate can be ascribed to the non-static air of the bottom-up furnace used in this experiment; during the introduction of the sample inside the furnace, cold air enters the chamber and, upon heating, gives rise to turbulent flow which contributes to material removal from the surface of the specimen.

Moreover since the oxidation tests were carried out on small bars, the specimens underwent oxidation both on the surface and on the sides. For the application as thermal protection systems for the leading edges of aerospace vehicles, where fibres normally do not face outwards, only the outer surface of the tile would be exposed to the corrosive atmosphere [41]. The results obtained in this work also account for potential oxidation phenomena that may take place on the sides of the specimen (e.g. as a result of a crack or defect and subsequent exposure of the underlying material, or when used

for the fabrication of nozzle inserts where multiple fibre orientations may be chosen). The oxidation of fibre reinforced composites for fibres exposed to air parallel and perpendicular to the fibre axis is schematized in Fig. 4.28.

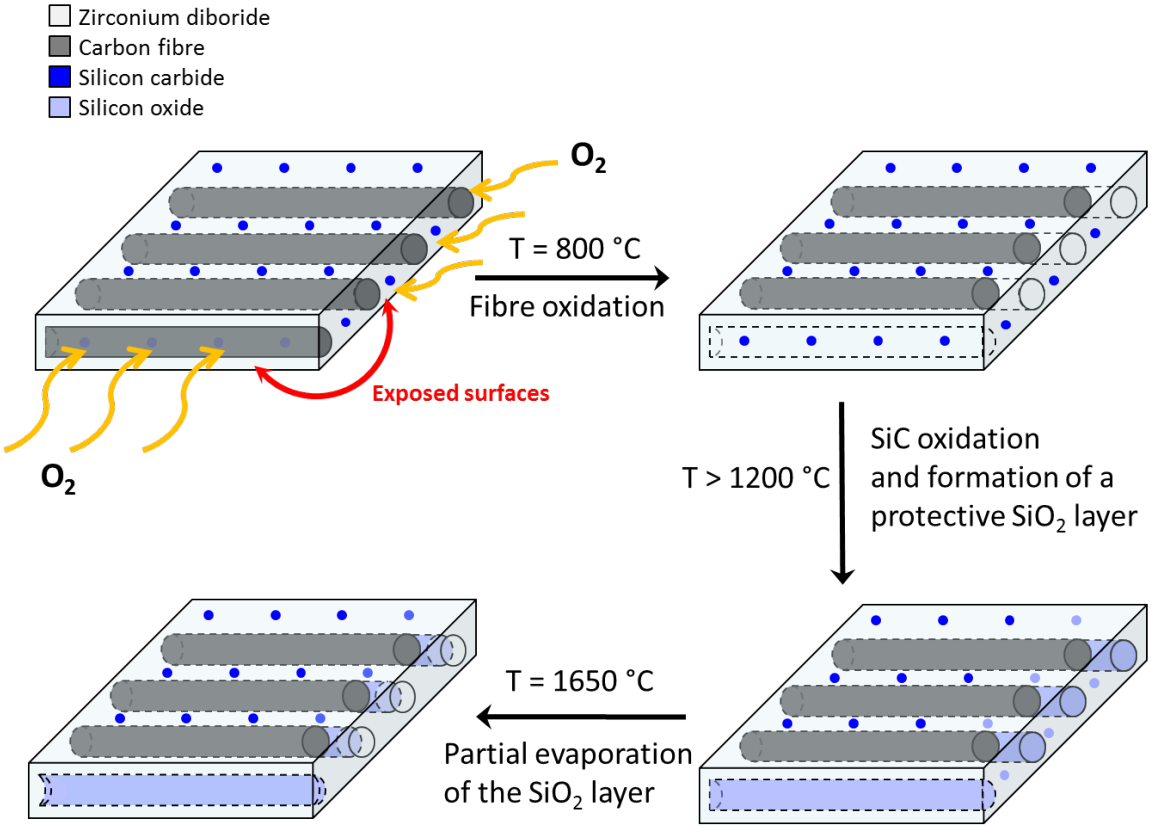

Figure 4.28. Model for the lateral oxidation of fibres exposed to air parallel and perpendicular to the fibre axis: initially the outer fibres completely burn while the inner fibres get partially oxidized. Then the SiC from the matrix turns to liquid SiO_2 that fills the holes left by the oxidation of the fibres. At 1650 °C the silica layer partially evaporates.

If the side of the fibres is exposed, which is what happens on the surface as discussed before, the outer fibres readily burn and leave behind a layer of continuous ceramic matrix that behaves like a conventional bulk ceramic. On the other hand, if the fibre section is exposed, the oxidation of carbon results in the formation of channels that favour further diffusion of oxygen inside the material. In this case, the increasing amount of SiC leads to the progressive coverage of the holes left by the fibre oxidation in the section which ultimately results in the halted oxidation of the material (Fig. 4.29).

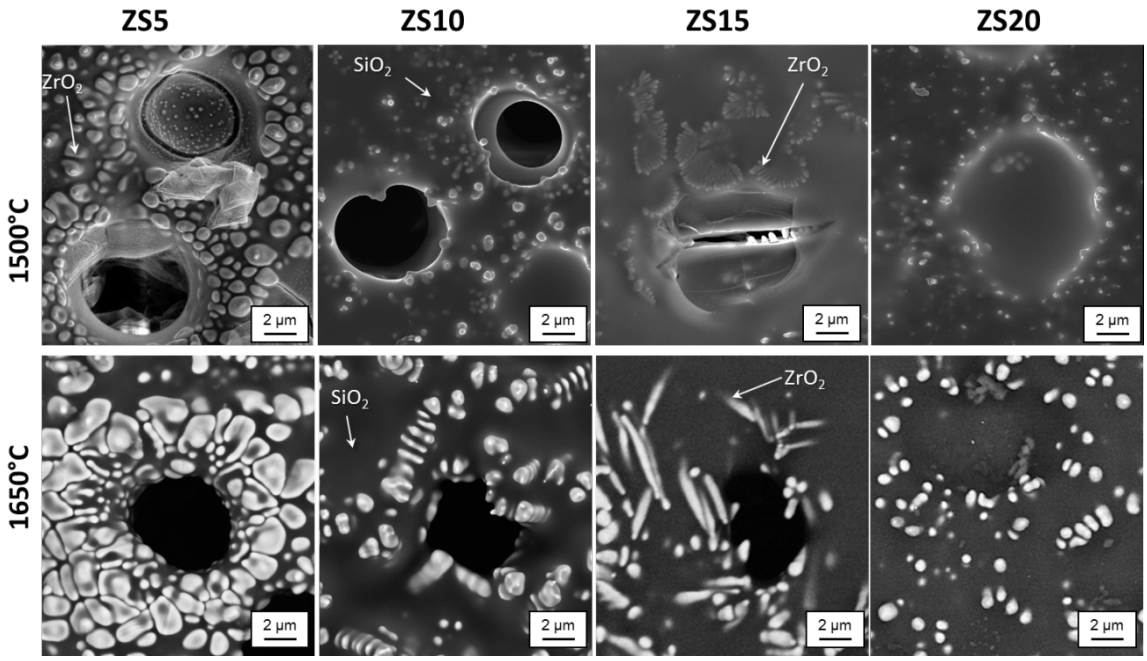

Figure 4.29. High magnification micrographs of the lateral section of the oxidized samples at 1500 and 1650 °C. The dark and light grey phases represent SiO_2 and ZrO_2 respectively. The holes (black) are due to fibre burnout.

4.7 Conclusions

The mechanical properties and oxidation behaviour of carbon fibre reinforced ZrB_2/SiC composites were investigated. Preliminary studies were carried out on a baseline composition containing ZrB_2 + 10 vol% SiC.

The flexural strength is lower than conventional ZrB_2/SiC bulk ceramics due to a higher degree of porosity and delamination, but a marked increase in fracture toughness and ultimate failure strain was registered.

With the increase of SiC content, grain size decreased slightly from 3 to 2.5 µm Initially the microstructure did not show significant signs of reaction with the fibres, but a more in-depth study on the fracture surfaces revealed hindered pull-out for higher amounts of SiC.

From random forest and regression tree analysis, the ratio between SiC and carbon fibre amount emerged as the most important parameter. Combining the results of both the statistical analysis, it can be said that in order to obtain a high-strength high-toughness composite, the composite should have a low volumetric fraction of matrix, and consequently a high amount of fibre, and a high SiC/fibre ratio. The first indication implies a low contribution from the weaker of the two phases making the composite.

The second indication points out the importance of having a proper fibre/matrix interface to activate the load-transfer mechanism.

As far as oxidation resistance is concerned, kinetic parameters were evaluated by curve fitting of the isothermal curves. Four major phenomena have been identified: at 750 °C the slight mass gain signals the onset of ZrB_2 oxidation, which is then followed by the rapid combustion of the exposed carbon fibres up to 1100 °C. Past this point the oxidation of SiC to SiO_2 becomes predominant and leads to the formation of a protective borosilicate layer which prevents the further oxidation of carbon fibres up to 1500 °C. From 1500 to 1550 °C, the change in the slope was attributed to the volatilization of the superficial borosilicate layer.

The critical temperatures for these composites are between 800 – 1000 °C; in this temperature range, the kinetic of formation of the protective borosilicate layer is still slow and the carbon fibres get rapidly oxidized, following an exponential mass decay law. Higher heating rates allow to quickly reaching the target temperature at which this protective layer forms, resulting in the parabolic mass gain. This property can prove useful in environments where high temperatures are reached within a very short time, exploiting the oxidation resistance provided by ZrB_2 – SiC system while retaining the increased damage tolerance provided by the continuous carbon fibres.

From the oxidation tests in air at 1500°C and 1650°C it was found that for SiC content s <5 vol.%, the formation of the protective glass is not sufficient and this leads to excessive local burnout of the fibres, ultimately resulting in the rupture of the oxide layer. Moreover the higher degree of porosity promotes the inward diffusion of oxygen and further oxidation of the material. For SiC > 15 vol. %, the borosilicate layer covers the entire sample and this results in increased oxidation resistance. At 1650 °C the outer glassy phase partially evaporates, exposing dendritic zirconia precipitated from the molten borosilicate glass. The thickness of the oxidized layer decreases with the increase of SiC content at all temperatures. The sample containing 20 vol. % SiC in the matrix is the least affected by oxidation and gets effectively passivated with no relevant changes to the microstructure and the weight loss.

4.8 References

1. Bray, D. & Ba, S. Ceramic Engineering and Science Proceedings. *Ceram. Eng. Sci. Proc.* **29,** 553–558 (1988).
2. Fahrenholtz, W. G., Hilmas, G. E., Talmy, I. G. & Zaykoski, J. A. Refractory diborides of zirconium and hafnium. *J. Am. Ceram. Soc.* **90,** 1347–1364 (2007).
3. Sciti, D., Natali Murri, A., Medri, V. & Zoli, L. Continuous C fibre composites with a porous ZrB_2 Matrix. *Mater. Des.* **85,** 127–134 (2015).
4. Silvestroni, L., Dalle Fabbriche, D., Melandri, C. & Sciti, D. Relationships between carbon fiber type and interfacial domain in ZrB_2-based ceramics. *J. Eur. Ceram. Soc.* **36,** 17–24 (2016).
5. Zhang, S. C., Hilmas, G. E. & Fahrenholtz, W. G. Mechanical properties of sintered ZrB_2-SiC ceramics. *J. Eur. Ceram. Soc.* **31,** 893–901 (2011).
6. Watts, J., Hilmas, G. & Fahrenholtz, W. G. Mechanical characterization of ZrB_2-SiC composites with varying SiC particle sizes. *J. Am. Ceram. Soc.* **94,** 4410–4418 (2011).
7. Monteverde, F., Guicciardi, S. & Bellosi, A. Advances in microstructure and mechanical properties of zirconium diboride based ceramics. *Mater. Sci. Eng. A* **346,** 310–319 (2003).
8. Neuman, E. W., Hilmas, G. E. & Fahrenholtz, W. G. Mechanical behavior of zirconium diboride-silicon carbide ceramics at elevated temperature in air. *J. Eur. Ceram. Soc.* **33,** 2889–2899 (2013).
9. Chamberlain, A. L., Fahrenholtz, W. G., Hilmas, G. E. & Ellerby, D. T. High-strength zirconium diboride-based ceramics. *J. Am. Ceram. Soc.* **87,** 1170–1172 (2004).
10. Lee, Y.-J. Formation of silicon carbide on carbon fibers by carbothermal reduction of silica. *Diam. Relat. Mater.* **13,** 383–388 (2004).
11. Lantz, B. *Machine Learning with R - Second Edition*. *Packt Publishing* (2015).
12. Breiman, L. Random Forests. *Mach. Learn.* **45,** 5–32 (2001).
13. Yu-Wei, C. (David C. *Machine Learning with R Cookbook*. (2015).
14. Evans, A. G. & Zok, F. W. The physics and mechanics of fibre-reinforced brittle matrix composites. *Journal of Materials Science* **29,** 3857–3896 (1994).
15. Yue, C., Liu, W., Zhang, L., Zhang, T. & Chen, Y. Fracture toughness and toughening mechanisms in a (ZrB2-SiC) composite reinforced with boron nitride nanotubes and boron nitride nanoplatelets. *Scr. Mater.* **68,** 579–582 (2013).

16. Asl, M. S., Kakroudi, M. G. & Noori, S. Hardness and toughness of hot pressed ZrB_2-SiC composites consolidated under relatively low pressure. *J. Alloys Compd.* **619,** 481–487 (2015).
17. Gui, K., Hu, P., Hong, W., Zhang, X. & Dong, S. Microstructure, mechanical properties and thermal shock resistance of ZrB_2 -SiC-C f composite with inhibited degradation of carbon fibers. *J. Alloys Compd.* **706,** 16–23 (2017).
18. Guo, W. M., You, Y., Zhang, G. J., Wu, S. H. & Lin, H. T. Improvement of fracture toughness of ZrB_2-SiC composites with carbon interfaces. *J. Eur. Ceram. Soc.* **35,** 1985–1989 (2015).
19. Zoli, L. *et al.* Rapid spark plasma sintering to produce dense UHTCs reinforced with undamaged carbon fibres. *Mater. Des.* **130,** 1–7 (2017).
20. Hong, W., Gui, K., Hu, P., Zhang, X. & Dong, S. Preparation and characterization of high-performance ZrB_2-SiC-Cf composites sintered at 1450 {\textdegree}C. *J. Adv. Ceram.* **6,** 110–119 (2017).
21. Lamon, J. Interfaces and interfacial mechanics: influence on the mechanical behavior of ceramic matrix composites (CMC). *J. Phys.* **3,** 1607–1616 (1993).
22. Evans, A. G. & Marshall, D. B. Overview no. 85 The mechanical behavior of ceramic matrix composites. *Acta Metall.* **37,** 2567–2583 (1989).
23. Jessen, T. L., Bender, B. A. & Greenhut, V. A. Effect of bridged boron nitride coatings on the flexure behavior of a unidirectional ceramic-fiber ceramic-matrix composite. *J. Am. Ceram. Soc.* **83,** 3231–3233 (2000).
24. Xu, B., Zhou, S., Hong, C., Zhang, X. & Han, J. Fabrication and properties of lightweight ZrB_2 and SiC-modified carbon bonded carbon fiber composites via polymeric precursor infiltration and pyrolysis. *RSC Adv.* **4,** 47106–47113 (2014).
25. Tang, S., Deng, J., Wang, S. & Liu, W. Fabrication and characterization of an ultra-high-temperature carbon fiber-reinforced ZrB_2-SiC matrix composite. *J. Am. Ceram. Soc.* **90,** 3320–3322 (2007).
26. Tripp, W. C. & Graham, H. C. Thermogravimetric study of the oxidation of ZrB2 in the temperature range of 800C to 1500C. *J. Electrochem. Soc. J. Electrochem. Soc.* **118 No.7,** 1195–1199 (1971).
27. Zhang, L. & Kurokawa, K. Effect of SiC Addition on Oxidation Behavior of ZrB2 at 1273 K and 1473 K. *Oxid. Met.* **85,** 311–320 (2016).
28. Kazemzadeh Dehdashti, M., Fahrenholtz, W. G. & Hilmas, G. E. Effects of transition metals on the oxidation behavior of ZrB_2 ceramics. *Corros. Sci.* **91,**

224–231 (2015).

29. Silvestroni, L. & Sciti, D. Densification of ZrB_2-$TaSi_2$ and HfB_2-$TaSi_2$ Ultra-High-Temperature Ceramic Composites. *J. Am. Ceram. Soc.* **94,** 1920–1930 (2011).
30. Halbig, M. C. & Eckel, A. J. Oxidation of Continuous Carbon Fibers Within a Silicon Carbide Matrix Under Stressed and Unstressed Conditions. *Nasa* **TM-2000-21,** (2000).
31. Rezaie, A., Fahrenholtz, W. G. & Hilmas, G. E. The effect of a graphite addition on oxidation of ZrB 2-SiC in air at 1500??C. *J. Eur. Ceram. Soc.* **33,** 413–421 (2013).
32. Yang, F., Zhang, X., Han, J. & Du, S. Characterization of hot-pressed short carbon fiber reinforced ZrB_2-SiC ultra-high temperature ceramic composites. *J. Alloys Compd.* **472,** 395–399 (2009).
33. Nickel, K. G. Ceramic matrix composite corrosion models. *J. Eur. Ceram. Soc.* **25,** 1699–1704 (2005).
34. Roh, J. Oxidation Kinetics of Carbon Fibers. *Carbon Sci.* **6,** 1–5 (2005).
35. Gao, D. *et al.* Oxidation of zirconium diboride-silicon carbide ceramics under an oxygen partial pressure of 200Pa: Formation of zircon. *Corros. Sci.* **52,** 3297–3303 (2010).
36. Vinci, A., Zoli, L., Landi, E. & Sciti, D. Oxidation behaviour of a continuous carbon fibre reinforced ZrB2–SiC composite. *Corros. Sci.* **123,** 129–138 (2017).
37. Karlsdottir, S. N. & Halloran, J. W. Oxidation of ZrB_2-SiC: Influence of SiC content on solid and liquid oxide phase formation. *J. Am. Ceram. Soc.* **92,** 481–486 (2009).
38. Fahrenholtz, W. G. Thermodynamic analysis of ZrB_2-SiC oxidation: Formation of a SiC-depleted region. *J. Am. Ceram. Soc.* **90,** 143–148 (2007).
39. Karlsdottir, S. N. & Halloran, J. W. Formation of Oxide Films on ZrB2–15 vol% SiC Composites During Oxidation: Evolution with Time and Temperature. *J. Am. Ceram. Soc.* **92,** 1328–1332 (2009).
40. Vinci, A., Zoli, L., Landi, E. & Sciti, D. Oxidation behaviour of a continuous carbon fibre reinforced ZrB_2–SiC composite. *Corros. Sci.* **123,** (2017).

41. Glass, D. Ceramic Matrix Composite (CMC) Thermal Protection Systems (TPS) and Hot Structures for Hypersonic Vehicles. *15th AIAA Int. Sp. Planes Hypersonic Syst. Technol. Conf.* 1–36 (2008). doi:10.2514/6.2008-2682

5. ZrB_2/SiC/WC based UHTCMCs

5.1 Introduction

A strongly recommended functionality for materials to be used in extreme environments is self-healing capability. For bulk ceramics, self-healing is defined as the ability to partially or completely seal cracks through a thermal treatment (also called crack-healing). The addition of WC was reported to impart a self-healing capability to UHTCs thanks to sintering of the oxidation products (ZrO_2, B-O glasses) developed during high temperature exposure [1]. Similarly, it was reported that the addition of W into B_2O_3 increases the stability of the protective liquid/glassy layer resulting in higher oxidation resistance for $(Zr,W)B_2$ compared to nominally pure ZrB_2 [2]. Binner et al also reported the increased oxidation resistance of ZrB_2/SiC ceramics with the introduction of WC in environments with low partial pressure of oxygen due to the promotion of passive oxidation of SiC to SiO_2 [3]. In this work the influence of WC addition on the mechanical properties and oxidation resistance of carbon fibre reinforced ZrB_2 – SiC composites was investigated.

Three carbon fibre reinforced composites containing 90 vol% ZrB_2, 5 vol% SiC and 5 vol% WC, labelled ZSW18, ZS19 and ZS20, were hot pressed respectively at 1800, 1900 and 2000°C to find the best sintering conditions. Then mechanical and oxidation tests were carried out and compared with a baseline un-doped composite.

5.2 ZSW

4.2.1 Sintering behaviour

Different sintering temperatures were investigated to find the best hot pressing conditions. The hot pressing curves of ZSW at 1800, 1900 and 2000°C are shown in figure 5.1. An initial pressure of 20 MPa was applied at 900°C. Then the pressure was gradually increased to 30 MPa at 1700°C and 40 MPa to 1900°C. (fig. 5.1). The displacement of the hot pressing machine, which is related to the displacement of the sample, is monitored during the hot pressing cycle. At 1700°C a jump is observed due to the increase of pressure to 30 MPa and only at the target temperature a pressure of 40 is applied. Increasing the hot pressing temperature to 2000°C leads to a considerable degree of densification, while at 1800°C sintering is severely hindered.

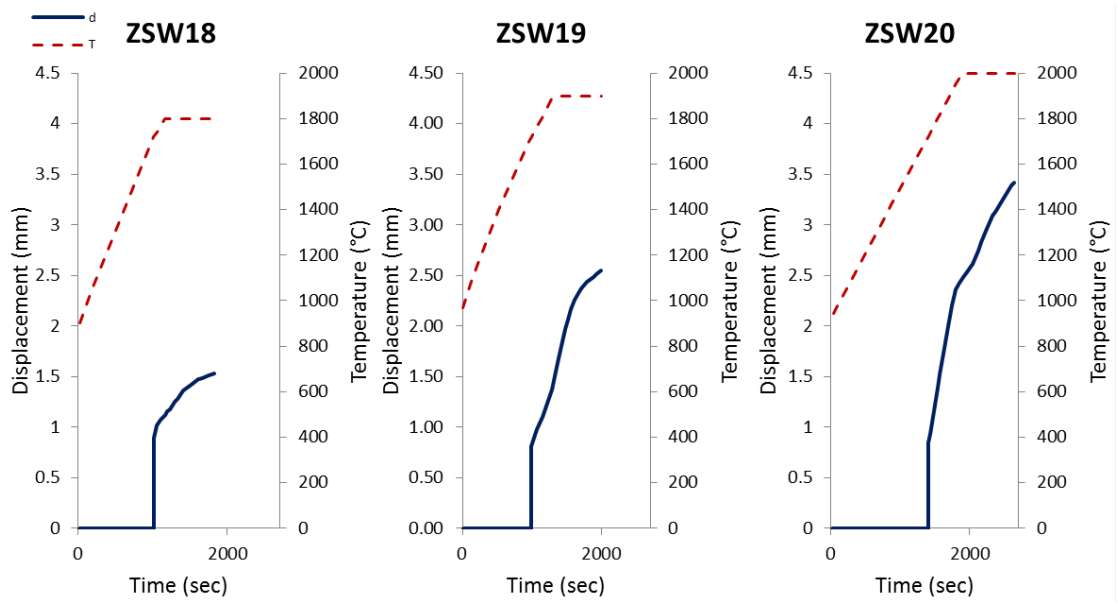

Figure 5.1 Load vs displacement curves of samples ZS18, ZS19 and ZS20. The blue line represents the displacement of the hot pressing element while the temperature ramp is in red. Pressure was applied in steps: 20 MPa at 900°C, 30 MPa at 1700°C and 40 MPa at 1800, 1900 and 2000°C respectively.

5.2.2 Microstructure

Table 1 summarizes hot pressing parameters and the respective physical properties of the sintered pellets.

Table 5.1 Compositions, sintering cycles, fibre contents, grain size and mechanical properties of WC-doped ZrB_2/SiC composites compared with a WC-free composite (ZS5)

Sample	Hot Pressing Temp. (°C)	Fibre (vol%)	Density (g/cm^3)	Porosity (vol%)	ZrB_2 grain size (μm)	σ (MPa)	K_{IC} ($MPa \cdot m^{0.5}$)
ZS5	1900	40	3.65	12.9	3.00	198 ± 12	4.7 ± 0.3
ZSW18	1800	39	3.70	20.6	1.26	91 + 12	4.6 + 0.3
ZSW19	1900	37	4.51	8.1	1.66	160 + 25	4.0 + 0.4
ZSW20	2000	36	4.87	< 1	2.68	96 + 11	-

Density and porosity are largely affected by the sintering temperature. A residual porosity of 20% is observed after densification at 1800°C, decreasing to 8% when raising the temperature to 1900°C. At 2000°C full density is reached. Microstructural features of the matrix (in Fig. 5.2) are consistent with the density data. Residual pores and a non-perfect cohesion between fibre and matrix is observed in the case of ZSW18. Scattered pockets of bright contrasting particles belonging to WC are observed in the matrix, while the dark and light grey phases belong to SiC and ZrB_2 respectively. On

the contrary, for the sample densified at 2000°C, grain growth, coalescence and fibre degradation due to excessive reactivity with the ceramic matrix is observed. Sintering carried out at 1900°C resulted in the most homogeneous microstructure. Solid solutions with W-rich ZrB_2 shells grown onto ZrB_2 cores are well recognizable in the polished surface. This is a very well-known phenomenon due to W diffusion inside the ZrB_2 lattice [4]. Parallel formation of WB phases is also observed (Fig. 5.2).

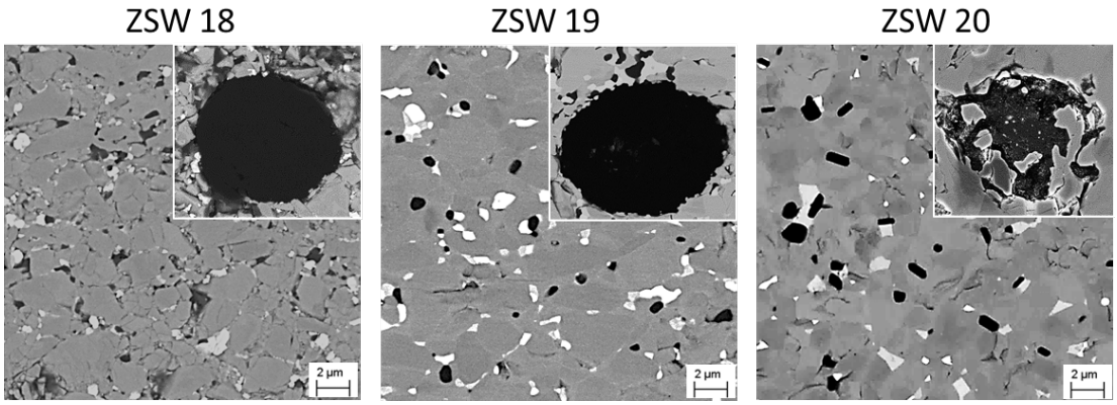

Figure 5.2 Microstructural features of samples ZSW18, ZSW19 and ZSW20. White, grey and dark grey phases represent WC, ZrB2 and SiC particles respectively. The insert shows the cross section of the fibre (black)

Comparing sample ZSW 19 with a reference material without WC, labelled ZS5, sintered at the same temperature and shown in the previous chapter (ZS5a) it is possible to see that the addition of WC improves the densification by lowering porosity (8.1% for ZSW19 and 12.9% for ZS5) and further impairs the grain growth of ZrB_2. The microstructure is also different and the sample containing WC is characterized by a larger amount of high aspect ratio ZrB_2 grains, whereas sample ZS5 has a more homogeneous microstructure.

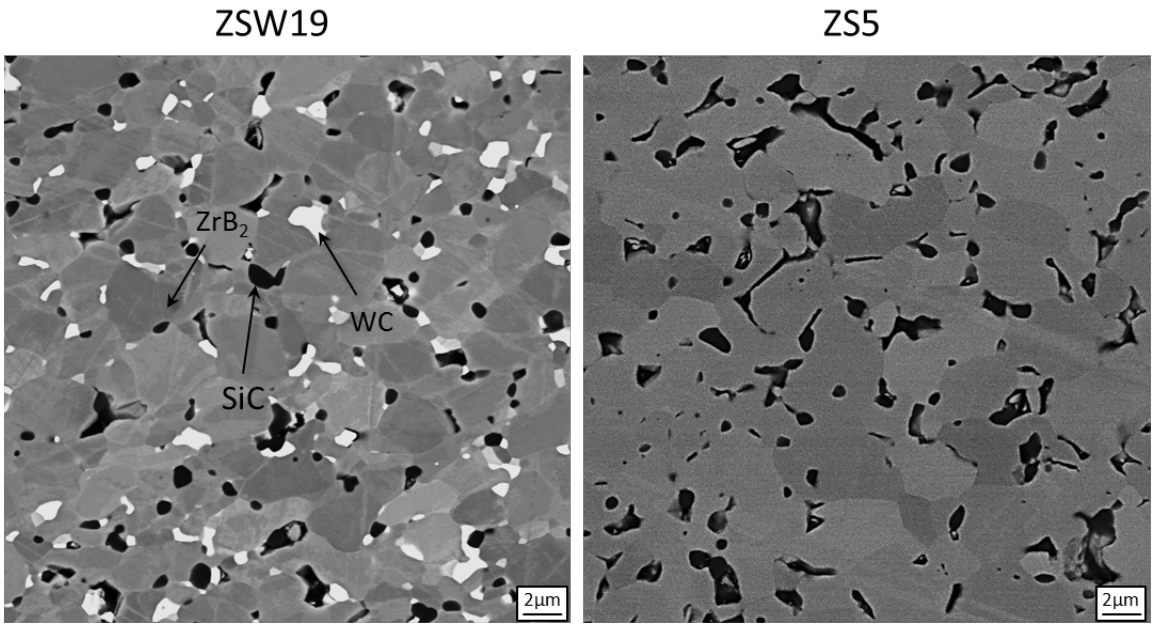

Figure 5.3 Microstructure of ZSW19 and ZS5. Light and dark grey phases are ZrB_2 and SiC respectively, while white phases are WC.

5.2.3 Mechanical properties

Values of bending strength are negatively affected either by porosities larger than 10% for sintering at 1800°C (91 MPa) or by fibre degradation for sintering at 2000°C (96 MPa). A strength of 160 MPa was obtained for the composite sintered at 1900°C which is slightly lower than the strength of the WC-free composite of ~190 MPa. Looking at the load/displacement curves (fig. 5.4), it is evident that a sintering temperature of 2000°C leads to excessive reaction between the fibre and the matrix, ultimately promoting brittle failure. On the other hand, a sintering temperature below 1900°C leads to a weaker fibre/matrix interface and composite behaviour.

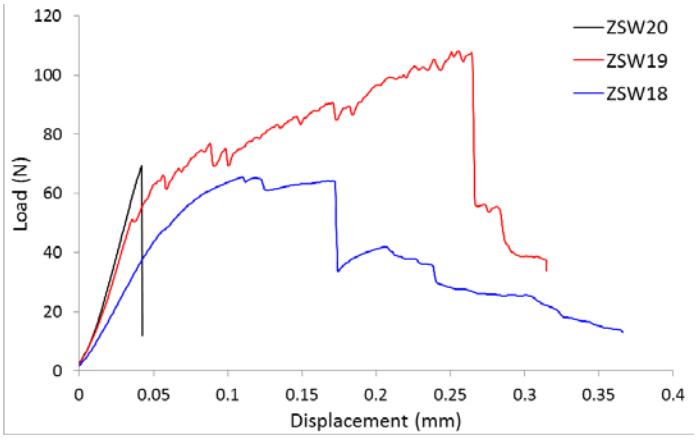

Figure 5.4 Load vs displacement curves for samples ZSW18, ZSW19 and ZS20 tested by 4-point bending strength at room temperature.

As far as fracture toughness is concerned, the highest value was found for ZSW18 (4.6 MPa·$m^{0.5}$) due to weaker fibre/matrix interface which allowed extensive pull-out than ZSW19 and ZSW20 (fig. 5.5). The latter was difficult to machine because it was very brittle, therefore K_{IC} values for this specimen are not available. Even in the case of fracture toughness, the addition of WC does not seem to bring significant improvements over the un-doped ZrB_2/SiC composite characterized in previous works. Possible causes are the strong fibre/matrix interface compared to ZS5a allowing a limited fibre pull-out, and the high modulus of the ceramic matrix that does not favour an efficient load transfer. The highest value is indeed found for the sample with the lowest density (ZSW18), due to higher residual porosity and poor matrix/fibre adhesion.

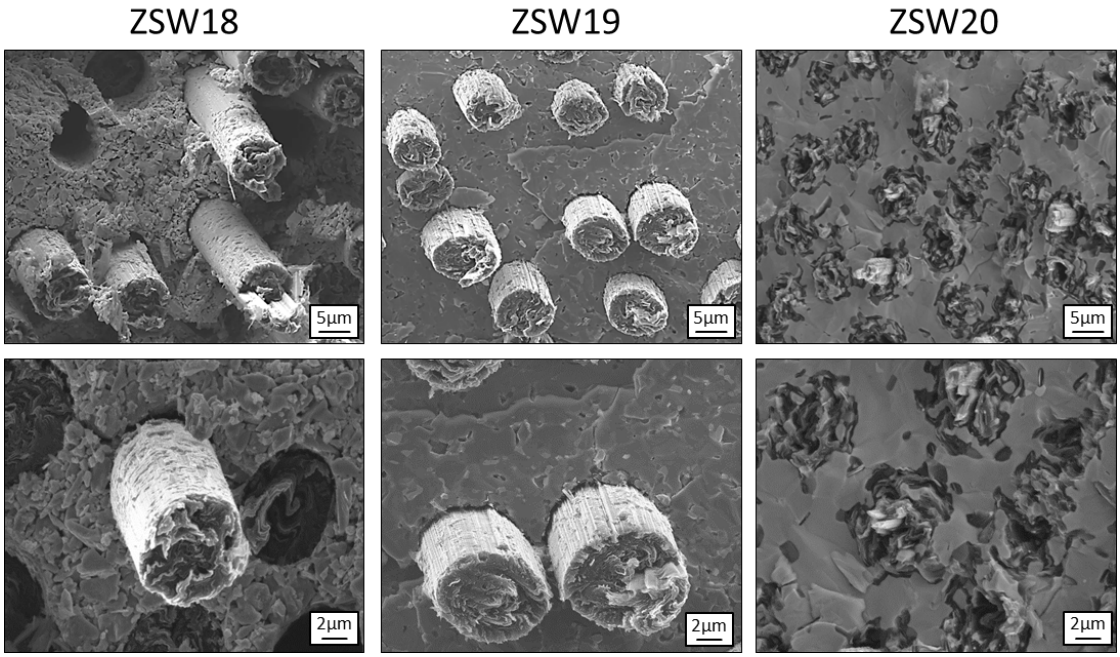

Figure 5.5 Cross section of the fractured samples showing progressively lower fibre pull-out extent with the increase of sintering temperature and fibre/matrix strengthening.

Comparison with the literature data is more difficult due to different specimen dimensions and different testing conditions: H. Hu [5] in reported a flexural strength of 163 MPa for a C/SiC material enriched with about 25% of ZrB_2, Q. Li [6] reported a bending stress of 248 MPa for a 3D-C/SiC enriched with 23% of ZrB_2-ZrC phases, L. Li [7] found a value of 255 MPa for 2D-C/SiC enriched with a ZrB_2 -TaC mixture. From what was observed so far, it can be concluded that the addition of WC is not the best possible option at this stage of the research. The main reason is WC favours a marked reactivity at the matrix/fibre interface, favouring a strong adhesion. On the other hand it contributes to increase the matrix density and its rigidity).

5.2.4 Oxidation resistance

Oxidation tests at 1650°C in air were carried out on sample ZSW19 and compared with the WC-free sample, ZS5, previously described in 4.3.5. SEM analysis was carried out on the surface and cross section of the oxidized samples (fig 5.6).

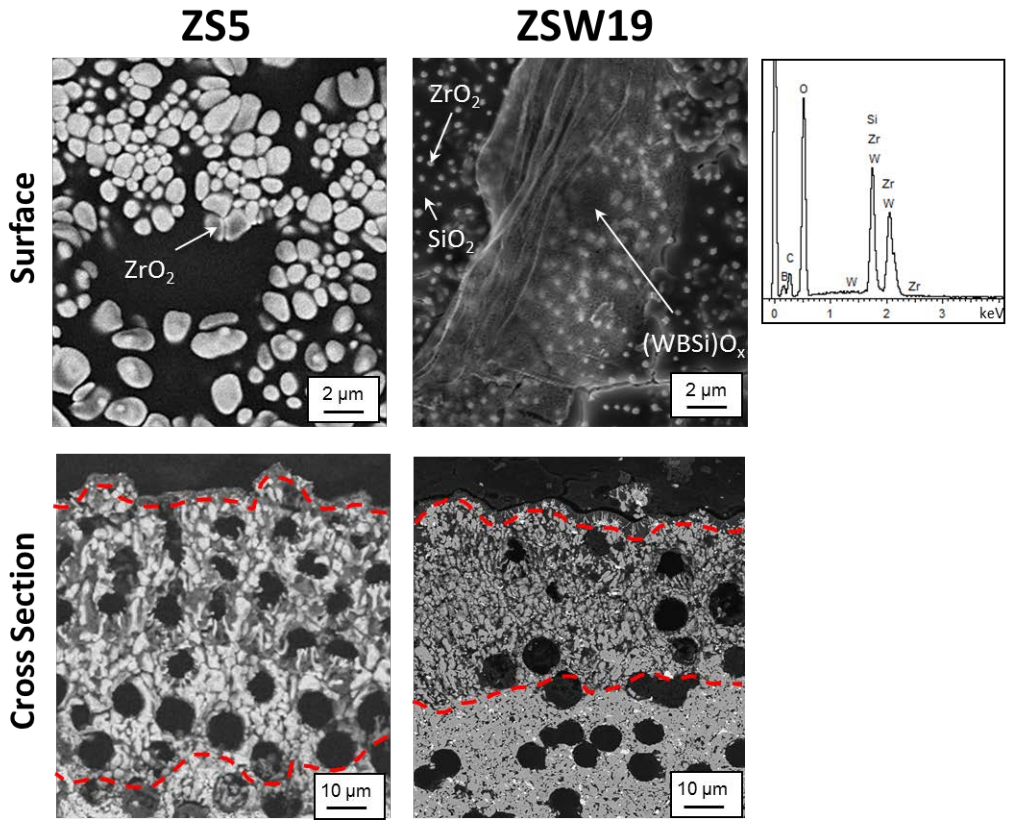

Figure 5.6 Surface and cross section micrographs of ZS5 and ZSW19 oxidized at 1650°C in air. The white areas are constituted mainly by monoclinic ZrO_2, while the dark grey zones consist mainly of amorphous borosilicate glass.

The sample doped with WC retains a higher amount of silica glass on the surface compared to the un-doped specimen. Zirconia grains on the surface are much smaller and it is even possible to see the formation of platelets containing mixed B_2O_3-SiO_2-WO_3 oxides. B_2O_3 platelets were visible only at 1500°C for the samples investigated in 4.3.5. In the case of ZSW19, the presence of tungsten oxides leads to an increase of the viscosity of the boro-silicate glass which is retained even at 1650°C [8].

On closer inspection of the oxide scale (fig. 5.7), four distinct layers can be observed: 1) an outer silica layer, 2) an intermediate ZrO_2-SiO_2-WO_3 scale, with needle-like WO_3 crystals growing together with equiaxed ZrO_2 grains 3) SiC/WC depleted layer with columnar ZrO_2 grains 4) unreacted matrix bulk. The oxide layer of ZSW19

(42 μm) is thinner than ZS5 (85 μm) and more compact, in accordance with previous studies on ZrB_2/SiC/WC ceramics [9]. The presence of the tungsten has been shown to promote the densification of zirconia scales on the top of ZrB_2 via the formation of a ZrO_2-WO_3 liquid phase during oxidation which might alter the shape and further accelerate the coarsening of ZrO_2 grains [3,10].

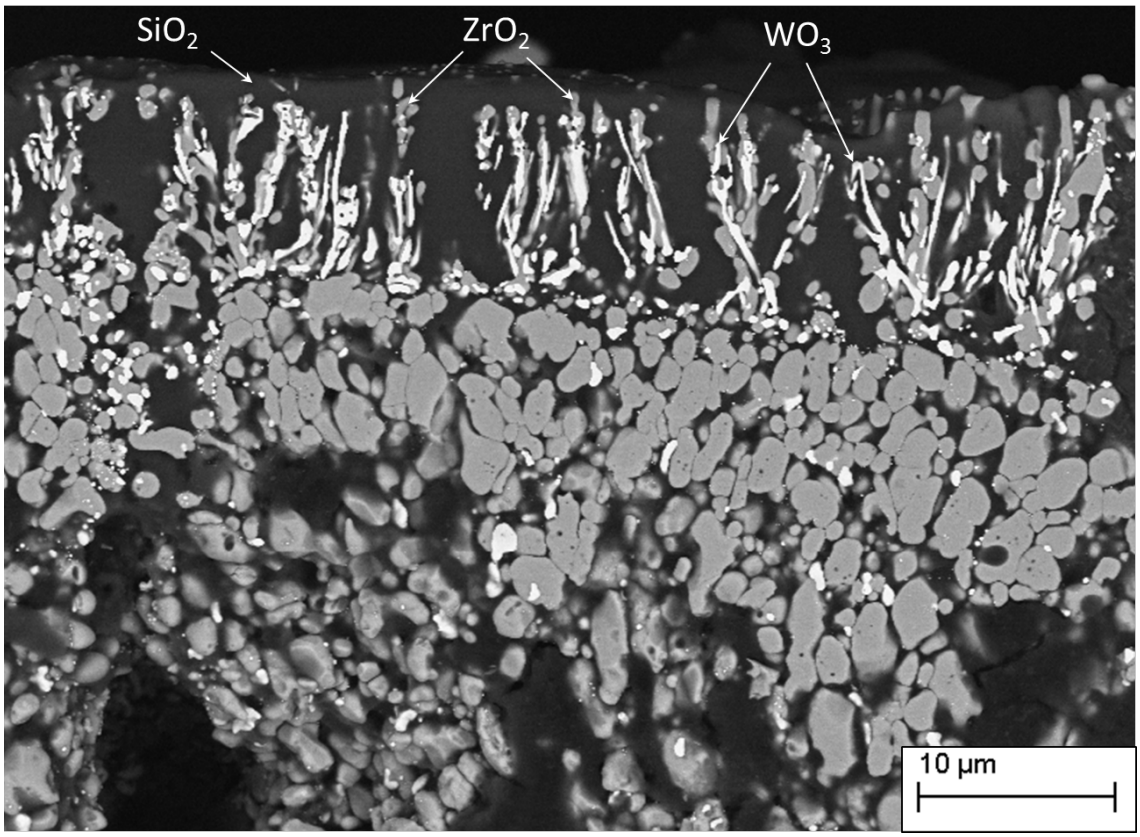

Figure 5.7 Detail of the oxide scale of sample ZSW19 oxidized at 1650°C in air. The white phases represent WO_3, while the dark and light grey phases are SiO_2 and ZrO_2.

5.3 Conclusions

The sintering, mechanical properties and oxidation behaviour of carbon fibre reinforced ZrB_2/SiC/WC composites were investigated and compared with an un-doped reference sample.

A sintering temperature of 1900°C has been found to be optimal for the sintering for ZrB_2/SiC/WC composites because it allows to reach relative densities >92% while minimizing the reaction at the fibre/matrix interface.

ZSW19 is characterized by higher strength than ZSW18 due to a stronger fibre/matrix interface that allows a better load transfer to the fibres, while the latter shows higher toughness due to a weaker fibre/matrix interface that allows for extensive fibre pull-out. ZSW20 is characterized by overall low mechanical properties and brittle

behaviour due to excessive degradation of the fibres. The mechanical properties are comparable with those of the un-doped specimen, with no significant changes induced by the introduction of WC.

As far as oxidation resistance is concerned, the presence of WC leads to the formation of a significantly more compact oxide layer that prevents further oxygen diffusion in the composite, showing the capability to heal the cracks and pores left by the oxidation of ZrB_2.

5.4 References

1. Westwood, M. E., Webster, J. D., Day, R. J., Hayes, F. H. & Taylor, R. Review Oxidation protection for carbon fibre composites. *J. Mater. Sci.* **31,** 1389–1397 (1996).
2. Dehdashti, M. K. Improving the oxidation resistance of diboride- based ceramics. *ProQuest Diss. Theses Glob.* 4–10 (2014).
3. Zou, J., Rubio, V. & Binner, J. Thermoablative resistance of ZrB_2-SiC-WC ceramics at 2400 °C. *Acta Mater.* **133,** 293–302 (2017).
4. Monteverde, F. & Silvestroni, L. Combined effects of WC and SiC on densification and thermo-mechanical stability of ZrB_2 ceramics. *Mater. Des.* **109,** 396–407 (2016).
5. Hu, H. *et al.* Preparation and characterization of C/SiC–ZrB_2 composites by precursor infiltration and pyrolysis process. *Ceram. Int.* **36,** 1011–1016 (2010).
6. Li, Q., Dong, S., Wang, Z. & Shi, G. Fabrication and properties of 3-D Cf/ZrB_2-ZrC-SiC composites via polymer infiltration and pyrolysis. *Ceram. Int.* **39,** 5937–5941 (2013).
7. Li, L., Wang, Y., Cheng, L. & Zhang, L. Preparation and properties of 2D C/SiC-ZrB_2-TaC composites. *Ceram. Int.* **37,** 891–896 (2011).
8. Zhang, S. C., Hilmas, G. E. & Fahrenholtz, W. G. Oxidation of zirconium diboride with tungsten carbide additions. *J. Am. Ceram. Soc.* (2011). doi:10.1111/j.1551-2916.2010.04216.x
9. Paul, A. *et al.* UHTC-carbon fibre composites: Preparation, oxyacetylene torch testing and characterisation. *J. Eur. Ceram. Soc.* **33,** 423–432 (2013).
10. Zhang, S. C., Hilmas, G. E. & Fahrenholtz, W. G. Oxidation of zirconium diboride with tungsten carbide additions. *J. Am. Ceram. Soc.* **94,** 1198–1205 (2011).

6. ZrC/SiC based UHTCMCs

6.1 Introduction

Reusable components for hypersonic flight, next generation rocket engines, and thermal protection systems require materials able to withstand extreme environments. For example, the requirements of rocket combustion chambers, nozzles and thrusters, include high strength at temperatures above 2000°C, oxidation and wear resistance, and the ability to withstand high heat fluxes and thermal shock. the carbides are being investigated as potential candidates for the fabrication of rocket nozzle inserts or the leading edges of hypersonic aircraft owing to their high ablation resistance and hardness [12]. However, their low fracture toughness and poor thermal shock resistance pose major obstacles to their implementation [3]. As a result, fibre reinforcement has been examined to improve the damage tolerance of these materials.

Among carbides, ZrC has been investigated because of its relatively low density and hardness. Leipold *et al.* studied the high temperature mechanical properties of ZrC and found that the material experienced a severe drop in strength at high temperature but also noted that impurities such as N, O and free carbon played a significant role on the high temperature properties [4]. Fibre reinforcement has been considered to increase the structural reliability of ZrC. Zhu and Chen obtained fibre reinforced ZrC by reactive melt infiltration of a C/C preform with molten Zr_2Cu, by forming in-situ ZrC [5–7]. However the presence of unreacted melt severely impairs high temperature properties due to the low melting point of the Zr_2Cu melt (1000°C) [8]. Other authors have attempted the fabrication of fibre reinforced ZrC composites via reactive routes such as the pyrolysis of a ZrC precursor and reported strengths up to 213 MPa at 1700°C . However no studies have been carried out at temperatures above 2000°C.

The aim of the present work is to investigate the microstructure and mechanical behaviour of carbon fiber reinforced ZrC/SiC composites up to 2100°C.

6.2 ZC20 0/0

Powder mixtures containing ZrC + 20 vol% SiC (designated ZC20) were prepared by wet ball milling of the commercial powders and then dried with a rotary evaporator. The composites were fabricated through slurry infiltration of unidirectional carbon fibre preforms and hand lay-up in a unidirectional (0/0°) configuration. Hot pressing was carried out at 1900°C, using a pressure of 40 MPa and a holding time of 15 min, on the

basis of previous studies [9]. Thermodynamic simulations were performed using computer-based minimization of Gibbs' free energy (FactSage 7.1). Inputs assumed that the constituents (ZrC, SiC, and graphite) were present as pure condensed solids and that the atmosphere was gaseous argon containing ~1 ppm oxygen as an impurity. The total pressure was fixed at 1 atm and the temperature was set at 2100°C. The predominant gas species predicted by the first simulation were then used as input for a second simulation. The species were equilibrated at 25°C to evaluate the solid products that would deposit from the volatilized species when the furnace was cooled.

6.2.1 Sintering behaviour

The hot pressing curve of ZC20 is reported in fig. 6.1. A pressure of 40 MPa was applied only when a temperature of 900°C was reached. The displacement of the hot pressing machine, which is related to the displacement of the sample, is monitored during the hot pressing cycle. The first part of the curve is relative to mechanical displacement; at 900°C the diffusional processes are still very slow and the displacement observed is purely mechanical. After the initial constant displacement, the curve is reset. At 1800°C diffusional processes become significant and further displacement is observed.

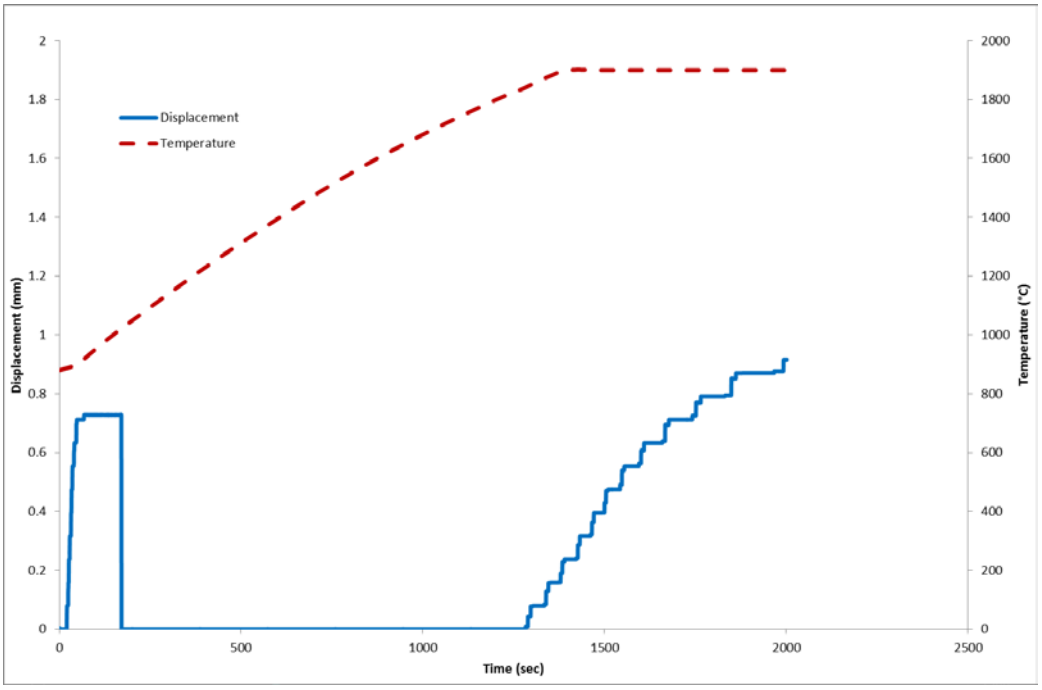

Figure 6.1 Displacement vs time curve relative to the hot pressing cycle carried out on sample ZC20 at 1900°C.

6.2.2 Microstructure

The composite with the ZrC matrix had a porosity of 16.8%. This was attributed to the presence of oxide species, namely ZrO_2, that were present in the starting ZrC powders and that hindered densification of the ZrC matrix [10]. The grain size of the predominant carbide phase is in the range of 1.3 to 1.5 μm, while SiC did not show any sign of coarsening, retaining a mean grain size of ~0.50 μm. The relatively small grain size of the carbides was attributed to the presence of SiC that inhibited grain growth. In addition, the problem related to the potential presence of SiO_2 is overcome thanks to the abundance of carbon from the carbon of fibres that can react to provide additional SiC according to reaction 1 [11]:

$$SiO_2 + C \rightarrow SiC + CO_{2(g)} \quad (1)$$

Table 6.1 Values of bulk density, porosity, fibre content, and grain size of the carbide phase (ZrC) and the additive (SiC).

Sample	Density (g/cm3)	Fibre (vol%)	Porosity (vol%)	Grain size (μm)	
				ZrC/TaC	SiC
ZC20	3.52	46.7	16.8	1.35	0.48

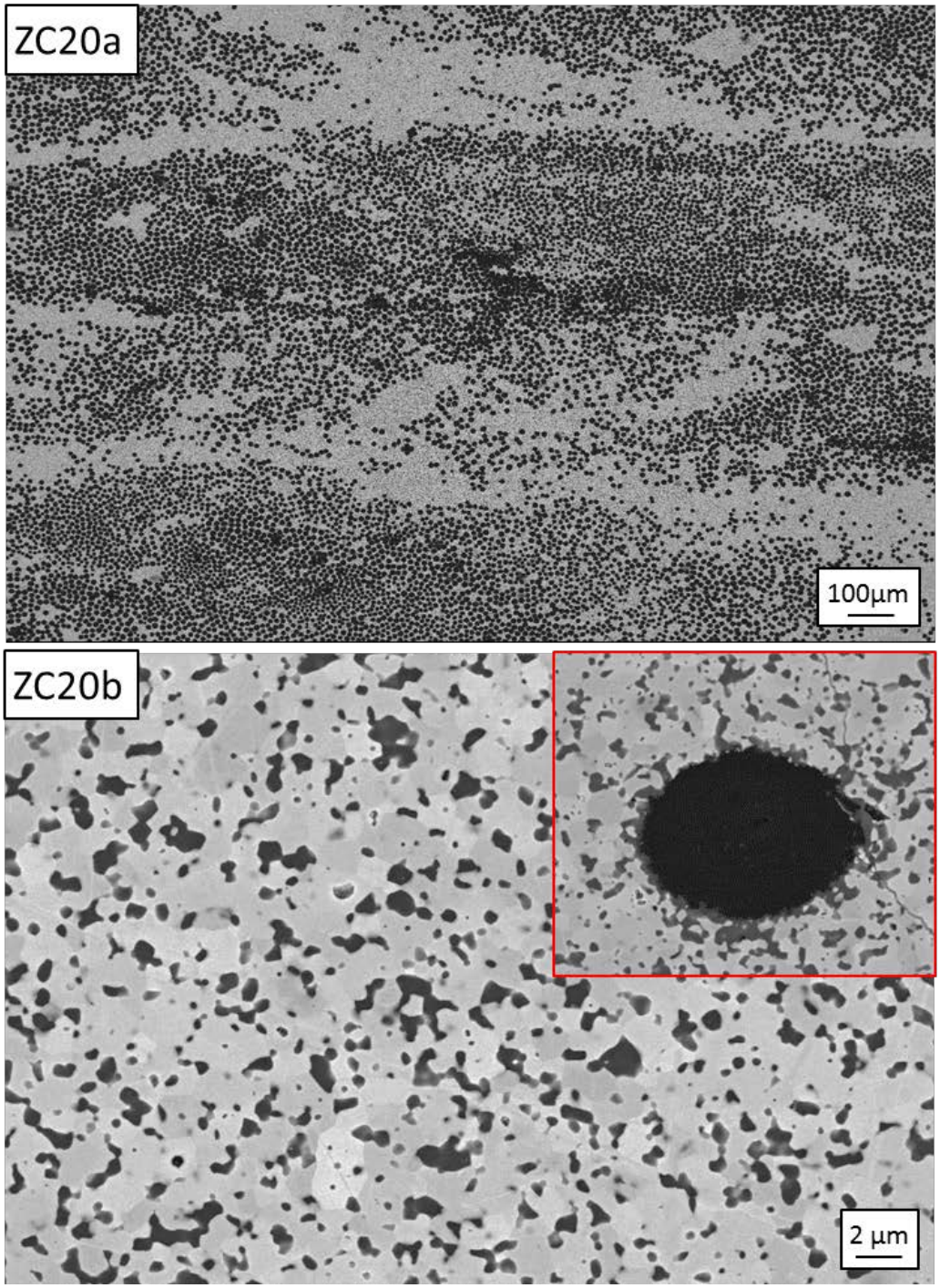

Figure 6.2 Images of cross sections of the sintered specimen, ZC20. The light grey phase represents ZrC, the dark grey phase is SiC, while the black dots are carbon fibres.

In the high magnification micrographs of the matrix and fibre microstructure of sample ZC20 (Fig. 6.2 ZC20b), the light grey phase is the predominant carbide matrix (ZrC) while the dark grey phase is SiC. SiC was homogeneously dispersed as small round particles in the ZrC matrix. From the fibre regions, no evidence was found to indicate any chemical reaction between the fibre and the matrix as the fibres retained

their original round shape. Degradation of mechanical properties is still possible considering stresses induced by the mismatch between the coefficients of thermal expansion (CTE), but assessment of fibre damage is out of the scope of this study.

Common defects of these composites included non-infiltrated areas and cracks in the matrix-rich regions originating from the constrained shrinkage of the ceramic matrix during sintering and the mismatch between the CTE of the matrix ($6.74 \cdot 10^{-6}$ K^{-1}) and fibres ($2 \cdot 10^{-6}$ K^{-1} [12]). In the present work it was possible to obtain a discrete distribution of fibres in the matrix (figure 1), even though some aggregated fibres were observed. This was usually associated with the difficult infiltration of the fibre preform with highly viscous powder suspensions that do not readily allow the penetration of the powders inside the fibre bundles (Fig. 6.2, ZC20a).

6.2.3 High temperature strength

The values of strength at room temperature was 263 MPa. This values is lower than the corresponding strength of bulk ceramics of similar composition produced in other studies, which were ~400 MPa for ZrC with 20 vol% SiC [13,14] The lower strength of the composite could be due to internal defects related to the presence of the carbon fibres in the ceramic matrix or microcracks generated during cooling from the densification temperature due to the CTE mismatch between the fibres and the matrix. In addition, the slope of the room temperature load/displacement curves (fig 6.3, black lines) decreases as load increases. This effect was attributed to the weak fibre/matrix interface and the premature failure of the matrix in that composition. As the initial load is applied, stresses are mainly concentrated in the ceramic matrix. As the load increases, cracks start to open in the ceramic matrix and the load is transferred to the fibres.

The strengths were significantly higher at 1500°C (450 MPa). The specimens tested at R.T. and 1500°C remained in one piece after testing thanks to the entangled fibres holding the two halves of the test specimens together [15]. Previous studies carried out on bulk UHTCs, such as ZrB_2, generally showed a decrease in the Young modulus but an increase in strength [16]. The increase in strength observed in the present study was attributed to the release of residual stresses accumulated during hot pressing.

At 1800°C, the strength was still above the room temperature value (408 MPa), but lower than at 1500°C. Values of stiffness and Young modulus were not calculated for these materials, but the slopes of the load/displacement curve decreased noticeably

at 1800°C, which indicated that the stiffness and Youngs' modulus were lower. Even with the lower values, no signs of plastic deformation were observed.

At 2100°C, plastic deformation was evident. Due to inaccuracy in measuring the true strain using the load-displacement curves generated by the four-point bending setup, the true strength of the material is only reliable up to the proportional limits in the curves. This was calculated using the maximum load which was determined from the best fit of the linear portion of the load/displacement curves, which had R^2 values between 0.9971 and 0.9977. Using this method, ZC20 retained an overall higher ultimate apparent strength (368 MPa) but the specimen yielded at a lower load. ZC20 experienced significant plastic deformation before rupture and yielded at ~210 MPa.

Table 6.2: Flexural strength values at RT, 1500, 1800 and 2100°C for ZC20. For specimens tested at 2100°C, the strength calculated using the proportional limit is reported. The ultimate strength at rupture is shown in parentheses.

Sample	σ_{RT} (MPa)	$\sigma_{1500°C}$ (MPa)	$\sigma_{1800°C}$ (MPa)	$\sigma_{2100°C}$ (MPa)
ZC20	263 ± 50	450 ± 52	408 ± 51	211 ± 16 (368)

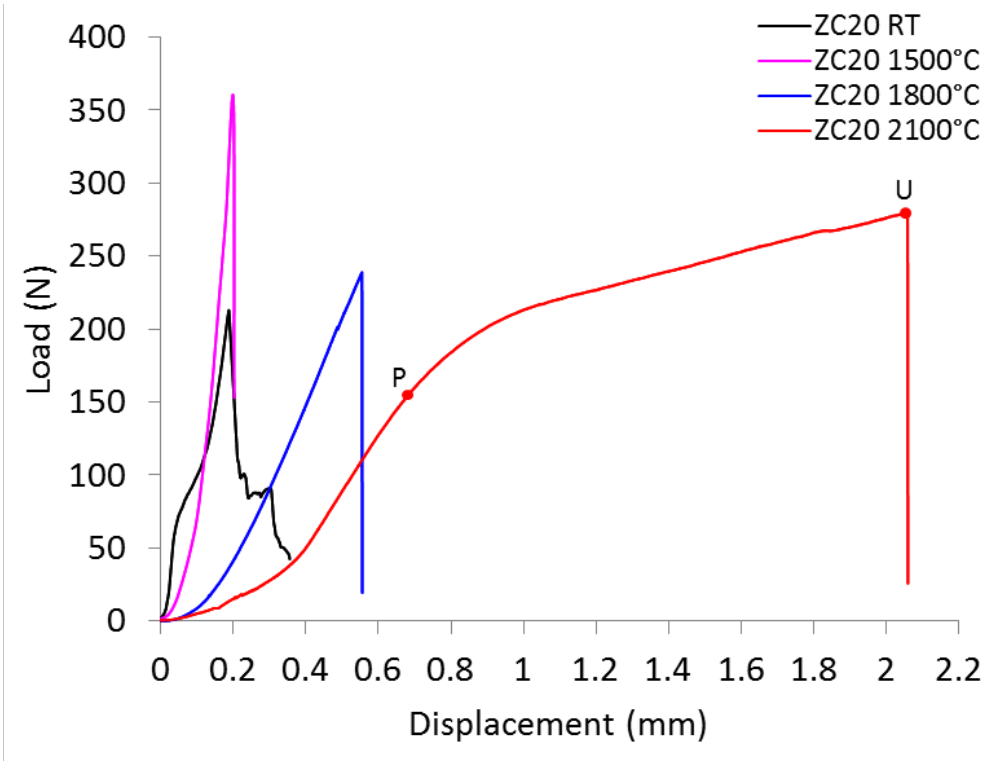

Figure 6.3 Load-displacement curves at RT, 1500, 1800 and 2100°C for sample ZC20. The mechanical behaviour is consistent in all specimens tested, therefore only one curve per temperature was shown. For the test at 2100°C, the strength at the proportional limit (P) and the ultimate strength (U) are shown.

6.2.4 Microstructure of the material after testing

After testing at 2100°C, ZC20 had several cracks both perpendicular and parallel to fibre orientation. The former are believed to originate from the relatively high strain experienced by the sample which resulted in cracking of the ceramic matrix and sliding of the fibres, while the latter likely originated from the evolution of volatile species during testing. The surface morphology evolution is shown in figure 6.4. At 1500°C the surface is characterized by coalesced nano-sized grains and inter-connected porosity. Despite the observation of what appears to be vapour-deposited material by SEM, only zirconium and carbon were detected by EDX analysis. Below the surface, no grain growth or deformation were observed after testing. Fibres maintained their original shape despite the harsh conditions of the tests and no reaction at the interface was detected. Therefore, the observed plastic deformation was attributed to grain boundary sliding rather than a diffusional process [17].

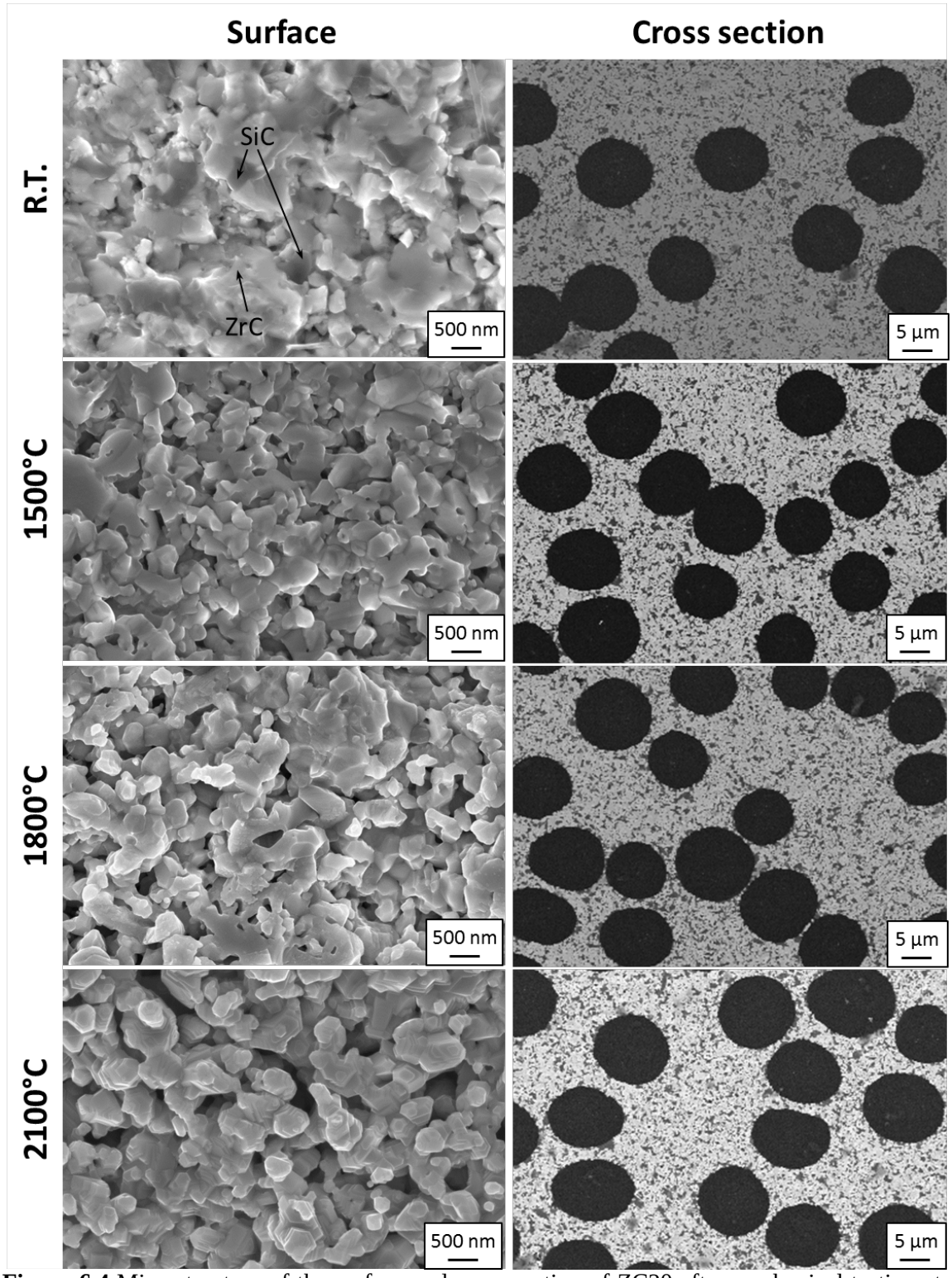

Figure 6.4 Microstructure of the surface and cross section of ZC20 after mechanical testing at R.T., 1500, 1800 and 2100°C.

X-Ray diffraction analysis was carried out before and after testing at 1500, 1800 and 2100°C in an attempt to identify the species that formed on the surface of the ZC20 (Fig. 6.5). At room temperature, the observed peaks were indexed to cubic ZrC

(PDF#35-0784) and 6h-SiC (PDF#29-1131) from the matrix and graphite (PDF#41-1487) from the carbon fibres. At 1500°C SiC is still present and peaks relative to the formation of oxides, namely ZrO_2 (PDF#86-1451) and SiO_2 (PDF#42-0005), were detected, while the predominant phase remained ZrC (PDF#35-0784). The presence of oxides was attributed to the testing conditions in the test furnace which was not air tight, therefore a small amount of oxygen was present. Additional signals relative to carbon fibres were identified and indexed to the formation of different carbon species (PDF#75-1621 and PDF#75-0444). After testing at 1800°C, only peaks relative ZrC and carbon were detected, which indicated that the majority of SiC was removed from the region near the surface during mechanical testing. No oxide species were revealed, which could be due to the partial evaporation of the thin layer that was homogeneously formed across the surface of the sample. At 2100°C only ZrC and a small amount of carbon were detected, while signals relative to SiC and other carbon species were absent.

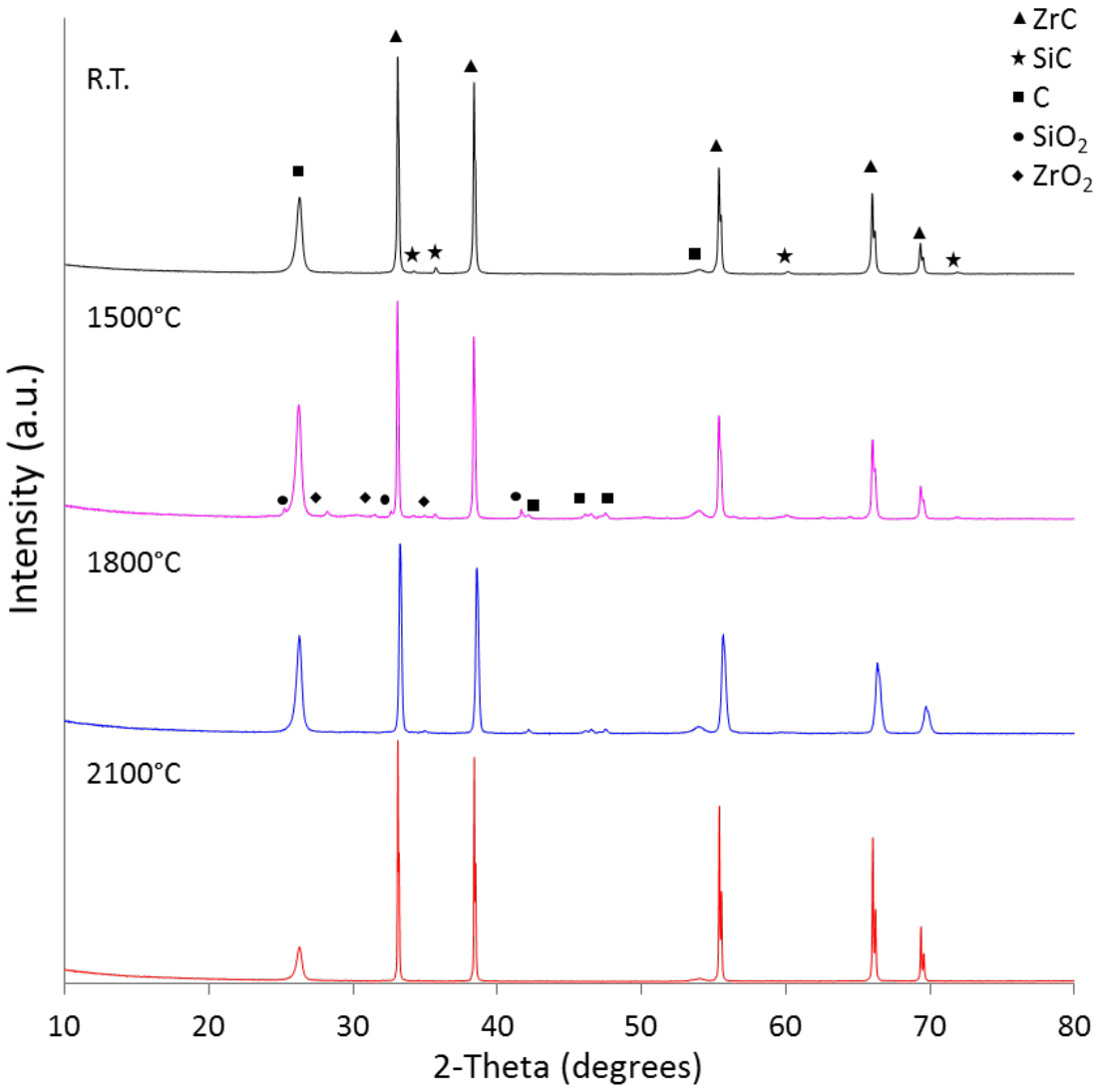

Figure 6.5 X-Ray diffraction patterns of the surface of ZC20 before and after testing at 1500, 1800 and 2100°C in argon

6.2.5 Thermal diffusivity

Thermal diffusivity curve from 200 to 2000°C is reported in fig. 6.6.

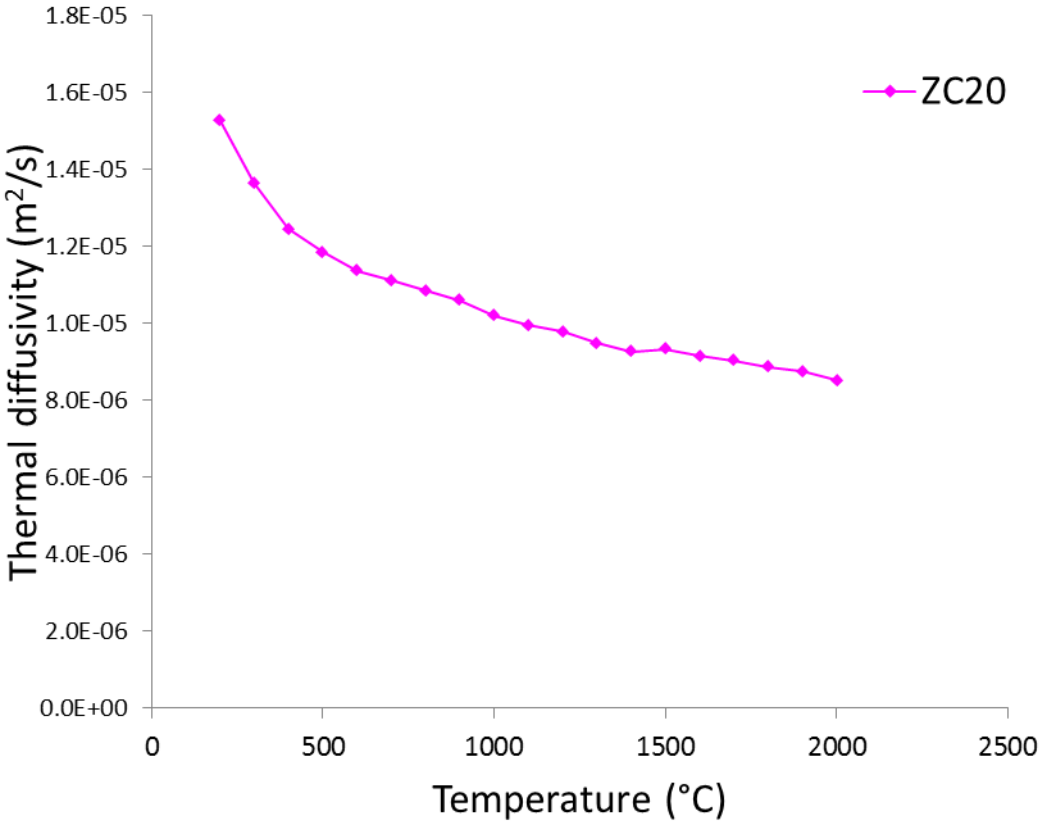

Figure 6.6 Thermal diffusivity vs temperature of sample ZC20. Measurements were recorded from 200 to 2000°C, with steps of 100°C. Each value is the average of 5 recordings at the same temperature.

Thermal diffusivity decreases with the increase of temperature as the molecular vibrations increase, obstructing the flow of free electrons and reducing the conductivity. In the present case study, no further assessment of specific heat capacity was carried out, therefore it is not possible to extrapolate the value of thermal conductivity. However, for a given volume of material, the heat required to raise the temperature a given amount depends on its heat capacity and the density, therefore thermal diffusivity provides a normalized value of thermal conductivity on heat capacity and density. In this sense, a material with low thermal diffusivity may actually have high thermal conductivity but the product of its heat capacity and density is very high and therefore diffusivity is low.

6.3 References

1. Levine, S. R. *et al.* Evaluation of ultra-high temperature ceramics for aeropropulsion use. *J. Eur. Ceram. Soc.* **22,** 2757–2767 (2002).
2. Opeka, M. M., Talmy, I. G., Wuchina, E. J., Zaykoski, J. a. & Causey, S. J. Mechanical, Thermal, and Oxidation Properties of Refractory Hafnium and zirconium Compounds. *J. Eur. Ceram. Soc.* **19,** 2405–2414 (1999).
3. Sha, J. J. *et al.* Improved microstructure and fracture properties of short carbon fiber-toughened ZrB_2-based UHTC composites via colloidal process. *Int. J. Refract. Met. Hard Mater.* **60,** 68–74 (2016).
4. LEIPOLD, M. H. & NIELSEN, T. H. Mechanical Properties of Hot-Pressed Zirconium Carbide Tested to 2600°C. *J. Am. Ceram. Soc.* **47,** 419–424
5. Chen, S., Zhang, C., Zhang, Y. & Hu, H. Influence of pyrocarbon amount in C/C preform on the microstructure and properties of C/ZrC composites prepared via reactive melt infiltration. *Mater. Des.* **58,** 570–576 (2014).
6. Zhu, Y. *et al.* Microstructure and mechanical properties of Cf/ZrC composites fabricated by reactive melt infiltration at relatively low temperature. *Ceram. Int.* **39,** 9085–9089 (2013).
7. Wang, D. *et al.* Fabrication and microstructure of 3D Cf /ZrC-SiC composites: Through RMI method with ZrO_2 powders as pore-making agent. *Ceram. Int.* **42,** 6720–6727 (2015).
8. Ning, J. *et al.* Structural, elastic, electronic, and thermodynamic properties of intermetallic Zr_2Cu: A first-principles study. *Intermetallics* **54,** 7–14 (2014).
9. Sciti, D., Natali Murri, A., Medri, V. & Zoli, L. Continuous C fibre composites with a porous ZrB_2 Matrix. *Mater. Des.* **85,** 127–134 (2015).
10. Zhang, S. C., Hilmas, G. E. & Fahrenholtz, W. G. Pressureless sintering of ZrB2-SiC ceramics. *J. Am. Ceram. Soc.* **91,** 26–32 (2008).
11. Lee, Y.-J. Formation of silicon carbide on carbon fibers by carbothermal reduction of silica. *Diam. Relat. Mater.* **13,** 383–388 (2004).
12. Elliott, R. O. & Kempter, C. P. Thermal Expansion of Some Transition Metal Carbides. *J. Phys. Chem.* **62,** 630–631 (1958).
13. Cheng, Y., Hu, P., Zhou, S., Zhang, X. & Han, W. Using macroporous graphene networks to toughen ZrC–SiC ceramic. *J. Eur. Ceram. Soc.* **38,** 3752–3758 (2018).

14. Liu, H., Liu, L., Ye, F., Zhang, Z. & Zhou, Y. Microstructure and mechanical properties of the spark plasma sintered TaC/SiC composites: Effects of sintering temperatures. *J. Eur. Ceram. Soc.* **32,** 3617–3625 (2012).
15. Jackson, H. F. & Lee, W. E. in *Comprehensive Nuclear Materials* (2012). doi:10.1016/B978-0-08-056033-5.00023-9
16. Neuman, E. W., Hilmas, G. E. & Fahrenholtz, W. G. Mechanical behavior of zirconium diboride–silicon carbide–boron carbide ceramics up to 2200 °C. *J. Eur. Ceram. Soc.* **35,** 463–476 (2015).
17. Hynes, A. & Doremus, R. Theories of creep in ceramics. *Crit. Rev. Solid State Mater. Sci.* **21,** 129–187 (1996).

7. TaC/SiC based UHTCMCs

7.1 Introduction

Tantalum carbide is the second system investigated in this thesis due to its very high melting point and chemical inertness, even though the high density is an issue that needs to be addressed.

Previous studies on fibre reinforced TaC composites have been carried out by Kim et al who obtained graphite fibres coated with TaC powders by hot isostatic pressing at high temperature and pressure, highlighting how the fibres get severely damaged by TaC particles indentation [1]. Zhang et al fabricated carbon fibre reinforced TaC/SiC composites by slurry infiltration and PIP and achieved a flexural strength of 356 MPa, but no high temperature characterization was carried out [2].

The aim of the present work is to investigate the microstructure and mechanical behaviour of carbon fiber reinforced TaC/SiC composites up to 2100°C.

7.2 TC20 0/0

Powder mixtures containing TaC + 20 vol% SiC (designated TC20) were prepared by wet ball milling of the commercial powders and then dried with a rotary evaporator. The composite were fabricated through slurry infiltration of unidirectional carbon fibre preforms and hand lay-up in a unidirectional (0/0°) configuration. Hot pressing was carried out at 1900°C, using a pressure of 40 MPa and a holding time of 15 min, on the basis of previous studies [3].

7.2.1 Sintering behaviour

The hot pressing curve of TC20 is shown in fig.7.1. Just like ZC20, a pressure of 40 MPa was applied at 900°C and maintained during the whole run to 1900°C. The trend is very similar to ZC20 but the densification is more difficult as expected due to the higher refractoriness of TaC compared to ZrC.

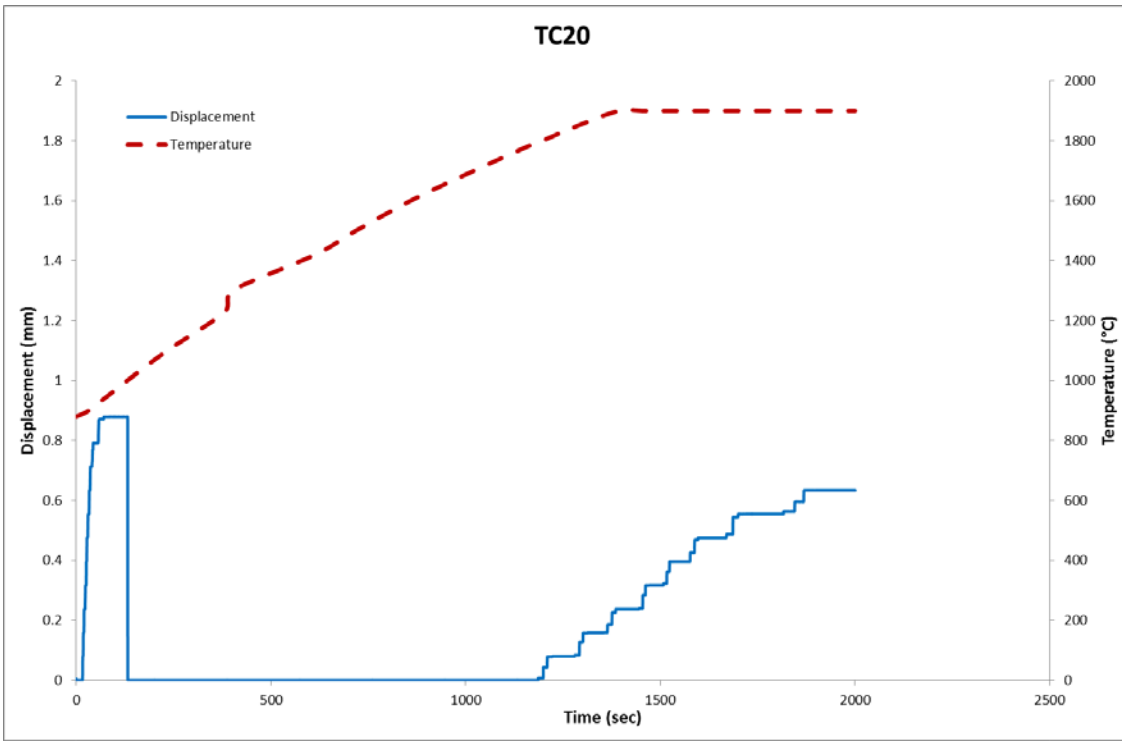

Figure 7.1 Displacement vs time curve relative to the hot pressing cycle carried out on sample TC20 at 1900°C.

7.2.2 Microstructure of the sintered material

The composite with the TaC matrix had a lower degree of porosity (13.3%) than the ZrC matrix composite (16.8%) (Table 7.1). This was attributed to the presence of a higher amount of oxide impurities in ZC20 than TC20 that hindered densification of the ZrC matrix [4]. Even for TC20, the grain size of the predominant carbide phase is in the range of 1.3 to 1.5 µm, while SiC did not show any sign of coarsening, retaining a mean grain size of ~0.50 µm.

Table 7.1. Values of bulk density, porosity, fibre content, and grain size of the carbide phase (ZrC and TaC) and the additive (SiC).

Sample	Density (g/cm3)	Fibre (vol%)	Porosity (vol%)	Grain size (µm)	
				ZrC/TaC	SiC
TC20	7.03	44.0	13.3	1.46	0.51

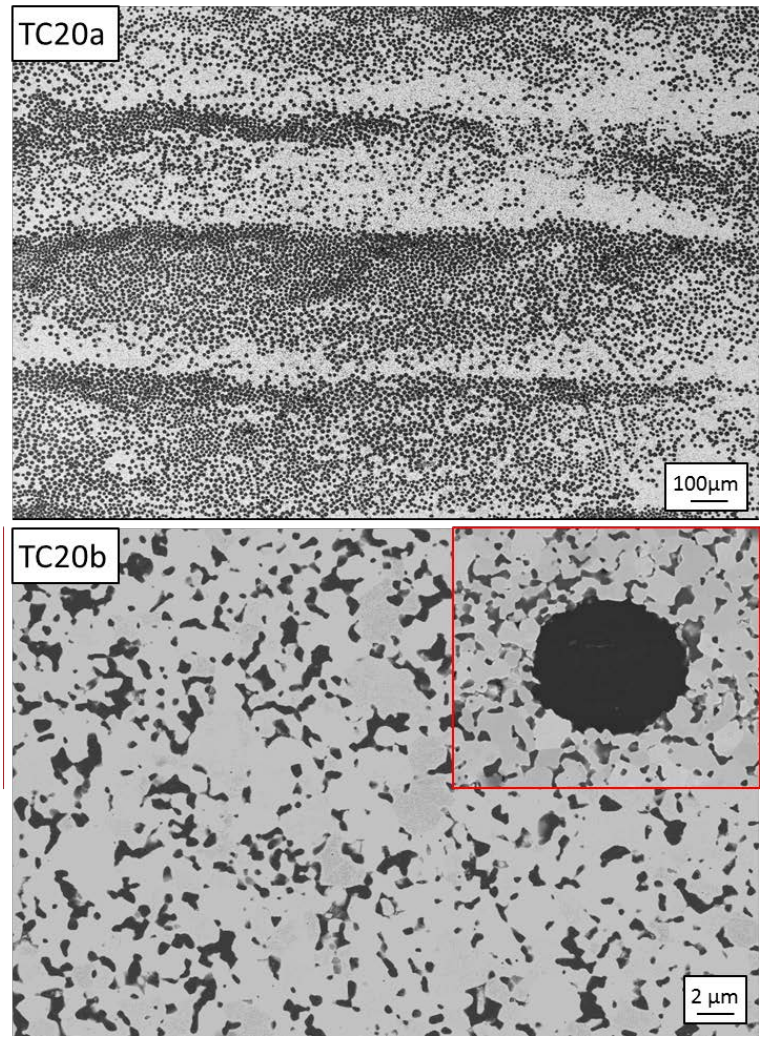

Figure 7.2 Images of cross sections of the sintered specimen, TC20. The light grey phase represents TaC, the dark grey phase is SiC, while the black dots are carbon fibres.

The distribution of SiC was different between ZC20 and TC20. In the high magnification micrographs of the matrix and fibre microstructure of sample TC20 (fig. 7.2 TC20b), the light grey phase is the predominant carbide matrix (TaC) while the dark grey phase is SiC. For ZC20, SiC was homogeneously dispersed as small round particles in the ZrC matrix, whereas for TC20, SiC formed aggregates in TaC grain boundaries, taking on the appearance of flattened particles. Liu *et al.* observed a similar phenomenon during the sintering of a TaC/SiC ceramic composite and attributed this morphology to Ostwald ripening and the re-precipitation of SiC from a liquid phase during sintering at 1900°C [5]. From the fibre regions, no evidence was found to indicate any chemical reaction between the fibre and the matrix as the fibres retained their original round shape.

7.2.3 High temperature strength

The value of strength at room temperature was 301 MPa for TC20 (Table 7.2). This value is lower than the corresponding strength of bulk ceramics of similar composition produced in other studies, which was ~700 MPa (TaC with 20 vol% SiC) [67]. The lower strength of the composites could be due to internal defects related to the presence of the carbon fibres in the ceramic matrix or microcracks generated during cooling from the densification temperature due to the CTE mismatch between the fibres and the matrix. In addition, the slope of the room temperature load/displacement curves (fig 7.3, black lines) decreases as load increases. This effect is more pronounced for Z20 and is attributed to the weak fibre/matrix interface and the premature failure of the matrix in that composition. The change in the slope is less marked for TC20 due to the higher density and stronger adhesion at the fibre-matrix interface.

The strength was higher at 1500°C (461 MPa for TC20). Even in the case of TC20, the increase in strength observed was attributed to the release of residual stresses.

At 1800°C, the strength for both specimens was still above the RT values (413 MPa for TC20), but lower than at 1500°C. The slopes of the load/displacement curve decreased noticeably at 1800°C, which indicates that Youngs' modulus was lower. Even with the lower values, no signs of plastic deformation were observed.

At 2100°C, plastic deformation occurred but was less marked than ZC20. TC20 retained an overall higher ultimate apparent strength (440 MPa) and remained relatively stiff in the elastic portion of the curve, but the specimen yielded at a lower load. The calculated strength at the proportional limit was 319 MPa, which was higher than the R.T. value. On the other hand, ZC20 experienced significant plastic deformation before rupture at ~210 MPa, with an ultimate apparent strength of 368 MPa.

Table 7.2: Flexural strength values at RT, 1500, 1800 and 2100°C for TC20. For specimens tested at 2100°C, the strength calculated using the proportional limit is reported. The ultimate strength at rupture is shown in parentheses.

Sample	σ_{RT} (MPa)	$\sigma_{1500°C}$ (MPa)	$\sigma_{1800°C}$ (MPa)	$\sigma_{2100°C}$ (MPa)
TC20	301 ± 50	461 ± 74	413 ± 15	319 ± 23 (440)

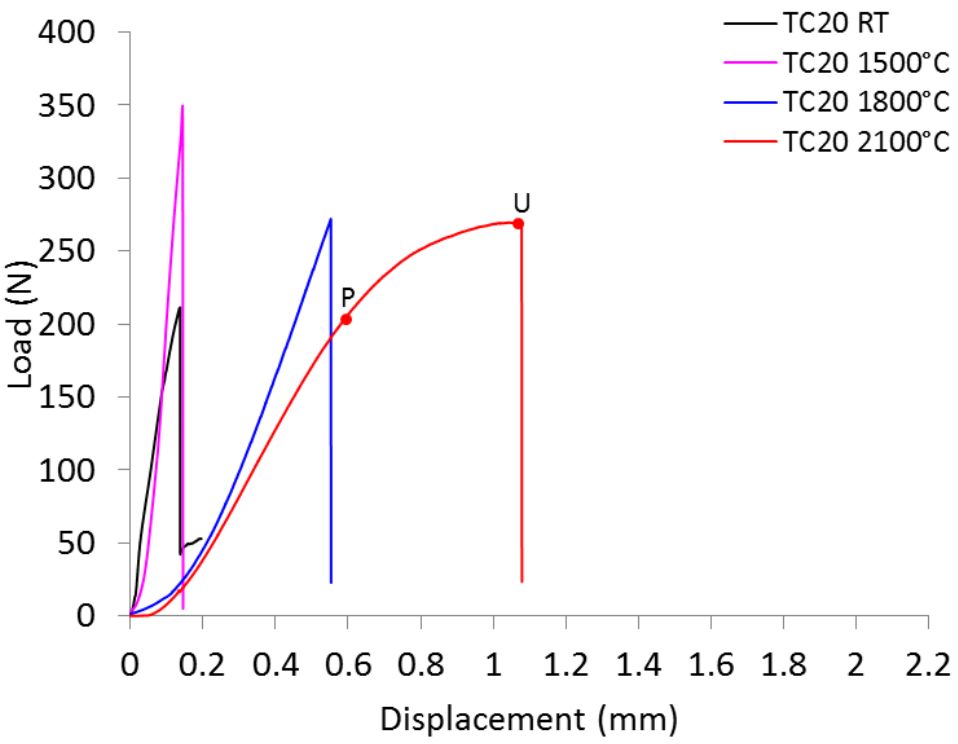

Figure 7.3 Load-displacement curves at RT, 1500, 1800 and 2100°C for TC20. The mechanical behaviour is consistent in all specimens tested, therefore only one curve per temperature was shown. For the test at 2100°C, the strength at the proportional limit (P) and the ultimate strength (U) are shown.

7.2.4 Microstructure of the material after testing

For TC20 a different surface morphology was observed compared to ZC20. SiC particles were detected even after testing at 1800°C and the formation of oxides was revealed by EDS (Fig. 7.4). At 2100°C no silicon species were observed but it was possible to see the formation of blisters on the surface, which was attributed to the evolution of gaseous species, such as SiO, or volatile tantalum oxides. Even in this case the microstructure of the ceramic matrix at 2100°C was very porous. The cross section of the specimen was similar to that of ZC20, with no observed grain growth or reaction at the fibre interface in any test condition.

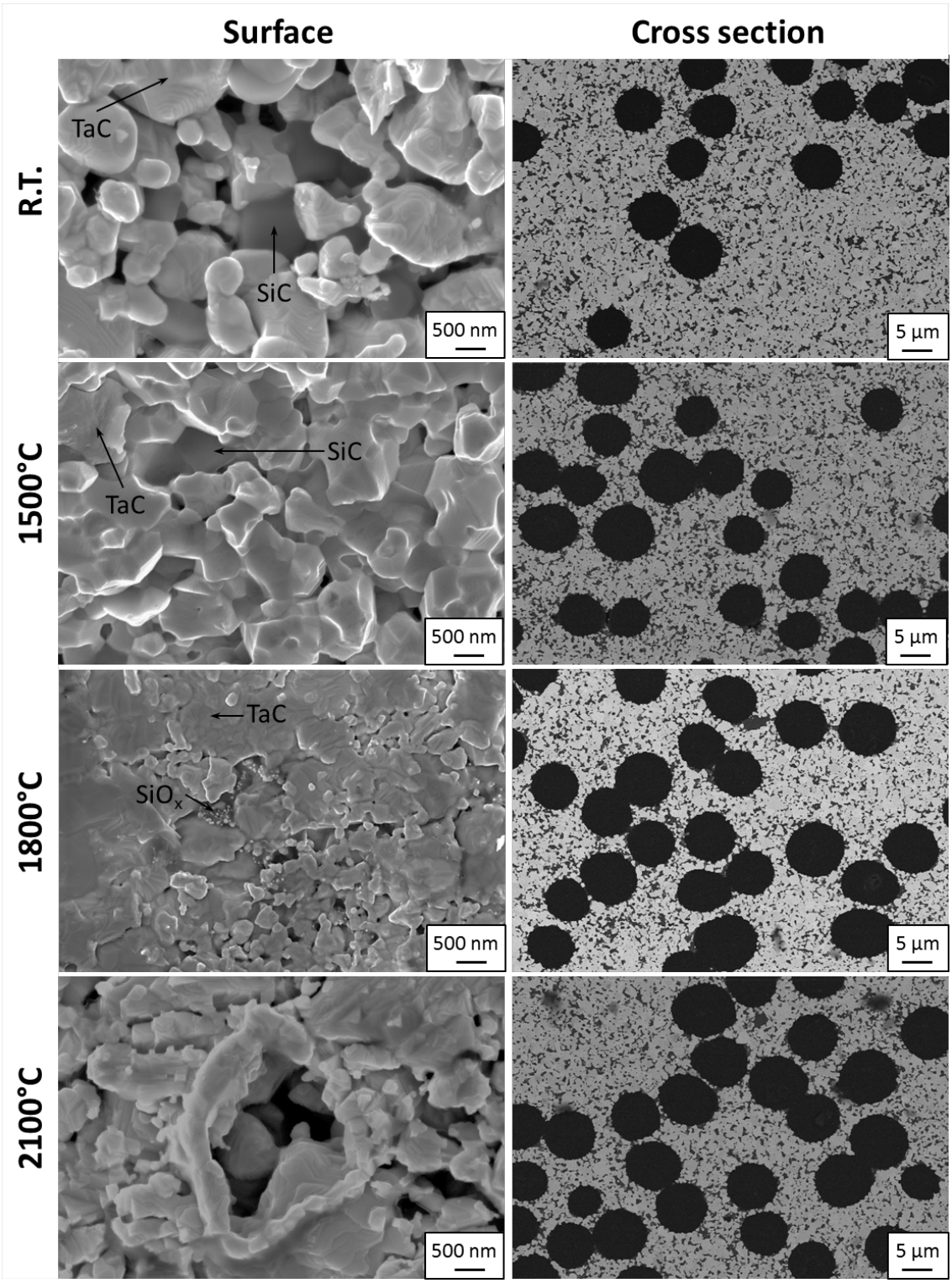

Figure 7.4 Microstructure of the surface and cross section of TC20 after mechanical testing at R.T., 1500, 1800 and 2100°C.

X-Ray diffraction analysis carried out before and after testing on the surface of TC20 showed similar results to ZC20 (Fig. 7.5). At room temperature, TaC (PDF#65-0282), SiC (PDF#29-1131) and graphite (PDF#41-1487) from the carbon fibres were detected.

After testing at 1500°C, the formation of silicon oxide species (PDF#79-1915) and sub-stoichiometric tantalum oxides (73-0005) were detected, together with other carbon species already observed in ZC20. Unlike ZC20, silicon species were retained even at 1800°C. After testing at 2100°C, only the signals from TaC and carbon were observed, with no silicon species detected on the surface. Moreover the signals relative to carbon had lower intensity and some peaks disappeared like ZC20.

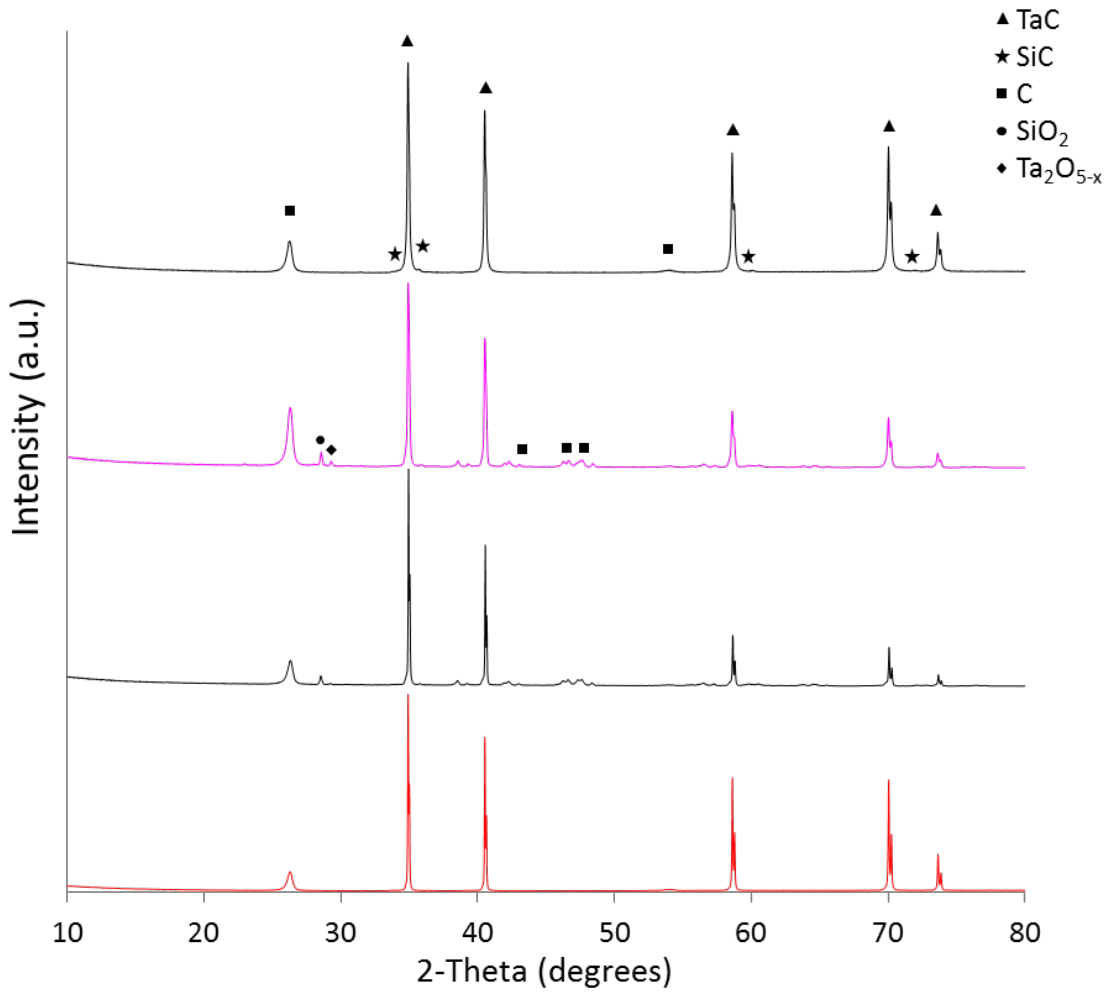

Figure 7.5 X-Ray diffraction patterns of the surface of TC20 before and after testing at 1500, 1800 and 2100°C in argon

7.2.5 Thermal diffusivity

As for ZC20, TC20 also presents decreasing thermal diffusivity curve with the increase of temperature which was attributed to the increase of molecular vibrations (fig. 7.5). Compared to ZC20, TC20 thermal diffusivity decreases more sharply with temperature, starting with an upper value of $1.3 \cdot 10^{-5}$ m^2/s and decreasing down to $3.2 \cdot 10^{-6}$ m^2/s.

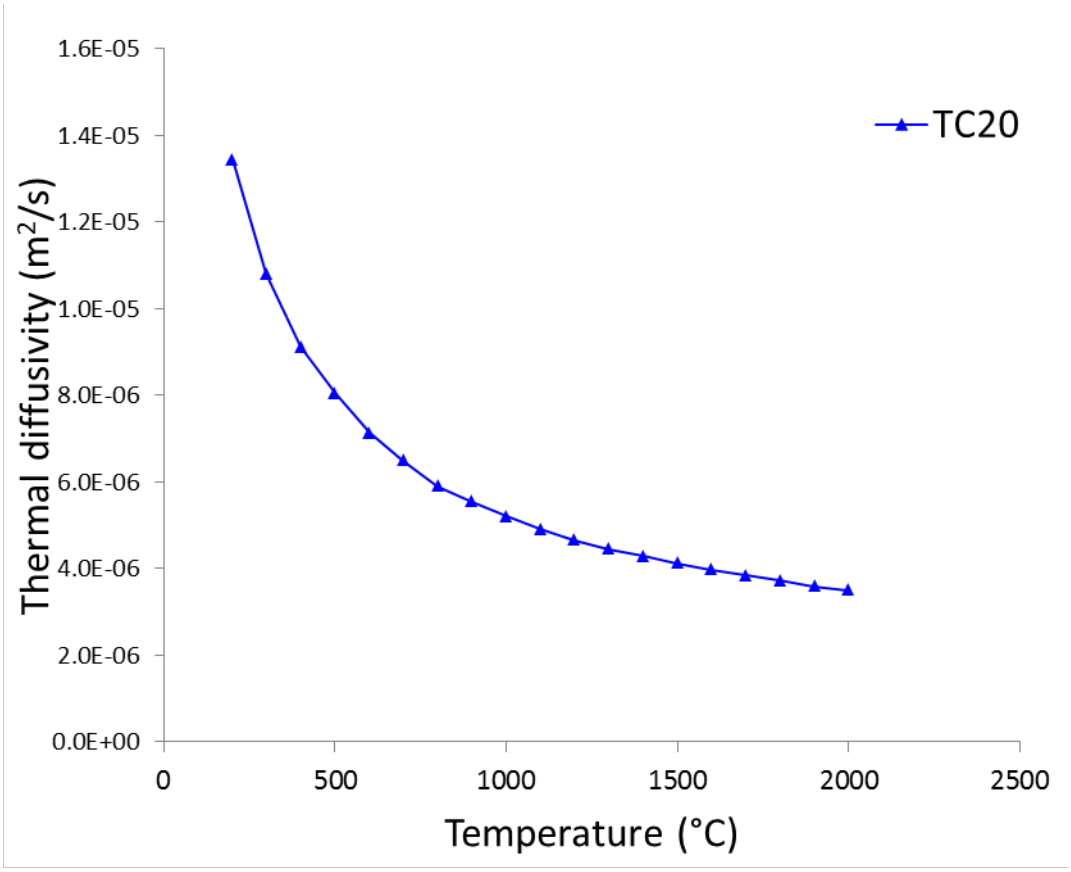

Figure 7.5 Thermal diffusivity vs temperature for sample TC20 from 200 to 2000°C in argon. Thermal diffusivity was recorded in steps of 100°C. For each value, at least 5 measurements were carried out.

7.3 References

1. Kim, C., Grummon, D. S. & Gottstein, G. Processing and interface characteristics of graphite fiber reinforced tantalum carbide matrix composites. *Scr. Metall. Mater.* **25,** 2351–2356 (1991).
2. Zhang, Y., Zhang, C., Hu, H. & Zhou, Y. Preparation and properties of 2D C/SiC-TaC composites. *Key Eng. Mater.* **368–372 PA,** 1771–1773 (2008).
3. Sciti, D., Natali Murri, A., Medri, V. & Zoli, L. Continuous C fibre composites with a porous ZrB_2 Matrix. *Mater. Des.* **85,** 127–134 (2015).
4. Zhang, S. C., Hilmas, G. E. & Fahrenholtz, W. G. Pressureless sintering of ZrB_2-SiC ceramics. *J. Am. Ceram. Soc.* **91,** 26–32 (2008).
5. Zhang, C. High Temperature Oxidation Study of Tantalum Carbide-Hafnium Carbide Solid Solutions Synthesized by Spark Plasma Sintering. (2016). doi:10.25148/etd.FIDC001239
6. Cheng, Y., Hu, P., Zhou, S., Zhang, X. & Han, W. Using macroporous graphene networks to toughen ZrC–SiC ceramic. *J. Eur. Ceram. Soc.* **38,** 3752–3758 (2018).
7. Liu, H., Liu, L., Ye, F., Zhang, Z. & Zhou, Y. Microstructure and mechanical properties of the spark plasma sintered TaC/SiC composites: Effects of sintering temperatures. *J. Eur. Ceram. Soc.* **32,** 3617–3625 (2012).

8. HfC/SiC based UHTCMCs

8.1 Introduction

Hafnium carbide is the third system studied in this thesis. Just like TaC, HfC is interesting due to its very high melting point and chemical inertness, even though the high density is a recurrent issue (12.2 g/cm^3). Increasing the fibre content partially helps to reduce the overall density of the composite that can be as low as 5 g/cm^3.

Literature on HfC/C composites is very scarce. The only carbon fibre reinforced HfC composite reported dates back to 2004 with the work of Sayir who fabricated a C/HfC composite by chemical vapour deposition of HfC on carbon fibres in order to promote graceful failure of the UHTC ceramic [1]. Even though homogenous coatings of HfC were achieved with the presence of very few voids, the strength of the composite amounted to only 26 MPa and was not investigated further.

Other works on HfC composites mainly employ the UHTC phase as a minor particle reinforcement of C/C composites to increase the ablation resistance, or in laminate coatings to increase oxidation resistance [23]. Very few attempts have been made to incorporate long continuous fibres in a HfC matrix due to the difficulty in sintering the ceramic matrix without excessively damaging the fibres.

In the present work the microstructure and mechanical behaviour of carbon fibre reinforced HfC/SiC composites was investigated up to 2100°C.

8.2 HC20 0/0

Powder mixtures containing HfC + 20 vol% SiC (designated HC20) were prepared by wet ball milling of the commercial powders and then dried with a rotary evaporator. The composite was fabricated through slurry infiltration of unidirectional carbon fibre preforms and hand lay-up in a unidirectional (0/0°) configuration. Hot pressing was carried out at 1900°C, using a pressure of 40 MPa and a holding time of 15 min, on the basis of previous studies [4].

8.2.1 Sintering behaviour

Of the three carbide systems studied, HfC apparently shows the lowest degree of densification despite the finer starting particle size. The reason behind this was attributed to the higher refractoriness of HfC and to a higher amount of oxide impurities in the starting powders that hindered sintering.

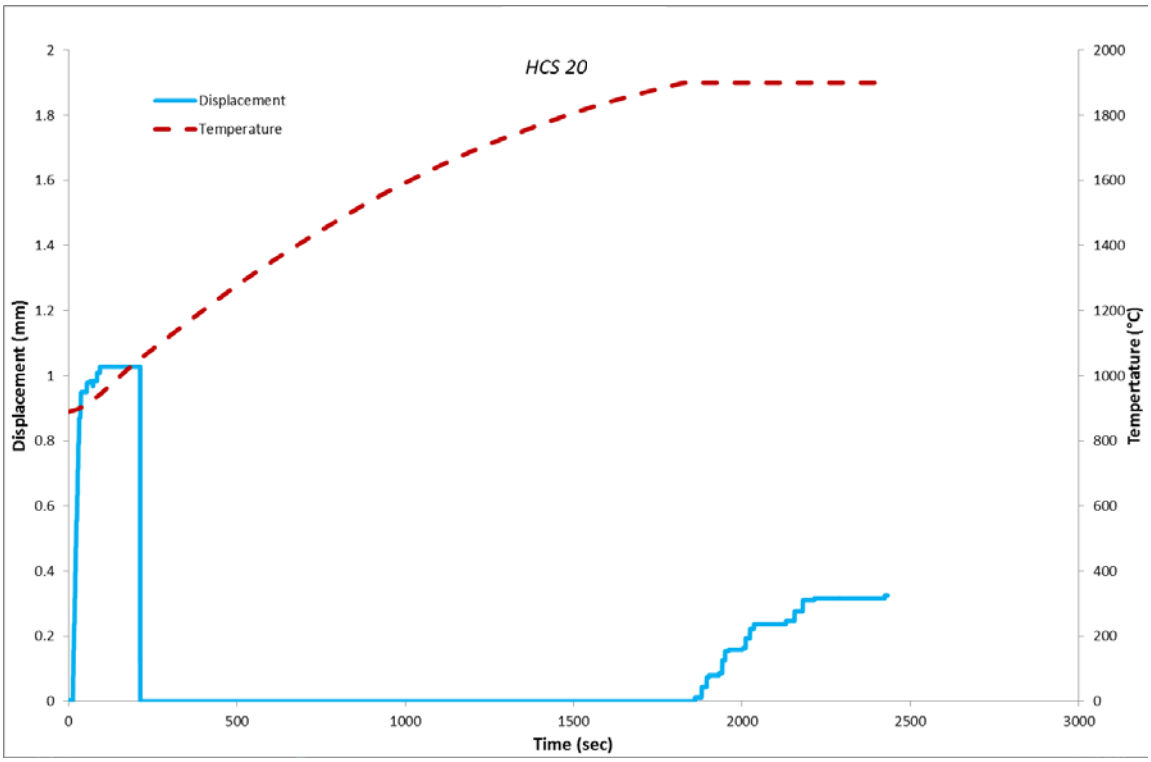

Figure 8.1 Displacement vs time curve relative to the hot pressing cycle carried out on sample HC20 at 1900°C.

8.2.2 Microstructure of the sintered material

Despite what was observed during hot pressing, the composite with the HfC matrix had lower porosity (8.8%) than ZC20 (16.8%) and TC20 (13.3%) (Table 8.1), even though it nominally had a higher amount of oxide impurities that could have hindered densification of the HfC matrix [5]. The higher relative density was attributed to the smaller size of the starting powders that compensated for the presence of oxides and allowed sintering to proceed, even though this was not reflected in further displacement during hot pressing. After hot pressing, the average grain size of the HfC phase was 0.68 μm, lower than that observed for ZC20 and TC20 or 1.3 – 1.5 μm, while SiC particles ranged between 0.48 for the finely dispersed SiC, and 2.36 μm for the aggregates.

Table 8.1. Values of bulk density, porosity, fibre content, and grain size of the carbide phase MeC (Me = Ta, Zr or Hf) and the additive (SiC).

Sample	Density (g/cm3)	Fibre (vol%)	Porosity (vol%)	Grain size (μm)	
				MeC	SiC
HC20	5.99	42.3	8.16	0.68	0.48 – 2.36

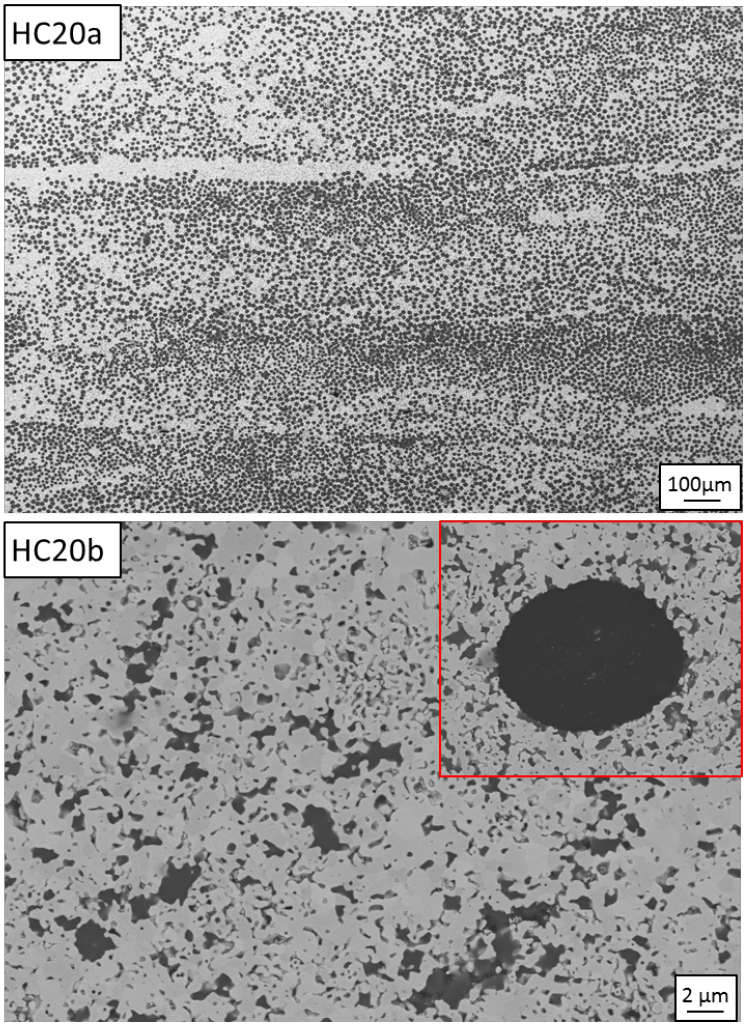

Figure 8.2. Images of cross sections of the sintered specimen, HC20. The light grey phase represents HfC, the dark grey phase is SiC, while the black dots are carbon fibres.

The distribution of SiC in HC20 was more similar to that of ZC20 than TC20 but less homogeneous, with the presence of a small amount of SiC aggregates (Fig. 8.2). In the high magnification micrographs the light grey phase is the predominant carbide matrix (HfC) while the dark grey phase is SiC. From the fibre regions, no evidence was found to indicate any chemical reaction between the fibre and the matrix as the fibres retained their original round shape.

8.2.3 High temperature strength

The value of strength for HC20 at room temperature was 339 MPa (Table 8.2). It is difficult to make a direct comparison of mechanical properties with previously studied composites, but the only strength value found for HfC/C composites is related to the tensile strength of a fibre reinforced HfC composite and amounts to 26 MPa, which

is one order of magnitude lower than what found in this work. The low strength observed by Sayir could be attributed to a non-optimal interface between the fibre and the ceramic matrix. Moreover the lack of secondary phases such as SiC, that was shown to strengthen the fibre/matrix interface [6], contributes to an overall poor load transfer to the fibre and therefore low mechanical properties.

The strength of HC20 was higher at 1500°C like the other two carbide systems studied. Even in the case, the increase in strength was attributed to the release of residual stresses.

At 1800°C, the strength was still above the RT values (433 MPa) and slightly lower than at 1500°C. Even for HC20, the slopes of the load/displacement curve decreased at 1800°C, which indicated that the Youngs' modulus was lower. Even with the lower values, no signs of plastic deformation were observed.

At 2100°C HC20 showed mixed behaviour between ZC20 and TC20 (Fig. 8.3). It retained an overall higher ultimate apparent strength (534 MPa) like TC20, but also underwent significant strain like ZC20. The calculated strength at the proportional limit was 334 MPa, which was equal to the R.T. value.

Table 8.2: Flexural strength values at RT, 1500, 1800 and 2100°C for HC20. For specimens tested at 2100°C, the strength calculated using the proportional limit is reported. The ultimate strength at rupture is shown in parentheses.

Sample	σ_{RT} (MPa)	$\sigma_{1500°C}$ (MPa)	$\sigma_{1800°C}$ (MPa)	$\sigma_{2100°C}$ (MPa)
HC20	339 ± 25	459 ± 44	433 ± 130	334 ± 19 (534)

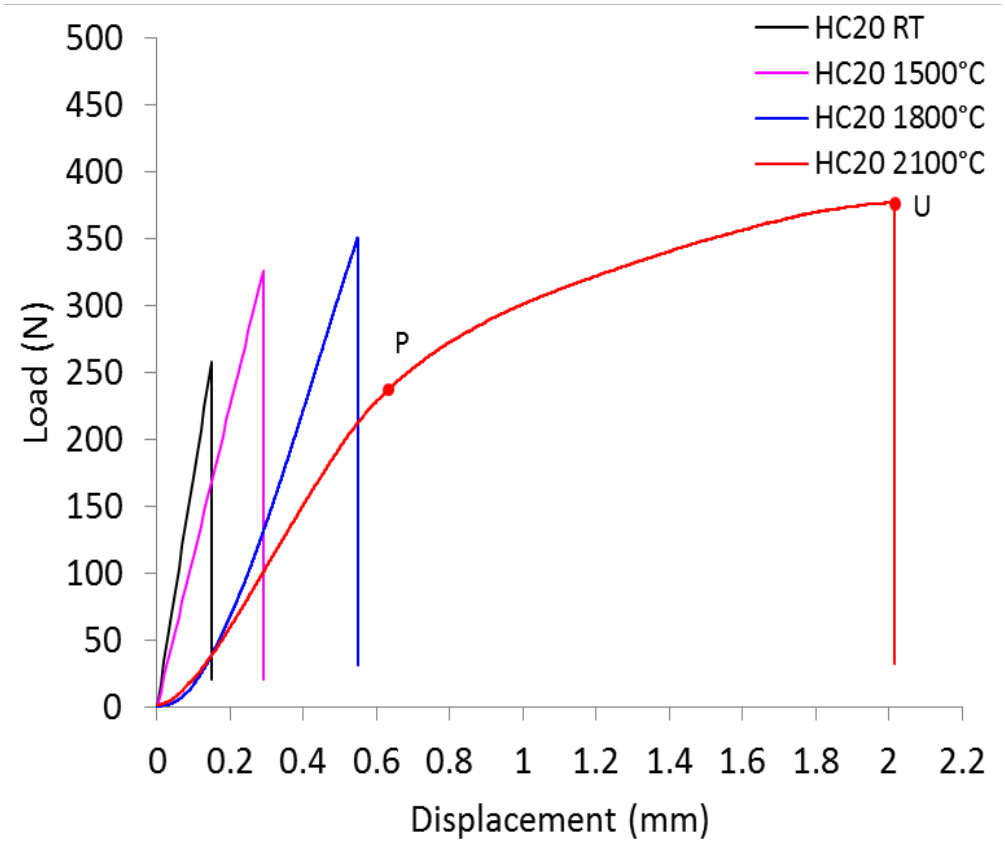

Figure 8.3 Load-displacement curves at RT, 1500, 1800 and 2100°C for HC20. The mechanical behaviour is consistent in all specimens tested, therefore only one curve per temperature was shown. For the test at 2100°C, the strength at the proportional limit (P) and the ultimate strength (U) are shown.

8.2.4 Microstructure of the material after testing

For HC20 the surface morphology was similar to that of ZC20 (Fig. 8.4). SiC particles were detected only up to 1500°C but not at 1800°C. At 2100°C only HfC was detected by EDS and it was possible to see the formation of coalesced HfC grains on the surface. Even in this case, no significant changes were observed in the cross section of the specimen.

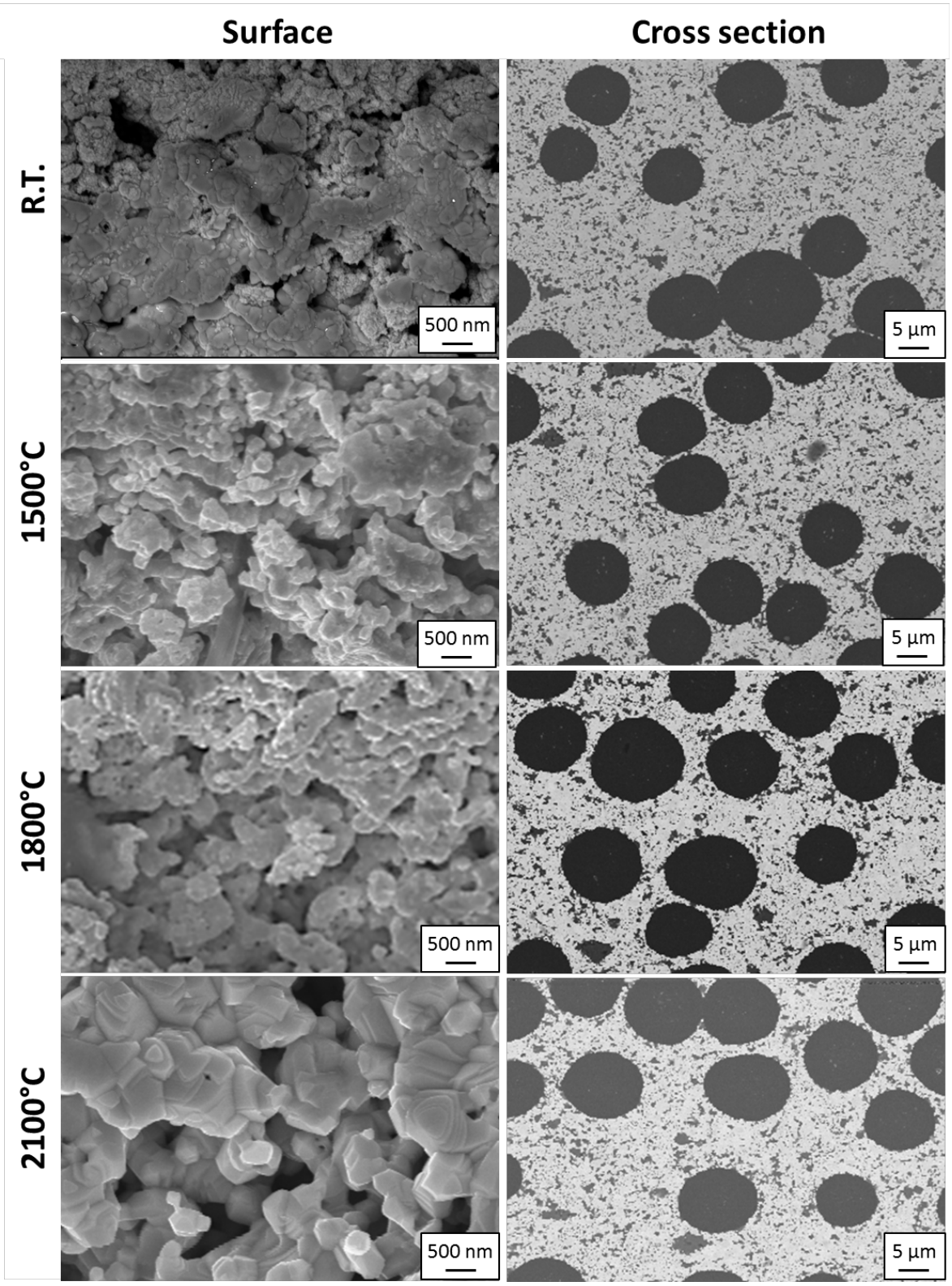

Figure 8.4 Microstructure of the surface and cross section of HC20 after mechanical testing at R.T., 1500, 1800 and 2100°C.

X-Ray diffraction analysis carried out before and after testing on the surface of HC20 showed similar results to ZC20 (Fig. 8.5). At room temperature, HfC (PDF#65-0975),

SiC (PDF#73-1663) and graphite (PDF#41-1487) from the carbon fibres were detected. After testing at 1500°C, the formation of silicon oxide species (PDF#73-1748) and graphite (PDF#40-1498) were detected, together with other carbon species already observed in ZC20. Like ZC20, silicon species were absent at 1800°C. After testing at 2100°C, only the signals from HfC and carbon were observed.

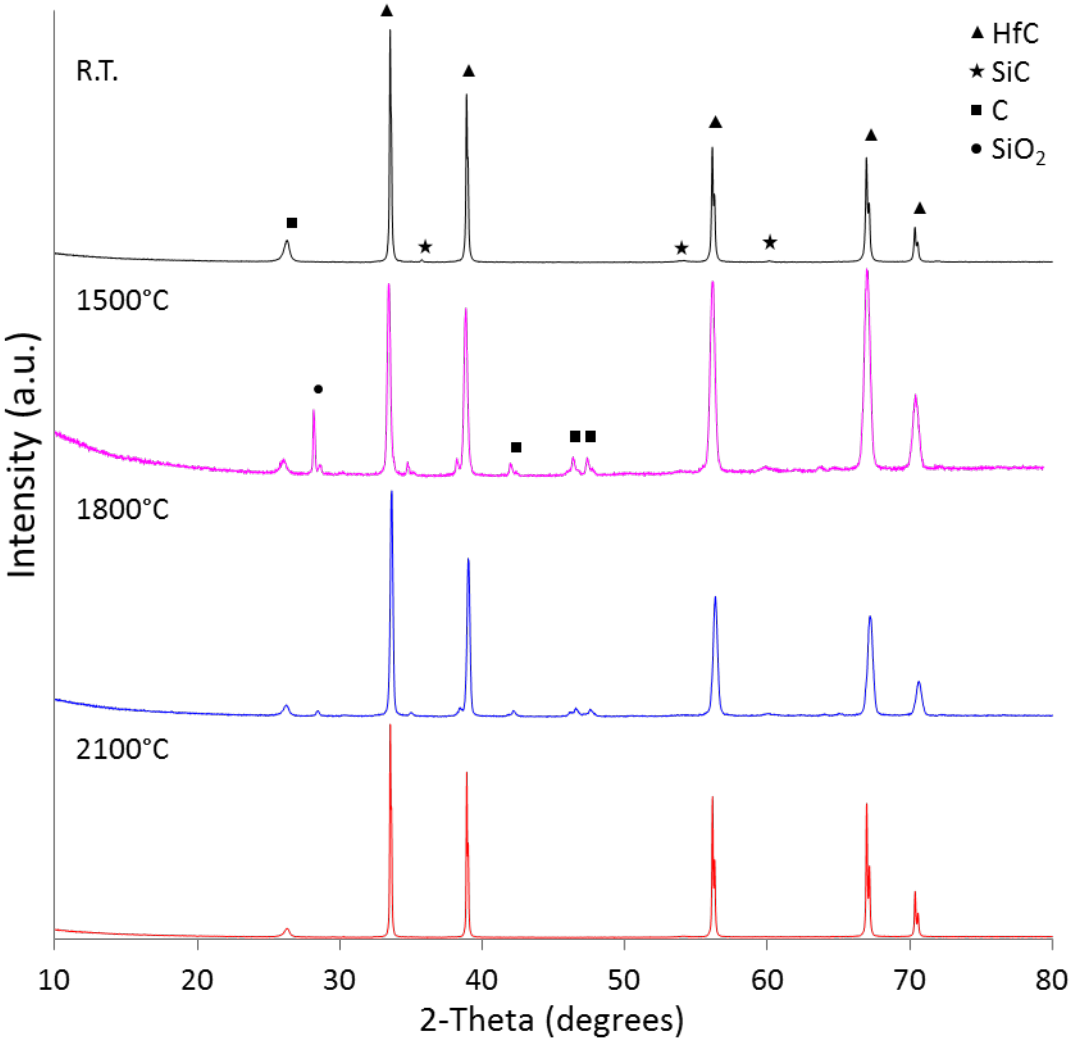

Figure 8.5 X-Ray diffraction patterns of the surface of HC20 before and after testing at 1500, 1800 and 2100°C in argon

Thermodynamic calculations revealed that SiC volatilization was possible under the mechanical testing conditions for all specimens. At 2100°C, SiC was predicted to partially volatilize producing predominant gas species of $Si_{(g)}$, $SiC_{2(g)}$, $Si_2C_{(g)}$, $Si_{2(g)}$, and $CO_{(g)}$, as summarized in Table 8.3 with no differences in the pressures or species for the two different composites. The vapour pressures ranged from 10^{-4} atm to 10^{-6} atm, which was high enough to justify removal of SiC from the near-surface region by vaporization

during mechanical testing. Additional analysis was performed by cooling the predominant gas species from 2100°C to room temperature. That analysis predicted that the gases would react to form condensed phases of SiC, Si, and SiO_2 upon cooling, which could explain the presence of the thin, porous reaction layer on the surface of the composites after testing (Fig 8.3).

Table 8.3. Predominant gas species predicted when ZC20, TC20 and HC20 were heated to 2100°C in argon.

Gas	Pressure (atm)
Ar	0.9950
Si	3×10^{-4}
SiC_2	1×10^{-4}
Si_2C	9×10^{-5}
Si_2	3×10^{-6}
CO	2×10^{-7}
O_2	4×10^{-45}

From these results, it seems likely that all composites had a finite quantity of some impurity, most likely oxide species already present in the starting powders or introduced during processing. Oxides can volatilize when heated to temperatures above 1600°C in the graphite furnace. For example, Al_2O_3 is not stable in the graphite furnace at elevated temperatures and vaporizes rapidly.

8.2.5 Fracture surfaces

Several factors may contribute to the increased plasticity of ZC20 and HC20 compared to TC20. The grain sizes of the main carbide phases (ZrC, TaC and HfC) were similar. In addition, the grain size of SiC was comparable for all specimens as were the fibre and porosity amounts. The main difference after testing at 2100°C was the surface of the materials with no significant microstructural changes observed in the cross section of either specimen and no grain growth or deformation observed for either material, leading to the assumption that most of the plastic deformation occurred by grain boundary sliding.

SEM analysis carried out on the fracture surface of ZC20, TC20 and HC20 showed that fibre pull-out is more marked for ZC at room temperature (fibre pull-out extent of ~15 μm), while little to no fibre pull-out occurs at 1500 and 1800°C for all specimens (Fig. 8.6). At 2100°C ZC20 shows again extensive fibre pull-out (fibre pull-out extent of >20 μm), whereas in the case of TC20 the interaction between the fibre and the matrix is still

very strong, leading to minimal pull-out. For HC20 an intermediate behaviour was observed, with

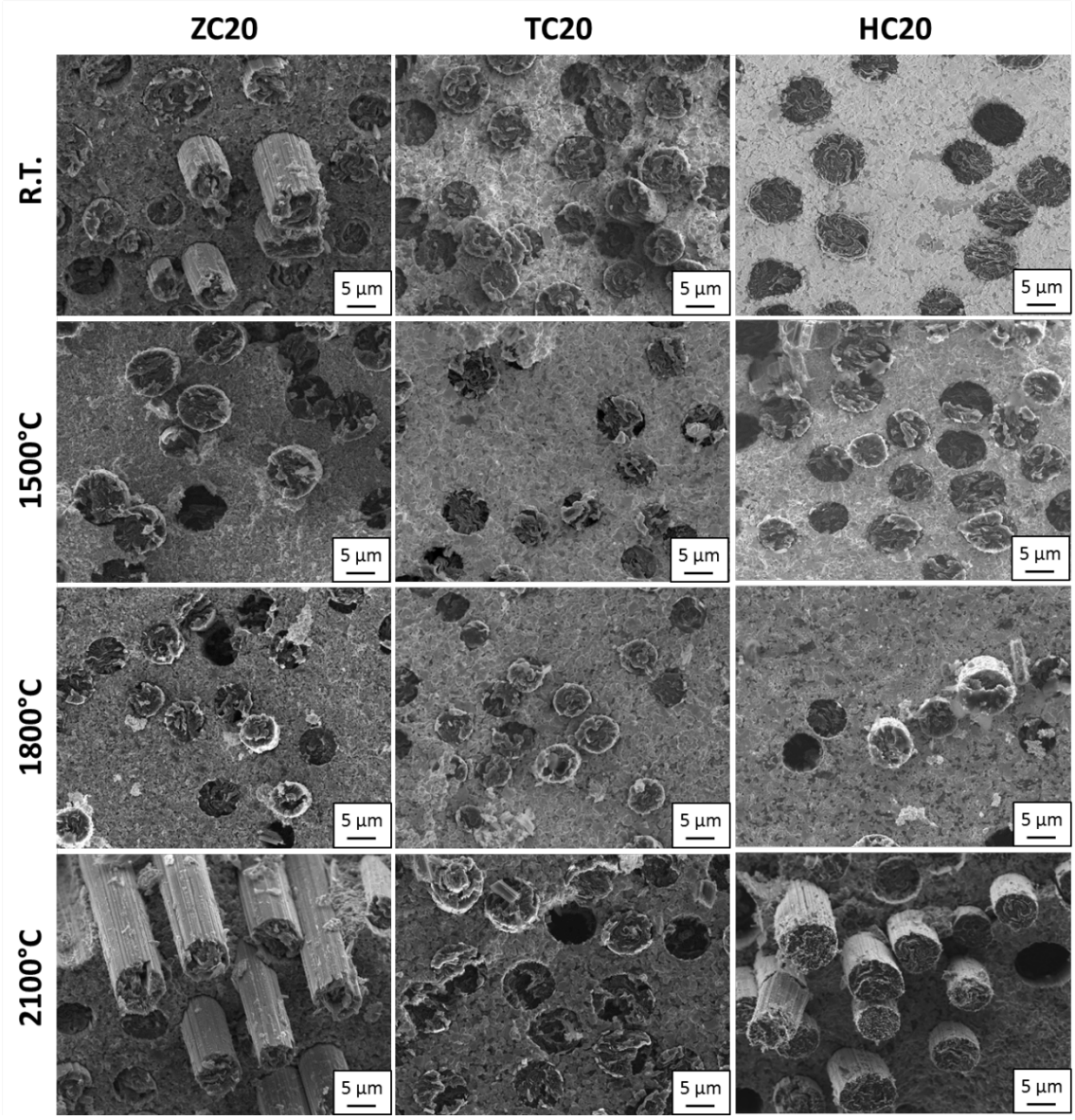

Figure 8.6 Fracture surfaces of ZC20, TC20 and HC20 after testing at R.T., 1500, 1800 and 2100°C.

ZC20 showed signs of a weaker fibre/matrix interface already at room temperature and it is believed that at 2100°C, when ZrC grains were sliding past each other, there was lower load transfer to the fibre, resulting in a higher ultimate strain and cracking of the matrix. On the other hand, for TC20 and HC20, a stronger fibre/matrix interface was observed at room temperature and was maintained at elevated temperatures, as evidenced by the significantly lower fibre pull-out and ultimate strain on the test specimens prior to failure. Only the latter showed fibre pull-out at 2100°C. The factors

responsible for the increased plasticity and lower strength of ZC20 at 2100°C appear to be the overall lower melting point of ZrC (3542°C) compared to that of TaC (3880°C) and HfC (3900°C) and the weaker fibre/matrix interface that enabled significant matrix stain before failure. The lower fibre/matrix interface strength of ZC20 compared to TC20 can be attributed to the higher degree of porosity, in agreement with previous studies on fibre reinforced ZrB_2/SiC composites [6]. HC20 shows mixed behaviour between ZC20 and TC20; the load/displacement curve shows relatively high strength at the proportional limit and limited pull-out up to 1800°C like TC20, but is also characterized by extensive strain and marked fibre pull-out at 2100°C. The increased plasticity of the latter compared to TC20 was attributed to the finer grain size which allowed better grain boundary sliding.

8.2.6 Thermal diffusivity

The curves relative to thermal diffusivity of all the carbide based composites are summarized in figure 8.7. HC20 is characterized by the lowest thermal diffusivity that does not change significantly with temperature and remains almost constant throughout the temperature range investigated.

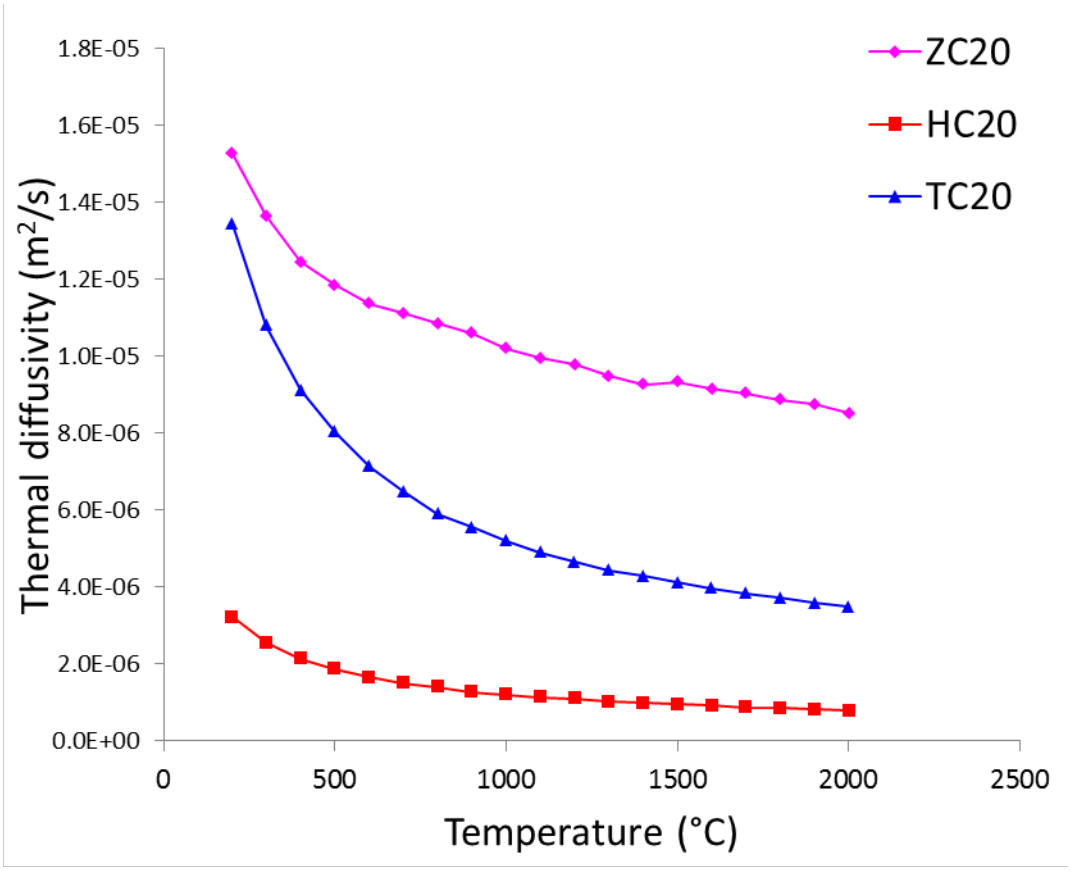

Figure 8.7 Thermal diffusivity vs temperature for sample TC20 from 200 to 2000°C in argon. Thermal diffusivity was recorded in steps of 100°C. For each value, at least 5 measurements were carried out.

Without the data relative to heat capacities, it is difficult to make a direct comparison between the carbide based composites studied so far, but considering that the carbide phases, ZrC, TaC and HfC, all possess similar thermal conductivities (20.5, 22 and 20 W/mK respectively) and that the composites have comparable amounts of carbon fibres, the lower thermal diffusivity of TC20 and HC20 could be reasonably attributed to the higher density of TaC (14.3 g/cm^3) and HfC (12.2) compared to ZrC (6.73 g/cm^3) [7].

8.3 Influence of carbon fibre content

On the composition containing HfC further tests were carried out in order to assess the influence of carbon fibre content on the high temperature properties. A second specimen with a higher carbon fibre content was fabricated following the procedures described in 8.2.

8.3.1 Microstructure

The physical properties of the HfC-based composites are reported in table 8.3. The specimen containing a higher fibre content, labelled HC20b, is characterized by a higher degree of porosity (11.6%) compared to the baseline HC20 (8.16) (Table 8.4), which is in accordance with previous studies on carbon fibre reinforced UHTCs, since fibres hinder sintering. After hot pressing, the average grain size of the HfC phase was the same as the baseline HC20 (0.68 μm), but SiC aggregates were smaller (~1.80 μm)

Table 8.4. Values of bulk density, porosity, fibre content, and grain size of HfC and the additive (SiC) for specimens HC20 and HC20b.

Sample	Density (g/cm3)	Fibre (vol%)	Porosity (vol%)	Grain size (μm)	
				HfC	SiC
HC20	5.99	42.3	8.16	0.68	0.48 – 2.36
HC20b	4.73	54.1	11.6	0.68	0.47 – 1.80

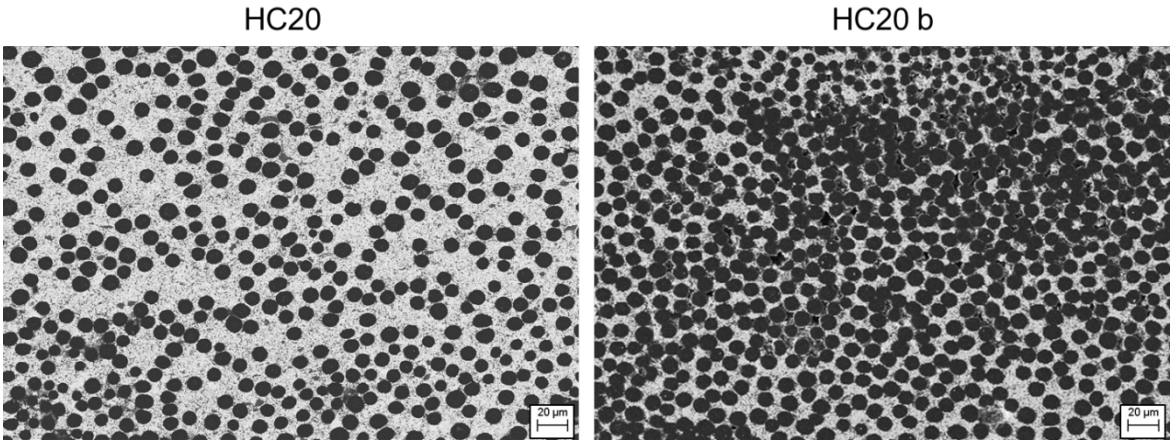

Figure 8.8 SE micrograph of the cross section of samples HC20 and HC20b showing the fibre distribution (black) in the ceramic matrix (light grey).

In the SEM micrographs in figure 8.8 it is possible to see how fibres (black) are homogeneously distributed in the ceramic matrix (light grey) independently from the fibre content. Even in the case of HC20b, no reaction was observed at the interface.

8.3.2 Mechanical behaviour

The strength of HC20b at room temperature was slightly higher (379 MPa) than the baseline HC20 (339 MPa) (Table 8.5). It was not possible to measure the flexural strength at 1500°C, but all other high temperature tests were carried out in the same conditions.

At 1800°C, the strength increased (439 MPa) and was comparable to the baseline HC20 (433 MPa), with no clear influence of the carbon fibre content and no signs of plastic deformation.

At 2100°C HC20b showed a very different behaviour, even though the strength at the proportional limit (317 MPa) and the ultimate strength (520 MPa) were comparable to the baseline HC20b. Sample HC20b is characterized by a more marked ultimate strain and the load/displacement curve is more complex, with an elastic region, plastic region, a yield point and a strain-hardening section.

Table 8.5: Flexural strength values at RT, 1500, 1800 and 2100°C for HC20. For specimens tested at 2100°C, the strength calculated using the proportional limit is reported. The ultimate strength at rupture is shown in parentheses.

Sample	σ_{RT} (MPa)	$\sigma_{1500°C}$ (MPa)	$\sigma_{1800°C}$ (MPa)	$\sigma_{2100°C}$ (MPa)
HC20	339 ± 25	459 ± 44	433 ± 130	334 ± 19 (534)
HC20b	379 ± 22	-	439 ± 39	317 ± 30 (520)

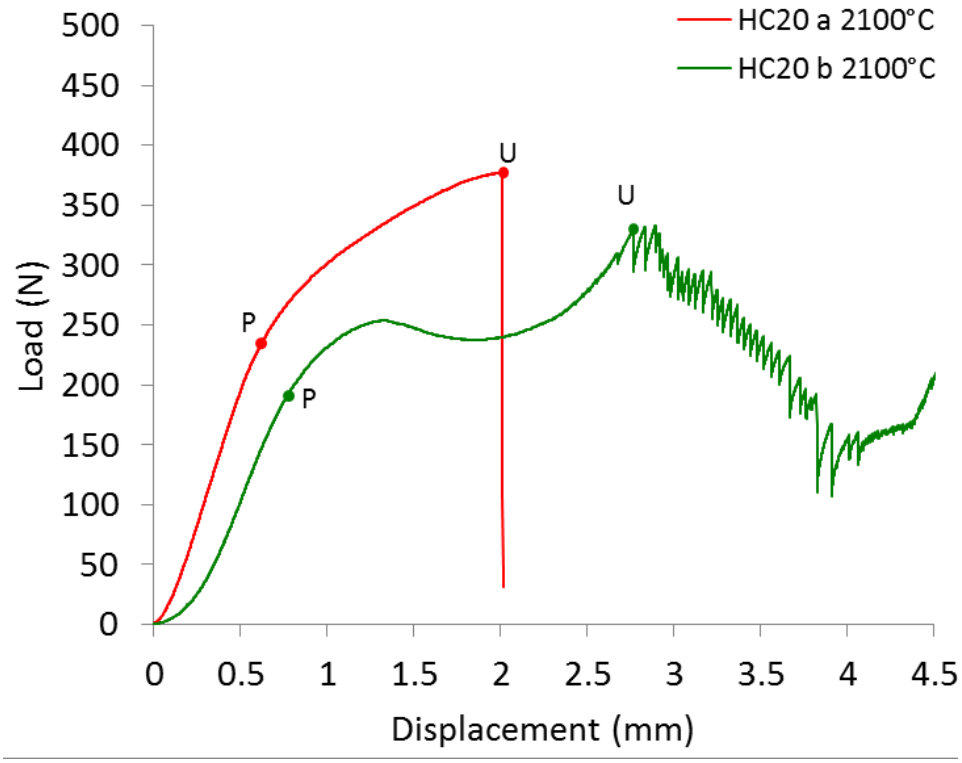

Figure 8.5 Load-displacement curves at 2100°C for HC20 and HC20b. The mechanical behaviour is consistent in all specimens tested, therefore only one curve per temperature was shown. The strength at the proportional limit (P) and the ultimate strength (U) are shown.

By looking at the specimen bar after testing (fig. 8.9) it is possible to see that the sample was never fractured in two halves but was plastically deformed following the geometry of the 4-point sample holder set-up. It is believed that the marked plastic deformation of HC20b occurred because of creep mechanisms. Possible reasons comprehend the overall low refractory matrix content and a higher degree of porosity. Another reason can be attributed to the high fibre amount. Further support to this thesis is found in the works of Lamon *et al.* who investigated the high temperature behaviour of pitch fibres at 2000°C, showing how fibres undergo extensive strain at high temperatures [8].

Figure 8.9 Specimen HC20b after testing at 2100°C. The extensive plastic deformation, which followed the 4-point geometry of the sample holder, occurred due to creep phenomena.

8.4 Conclusions

Carbon fibre reinforced ZrC/SiC, TaC/SiC and HfC/SiC were produced by slurry infiltration and hot pressing.

The flexural strength for all the carbide systems investigated is in the range 280 – 340 MPa and increases up to 450 MPa at 1500°C due to stress relaxation.

All specimen experience a slight strength and modulus drop at 1800°C down to 400 MPa, which is still higher than the R.T. value

At 2100°C plastic deformation occurs via grain boundary sliding. ZC20 and HC20 are characterized by the highest failure strain due to weak fibre/matrix interface, whereas TC20 remains relatively stiff at all temperatures. TC20 and HC20 retain an overall higher strength (400 – 500 MPa), whereas ZC20 fails prematurely at 200 – 300 MPa.

Increasing the fibre content in sample HC20 led to a significantly different behaviour at 2100°C, with marked plastic deformation and very high failure strain. The overall strength is similar in value, but HC20b did not rupture after the test.

As far as thermal conductivity is concerned, it is not possible to draw definite conclusions from thermal diffusivity data without the data relative to heat capacity, but the lower thermal diffusivity of TC20 and HC20 compared to ZC20 could be reasonably attributed to the high density of the former (12.2 – 14.3 g/cm^3) compared to the latter (6.73 g/cm^3).

8.5 References

1. Sayir, A. Carbon fiber reinforced hafnium carbide composite. *J. Mater. Sci.* **39,** 5995–6003 (2004).
2. Verdon, C., Szwedek, O., Jacques, S., Allemand, A. & Le Petitcorps, Y. Hafnium and silicon carbide multilayer coatings for the protection of carbon composites. *Surf. Coatings Technol.* **230,** 124–129 (2013).
3. Jiang, J., Wang, S., Li, W. & Klein, L. Preparation and Characterization of UltraHigh-Temperature Ternary Ceramics Ta_4HfC_5. *J. Am. Ceram. Soc.* **99,** 3198–3201 (2016).
4. Sciti, D., Natali Murri, A., Medri, V. & Zoli, L. Continuous C fibre composites with a porous ZrB_2 Matrix. *Mater. Des.* **85,** 127–134 (2015).
5. Zhang, S. C., Hilmas, G. E. & Fahrenholtz, W. G. Pressureless sintering of ZrB_2-SiC ceramics. *J. Am. Ceram. Soc.* **91,** 26–32 (2008).
6. Vinci, A., Zoli, L., Sciti, D., Melandri, C. & Guicciardi, S. Understanding the mechanical properties of novel UHTCMCs through random forest and regression tree analysis. *Mater. Des.* **145,** 97–107 (2018).
7. Radosevich, L. G. & Williams, W. S. Thermal Conductivity of Transition Metal Carbides. *J. Am. Ceram. Soc.* **53,** 30–33
8. Sauder, C., Lamon, J. & Pailler, R. The tensile behavior of carbon fibers at high temperatures up to 2400 °C. *Carbon N. Y.* **42,** 715–725 (2004).

9. ZrB_2/ZrC based UHTCMCs

9.1 Introduction

An alternative route for the fabrication of carbon fibre reinforced ZrB_2 composites is based on the reactive melt infiltration of boron-containing powders (i.e. B, B_4C) with liquid zirconium alloys. Typically Zr_2Cu alloy is employed as liquid melt due to its lower melting point (~1000°C) compared to elemental zirconium (1855°C), to form in-situ ZrB_2 according to reaction 1 [1–3]:

$$4\ B + Zr_2Cu \rightarrow 2\ ZrB_2 + Cu \qquad (1)$$

This allows to obtain near full density materials without the need of high temperatures and pressures required for the conventional sintering of UHTCs. The main drawbacks of this process are the powder wettability, which may hinder infiltration, and the presence of residual melt at the end of the infiltration which can lower the high temperature mechanical properties. Moreover the formation of in-situ ZrB_2 leads to a volume expansion which may choke infiltration at the reaction front [1]. In case of fibre reinforced ZrB_2 matrix composites, RMI achieves a lower temperature exposure of the fibres compared to HP or SPS, with no additional mechanical pressure, but reaction with the liquid melt can lead to a degradation of the mechanical properties of the fibres (reaction 2) [4].

$$2\ C + Zr_2Cu \rightarrow 2\ ZrC + Cu \qquad (2)$$

In the present work carbon fibre reinforced ZrB_2/ZrC composites were fabricated via RMI. Carbon fibre preforms were first infiltrated with aqueous powder suspensions containing elemental boron according to the procedures described in 3.1. Commercial ZrB_2 powders were added to the boron slurries as filler in amounts ranging between 25 – 75 vol% in order to prevent the premature interruption of the infiltration due to volume expansion from in-situ formation of ZrB_2. The green body is then dried and heated in a furnace to 1200°C with a rate of 500°C/h in flowing argon atmosphere. After the target temperature is reached, the chamber is evacuated (vacuum < 5 mbar) and the sample is dipped in a graphite crucible containing the liquid Zr_2Cu melt for 2 min. Finally the sample is taken out of the crucible and let to cool down naturally to room temperature in the furnace.

9.2 RMI of C-B/ZrB_2 with Zr_2Cu

9.2.1 Mixture compositions

The compositions of the powder mixtures are reported in table 9.1. Aqueous powder suspensions containing elemental boron and commercial zirconium diboride were prepared following the procedures described in 3.1.

Table 9.1 Powder mixture compositions for samples B25, B50 and B75 used for RMI

Sample	B (vol%)	ZrB_2 (vol%)
B25	25	75
B50	50	50
B75	75	25

With these slurries, uni-directional fibre preforms of dimensions 50 x 50 mm were infiltrated, stacked in a 0/0° configuration and then dried at 100°C in an oven. The ratio between the fibre and the ceramic powder volumetric amount was kept 1:1. Then the green bodies were clamped between graphite plates and infiltrated with liquid Zr_2Cu melt at 1200°C in vacuum. Sample ZB75 required a second infiltration due to excessive volume expansion from the formation of in-situ ZrB_2 and premature arrest of the infiltration.

9.2.2 Microstructure

Table 9.2 summarizes the physical properties of the infiltrated samples.

Table 9.2 Compositions, densities, fibre contents, strengths and ZrB_2 grain size for specimens B25, B50 and B75 infiltrated by RMI.

Sample	Density (g/cm^3)	Porosity (vol%)	Fibre after RMI (vol%)	ZrB_2 particle size powders (μm)	ZrB_2 particle size RMI (nm)	σ (MPa)
B25	6.36	< 1	13.4 ± 0.4	3.00	172	332 ± 15
B50	6.64	< 1	16.5 ± 1.4	2.32	140	563 ± 154
B75	6.12	< 1	24.7 ± 4.5	2.46	289	563 ± 29

All samples were characterized by little to no porosity. The final fibre content is much lower than the initial fibre volume. There are two main explanations to this:

1) the starting fibre volumetric amount was ~50 vol%, but since the green bodies experienced a volume expansion of ~50% during RMI, the final fibre content was actually ~33 vol%

2) some fibres reacted with the surrounding Zr_2Cu melt leading to the formation of ZrC at the interface, further lowering the final carbon fibre content. In some cases (B25 and B50), the extent of reaction progressed enough to consume as much as 50% of the fibre.

All samples contained large amounts of unreacted melt which contributed to increase the final density of the materials. From the SEM micrographs on the infiltrated samples it is possible to see the coarse ZrB_2 particles from the starting commercial powders and very fine ZrB_2 particles originated from the reaction between boron and the Zr_2Cu melt (Fig. 9.2). Fibres are surrounded by a rim of ZrC which originates from the reaction of the carbon of the fibre and the liquid melt. For sample B25 fibres were more damaged due to uncontrolled reaction with the excess melt, but for B50 and B75 the degree of fibre degradation was lower since the majority of Zr_2Cu melt reacted with the boron. In this regard, B75 retained the highest fibre content.

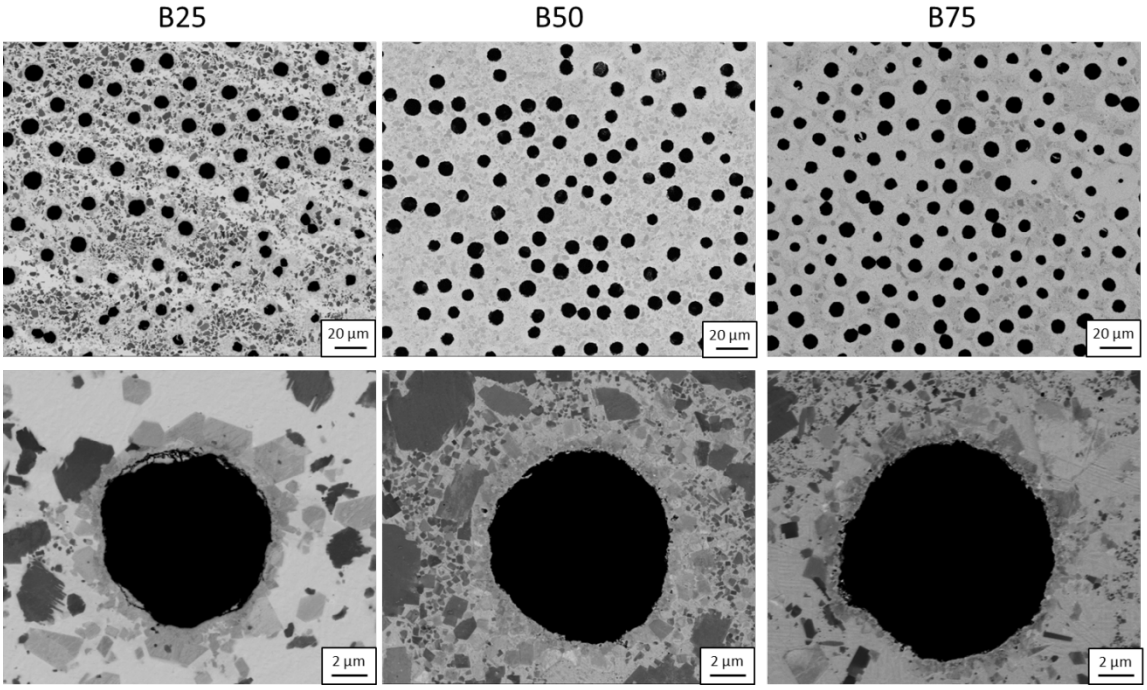

Figure 9.2 SEM image of the polished cross section of samples B25, B50 and B75. The black phase is carbon from the fibres, dark grey and light grey phases are ZrB_2 and ZrC respectively while the white phase is the residual Zr_2Cu melt.

The ZrB_2 from the commercial powders retained its starting particle size of 2 – 3 µm, while the fine ZrB_2 particles formed in-situ by the reaction between elemental boron and the Zr_2Cu melt had a particle size below 300 nm and were homogeneously dispersed in the ceramic matrix (Fig. 9.3).

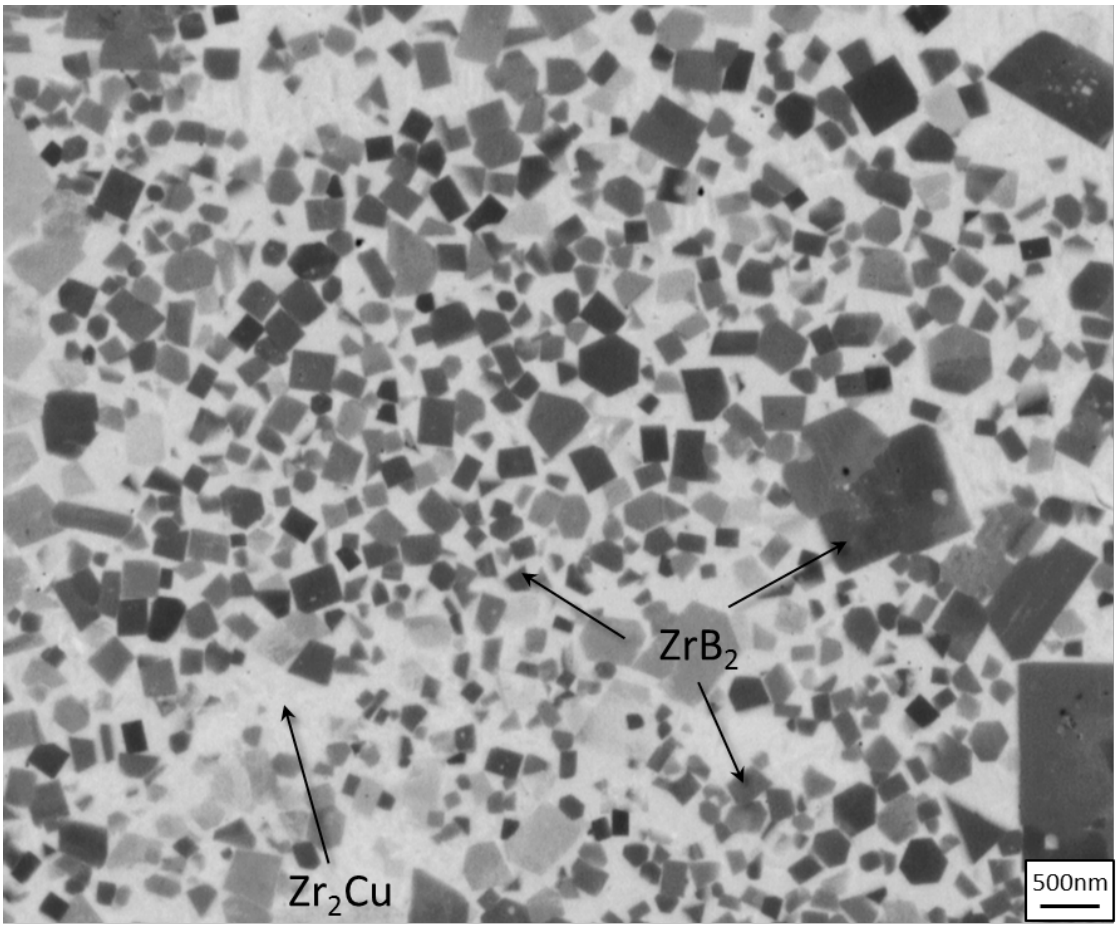

Figure 9.3 Detail of the microstructure of B75 showing the fine grained ZrB_2 originating from the reaction between elemental boron and Zr_2Cu melt

The volumetric fraction of the fine ZrB_2 particles increased with the increase of boron content in the starting powders as expected. The microstructure of B50 is very similar to that of B75, with little leftover residual melt. Cubic ZrC grows on the surface of the fibres as the latter react with the melt. Fibre-dense regions are affected the least by fibre degradation since the majority of the melt is consumed to form ZrB_2, whereas less infiltrated peripheral fibres are almost completely converted into ZrC. From image analysis, ~40% of the original volumetric amount of fibres was converted into ZrC, leading to final carbon contents of 15 – 25 vol%.

X-Ray diffraction analysis carried out on the polished cross section of sample B25 (fig. 9.4), used as reference, revealed the presence of ZrB_2 (PDF#34-0423), ZrC (PDF#65-0973) and minor amounts of the residual melt, Zr_3Cu (PDF#65-2803), and B (PDF#72-1705). No carbon was detected.

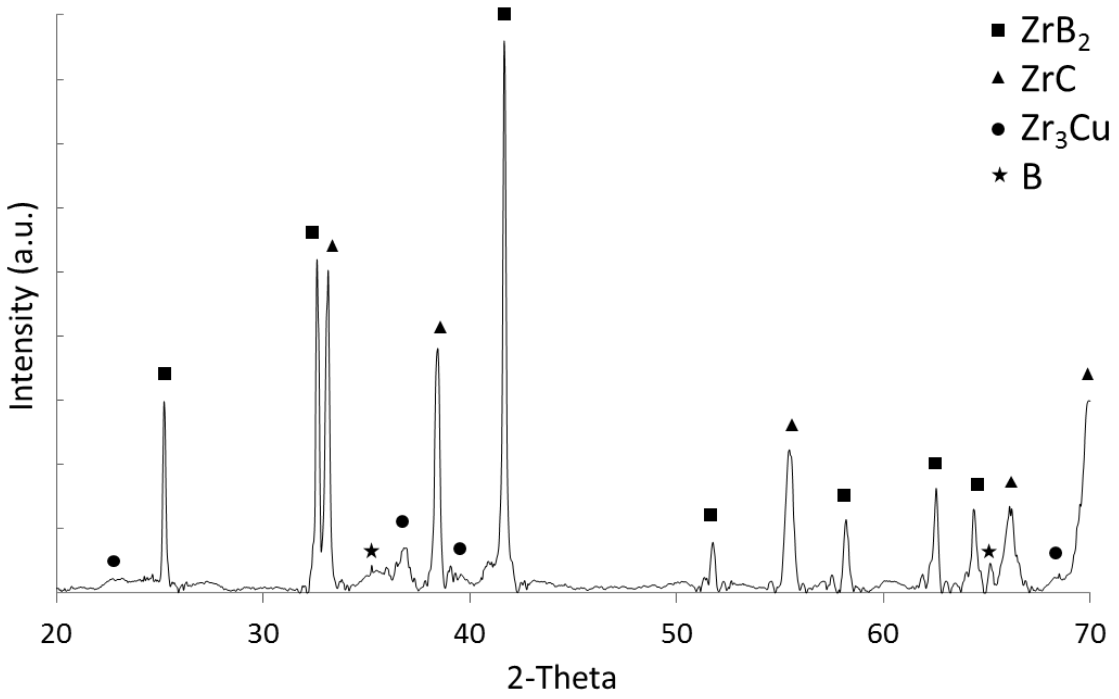

Figure 9.4 X-Ray diffraction pattern on the polished cross section of sample B25 after infiltration with Zr_2Cu.

9.2.3 Mechanical properties

The values of flexural strength are reported in table 9.2. All specimens fracture in a predominantly brittle mode due to the low final fibre content and to the strong adhesion between fibre and matrix and behave similarly to cermet materials. The higher strength of B50 and B75 compared to B25 could be attributed to the higher amount of fine ZrB_2 particles in the metal matrix that provide a better particle reinforcement. Even though B75 retained a higher amount of undamaged fibres, the strength was comparable to that of B50.

From the stress/displacement curves, all samples display very similar slopes (Fig. 9.5a) despite the different composition and microstructure. The fracture surface (Fig. 9.5b) is typically characterized by very short fibre pull-out (< 5 μm) and is more similar to that of conventional ceramics.

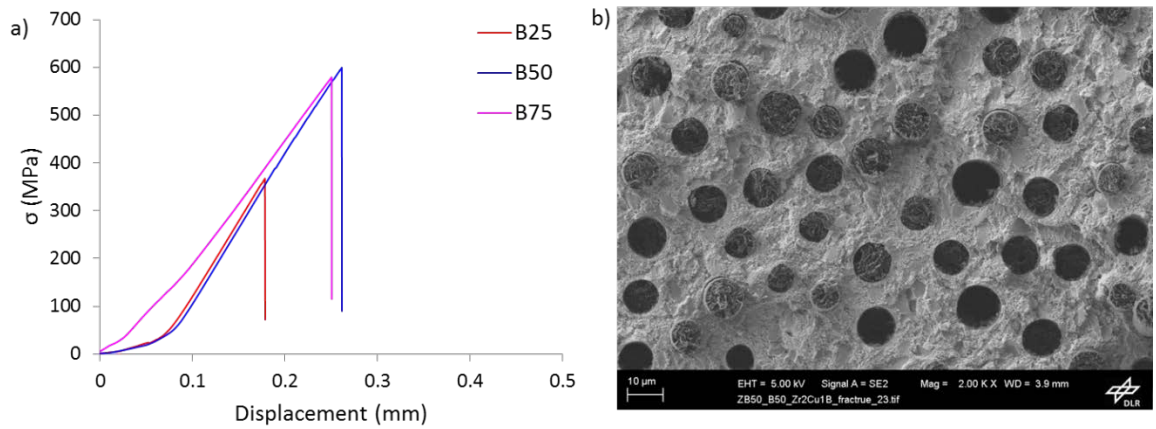

Figure 9.5 a) Stress vs displacement curves for samples B25, B50 and B75 tested by 4-point bending strength at room temperature. b) Fracture surface of sample B50 as reference.

9.4 Conclusions

A new processing route for the fabrication of fibre reinforced UHTCs was investigated. Carbon fibre preforms containing B/ZrB_2 mixtures in varying ratios were infiltrated with Zr_2Cu melt at 1200°C. All specimens display little to no porosity. The microstructure is characterized by coarse ZrB_2 from the commercial powders and fine ZrB_2 particles from the reaction between B and Zr_2Cu embedded in a matrix of Zr_2Cu. Increasing the boron content in the starting powders leads to an increase of the fine ZrB_2 particles fraction originating from RMI. This in turns minimizes the reaction between the fibre and the melt, resulting in a higher carbon content for B75. The strength of the composites is in the range of 350 – 560 MPa, with the highest values obtained for B50 and B75. This was attributed to a higher volumetric fraction of the fine ZrB_2 and to an overall lower amount of residual melt. All specimens fail catastrophically and the fracture surface is characterized by minimal fibre pull-out, indicating that RMI samples behave more like cermet materials.

9.5 References

1. Kütemeyer, M., Schomer, L., Helmreich, T., Rosiwal, S. & Koch, D. Fabrication of ultra high temperature ceramic matrix composites using a reactive melt infiltration process. *J. Eur. Ceram. Soc.* **36,** 3647–3655 (2016).
2. Ning, J. *et al.* Structural, elastic, electronic, and thermodynamic properties of intermetallic Zr_2Cu: A first-principles study. *Intermetallics* **54,** 7–14 (2014).
3. Zhao, Y. W., Wang, Y. J., Peng, H. X. & Zhou, Y. Dense sub-micron-sized ZrC-W composite produced by reactive melt infiltration at 1200 °c. *Int. J. Refract. Met. Hard Mater.* **30,** 196–199 (2012).
4. Zhu, Y. *et al.* Microstructure and mechanical properties of Cf/ZrC composites fabricated by reactive melt infiltration at relatively low temperature. *Ceram. Int.* **39,** 9085–9089 (2013).

10. Conclusions

ZrB_2/SiC based UHTCMCs

The mechanical properties and oxidation behaviour of carbon fibre reinforced ZrB_2/SiC composites were investigated. The first studies were carried out on a baseline composition containing ZrB_2 + 10 vol% SiC.

The flexural strength is lower than conventional ZrB_2/SiC bulk ceramics due to a higher degree of porosity and delamination, but a marked increase in fracture toughness and ultimate failure strain was registered.

With the increase of SiC content, grain size decreased slightly from 3 to 2.5 μm Initially the microstructure did not show significant signs of reaction with the fibres, but a more in-depth study on the fracture surfaces revealed hindered pull-out for higher amounts of SiC.

From random forest and regression tree analysis, the ratio between SiC and carbon fibre amount emerged as the most important parameter. Combining the results of both the statistical analysis, it can be said that in order to obtain a high-strength high-toughness composite, the composite should have a low volumetric fraction of matrix, and consequently a high amount of fibre, and a high SiC/fibre ratio. The first indication implies a low contribution from the weaker of the two phases making the composite. The second indication points out the importance of having a proper fibre/matrix interface to activate the load-transfer mechanism.

As far as oxidation resistance is concerned, kinetic parameters were evaluated by curve fitting of the isothermal curves. The critical temperatures for these composites are between 800 – 1000 °C; in this temperature range, the kinetic of formation of the protective borosilicate layer is still slow and the carbon fibres get rapidly oxidized, following an exponential mass decay law. Higher heating rates allow to quickly reaching the target temperature at which this protective layer forms, resulting in the parabolic mass gain.

From the short term oxidation tests in air at 1500°C and 1650°C it was found that for SiC contents <5 vol.%, the formation of the protective glass is not sufficient and this leads to excessive local burnout of the fibres, ultimately resulting in the rupture of the oxide layer. For SiC > 15 vol. %, the borosilicate layer covers the entire sample and this results in increased oxidation resistance. At 1650 °C the outer glassy phase partially

evaporates, exposing dendritic zirconia precipitated from the molten borosilicate glass. The thickness of the oxidized layer decreases with the increase of SiC content at all temperatures. The sample containing 20 vol. % SiC in the matrix is the least affected by oxidation and gets effectively passivated with no relevant changes to the microstructure and the weight loss.

ZrB_2/SiC/WC UHTCMCs

The mechanical properties and oxidation behaviour of carbon fibre reinforced ZrB_2/SiC/WC composites were investigated and compared with an un-doped reference sample.

The flexural strength is lower than conventional ZrB_2/SiC bulk ceramics due to a higher degree of porosity and delamination, but a marked increase in fracture toughness and ultimate failure strain was registered.

As far as oxidation resistance is concerned, the presence of WC leads to the formation of a more compact oxide layer that prevents further oxygen diffusion in the composite.

Carbide based UHTCMCs

The flexural strength for all the carbide systems investigated is in the range 280 – 340 MPa and increases up to 450 MPa at 1500°C due to stress relaxation.

All specimens experience a slight strength and modulus drop at 1800°C down to 400 MPa, which is still higher than the R.T. value

At 2100°C plastic deformation occurs via grain boundary sliding. ZC20 and HC20 are characterized by the highest failure strain due to weak fibre/matrix interface, whereas TC20 remains relatively stiff at all temperatures. TC20 and HC20 retain an overall higher strength (400 – 500 MPa), whereas ZC20 fails prematurely at 200 – 300 MPa.

Increasing the fibre content in sample HC20 led to a significantly different behaviour at 2100°C, with marked plastic deformation and very high failure strain. The overall strength is similar in value, but HC20b did not rupture after the test.

As far as thermal conductivity is concerned, it is not possible to draw definitive conclusions from thermal diffusivity data without the data relative to heat capacity, but the lower thermal diffusivity of TC20 and HC20 compared to ZC20 could be reasonably

attributed to the high density of the former (12.2 – 14.3 g/cm3) compared to the latter (6.73 g/cm3).

ZrB_2/ZrC UHTCMCs from RMI

A new processing route for the fabrication of fibre reinforced UHTCs was investigated. Carbon fibre preforms containing B/ZrB_2 mixtures in varying ratios were infiltrated with Zr_2Cu melt at 1200°C. All specimens display little to no porosity.

The microstructure is characterized by coarse ZrB_2 from the commercial powders and fine ZrB_2 particles from the reaction between B and Zr_2Cu embedded in a matrix of Zr_2Cu. Increasing the boron content in the starting powders leads to an increase of the fine ZrB_2 particles fraction originating from RMI. This in turns minimizes the reaction between the fibre and the melt, resulting in a higher carbon content for B75.

The strength of the composites is in the range of 350 – 560 MPa, with the highest values obtained for B50 and B75. This was attributed to a higher volumetric fraction of the fine ZrB_2 and to an overall lower amount of residual melt. All specimens fail catastrophically and the fracture surface is characterized by minimal fibre pull-out, indicating that RMI samples behave more like cermet materials.

11. Acknowledgements

In primo luogo ringrazio i miei relatori, Diletta e Luca, per avermi guidato in questo percorso, correggendo i miei errori e lasciandomi sempre abbastanza libero di esplorare questa ricerca.

Ringrazio Stefano per la sua pazienza e le sue conoscenze scientifiche indispensabili per portare a termine i lavori sulle proprietà meccaniche.

Ringrazio Cesare per la sua pazienza e disponibilità in laboratorio, per le innumerevoli richieste di prove meccaniche e per le chiacchere extra.

Ringrazio Daniele per la sua precisione e affidabilità e per i suoi sforzi (invano) di farmi muovere.

Ringrazio Claudio per il suo supporto tecnico e la pazienza di avermi sopportato mentre sporcavo il suo laboratorio senza pietà.

Ringrazio Mauro e Frederic per le loro conoscenze e trucchi sul SEM.

Ringrazio Jan per il suo aiuto con i tagli e la lucidatura e per la sua grande pazienza quando rigavo i dischi.

Ringrazio Andreana e Guia per la loro puntualità e professionalità per le prove di reologia e granulometria.

Ringrazio i professori Bill Fahrenholtz e Greg. Hilmas, e Jeremy per avermi ospitato a Rolla, in Missouri, ed essersi sempre resi disponibili per qualunque cosa, sia dentro che fuori l’università, e per aver cercato di alleviare le mie sofferenze con il caldo infernale.

Ringrazio il prof. Dietmar Koch per avermi ospitato presso i laboratori del DLR a Stoccarda, Thomas per avermi aiutato con gli esperimenti a 2000°C e per la sua puntualità tedesca, e Marius per l’ottima birra.

Infine ringrazio i miei genitori e i miei zii, Aldo e Carmela, per avermi sempre sostenuto in questi anni.

La mia attività di ricerca e il periodo di ricerca presso i laboratori del DLR sono stati finanziati dall' European Union's Horizon 2020 "Research and innovation programme" under grant agreement N°685594 (C3HARME).

Si ringrazia inoltre l'organizzazione JECS Trust per i fondi ricevuti per il periodo all'estero in Missouri e per la partecipazione ai workshop e convegni.